PULSED LASER ABLATION OF CALCIFIED BIOLOGICAL TISSUE: PHYSICAL MECHANISMS AND CLINICAL APPLICATIONS

by

JOSEPH ADAM IZATT

B.S., Physics, Massachusetts Institute of Technology
(1986)
M.S., Nuclear Engineering, Massachusetts Institute of Technology
(1988)

SUBMITTED TO THE DEPARTMENT OF
NUCLEAR ENGINEERING
IN PARTIAL FULFILLMENT OF THE REQUIREMENTS
FOR THE DEGREE OF

DOCTOR OF PHILOSOPHY

at the

MASSACHUSETTS INSTITUTE OF TECHNOLOGY

June 1991

Signature of Author Signature redacted
Department of Nuclear Engineering
May 17, 1991

Certified by Signature redacted
Michael S. Feld
Professor of Physics
Thesis Supervisor

Certified by Signature redacted
Sow-Hsin Chen
Professor of Nuclear Engineering
Thesis Reader

Accepted by Signature redacted
Allan F. Henry
Chairman, Department Committee on Graduate Students

PULSED LASER ABLATION OF CALCIFIED BIOLOGICAL TISSUE: PHYSICAL MECHANISMS AND CLINICAL APPLICATIONS

by

JOSEPH ADAM IZATT

Submitted to the Department of Nuclear Engineering on May 17, 1991 in partial fulfillment of the requirements for the Degree of Doctor of Philosophy in Nuclear Engineering.

Abstract

The goals of this thesis are 1) through a systematic study of the calcified tissue ablation process, to contribute to an understanding of the underlying physical mechanisms, and 2) to demonstrate the application of the new knowledge gained to a novel system for treatment of atherosclerosis through an optical fiber-based laser angiosurgery catheter.

The mechanisms for pulsed laser light interaction with calcified biological tissue are reviewed. For the purpose of modeling ablation, a simple exponential distribution of light in tissue is assumed, with the penetration depth determined experimentally from Kubelka-Munk theory. The steady-state model of ablation, which predicts an ablation fluence threshold and a constant ablation velocity, is used to analyze near-threshold ablation dosimetry data. Preliminary consideration of the gasdynamics of ablation at high irradiance, considered together with the composite nature of calcified tissue, suggests a two-component ablation mechanism in which the soft, connective tissue component is explosively vaporized, entraining and removing the hard calcium salt component. This newly proposed mechanism accomplishes highly efficient ablation on a fine scale at a lower temperature than is required to vaporize all tissue components.

Light penetration depths in compact bovine bone, obtained with Kubelka-Munk theory from total reflection and transmission measurements of thin samples, range from ~100 um at λ=250 nm to ~600 um at λ=700 nm. Between λ~300-700 nm, scattering dominates absorption by up to a factor of 10. Water, collagen, and hydroxyapatite all combine to absorb very strongly in the 3 μm wavelength region, resulting in penetration depths on the order of microns.

With the appropriate choice of irradiance, fluence, and wavelength, a variety of ablative effects are observed in calcified tissue. Irradiances on the order of MW/cm^2 produce char-free cutting without plasma generation. Tissue removal is linear with pulse fluence up to a few times threshold, although crater volume varies nonlinearly with both spot diameter and the number of shots fired into each crater. Ablation of calcified tissue with visible wavelengths longer than about 400 nm creates jagged-edge craters and large debris flakes and particles. Visible and near-ultraviolet wavelengths below 400 nm, as well as wavelengths near 3 μm, are capable of cutting with resolution and debris particle sizes on the order of tens of μm, with ~50 μm of peripheral thermal coagulation, allowing for the possibility of tissue micromachining. Ablation dosimetry studies indicate that those laser wavelengths which exhibit the sharpest cutting also have the lowest fluence thresholds and the highest ablation yields. Calculated values of penetration depth in tissue during ablation are dramatically smaller than penetration depth values measured spectroscopically in tissue

not undergoing ablation. Ablation thresholds in soft tissue and calcified plaque are approximately the same as for bone, but ablation yields are higher by a factor of ~1-5 for calcified plaque, and ~2-10 for soft tissue. Fluence thresholds for ablation under saline and a quartz microscope slide are approximately twice air thresholds.

Fast laser strobe photography (scattergraph configuration) of ablation reveals that material is ejected from the tissue surface beginning as soon as 100 nsec after the end of the ablation pulse, at velocities up to 600 m/s. The velocity and size distributions of debris particules ejected during ablation are very similar for strongly absorbed wavelengths in the near-ultraviolet (λ = 355 nm) and mid-infrared (λ = 2.8 μm) wavelength regions. Fast laser strobe shadowgraphs reveal spherical blast waves, visible as soon as 25 nsec after the ablation pulse, travelling outward from the ablation site at velocities on the order of 1000 m/s. These shocks travel faster than theory predicts for purely dissipative blast waves, implying exothermic processes in the ablation plume.

Results from ablation with two pulses separated by a variable time delay imply that the volume of tissue removed is insensitive to temporal pulse structure over the first few hundred nsec. Dual color sequenced pulse ablation experiments show that two sub-threshold pulses of different wavelengths combine to ablate tissue with the cutting characteristics determined by the more strongly absorbed wavelength.

The components of a new system for laser angiosurgery (LAS II) responsible for tissue ablation and laser light delivery through a catheter containing multiple, separately addressable optical fibers are described. Frequency-tripled light at λ = 355 nm from a solid-state Nd:YAG laser is used for plaque ablation in this system due to its excellent tissue cutting characteristics, avoidance of the potential for mutagenicity, and the laser's intrinsic advantages of high beam quality, safety, and reliability in a hospital environment.

The mechanism for laser-induced breakdown in the 200 μm core diameter optical fibers contained in the LAS II catheter is surface breakdown. In these fibers, breakdown fluence scales with pulse duration to the 0.85 power in the nsec regime. A novel two-stage passive pulse stretcher has been designed and built to stretch the 7.5 nsec duration pulses from two Q-switched Nd:YAG lasers to 210 nsec each, while maintaining high beam quality. When these stretched pulses are sequenced ~200 nsec apart, sufficient fluence is conducted down the fibers without breakdown to ablate densely calcified plaque at the other end, with enough left over to allow the beam exiting the fibers to expand in area by a factor of 7 to illuminate the entire catheter output surface.

All types of atherosclerotic plaque are successfully ablated with the completed LAS II system, generating craters large enough to pass the catheter in soft tissue. Dosimetry with the working LAS II catheter is consistent with results obtained previously by ablating vascular tissue with a focussed beam under saline and a simulated shield, although the advancement rate depends upon the catheter applied force on the tissue. Histology of tissue craters made with the LAS II system exhibits no charring, ~150 μm of thermal coagulation peripheral to laser craters, and significant disruption in soft tissue ablated at ~>10 gm catheter applied force.

Thesis Committee:
Supervisor: Michael S. Feld, Professor of Physics, M.I.T.
Reader: Sow-Hsin Chen, Professor of Nuclear Engineering, M.I.T.
Gordon Brownell, Professor of Nuclear Engineering, M.I.T.
Ashley J. Welch, Professor of Electrical and Computer Engineering, University of Texas at Austin
Irving Itzkan, Senior Research Scientist, M.I.T. Spectroscopy Laboratory

Acknowledgements

This work was conducted while I was a member of the Lester Wolfe Laser Angiosurgery Group at the M.I.T. Spectroscopy Laboratory. The scientific input and encouragement of all members of this group, as well as our collaborators at the Cleveland Clinic Foundation and G.V. Medical, Inc., is gratefully acknowledged.

I wish to thank my thesis committee for their attentive participation. Professor Feld served as my thesis supervisor for not only this but for two previous theses as well. His enthusiastic guidance and mentorship over the past six and one-half years has been very much appreciated. Dr. Irving Itzkan provided direction and day-to-day expert advice to the hard tissue ablation group. Many of the ideas contained in this thesis originated with him, including the two-component picture of ablation. Professors Chen and Brownell kept my work focussed, and relevant to the radiation science and technology program in the Nuclear Engineering Department. Professor Welch provided expert perspective on the place of my work in the larger community of laser-tissue interactions research.

Several staff members of the Spectroscopy Laboratory contributed to this research. Dr. G. Sargent Janes participated in the LAS II system implementation, in particular by playing a leading role in the invention and implementation of the pulse filler, and the fiber selection opto-mechanics. Gary Hayes invents and manufactures the world's best laser catheters, and participated directly in the LAS II dosimetry experiments. Dr. Ramachandra Dasari provided both scientific input, and much appreciated support in obtaining and maintaining facilities and equipment for our research effort.

I have worked with many former and current students on this work. Jay Jubas participated in some of the early parametric ablation studies. Doug Albagli worked closely with me on a large fraction of the work in this thesis, including some of the parametric ablation studies, all of the time-resolved ablation experiments, and all of the LAS II system development work. Doug took the lead role in advancing our understanding of optical fiber breakdown. Undergraduate UROP students who have assisted over the years have included Darius Sankey, who worked on ablation debris analysis, Mark Hamon, who did early work on fiber transmission, Matt Britton, who helped with ablation studies, and Bryan Banish, who contributed very substantially to our success in high energy fiber transmission.

Several members of our collaboration outside of M.I.T. deserve mention. Dr. John Kramer constantly steered our work toward clinical relevancy. Dr. Maryann Fitzmaurice provided analysis of laser crater histology. Several people at G.V. Medical, including Gary Moore, Jim Sharrow, John Brekke, Dave Liebl, Linda Madden, Tom Rasmussen, and Brett Demchuck provided support and assistance in design and construction of the LAS II system, and in dosimetry testing.

Portions of this work were supported by the National Institutes of Health through the administration of the M.I.T. Laser Biomedical Resource Center, by Baxter Technology and Ventures, Inc., and by G.V. Medical, Inc. I wish to thank Light Age, Inc., Questek, Inc., and Dr. Norman Nishioka and Mr. Yacov Domankevitch of the Wellman Laboratories of Photomedicine for the use of their facilities for some of the experiments described herein. During the past two years, I have received personal support as the Spectroscopy Laboratory Lester Wolfe Graduate Fellow, which I gratefully acknowledge.

Finally, I would like to acknowledge my family. My parents have provided continuous encouragement for my education since they dropped me off in Cambridge eleven years ago. My wife Susan, the original Dr. Izatt in our own small family, has given me much needed perspective and uncompromising support in this effort.

J.A.I.

Table of Contents

PART II: A PROTOTYPE SYSTEM FOR LASER ANGIOSURGERY

List of Symbols

Symbol	Typical Units	Description
a	mm	1/e radius of Gaussian spot profile
α	mm^{-1}	Kubelka-Munk linear attenuation coefficient
A_{shield}	mm^2	Area of LAS II catheter shield tip
c	J/gm-°C	Tissue specific heat
χ	–	Ratio of transport theory to Kubelka-Munk scattering coefficient
Δ	mm	Kubelka-Munk tissue section thickness
D	mm	Light penetration depth in tissue
d	mm	Laser spot diameter on tissue
δ	mm^{-1}	Characteristic depth for laser light attenuation in ablation debris
Δx	μm	Coherence length of strobe laser
E	V/cm	Laser electric field
$E_{1\ fiber\ catheter}$	mJ	Energy required to obtain fluence threshold on LAS II if only 1 fiber is fired
E_{fiber}	mJ	Energy per fiber in LAS II catheter
E_p	mJ	Laser pulse energy
Φ	W/mm^2	Fluence rate within the tissue
f	–	Geometrical efficiency factor for 3-D light distribution
ϕ	mJ/mm^2	Laser fluence on tissue surface
F_+	W/mm^2	Kubleka-Munk forward-propagating diffuse light flux
F_-	W/mm^2	Kubleka-Munk backward-propagating diffuse light flux
ϕ_0	mJ/mm^2	Fluence threshold for ablation
ϕ_{bkdn}	J/cm^2	Optical surface breakdown fluence
ϕ_{design}	mJ/mm^2	Design fluence for LAS II system
ϕ_{fiber}	mJ/mm^2	Fluence at fiber output ends in LAS II catheter tip
g	–	Average cosine of the phase function (anisotropy)
γ	–	Kubelka-Munk fluence rate correction factor
H	J	Amount of heat in "ablation cylinder"

η	–	Ratio of transport theory to Kubelka-Munk absorption coefficient
h_a	J/mm^3	Heat of ablation
η_{abl}	–	Efficiency of the ablation process
η_{IC}	probability/nsec	Probability per unit time for an electron to undergo an ionizing collision
I	W/mm^2	Laser irradiance on tissue surface
K	–	Constant for avalanche ionization breakdown
k	mm^{-1}	Kubelka-Munk absorption coefficient
k	mm^2/sec	Tissue thermal diffusivity
L	W/mm^2-steradian	Radiance
λ	nm	Laser wavelength
l	μm	Crater depth in tissue
m_{round}	–	Number of rounds in firing LAS II catheter
N	$electrons/cm^3$	Free electron population
n_{fiber}	–	Number of shots per fiber in firing LAS II catheter
n	–	Power of laser electric field for ionizing collision dependence
N_0	$electrons/cm^3$	Resting free electron population
$p(s,s')$		Transport theory phase function
P_1	kW	First threshold power for self-focussing
P_2	kW	Second threshold power for self-focussing
P_{av}	W	Average power at LAS II catheter tip
R		Radial beam profile
R_T		Total (integrated) reflectance from a tissue sample
ρ	gm/cm^3	Tissue mass density
r	mm	Radial coordinate parallel to the tissue surface
$\bar{r}$		Position vector
ρ_N	$particles/mm^3$	Number density of particles
σ	J/mm-sec-°C	Tissue thermal conductivity
s	mm^{-1}	Kubelka-Munk scattering coefficient
$\bar{s}$		Unit vector
σ_a	mm^2	Absorption cross-section of an individual particle
σ_s	mm^2	Scattering cross-section of an individual particle
T_T		Total (integrated) transmission through a tissue sample
T	°C	Tissue temperature

t	nsec	Time since the start of the laser pulse
τ	sec	Characteristic time for thermal diffusion in tissue
T_0	℃	Initial tissue temperature
t_0	nsec	Time to reach steady-state ablation velocity
τ_1	nsec	Laser pulse width corresponding to P_1 for self-focussing
τ_2	nsec	Laser pulse width corresponding to P_2 for self-focussing
t_p	nsec	Laser pulse duration
τ_{rec}	nsec	Electron-hole recombination time
τ_{sep}	nsec	Pulse separation in sequenced pulse experiment
U	W/mm^3	Power density distribution deposited in tissue by laser
u	J/mm^3	Energy density deposited in tissue by laser
v	m/s	Steady-state ablation velocity
$v_{catheter}$	mm/s	LAS II catheter advancement rate
ω	steradians	Solid angle
Y	mm^3/J	Ablation yield
Y_{bkdn}		Probability of surface breakdown
z	mm	Axial coordinate into the tissue
μ_a	mm^{-1}	Transport theory absorption coefficient
μ_s	mm^{-1}	Transport theory scattering coefficient
μ_s'	mm-1	Transport theory reduced scattering coefficient

Chapter 1
Introduction

The topic of this thesis is the ablation of calcified biological tissue with radiation from pulsed lasers, and its application to the treatment of atherosclerosis. In the introduction, the role of lasers in medicine in general, and in angiosurgery in particular, is outlined. Following the introduction, the thesis is divided into two parts. In Part I, the mechanisms of calcified tissue ablation are considered. Based upon an understanding of the the composition of calcified tissue, and the propagation of light and heat in tissue, a mechanism is described for efficient, precision-controlled ablation. Experimental work is presented concerning the dependence of ablation on irradiation parameters, and the time evolution of the ablation process. In Part II, the design and implementation of a prototype clinical system for laser angiosurgery is described. The choice of the ablation laser, and the implications for system engineering of the angiosurgery catheter design are discussed. Mechanisms for laser-induced breakdown in optical fibers are outlined, and the engineering design of a system to deliver high intensity light through fibers while avoiding breakdown is described. Studies of ablation dosimetry through the prototype catheter are presented. In the conclusion, the implications of this work for ablation modeling and clinical applications are summarized, and further studies are suggested.

Throughout this research project, there has been a close interaction between the basic ablation studies, described in Part I, and their application, described in Part II. In many cases, new developments on one of the two aspects motivated and provided new tools and ideas for further work on the other. For example, several components of the prototype angiosurgery system include features which provide unique facilities for basic ablation studies, in addition to their primary function. On the other hand, the two-pronged approach also led inevitably to compromises. In other instances, for example, further experiments on ablation mechanisms which would have been interesting to pursue were superseded by more practically relevant work on the angiosurgery system. Thus, the cohesiveness of this thesis depends critically on the interaction between both approaches.

The topics of calcified tissue ablation and laser angiosurgery are introduced in this chapter. First, a brief review of current research topics in laser medicine is given. Calcified tissue ablation is then placed in context relative to this background through a series of

sections which review relevant prior work. The problem of atherosclerosis is introduced, and prior research on laser treatment is reviewed. Finally, the chief aspects of the MIT approach to laser angiosurgery are described in sufficient detail to motivate the experimental studies which comprise the bulk of the thesis.

1.1. Applications of Lasers in Medicine

The growth of interest in recent decades in the applications of light, optics, and spectroscopy in medicine is related to several key technological advances which include, but are not limited to, the development of lasers [Itzkan 91]. The special qualities of lasers which makes the light they generate especially attractive for medical applications include high spatial coherence, tunability, and the production of high average power. Spatial coherence is important for beam handling, shaping, and focussing, and for efficient coupling into optical fibers. Tunability generates the capability of selecting optimal wavelengths for specific applications. High average power accompanying spatial coherence allows for the precise delivery of high energy densities to selected tissue sites.

The second major technical advance which has been critical to laser-tissue interactions research and applications is the development of optical fibers, which has been driven primarily by the communications industry [Katzir 86]. Making use of the spatial coherence of laser light, low loss optical fibers can deliver large fluences of laser light at high intensity to remote sites in the body, with minimal trauma to tissues which would otherwise have had to be cut away or removed to reveal the site of interest (see chapter 6).

The development of intensified detector arrays, particularly optical multichannel analyzers, has brought real-time spectroscopic analysis of tissue to the medical clinic and the operating room [Deckelbaum et al 88, Feld et al 91]. In many cases, the use of slower, conventional tools to accomplish the same task would not have been practical in the clinical setting. Finally, the development of computers for analysis and real-time control of medical instrumentation has amplified the impact of the other technical advances already mentioned.

Current research in laser applications in medicine may be roughly divided into four areas: biomedical optics, therapeutic applications, diagnostic applications, and biomedical instrumentation. Biomedical optics is the study of the intrinsic optical properties of tissue, primarily for the purpose of modeling light distributions in tissue. This includes theoretical work, such as analytical and numerical modeling of radiation transport, and experimental work, such as measuring tissue optical properties (for a review of light propagation models

and tissue property measurements, see section 2.2). The primary difficulty in modeling light propagation in tissue is that at most laser wavelengths, scattering dominates absorption in most biological tissues ([Cheong et al 90], chapter 3). While many approximate or numerical models have been suggested, no universally acceptable analytical models have been developed (see [Prahl 88]).

A relatively recent development in biomedical optics is the study of time-resolved photon migration in tissue [Chance 88, Wilson et al 90]. Using fast electronics and operating in either the time or frequency domain, the light scattering problem is simplified with this technique since the transit time of photons (and hence their approximate path length) is measured. Another advantage of this technique is that it is a particularly direct way to obtain absorption coefficients of tissues [Wilson et al 90]. Applications of time-resolved radiation transport have included *in situ* optical ranging in the skin, cornea, and retina [Fujimoto et al 86, Stern et al 89a, Huang et al 91] and initial steps toward optical tomography [Singer et al 90, Chance 88].

A second area of laser applications in medicine is in therapy. The most widely known and commercially successful therapeutic application is laser cutting or ablation of tissue, the "laser scalpel". Although an expensive technology, the advantages of laser cutting are still compelling under the proper circumstances. Requiring no physical contact between the light delivery system and the target tissue, the chance of infection is greatly reduced. In contrast to a sharp scalpel blade, which cuts by exerting pressure in excess of the local tissue tensile strength, laser ablation exerts no pressure on the tissue, aside from pressures generated by the process itself. (Unfortunately, tactile feedback to the surgeon is also absent [Walsh 88].) With the use of optical fibers inserted through endoscopes, catheters, and needles, surgery is possible in regions of the body which are inaccessible to the scalpel blade without the collateral damage which would have resulted from conventional surgery. The quantity of articles related to cutting and ablation in the journals Lasers in Surgery and Medicine and Lasers in the Life Sciences, along with the publication of several books on the topic, testify to its continuing relevance [Apfelberg 87, Breedlove et al 85, Dixon 87, Goldman 81, White et al 87]. The topic of this thesis also fits into this category.

Other applications of lasers in medical therapy do not involve tissue cutting. Nonablative laser treatments have been developed in dermatology, for example, which involve coagulation of subcutaneous blood vessels or destruction of pigment cells for treatment of skin disorders [Anderson et al 81, Tan et al 89]. Lasers are used as distributed heat sources for hyperthermia treatment [Svaasand et al 85]. Laser welding of tissue is an

active research topic for applications in vascular surgery and wound repair [Schober et al 86]. The activation with laser light of phototoxic exogenous chromophores, primarily hematoporphyrin derivatives, continues to receive attention as a treatment for cancer [Berns et al 86].

Thirdly, lasers are used for medical diagnosis and monitoring. Laser-induced fluorescence in tissue can serve as a probe for architectural and compositional changes signifying the onset and development of disease [Richards-Kortum 90]. Work in this area at MIT has demonstrated the successful identification and discrimination of various stages of atherosclerotic plaque, and neoplastic conversion in urinary bladder and gastro-intestinal tissues. Similar techniques using infrared wavelengths, which yield molecular level information, hold out the promise of gaining functional as well as morphological information [Rava et al 91].

Finally, several novel applications of lasers in biomedical instrumentation deserve comment. Laser-induced fluorescence microscopes are used in pathology research, contributing to the study of disease [Fitzmaurice et al 90]. Systems have been developed for rapid cell sorting by laser-induced fluorescence-based flow cytometry [Melamed et al 90]. Arthur Ashkin's "optical tweezers," which hold transparent microscopic objects at the focus of a laser beam through gradient forces, are capable of holding and manipulating individual, living biological cells [Ashkin et al 86, Ashkin et al 87]. This technique has been used to study the the mechanics of the biochemical motors contained in cells [Wright et al 90].

1.2. Laser Ablation of Tissue

Laser radiation is used routinely in medical applications to cut, shape, and remove tissue. In addition to the laser's usefulness as a general surgical cutting and cauterizing tool (see above), specialized laser treatments involving ablation have been developed for applications in many fields. The most advanced of these applications are found in the fields of ophthalmology, for intraocular photodisruption and corneal sculpting [Steinert and Puliafito 85, Zysset et al 89, Marshall et al 86], and cardiology, for laser angioplasty [Bohley et al 90, Goldenberg et al 90, Feld et al 91]. For a representative sample of the use of laser ablation in other medical specialties, see [ASLMS 91].

The lasers and wavelengths traditionally used for therapeutic applications were the cw Nd:YAG (λ = 1.06 μm) and argon-ion (λ = 488 nm) lasers for coagulation therapy, and

the cw CO_2 laser (λ = 10.6 μm) for cutting. The advent of new laser sources, however, combined with increased understanding of the role of wavelength and laser irradiance in obtaining desirable cutting quality, has resulted in a shift towards pulsed laser sources operating at strongly absorbed wavelengths (see chapter 4). Pulsed excimer lasers operating at several wavelengths in the ultraviolet (ArF, 193 nm; KrF, 248 nm; XeCl, 308 nm; XeF, 351 nm) are all very strongly absorbed in tissue, resulting in very clean cuts [Grundfest et al 85, Puliafito et al 87]. Light from several new pulsed solid-state crystal lasers operating in the mid-infrared (Thu:YAG, 2.0 μm, Ho:YSGG, 2.1 μm), while less strongly absorbed than ultraviolet light, is easier to couple high fluences into fibers, and has renewed interest in that wavelength region [Walsh 88, Nishioka et al 90]. Pulsed Er:YAG (2.9 μm) and hydrogen fluoride (2.6-3.1 μm) lasers have received considerable attention in the last few years because they operate near the strong water absorption peak at 2.9 microns in the infrared [Walsh 88, Izatt et al 90a, Wolbarsht 84, Valderrama et al 89, Valderrama et al 90]. Their strong absorption in tissue leads to clean cuts with very little thermal diffusion away from the ablation site, similar to the result obtained with the excimer lasers.

The literature concerning ablation of nonbiological materials with lasers, charged particles, and atmospheric friction dwarfs its biomedical counterpart. The earliest application of ablation (which bears little similarity to the process in tissue) was in aerospace, for ablative cooling of re-entry vehicles [Moss et al 86]. There are many ablative applications of lasers in welding, materials processing, and model making [Duley 83, Khrokhin 82]. Finally, ablation with lasers and particle beams of ballistic missiles received considerable attention in the past decade in the defense industry [APS 90]. Unfortunately, most of these applications involve highly absorbing media, so that ablation occurs at the surface. Thus, these studies have little relevance to the ablation process in highly scattering biological tissue. Modeling of the gasdynamic processes which occur above the tissue surface during ablation, however, does benefit from the materials ablation literature [Knight 79, 82].

A brief review of the literature concerning ablation mechanisms in different materials, and theoretical models for ablation, is given in section 2.4.

1.3. Hard versus Soft Tissue Ablation

Almost all laser cutting in current clinical practice targets soft tissues of the body, i.e. tissues of the eye or skin, or of the digestive, urinary, or gastrointestinal tracts, etc. The

remodeling of calcified tissue with lasers, however, has become an increasingly important problem in recent years. Examples of calcified tissue include bone, cartilage, teeth, and calcified atherosclerotic plaque. Although experimental procedures using CO_2 lasers for bone osteotomies have been under development for at least a decade [Horoszowski et al 87], several recent reports have indicated increased interest in the problem of calcified tissue removal for applications in orthopedics. Several authors have performed in vitro studies of ablation of bone and PMMA (used as a bone cement) with various ultraviolet and infrared lasers. Nelson et al [88] studied ablation of these materials at $\lambda = 2.9$ μm (Er:YAG); in the same group, Yow et al [89] continued the study at $\lambda = 308$ nm (XeCl excimer). The free electron laser, operating in the 3 micron range, was used to ablate bone samples [Dixon 88]. Systematic studies across several wavelengths have also appeared. Nuss et al [88] compared ablation in bone and PMMA at five infrared wavelengths ($\lambda = 1.06, 2.10, 2.94, 10.6$ μm). Izatt et al [90a] studied bone ablation at three HF laser wavelengths ($\lambda = 2.71, 2.83, 2.91$ μm), and later extended that study [91a, chapter 4 of this thesis] to a large number of wavelengths in the ultraviolet and visible region ($\lambda = 308$, 355, 375, 450, 503, 590 nm).

Interest is also high for calcified tissue ablation applications in dentistry, cardiology, and urology. Willenborg [89] reviews dental applications. Grundfest et. al. [85] started a revolution in laser angioplasty by reporting ablation of calcified plaque in vitro utilizing a pulsed XeCl excimer laser at $\lambda = 308$ nm; several commercial systems for laser angioplasty are based on excimer lasers (see section 1.4). Studies conducted at MIT [Kittrell et al 86] showed that plasma-mediated ablation with high-intensity pulsed Nd:YAG laser radiation at 1064 nm, 532 nm, and 266 nm cut through calcified plaque almost as easily as it cut the soft tissue of normal arterial walls. More recently, attention in the MIT group has shifted to non-plasma calcified plaque ablation in the near ultraviolet ($\lambda = 355$ nm) region [Izatt et al 91a, Feld et al 91]. Teng et. al. [87] removed kidney stones in vivo utilizing flashlamp-pumped dye laser light delivered through an optical fiber. The stones fragmented when irradiated with a high-energy pulse; the authors believe that the primary mechanism of fragmentation was the acoustic shock generated by absorption of the pulse.

While much of this activity has been stimulated by the advent of new laser sources and light delivery technology, additional motivation has come from the realization that a laser scalpel which can cut only soft tissue is of limited usefulness. As techniques are developed for reproducible, well-controlled ablation in bone, teeth, and pathogenic calcified tissues, the potential is realized for precise laser machining of all human tissues. Although

ablation of sample hard tissues with a variety of lasers sources has been well documented, systematic studies of the calcified tissue ablation process have not yet appeared. The primary aim of Part I of this thesis project is to develop a sufficiently detailed understanding of calcified tissue ablation to be able to address specific clinical problems objectively, based upon the desired ablation mechanism and characteristics, rather than the availability or novelty of particular laser sources. The clinical problem which motivated this work is atherosclerosis, which is the topic of the next section.

1.4. Laser Treatment of Atherosclerosis

Arteriosclerosis, a generic term for thickening and hardening of the arterial wall, is responsible for the majority of deaths in the United States and most westernized countries [Bierman 83]. Atherosclerosis is a type of arteriosclerosis which occurs in the larger arteries, and is the major cause underlying coronary artery disease, aortic aneurysm, arterial disease of the lower extremities, and cerebrovascular disease. The ailment which is the primary target for laser treatment is coronary artery disease (CAD), which is responsible for about half of all deaths (~1 million) annually in the US [Bierman 83].

The normal artery wall consists of three layers; from the inside of the vessel outward, they are the intima, media, and adventitia. The intima is primarily a mesh of loose connective tissue, the basal lamina, delimited on the inside by a layer of endothelial cells and on the outside by the internal elastic lamina (IEL), which is a tube of elastic tissue. The media is composed of smooth muscle cells, which are the major connective tissue manufacturers of the artery wall, producing collagen, elastic fibers, and proteoglycans. The outer edge of the media is delimited by a sheet of elastic tissue less well defined than the IEL, the exterior elastic lamina (EEL). Beyond the EEL lies the adventitia, a loose mixture of collagen bundles, elastic fibers, smooth muscle cells, and fibroblasts. In a normal large coronary artery, the lumen diameter is typically ~1.5 - 2 mm, and the thicknesses of the intimal, medial, and adventitial layers are on the order of 100 μm, 500 μm, and 500μm, respectively [Bierman 83, Richards-Kortum 90].

Atherosclerotic lesions are commonly classified into fatty streaks, fibrous plaques, and complicated plaques. Fatty streaks appear in a large fraction of the population in childhood, and have no clinical significance. Fibrous plaques are elevated areas of intimal thickening, consisting of a central core of extracellular lipid and necrotic cell debris covered by a fibromuscular cap [Bierman 83]. These lesions appear earliest in men, in their thirties, and progress with age. The increase in intimal thickness causes narrowing of the arterial

lumen, reducing the flow of blood to tissues served by the artery. In complicated atherosclerotic plaque calcified deposits form in the lesion, complicated by increasing amounts of necrosis, thrombosis, and ulceration [Bierman 83]. In addition to intimal thickening the arterial wall also weakens, leading to the possibility of rupture, causing aneurysm, hemorrhage, or ischemic heart attack.

The three most common forms of treatment for coronary atherosclerosis are medical management, coronary artery bypass grafting (CABG), and percutaneous transluminal coronary angioplasty (PTCA). Medical management involves the use of vasoactive drugs which act to relax vascular smooth muscle, increasing the lumen diameter [Cohn 85]. CABG is an open chest operation in which a segment of artery or vein is grafted around the site of occlusion, providing an alternative path for blood flow. CABG has an operative mortality rate of only a few percent [Braunwald 84], and several hundred thousand such operations are performed in the United States each year [American Heart Association 85]. Despite its success, CABG is traumatic, expensive, and time consuming (7-10 days hospital stay). In addition, contraindications for CABG include disease which is too diffuse to be treated with a small number of grafts, stenoses in inaccessible locations, and the lack of suitable autograft material [Braunwald 84].

PTCA is an operation in which a catheter with a small balloon at its tip is inserted through an incision in a peripheral artery, and is threaded through the arterial tree to the point of occlusion in the coronary artery. The balloon is then inflated, fracturing and displacing the plaque and leaving an enlarged lumen. Dramatic growth in the use of PTCA has occurred since its introduction in 1979 [Gruntzig et al 79], since it is less invasive, less expensive, and requires a shorter hospitalization than CABG. PTCA cannot be used in total occlusions or near bifurcations, and also has reduced effectiveness in diffuse lesions. Even under ideal circumstances for PTCA, however, several recent studies have shown that the long-term results of PTCA are significantly inferior to CABG [Kramer et al 89, Henderson et al 89]. These studies showed that an average of only ~60% of patients treated with PTCA suffered no additional complications after five years, versus ~90% for CABG. The difference in efficacy between PTCA and CABG is usually attributed to restenosis, an accelerated intimal thickening process thought to be induced by balloon-induced vascular injury [Essed et al 83, Austin et al 85]. Attempts have been made to reduce the incidence of restenosis following balloon angioplasty through the use of drugs, with no success [McBride et al 88, Fanelli et al 90].

A number of new approaches to coronary artery revascularization have been attempted with the goal of reducing the likelihood of restenosis, but which take advantage of the percutaneous approach. Devices which mechanically remove or restrain tissue to create a viable lumen include atherectomy devices, intravascular stents, and hot tipped catheters. None of these have been shown superior to PTCA in terms of initial success and long-term restenosis. Several approaches have used lasers to remove or assist removal of tissue. The first laser-based devices were bare fibers, laser-assisted balloon angioplasty catheters, and laser-heated hot tips, none of which were successful in practice [Tobis et al 89]. Following this initial experience, a number of more sophisticated laser-based devices were developed, including the initial MIT laser angiosurgery (LAS) system which used a multifiber, shielded laser catheter to deliver cw argon laser light in controlled doses to coronary lesions [Cothren et al 86a, Cothren et al 86b, Kramer et al 90]. Two problems plagued this first generation of laser catheters: the inability to remove calcified plaque, and vessel perforation [Litvack et al 88, Seeger et al 90]. The first problem occurred because the cw light used in these devices was insufficiently intense to ablate calcified tissue. The second problem was mostly due to the lack of a guidance system for the catheters, since the laser light indiscriminantly ablated both plaque and normal artery wall. Since the time of these trials, additional laser angioplasty systems have come to market which address the problem of calcified tissue ablation by using pulsed excimer lasers [Bohley et al 90, Goldenberg et al 90]. These latest devices avoid perforation by ablating relatively small amounts of tissue per pass though the artery, and using many passes. It is not clear that this strategy reduces the amount of trauma caused to the vessel wall, however, and initial clinical results have shown no improvement in restenosis rates over PTCA.

1.5. LAS II - The MIT Approach

Research conducted in the Laser Biomedical Research Center, housed in the MIT Spectroscopy Laboratory, has led to the development of a new laser angiosurgery system. This new system, denoted LAS II, overcomes the shortcomings of previous approaches. It is capable of removing both soft fibrous plaque and densely calcified plaque. This is accomplished with well-calibrated dosimetry, so that precise amounts of tissue are removed under careful control. Using a multi-pixel, guidewire-equipped catheter, it also incorporates a laser-induced fluorescence feedback loop which interrogates the tissue directly in front of each ablation fiber before firing to determine if it is atherosclerotic and should be removed. These two features allow for re-establishment of a patent vessel lumen in one pass through an artery, while causing the least possible trauma to the vessel wall. Animal studies have

shown that removal of tissue from artery walls with lasers, if done atraumatically, leaves a surface compatible with healing by complete re-endothelialization without intimal proliferation [Gerrity et al 83, Kjellstrom et al 88].

The salient features of the new system are illustrated through a consideration of the LAS II catheter, which is an advanced version of the original MIT LAS catheter. Several characteristics of the catheter allow for delivery of laser light to diseased arterial tissue in such a manner as to minimize deleterious host response to the procedure (see Fig. 1.1). These characteristics include the use of multiple individually addressable optical fibers, the use of an "optical shield" at the catheter tip, and the incorporation of a guidewire [Feld et al 91]. These catheter characteristics combine with a carefully chosen ablation wavelength and fluorescence–based spectroscopic feedback to provide maximum selectivity of diseased tissue and minimal trauma to normal tissue. These catheter characteristics also place constraints on the design of the optical delivery system (see chapter 6).

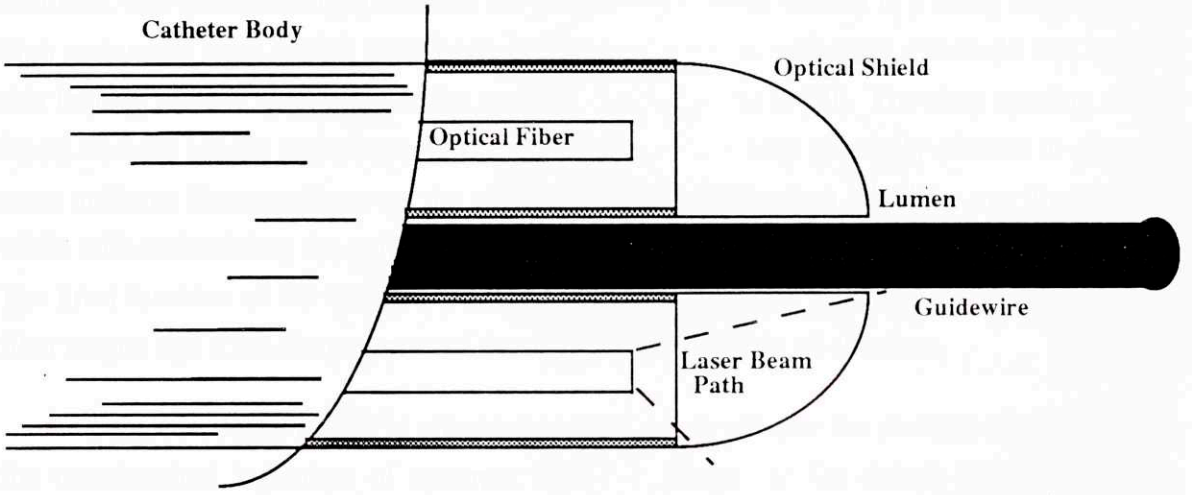

FIGURE 1.1. Schematic of the prototype LAS II laser angiosurgery catheter tip [Hayes 91].

Selectivity for ablation of only diseased tissue is accomplished through the use of multiple optical fibers. Twelve fibers are used in the current system, arranged in a ring at the catheter output face. These fibers are individually addressable by both the ablation and spectroscopic systems. This is in contrast to some competing laser angioplasty systems, in which the laser beam is focussed into an entire bundle of optical fibers [Bohley et al 90, Goldenberg et al 90].

Another prominent feature of the LAS II catheter is the employment of a transparent "optical shield" at the catheter tip [Cothren et al 86a, Cothren et al 86b]. The optical shield performs several functions important to the catheter performance. First, the shield is designed to be placed in contact with the lesion to be removed, displacing the intervening blood to provide a clear path for ablation and spectroscopic light passage. The shield being in contact with the tissue also holds the distance between the fiber tips and the tissue constant, allowing for accurate calibration of both ablation dosimetry and collected fluorescence intensity. The second major function of the optical shield is to provide a clear path for expansion of the light from the ends of the fiber to the catheter output face. This expansion is necessary to assure illumination of the entire catheter face, not just the regions directly in front of the fibers. It is important that the catheter completely ablates a composite hole as large as its own diameter, since if this is not the case, forcing the catheter through an ablated hole which is not large enough or through tissue which is not completely removed will cause severe trauma to the artery walls. Such trauma is a likely cause for the high restenosis rates which have been reported for several catheters which do not include this feature [Haase et al 90, Reeder et al 90, Untereker et al 90]. The ring spacing of the fibers and the length and shape of the optical shield are also carefully chosen to give the most uniform illumination over the catheter face possible when all fibers are illuminated, while still maintaining the selectivity of illuminating individual fibers or groups of fibers. The third function of the optical shield is to protect the highly polished and delicate optical fiber output tips from the contents of the artery and the rigors of ablation.

Finally, a central lumen is provided in the LAS II catheter for passage of a guidewire, for transluminal injection of contrast fluids or drugs, or for debris evacuation. The guidewire assists the spectroscopic diagnostic system to prevent perforation by maintaining a coaxial position of the catheter in the artery.

Development of the LAS II system at MIT has occurred along three complementary paths. The first was the invention, design, and development of construction techniques for the LAS II catheter. This has occurred over many years as an outgrowth of the original LAS catheter, involving contributions from all members of the MIT group and its medical and industrial collaborators. The second path was the development of a clinically effective ablation and light delivery scheme compatible with constraints imposed by catheter design. This is the area in which the author has had primary responsibility, and with which the bulk of Part II of this thesis is concerned. The third issue was the identification of a diagnostic feedback system for catheter guidance which works not only before a tissue site has been

fired upon, but after as well. Although this has been primarily the work of other people, it is mentioned where appropriate in this thesis, including its interaction with the rest of the system (see section 8.1).

All of the work described in this thesis was the result of a team research effort. Although the author played the lead role in performance and interpretation of basic ablation experiments, and in design and implementation of the ablation subsystem part of the LAS II system, most of the laboratory work was done in collaboration with other workers. In several cases, others directed work on component parts of the ablation subsystem. The role of other members of the group is noted in the Acknowledgements and in the relevant sections of this thesis. However, no research (in particular, no experiments) are presented here in which the author was not directly involved.

1.6. Conclusions

The quantity and variety of applications of lasers in medicine are numerous, and constantly increasing. Laser ablation of tissue continues to constitute a major proportion of laser-tissue interactions research, with increasing interest in the problem of calcified tissue ablation. A new laser angiosurgery system under development at MIT takes advantage of recent progress in calcified tissue ablation to provide a promising alternative to bypass surgery for treatment of coronary atherosclerosis. In contrast to competing systems, the new system ablates a lumen large enough to pass the catheter itself, does not cause excessive trauma to coronary vessel walls, and incorporates a guidance system to selectively ablate pathogenic tissue.

The goals of this thesis are to twofold: 1) through a systematic study of the calcified tissue ablation process, to contribute to understanding of the underlying physical mechanisms, and 2) to demonstrate the application of this knowledge to a new system for treatment of the important medical problem of atherosclerosis.

PART I

BASIC ABLATION STUDIES

Chapter 2
Mechanisms for the Interaction of Laser Light with Calcified Tissue

This chapter lays the groundwork for the experiments described in subsequent chapters. First, the structure and properties of calcified tissue relevant to ablation mechanisms are discussed. A brief review of tissue optics is given which is sufficient to generate simple estimates of light distribution in tissue. Finally, models for ablation are discussed. Most of this chapter is a review of previous work, although several new ideas are also presented.

2.1. Structure and Properties of Calcified Tissue Relevant to Ablation

A consideration of the morphology and thermal properties of calcified tissue is relevant to understanding ablation behavior. The tissues of primary interest in this thesis are bone and calcified atherosclerotic plaque. In the following, they are each discussed in turn.

2.1.1. Bone Structure and Function

Bone is a highly complex and adaptive tissue. The functions of bone in the body include structural support, protection of enclosed regions, serving as sources of muscular foundation and leverage, and housing of the marrow. Two primary organizations of bone tissue occur. Cortical or compact bone is densely packed tissue with few intervening spaces. Spongy, cancellous, medullary bone consists of less densely packed tissue with open spaces and canals within. Additional tissues line the outside surface of bones in varying thicknesses depending upon the location. The periosteum, a layer of dense connective tissue with no mineral content, lines the outer surface of bones and serves as the foundation for tendons and ligaments.

Compact bone exhibits a complex, hierarchical structure. Bone is formed in an appositional process, in which mineral salts are deposited upon largely parallel arrays of collagen fibers. The collagen fibers are of Type I, consisting of three nonidentical polypeptide chains. The fibers exhibit cross striations every 68 nm, corresponding to longitudinal gaps between tropocollagen molecules [Stryer 81]. These gaps are thought to

serve as nucleation sites for mineral deposition. The inorganic phase of bone is largely calcium hydroxyapatite [$Ca_{10}(PO_4)_6(OH)_2$], or variations of that salt in which sodium, potassium, magnesium, strontium, or radium are substituted for calcium, or in which fluoride is substituted for OH. Individual calcium hydroxyapatite crystals in bone are needle-shaped, with dimensions on the order of 2.5 x 2.5 x 30 nm [Brain 66].

Deposition of new bone occurs in microscopic layers called lamellae. Osteocytes, the primary constructive cells of bone tissue, occupy lacunae, spaces in the collagen-mineral matrix. The primary macroscopic structure of compact bone resides in the Haversian systems, which are lamellae arranged concentrically around a central canal. These systems run parallel along the length of long bones. In between Haversian systems, interstitial lamellae fill in the spaces. Small canals called canaliculi radiate perpendicular to the lamellae and allow communication between the osteocytes and the blood supply in the Haversion canals. The relative sizes of these systems depend upon the bone in question. Vaughan [70] provides micro-radiographs of adult human femoral cortex in cross-section, in which ~100 μm diameter Haversian canals are visible, with each entire Haversian system ~500 μm in diameter.

Typical dense cortical bone, which may be 85% mineralized by volume, consists of about 75% hydroxyapatite, 20% collagen, and 5% water by mass [Doty et al 76]. The mineral component provides compressive strength, while the soft connective tissue component provides tensile strength and resiliency. The unique structural properties of bone derive in part from this microscopic composite structure, and in part from its macroscopic organization along lines of stress.

2.1.2. Calcified Atherosclerotic Plaque

Atherosclerotic calcification is an advanced stage of the pathologic condition of atherosclerosis (see section 1.4). The initiation of calcification in atherosclerosis is not well understood, although there is evidence that calcium precipitation out of the bloodstream is promoted by acid phospholipids escaped from damaged artery wall cell membranes [Tomazic et al 88].

Calcified cardiovascular deposits are also composed of an intimate mixture of two phases, in which the soft component is about 5% water and 20% lipids and cross-linked proteins, and the hard component consists of a melange of apatite-like materials [Tomazic et al 88]. Optical and scanning electron microscopic examination of pulverized, deproteinated

deposits reveal a morphologically highly heterogenous material, consisting of particles and rough layers with dimensions on the order of μm [Tomazic et al 88].

2.1.3. Melting and Vaporization of Tissue Components

Water boils at 100 °C. Thermogravimetric analysis of dehydrated collagen indicates a boiling point for that substance on the order of 200 °C [Yannas 72]. Pure hydroxyapatite melts at 1670 °C [Windholtz 83]. Thus, the combination of water, collagen, and hydroxyapatite in bone represents a soft, low-vaporization temperature substance which resides in intimate contact with a hard, high melting temperature substance.

Thermogravimetric analysis of calcified cardiovascular plaque revealed that 1) the ~3-6% by mass water component was driven off between 40-140 °C, 2) the ~20% organic component was driven off in the temperature range 240-540 °C, and the remaining mineral component remained beyond the 1040 °C limit of the experiment [Tomazic et al 88]. This study confirms the similarity in microstructure and thermal characteristics between calcified plaque and bone.

The above aspects of calcified tissues suggests a mechanism for ablation in which the volatile component is rapidly vaporized, entraining and removing the calcium salts without their being vaporized. This two-component model of ablation is discussed further in section 2.4.7.

2.1.4. Justification of Bone as Primary Tissue Model

Although this thesis concerns the ablation of calcified tissue, most of the experiments reported herein were performed on bone. Bovine shank bone was selected as the primary calcified tissue model because of its homogeneity and sample-to-sample reproducibility, its ease of procurement and preparation, and for tissue handling safety considerations. The use of bone as the primary tissue model is justified by the morphological similarities between bone and other calcified tissues such as calcified plaque. Table 2.1 summarizes the information concerning the structure and properties of bone and calcified plaque from the previous sections. The similarities in structure and thermal properties between bone and calcified plaque justify using one as a model for the other, and several ablation studies reported in chapters 4 and 9 confirm this supposition in general, and test the differences in detail. Table 2.1 also includes information for two other calcified tissues, tooth and urinary calculi. In tooth enamel the soft component is keratin, and the tissue is ~90% mineralized. Most biliary calculi are composed of almost all hard component, and are therefore brittle.

Due to the low soft component content in these latter two tissues, their ablation is probably not well described by the two-component model motivated in the previous sections.

Tissue	Hard Component	Soft Component
Cardiovascular Calcified Deposits	75% Mixed Apatite Salts (m.p. ~1500°C) Granules ≤ 1 μm in size	20% Lipids, Cross-linked proteins (b.p. ~300°C) 5% Water (b.p. 100°C)
Bone	75% Hydroxyapatite (m.p. ~1500°C) Granules 1 to 10 μm in size	20% Collagen (b.p. ~300°C) 5% Water (b.p. 100°C)
Tooth Enamel	Hydroxyapatite	Keratin
Urinary Calculi	Calcium Oxalate	None

TABLE 2.1. The composite nature of some calcified tissues.

2.2. Tissue Optics

The distribution of laser light in tissue is a very complicated function of its wavelength-dependent intrinsic optical properties. Models for light distribution are important both for extracting optical properties from experimental data, and for using those properties to predict light distributions under new irradiation conditions. Many authors have presented models for light distribution in tissue, as well as measurements of tissue optical properties (see, for example, Welch et al [87], van Gemert et al [89], Yoon et al [87], Jacques et al [87], Prahl [88]; for an excellent review of optical property measurements, see Cheong et al [90]). It is beyond the scope of this thesis to review all recent developments in this field. However, understanding ablation requires at least a rudimentary understanding of the shape of light distribution in tissue (see section 2.4). In addition, a method which is at least approximately correct for extracting tissue optical properties from thin section transmission and reflection measurements is required to analyze the experiments described in chapter 3.

In order to satisfy these needs, a brief review of tissue optics is presented in this section. This review concentrates on practical analytical results, even though they are approximate. First, general methods of describing light distributions in tissues will be described, with the appropriate variables definitions given. Then, approximations to the

general relations appropriate to specific irradiation conditions will be presented and discussed.

2.2.1. Modeling Light Distribution in Tissue: Transport Theory

Light propagation in tissue can be considered as a special case of radiation transport in random media [Chandrasekhar 60, Ishimaru 78]. Conventional problems in electromagnetics usually deal with deterministic wave propagation, such as is encountered in antenna, waveguide, and diffraction theory. In contrast, problems of wave propagation in random media may involve unpredictable variations in wave amplitude and phase. Random media may consist of 1) a distribution of discrete absorbers and scatterers, such as in fog, schools of fish, or erythrocytes; 2) a continuous medium whose complex index of refraction varies randomly, such as in planetary atmospheres, air and water turbulence, and most biological tissues; or 3) rough surfaces, such as those on planets, the oceans, and at interfaces between layers of biological tissue.

In realistic models, tissue is rarely regarded as a random continuous medium. It is more usually approximated as a distribution of discrete absorbers and scatterers, each of which have intrinsic scattering properties. Starting with this description of tissue, two methods are available for modeling how light interacts with large collections of absorbers and scatterers. The first method, multiple scattering theory, starts with a description of the interaction of waves with individual particles, and then introduces the interaction effects of many particles with statistical averaging. This method is very difficult, and has not been applied to light propagation in tissue.

The second method for describing light distribution within a large collection of absorbers and scatterers is transport theory. Transport theory describes the propagation of intensities, based on phenomenological observations of transport characteristics. Therefore, it does not describe diffraction and interference between fields; in this sense it is less rigorous than multiple scattering theory.

Transport theory describes light propagation in a random collection of scatterers and absorption by the radiative transport equation:

$$\bar{s} \cdot \nabla L(\bar{r},\bar{s}) = -(\mu_a + \mu_s) L(\bar{r},\bar{s}) + \mu_s \int_{4\pi} p(\bar{s},\bar{s}') L(\bar{r},\bar{s}')\, d\omega'. \qquad (2.1)$$

Here $L(\bar{r},\bar{s})$ is the radiance ($W/mm^2/sr$) of light at position $\bar{r}$ travelling in the direction of the unit vector $\bar{s}$. The first term on the right represents the decrease in the radiance due to absorption and scattering out of the direction $\bar{s}$, while the second term describes the increase in the radiance due to scattering from other directions $\bar{s}'$ into the direction $\bar{s}$. Absorption and scattering are described by the coefficients μ_a and μ_s (mm^{-1}), and the phase function $p(\bar{s},\bar{s}')$. The overall absorption and scattering coefficients are connected to the cross sections for absorption (σ_a) and scattering (σ_s) of single particles by their number density, ρ_N (particles/mm^3):

$$\mu_a = \rho_N \cdot \sigma_a, \tag{2.2}$$

$$\mu_s = \rho_N \cdot \sigma_s. \tag{2.3}$$

The phase function $p(\bar{s},\bar{s}')$ represents the normalized probability that light scattered out of the direction $\bar{s}'$ is scattered into the direction $\bar{s}$. The form of this phase function is often unknown; for simplicity, it is usually assumed to be a function only of the angle between $\bar{s}$ and $\bar{s}'$, and is characterized by its average cosine, g:

$$g = \int_{4\pi} p(\bar{s},\bar{s}')(\bar{s}\cdot\bar{s}')\, d\omega'. \tag{2.4}$$

Here $d\omega'$ is the differential solid angle in the direction of $\bar{s}'$. The three quantities g, μ_a, and μ_s represent the fundamental tissue optical properties in most treatments of laser light distribution in tissue.

Heat deposition in tissue occurs by light absorption from all directions. The integral of the radiance over all solid angles is the fluence rate, Φ (W/mm^2, also called the space irradiance). The rate of energy deposition in the tissue per unit volume, the power density, U (W/mm^3), is given by the product of the local absorption coefficient and the fluence rate,

$$U = \mu_a \cdot \Phi . \tag{2.5}$$

2.2.1.1. Methods for Solution

Even with the simplification that the phase function depends only on the angle between $\bar{s}$ and $\bar{s}'$, analytical solutions for the radiative transport equation are not available. Two approaches are generally taken to obtain approximate solutions. The first is numerical simulation, in which individual photon trajectories through a model tissue are calculated

with monte carlo methods, and the resulting fluence rate is summed over a large number of trajectories. Although this method provides a complete solution, it does not yield analytical expressions, and is of little use here.

The second method for solution is to make approximations. In increasing order of complexity, commonly used approximations include Beer's law, Kubelka-Munk theory, and the diffusion approximation. The first two approximations, described below, are one-dimensional; and the third is only described qualitatively. Thus only one-dimensional light distributions are considered. This is reasonably accurate for most of the wavelengths and beam diameters used in this thesis (see chapter 4); ablation effects which depend upon the three-dimensional shape of the light distribution are modeled phenomenologically in section 2.4.5.2.

2.2.1.1.1. Beer's Law

If absorption dominates scattering, all scattering terms drop out of the transport equation. The fluence rate within the tissue falls off exponentially from its value at the surface, the irradiance (I):

$$\Phi = I \cdot \exp[-(\mu_a+\mu_s) \cdot z]. \qquad (2.6)$$

This result is accurate only for very strongly absorbed wavelengths, such as near 3 μm.

2.2.1.1.2. Kubelka-Munk Theory

An approximate one-dimensional model for light distribution in random media, which is valid for scattering comparable to or greater than absorption, is Kubelka-Munk theory [Kubelka 48, Kubelka 54]. This model has been widely used in tissue optics, since it provides simple formulas for optical properties as a function of reflectance and transmission of tissue samples. It is only relatively recently that this theory has been shown to represent an approximate solution of the equation of radiative transport [Ishimaru 78].

Kubelka-Munk theory models the light distribution in terms of two diffuse counter-propagating light fluxes, F_+ and F_-. The medium is assumed to be an laterally infinite slab with thickness Δ. The medium has an "absorption" coefficient k and a "scattering" coefficient s. Because only diffuse fluxes are considered, these coefficients are not the same as the transport absorption and scattering coefficients; the connections between the two sets of coefficients are described below. Since there are only two directions of

propagation in the medium, light which is scattered adds to the flux in the opposite direction. Thus, the change in flux in each direction over a small distance dz may be written:

$$\frac{dF_+}{dz} = -(k + s)\cdot F_+ + s\cdot F_- ; \tag{2.7}$$

$$\frac{dF_-}{dz} = (k + s)\cdot F_- - s\cdot F_+ . \tag{2.8}$$

Exponential attenuation of the flux in each direction is assumed, with coefficient α:

$$F_+ = C_1 e^{-\alpha z}; \qquad F_- = C_2 e^{+\alpha z}. \tag{2.9}$$

Inserting Eq. (2.9) in Eqs. (2.7-8), and solving for the attenuation coefficient yields:

$$\alpha = \sqrt{k(k+2s)}. \tag{2.10}$$

The coefficients C_1 and C_2 are determined by the boundary conditions: at z=0, the positive propagating flux equals the incident irradiance, while at $z=\Delta$, the negative propagating flux equals zero. Inserting these boundary conditions, and solving for the negative propagating flux at z=0, and the positive propagating flux at $z=\Delta$, yields expressions for the total reflection (R_T) and transmission (T_T), respectively. With considerable algebra, these expressions may be inverted for k and s as a function of R_T and T_T:

$$a = \frac{1 - R_T^2 - T_T^2}{2R_T}; \qquad b = \sqrt{a^2 - 1}\ ; \tag{2.11}$$

$$s = \frac{1}{\Delta\cdot b} \ln\left[\frac{1 - R_T(a-b)}{T_T}\right]; \qquad k = s\,(a - 1)\,. \tag{2.12}$$

The fluence rate is given by Klier [72] as a linear combination of the forward and backward propagating fluxes,

$$\Phi = \gamma[F_+ + F_-]. \tag{2.13}$$

Here γ approaches 1.0 for the case of dominant absorption, and 2.0 for dominant scattering. Although this expression appears to be a complicated function of α, for the cases of scattering ~ absorption, and scattering ~> absorption, it approximates an exponential decrease into the medium with attenuation coefficient α [Welch et al 87]. For scattering >> absorption, the fluence rate predicted by Kubelka-Munk is still approximately

exponential, but with a penetration depth greater than $1/\alpha$ (although the theory is still quite correct here). It will be shown in chapter 3 that throughout most of the near-ultraviolet and visible wavelegnth region, the scattering coefficient in bone ranges up to a few times the absorption coefficient, and that in the mid-infrared region, absorption dominates scattering. Thus, throughout this thesis, the distribution of light in tissue is assumed to be exponential with a penetration depth $D = 1/\alpha$.

Several workers have correlated the Kubelka-Munk coefficients k and s with the optical transport properties μ_a, μ_s, and g [Klier 72, van Gemert et al 87, Cheong et al 90]. van Gemert et al [87] provide a graph of the quantities η and χ which relate the Kubelka-Munk coefficients to the transport properties, assuming an anisotropic phase function:

$$\mu_a = \eta \cdot k \; ; \tag{2.14}$$

$$\mu_s(1-g) = \mu_s' = \chi \cdot s. \tag{2.15}$$

Only the reduced scattering coefficient $\mu_s(1-g)$, and not μ_s and g separately, are available from this analysis. A linear approximation to their graphical result, which is valid to within ~5% for $0 \le k/s \le 2$ is:

$$\chi \approx 1.333 + 0.245 \cdot \frac{k}{s} \; , \tag{2.16}$$

$$\eta \approx 0.5 + 0.05 \cdot \frac{k}{s} \; . \tag{2.17}$$

Kubelka-Munk theory and its enhancements provide approximately correct expressions for fluence rate and intrinsic tissue optical properties as a function of experimental variables. It is thus a useful tool when more sophisticated methods are not available or not warranted, which is the present case. Among its drawbacks are the assumptions of isotropic scattering, index-matched tissue boundaries, and diffuse fluxes. Nonetheless, the theory compares favorably to within 25% of predictions from diffusion theory and seven-flux theory for all ratios of scattering to absorption except for the extreme case of scattering >> absorption [Welch et al 87].

2.2.1.1.3. Diffusion Approximation

In the diffusion approximation, the radiance in Eq. (2.1) is separated into scattered and unscattered components:

$$L(\bar{r},\bar{s}) = L_c(\bar{r},\bar{s}) + L_d(\bar{r},\bar{s}). \qquad (2.18)$$

The unscattered component obeys Beer's law. The scattered component may be expressed as a truncated sum of Legendre polynomials, which when substituted back into Eq. (2.1) yield a solvable diffusion-like equation. Solutions to the diffusion equation have been obtained for the fluence rate, total reflectance and transmittance [Cheong et al 90]. Unfortunately, these expressions may not be inverted to give the optical properties as a function of reflectance and transmission, so values must be obtained through iteration. The diffusion approximation is accurate for optically dense and highly scattering media, far from tissue boundaries or internal sources of light. It is not described in more detail here since the Kubelka-Munk theory provides compact analytical expressions for tissue optical properties of sufficient accuracy for the present purpose.

2.2.2. Changes in Optical Properties Resulting from Irradiation

Several authors have investigated changes in tissue optical properties which result from heating, coagulation, and ablation. Thomsen et al [90] found irreversible increases in μ_a and $\mu_s(1\text{-}g)$ at $\lambda = 594$ and 633 nm upon heating myocardium, which they attributed to Mie scattering from thermally coagulated granular cellular proteins. Agah et al [90] also found increases in absorption and scattering at $\lambda = 514$ and 633 nm upon nonablative heating of aorta wall, which they attributed to Rayleigh scattering from thermally denatured collagen fibrils. An irreversible decrease in absorption in the mid-infrared was observed by Berry et al [89], on the other hand, upon heating corneal tissue.

Transient changes in tissue optical properties during ablation with visible and mid-infrared wavelengths have been proposed by Izatt et al [90a, 91a, 91b] and Letokhov [91]. These changes are suggested to account for a disagreement between attenuation depths in tissue measured in a spectrometer, and calculated from ablation results. This topic is discussed in chapter 4. Transient "bleaching" of polymer substrates during ablation has been observed and preliminary models suggested [Sauerbrey et al 89].

2.3. Heat Diffusion in Tissue

The previous sections have discussed the complicated problem of light distribution in tissue. Once the interplay of scattering and absorption determines this distribution, the energy deposited within each infinitesmal volume of the tissue is equal to the local fluence rate times the absorption coefficient (Eq. 2.5). As a first approximation which roughly

agrees with the predictions of both Beer's law and Kubelka-Munk theory, we assume that the resulting heat deposition profile falls off roughly exponentially from the surface of the tissue. This occurs with a profile characterized by the light penetration depth, D, which is to be determined experimentally (see chapter 3).

Absorption of visible and near-ultraviolet light in tissue occurs by exciting electronic transitions in tissue molecules, primarily proteins and lipids (see section 3.3). Near- and mid-infrared light is absorbed via vibrational-rotational excitations in biomolecules, as well as in water. The lifetimes of both the electronic and vibrational-rotational states are much less than laser pulse durations on the order of hundreds of nsec. As soon as the initial excited state distributions thermalize, the energy which was deposited by the laser pulse may be considered as heat, and its dissipation is described by thermal diffusion.

In the next section, thermal parameters of tissue relevant to heat diffusion are briefly discussed. Following that, solutions to the heat diffusion equation for practical laser energy deposition profiles are presented.

2.3.1. Thermal Diffusivity of Tissue

The thermal properties of tissue relevant to heating (without phase change) and heat diffusion are the density (ρ), specific heat (c), and thermal conductivity (σ). For thermal diffusion calculations, the important quantity is the thermal diffusivity, obtained from these quantities via:

ρc = specific heat per unit volume, and (2.19)

$$\kappa = \frac{\sigma}{\rho c} = \text{thermal diffusivity.} \qquad (2.20)$$

A compilation of estimates for ρc and κ in biological media made by various authors are listed in Table 2.2. Most of the estimates do not stray too far from the thermal properties of pure water, which comprises ~60-90% of all biological tissues excepting bone, teeth, hair, and pathogenic calcifications [Altman et al 72]. Estimates of thermal properties for bone are unfortunately not available.

Medium	Specific Heat per unit Volume, ρc ($J/°C\text{-}mm^3$)	Thermal Diffusivity, κ (mm^2/sec)	Reference
"Tissue water"	3.96×10^{-3}	0.106	Chato [69]
"Wet tissue"	3.66×10^{-3}	0.101	Jacques et al [87]
"Tissue"	–	0.130	Walsh [90]
Pure water	4.18×10^{-3}	0.146	Weast [78]

TABLE 2.2. Estimates of thermal properties of tissue.

2.3.2. Thermal Diffusion -- Semiinfinite Slab Geometry

Measured light penetration depths (D) in most tissues of clinical interest range from fractions of a micron in the 3 μm region, up to several millimeters in the near-infrared [Cheong et al 90]. In chapter 4, it is demonstrated that the best laser cutting of calcified tissue is obtained with wavelengths which are absorbed in less than a few hundred μm. Practical laser spot diameters on tissue (d), on the other hand, are rarely less than ~500 μm. For most situations of clinical interest, it is thus sufficient to consider the limit in which d>>D. In this limit, the illuminated region of the tissue corresponds to a disk of thickness D and diameter d. Most of the heat lost from the disk will occur out of the bottom, so a semi-infinite one-dimensional slab geometry may be used to describe heat diffusion.

The equation of heat conduction in this geometry reduces to [Carslaw et al 47]:

$$\frac{\partial T(z,t)}{\partial t} = \kappa \frac{\partial^2 T(z,t)}{\partial z^2} . \qquad (2.21)$$

Here T(z,t) is the temperature, a function of both distance into the tissue (z) and time after the (assumed short) laser pulse is over (t). This equation must be solved subject to the initial temperature distribution T(z,t=0) which the laser pulse deposits in the tissue. In order to gain an appreciation of the influence of the specific shape of the initial heat distribution on long-term diffusion behavior, solutions are obtained in the following for two trial initial heat distribution functions: a step-function heat distribution in which tissue to a depth D is initially heated, and an exponential heat distribution with a 1/e deposition depth D. The boundary condition of no heat diffusion across the tissue surface (z=0) is assumed.

For the step-function initial condition,

$$T(z,t=0) = \left\{ \begin{array}{ll} T_0 ; & 0 \le z \le D \\ 0 ; & z > D \end{array} \right\}, \tag{2.22}$$

the diffusion equation is solved by inserting a mirror initial condition above the tissue surface, and using Laplace's solution for the infinite solid. The solution is [Carslaw et al 47]:

$$T(z,t) = \frac{1}{2} T_0 \left[\mathrm{erf}\left(\frac{D - z}{2\sqrt{\kappa t}}\right) + \mathrm{erf}\left(\frac{D + z}{2\sqrt{\kappa t}}\right)\right]. \tag{2.23}$$

In Fig. 2.1, this function is plotted with T(z,t) in units of T_0, z in units of D, and t in units of

$$\tau = \frac{D^2}{4 \cdot \kappa}. \tag{2.24}$$

The solution of the heat diffusion equation for the exponential initial condition,

$$T(z,t=0) = T_0 \cdot e^{-z/D}, \tag{2.25}$$

is obtained using the same method as above. It is [Itzkan 91]:

$$T(z,t) = \frac{1}{2} T_0 \left\{ e^{(\kappa t/D^2 - z/D)} \left[1 + \mathrm{erf}\left(\frac{z}{2\sqrt{\kappa t}} - \frac{\sqrt{\kappa t}}{D} \right) \right] + e^{(\kappa t/D^2 + z/D)} \left[\mathrm{erfc}\left(\frac{z}{2\sqrt{\kappa t}} + \frac{\sqrt{\kappa t}}{D} \right) \right] \right\}. \tag{2.26}$$

This function is plotted in Fig. 2.2, also in terms of the same units. By comparing the two figures, it is clear that after ~τ/2, there remains relatively little qualitative difference between the heat profiles from the different initial conditions.

It is common in the literature to refer to τ as the characteristic time for thermal diffusion in tissue. This value is used both for determining how short laser pulse durations must be in order to avoid thermal damage in peripheral tissue, and also to determine the maximum repetition rate for avoiding thermal pile-up. It is instructive to investigate quantitatively how good of an approximation this is. Walsh et al [90] numerically integrated the total energy contained within the 1/e depth of an exponential heat deposition profile, and found that it took approximately 10 times τ before the energy was reduced to 1/e of its

initial value. In Fig. 2.3 below, the temperature value at depth D divided by its initial value is plotted for both the step-function and exponential initial conditions. Note that the initial temperature rise for the exponential initial condition is real, as can be verified by examing the temporal evolution of the temperature at depth D in Fig. 2.2. It is seen from Fig. 2.3 that it takes approximately 2 and 4 times τ for the temperature value at that point to relax by 1/e for the step-function and exponential initial heat distributions, respectively. This is contrasted in the figure to exponential relaxation with time constant τ, which is the essence of the common assumption. It appears from these arguments that if an exponential initial heat distribution is assumed, a better relaxation time constant τ_R for thermal diffusion is in the range 4 to 10 times τ.

Finally, it is useful to obtain an estimate for the thermal relaxation time in tissue at wavelengths of interest in this thesis. The wavelength chosen for the LAS II system, for example [chapter 6], has an attenuation depth in bone on the order of 200 μm [chapter 3], yielding an value for τ_R of

$$\tau_R \approx \frac{D^2}{\kappa} = \frac{(0.2\ \text{mm})^2}{0.106 \frac{\text{mm}^2}{\text{sec}}} = 377\ \text{msec.} \qquad (2.27)$$

This is very long on the time scale of pulsed lasers, so it is concluded that thermal diffusion is not a factor in the ablation process itself, which can occur on a very fast time scale (chapter 5). The value is so long, however, that it is relevant to the pulse repetition rate. A slight amount of charring on bone, for example, has been observed even for high irradiances at a repetition rate of 10 Hz (see Fig. 4.7(a)). This charring may be due to a temperature buildup over many pulses, each of which arrive well before the tissue has completely relaxed from the previous pulse.

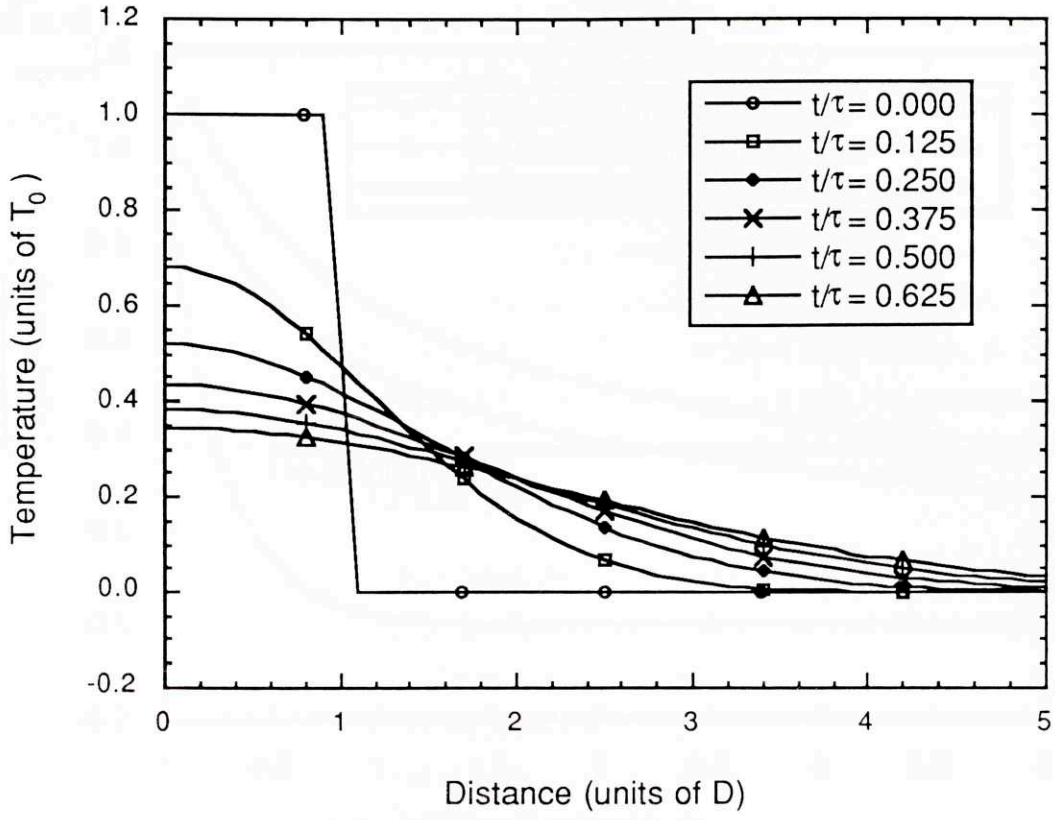

FIGURE 2.1. Temperature decay for the step-function initial heat distribution.

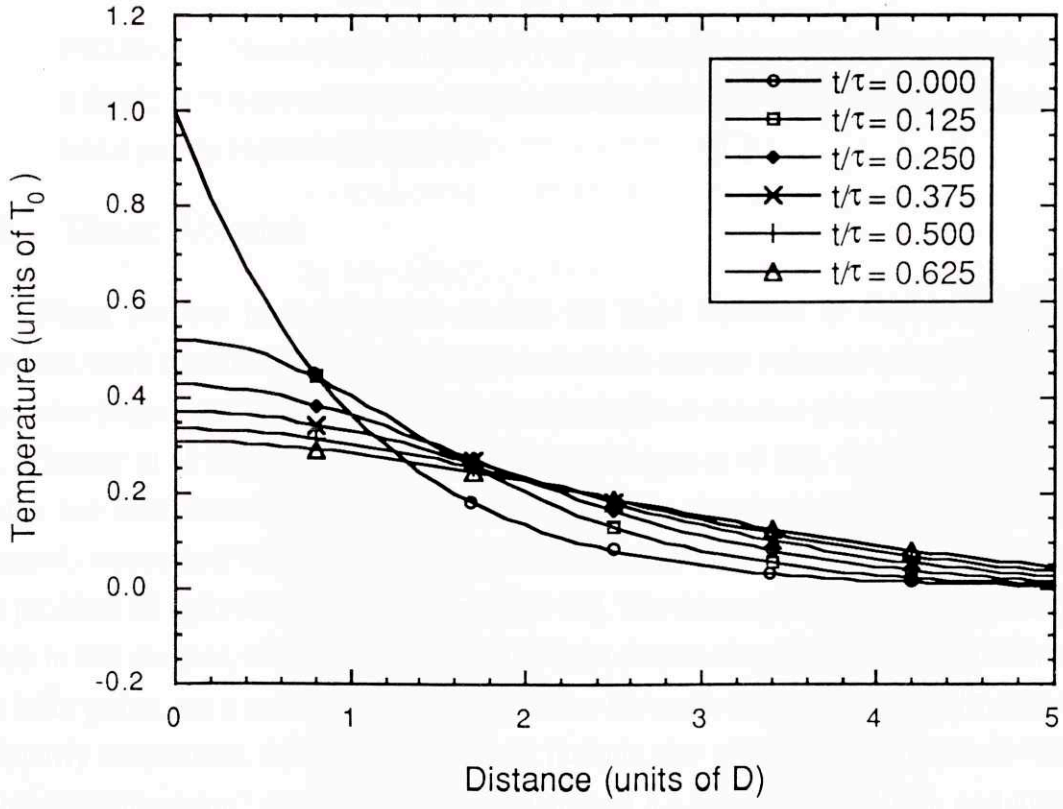

FIGURE 2.2. Temperature decay for the exponential initial heat distribution.

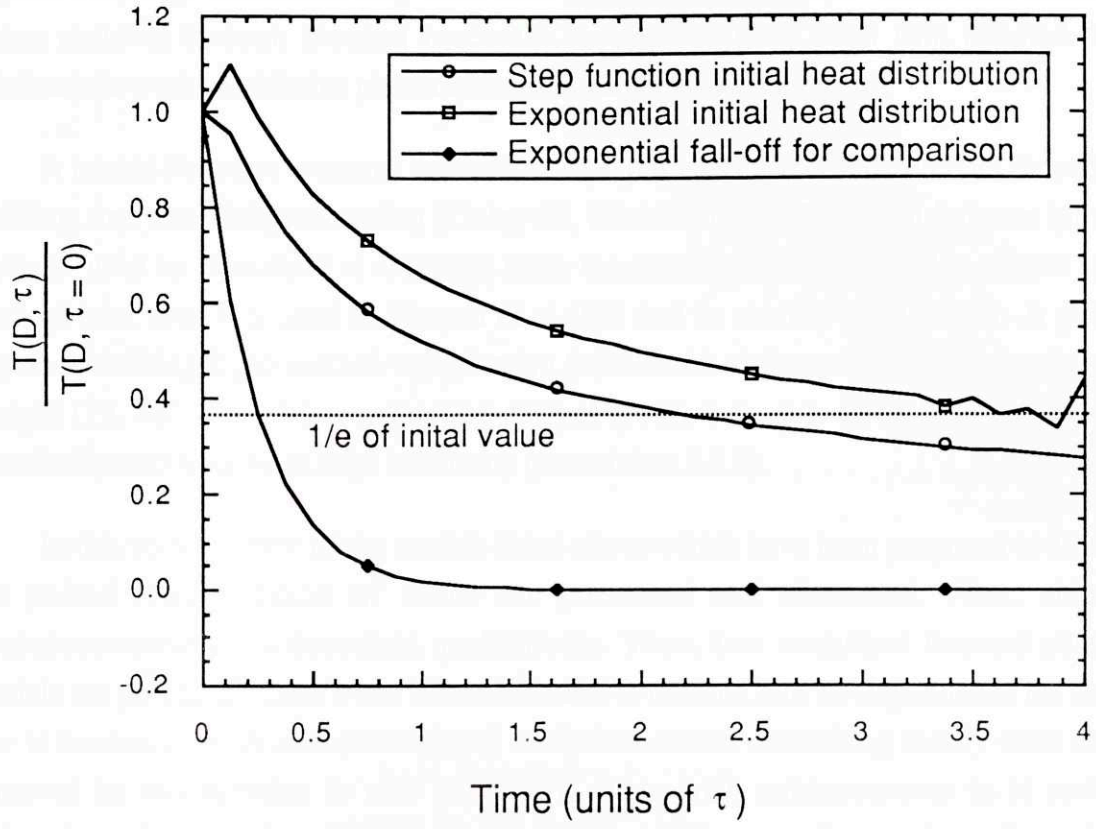

FIGURE 2.3. Normalized comparison of the temperature fall-off behavior at a depth of D between step and exponential initial heat distribution function, and a purely exponential fall-off.

2.4. Tissue Ablation

Many authors have proposed models for laser ablation of tissue. Much of this previous work describes ablation mechanisms which are not relevant to this work, such as explosive fragmentation [Teng et al 86] plasma-mediated ablation [Krokhin 82, Kittrell et al 86, Gitomer et al 90], and photospall ablation [Dingus et al 91]. Of the ablation models which are relevant to tissue ablation at sub-plasma threshold irradiances, several are primarily concerned with heat diffusion [Halldorsson et al 78], while others concentrate on the problem of light distribution [Langerholc 79]. The assumptions that have already been made in this chapter, of a simple exponential light distribution and no heat diffusion during the laser pulse, are a considerable simplification for most of these models. Models which primarily emphasize the removal process include the photochemistry-based "ablative photodecomposition" description [Srinivasan et al 82, Garrison et al 84], and numerical and analytical models based on vaporization of tissue components [van Gemert et al 85,

Partovi et al 87]. The commonly used Beer's law blowoff model, which also describes tissue removal through thermal processes, appears to have been first adapted from Srinivasan's work on ablative photodecomposition by Walsh et al [88].

A related literature concerns thermal ablation of metals and other materials for cutting, welding, and materials processing [Duley 83, Khrokhin 82]. The "heat balance integral method" used by Bertollotti et al [81] to study the melting front produced in silicon by an internal heat source is used in Partovi et al [87] and in section 2.4.4 below. A pair of papers describing rapid surface vaporization from metal surfaces into the atmosphere by Knight [79, 82] is useful in extending current ablation models to include gasdynamic contributions to ablation at high irradiance (see section 2.4.6).

In this section, three of the models listed above which have been proposed to account for pulsed laser ablation of tissue are presented and discussed. First, ablative photodecomposition is described qualitatively. Then, two analytical thermal ablation models are presented. Beer's law blowoff model is derived and its dependence on Beer's law is investigated. A one-dimensional analytical model describing steady-state tissue removal by vaporization is also discussed, along with enhancements to it such as absorption of the incident light by crater debris, and the extension to three dimensions. Following the discussion of the three simple ablation models, a brief review is given of work in progress on modeling two special features of pulsed laser ablation of calcified tissue: the gasdynamics of tissue vaporization and ejection at high incident irradiance, and the consequences of the two-component nature of calcified tissue.

2.4.1. Parameters for Ablation Models

The geometry for the ablation models discussed in this chapter is illustrated in Fig. 2.4. In the figure, a cylindrical laser beam of diameter d is assumed to be incident perpendicularly on the surface of a semi-infinite slab of tissue. The profile of power density in the tissue is U(z) (W/mm^3); when multiplied by the pulse duration, this quantity becomes the energy density u(z) (J/mm^3). The integral of U(z) over all z such that $0 \leq z \leq \infty$ is the irradiance, I (W/mm^2). The corresponding integral of the energy density is the laser fluence, ϕ (mJ/mm^2). Both thermal ablation models assume that when tissue reaches a critical energy density, the heat of ablation h_a (J/mm^3), it is vaporized. Ablation in the tissue creates a crater of depth l (μm). A summary of these quantities is included in the list of symbols.

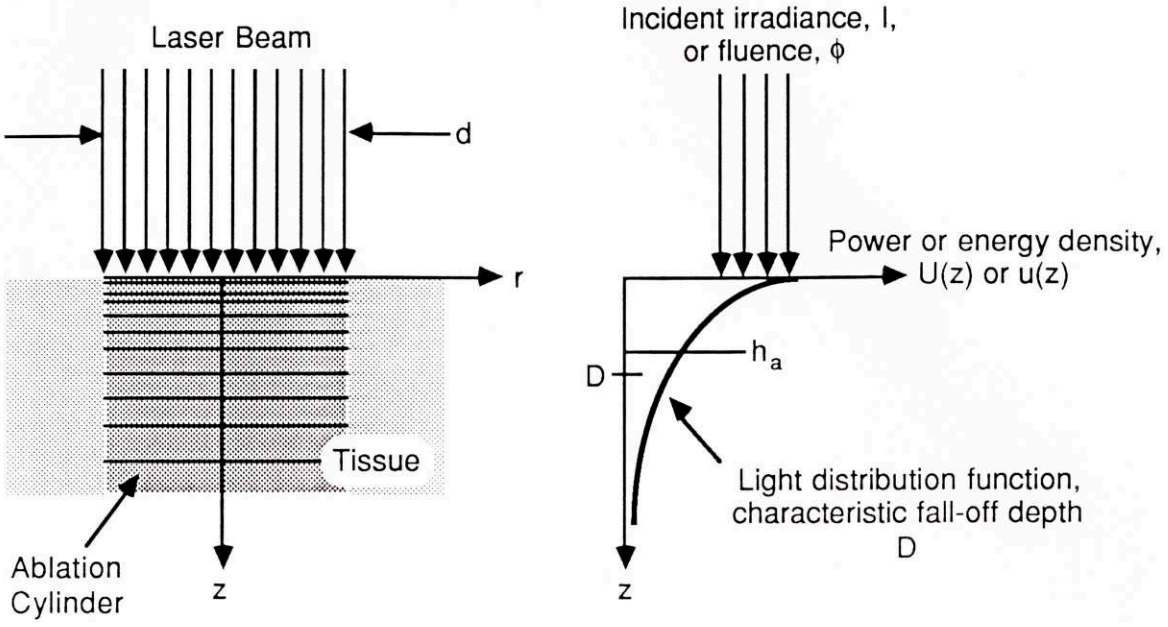

FIGURE 2.4. Geometry and variable definitions for ablation models.

Since the exact form of light distribution in tissue is unknown (see section 2.2), results are presented in this chapter for five sample light distribution functions. This is done in order to illustrate the dependence of each of the ablation models on the specific form of each light distribution. The five resulting energy density distributions are listed in the first two columns of Table 2.3. These functions are all normalized to have the same energy density at the tissue surface, and also to integrate to the same incident fluence (except for the inverse function, which is unbounded). Unless otherwise noted, the expressions are valid in the half-plane $0 \leq z \leq \infty$. These functions are plotted in Fig. 2.5.

Category [units]	Normalized Energy Density Distribution Functions, u(z) $\left[\frac{\text{energy}}{\text{unit volume}}\right]$	Fluence Threshold, ϕ_0 $\left[\frac{\text{energy}}{\text{unit area}}\right]$	Crater Depth, l (for $\phi \geq \phi_0$) [length]	Efficiency, η_{abl} [dimensionless]
Top-hat	$\left\{ \begin{array}{ll} \frac{\phi}{D}; & 0 \leq z \leq D \\ 0; & z > D \end{array} \right\}$	$h_a \cdot D$	D	$\frac{\phi_0}{\phi}$
Linear	$\left\{ \begin{array}{ll} \frac{\phi}{D}\left[1 - \frac{z}{2 \cdot D}\right]; & 0 \leq z \leq 2 \cdot D \\ 0; & z > 2 \cdot D \end{array} \right\}$	$h_a \cdot D$	$2D \cdot \left[1 - \frac{\phi_0}{\phi}\right]$	$2 \cdot \left[\frac{\phi_0}{\phi} - \left(\frac{\phi_0}{\phi}\right)^2\right]$
Exponential	$\frac{\phi}{D} \cdot \exp\left[-\frac{z}{D}\right]$	$h_a \cdot D$	$D \cdot \ln\left[\frac{\phi}{\phi_0}\right]$	$\frac{\phi_0}{\phi} \cdot \ln\left[\frac{\phi}{\phi_0}\right]$
Gaussian	$\frac{\phi}{D} \cdot \exp\left[-\frac{z^2\sqrt{\pi}}{2(D)^2}\right]$	$h_a \cdot D$	$D \cdot \sqrt{\frac{2}{\sqrt{\pi}} \ln\left[\frac{\phi}{\phi_0}\right]}$	$\frac{\phi_0}{\phi} \cdot \sqrt{\frac{2}{\sqrt{\pi}} \ln\left[\frac{\phi}{\phi_0}\right]}$
Inverse	$\frac{\phi}{z + D}$	$h_a \cdot D$	$\frac{\phi - \phi_0}{h_a}$	$\frac{\phi - \phi_0}{\phi}$

TABLE 2.3. Sample energy density profiles and predictions of the blowoff ablation model.

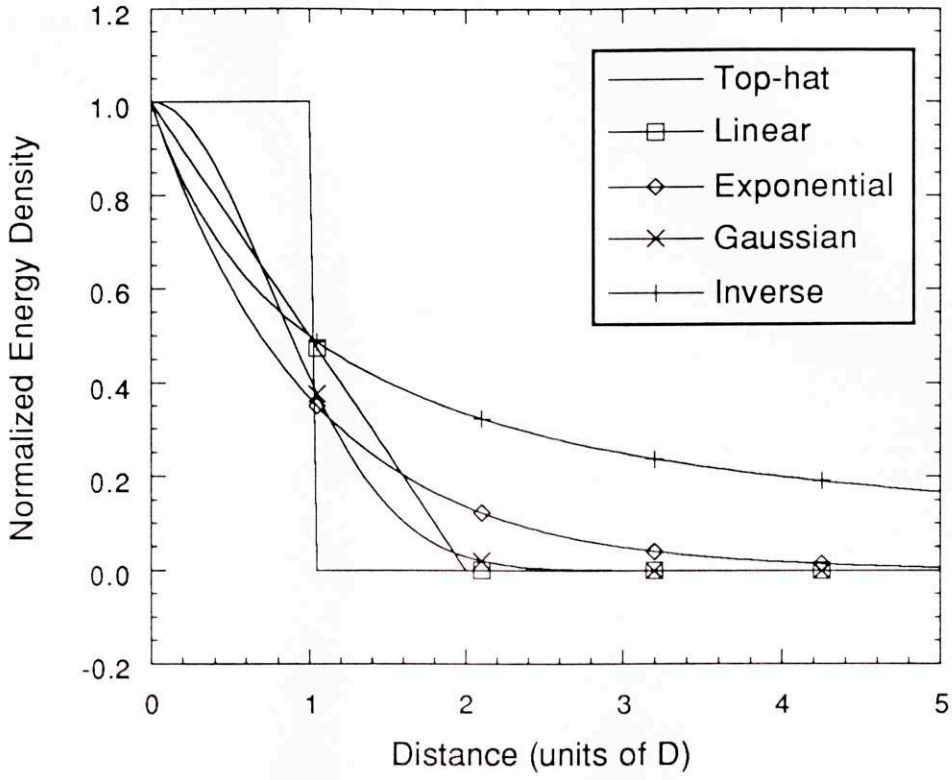

FIGURE 2.5. Sample energy density deposition profiles for ablation models.

2.4.2. Ablative Photodecomposition

The mechanism of ablative photodecomposition (APD) was first proposed as an explanation for the observation of clean etching of organic polymeric material, without melting of the remaining sample, at far-ultraviolet laser wavelengths (primarily 193 nm) [Srinivasan et al 82]. This mechanism was subsequently invoked to account for similar observations of "cold cutting" in biological tissues with pulsed excimer lasers operating at 193 nm [Srinivasan 86, Srinivasan et al 87] and 308 nm [Grundfest et al 85].

The APD model depends upon the fact that in the far-ultraviolet, both the light absorption coefficient and the quantum yield for bond breakage in organic polymers are high [Garrison et al 84]. The combination of these two factors leads to a situation in which the density of absorbed photons approaches the density of chromophores in the material, resulting in instantaneous cleavage of the polymer into individual molecules, monomer units, or clusters of monomer units [Sauerbrey et al 89]. Garrison et al [84] performed a molecular dynamics simulation which showed that the increase in specific volume accompanying the polymer photolysis was sufficient to cause perpendicular ejection of

material at supersonic velocity, without melting in the material left behind. The simulation also predicted the existence of a fluence threshold for APD, below which the quantity of reactive monomers produced was insufficient to cause substantial material ejection.

Assuming exponential attenuation of light in the material, APD predicts that crater depth increases with the logarithm of the ratio of the incident fluence to a fluence threshold [Deutsch and Geis 83, Srinivasan 86]. This is identical to the prediction of the thermal version of the Beer's law blowoff model (see section 2.4.3), which was adapted from it, except that the deposited energy density required for APD is replaced by the heat of ablation, h_a.

The mechanism of APD is not used as an explanation for any of the experimental results of this thesis. While the mechanism appears to be well established as a model for polymer ablation in the far-ultraviolet, the case for APD occuring in tissue in the near-ultraviolet is much less convincing. In fact, several results presented in this thesis strongly indicate that APD is not important in tissue ablation at any wavelength studied. Evidence from scanning electron microscopy of ablation products, coupled with fast laser strobe photography of ablation (sections 4.5.1.3 and 5.2) indicate that as soon as a few hundred nsec after the ablation pulse is over, the dynamics of tissue ejection from ablation at $\lambda = 355$ nm and $\lambda = 2.8$ μm (where APD is very unlikely) appear identical. Studies of tissue ablation with sequenced pulses at $\lambda = 355$ nm showed that irradiation with thousands of barely sub-threshold pulses caused no tissue removal (see section 5.3.3). This indicates that the effects of sub-threshold irradiation on the tissue are completely reversible, in contrast to the APD explanation of fluence threshold given above. Finally, the results of a comprehensive study of ablation dosimetry as a function of wavelength (section 4.5) showed that the deposited energy density required to ablate tissue (h_a) was essentially constant throughout the near-ultraviolet and the visible wavelengths regions. Thus, separate mechanisms with separate values of h_a are not required to explain any of the available data. In this thesis, the assumption is made that whatever amount of laser energy which is deposited into bond breaking in the tissue is quickly converted into heat, so that ablation may be described by thermal mechanisms.

2.4.3. Blow-off Model

The blow-off model of ablation operates on the assumption that heat from the incident light distribution is deposited in tissue before any phase change or tissue movement can occur [Walsh et al 88, Walsh 88]. It is assumed that once the heat is deposited, all tissue

which has had at least h_a J/mm^3 deposited in it will be vaporized. Although this model usually appears in the literature as the "Beer's law blow-off model," based on an exponential light distribution, results are presented here for all of the energy density distributions listed in Table 2.3.

The depth of a crater predicted in the blowoff model is just the depth of tissue to which at least h_a has been deposited. Expressions for crater depth as a function of incident fluence may be obtained by substituting into the normalized energy density distribution functions the equality

$$u(l) = h_a, \tag{2.28}$$

and solving for l. The fluence at which $l = 0$ is the fluence threshold, ϕ_0. Expressions for $l(\phi)$ and ϕ_0 obtained in this manner for the five sample energy density distributions are listed in the third and fourth columns of Table 2.3, and the results are plotted in Fig. 2.6. Since all five distributions were normalized to give the same energy density at the tissue surface, they all predict the same fluence threshold.

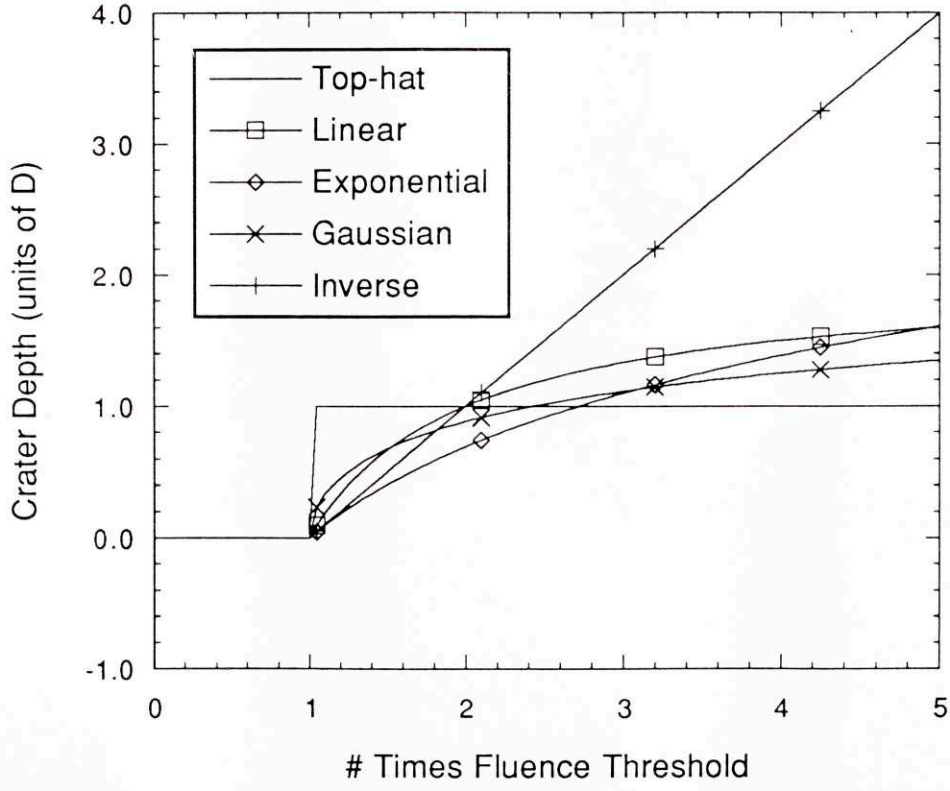

FIGURE 2.6. Predicted crater depth versus fluence for the five sample energy density profiles.

It is interesting that crater depth at a given number of times ϕ_0 varies depending upon the energy density deposition profile. The inverse energy density profile was chosen because it generates a linear growth of depth versus fluence, which is also the prediction of the steady-state ablation model discussed in the next section. Note that it takes an unphysical profile in the blowoff model to reproduce the result of the steady-state model.

The efficiency of the ablation process, η_{abl}, may be defined as the amount of energy actually used by ablation, divided by the total energy deposited in the tissue. This definition of efficiency discounts energy both 1) deposited in excess of the critical energy density required for ablation, and 2) deposited in regions which are not ablated. Thus,

$$\eta_{abl} = \frac{\text{volume of tissue removed} \cdot h_a}{\text{total energy deposited in tissue}} = \frac{(\text{beam area}) \cdot l \cdot h_a}{(\text{beam area}) \cdot \phi} = \frac{l \cdot h_a}{\phi} . \quad (2.29)$$

Expressions for η_{abl} for the five sample energy density distributions are listed in the fifth column of Table 2.3, and plotted in Fig. 2.7. Obviously, among the first four distributions, those models which are the most top-hat shaped are the most efficient for up to a few times ϕ_0. At many times ϕ_0, however, the exponential energy density profile wins out. Only for the unphysical inverse energy density profile is efficiency an increasing function of fluence beyond a few times threshold.

Since most ablation experiments described in this thesis only test ablation up to a few times threshold, it is difficult to use that data to distinguish between any of the theoretical curves in Fig. 2.6, except to eliminate the step-function prediction. The blowoff model does encounter difficulty, however, in explaining ablation with very short pulses. The premise of the model is that all of the incident light is deposited before tissue can undergo a phase change or be removed. For very short pulses, one would expect the blowoff model to be most accurate, predicting lower efficiency at the same fluence threshold than the steady-state model. In fact the opposite is observed in experiments: several authors have reported lower fluence thresholds and deeper craters at a given fluence for fsec and psec pulses as compared to nsec or μsec pulses [Stern et al 89b, Letokhov 91].

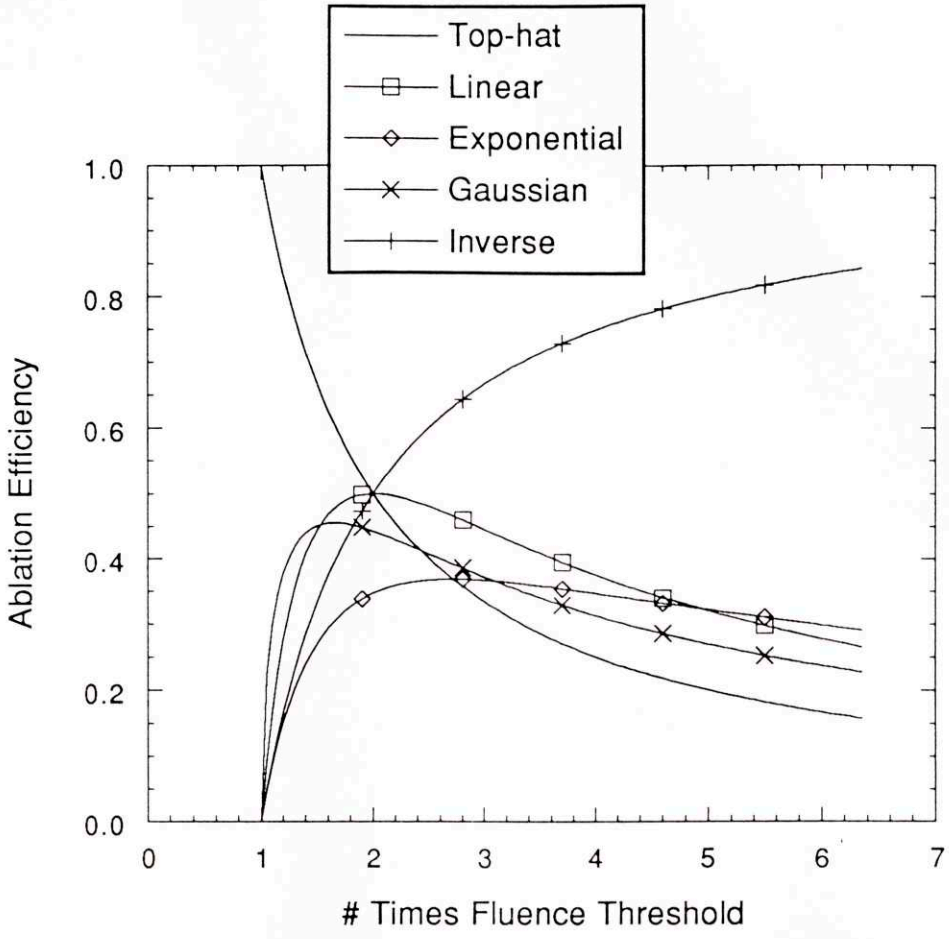

FIGURE 2.7. Ablation efficiencies for the five sample energy density profiles.

2.4.4. Steady-State Ablation Model

The steady-state model of ablation differs from the blowoff model in that heat deposition by the incident light beam is not assumed to be instantaneous, but rather that ablation proceeds during heat deposition. This mode of ablation has been demonstrated as the way in which ablation with cw lasers occurs in soft tissue; Cothren et al [86a], for example, found crater depths in aorta wall to be a linear function of exposure time. Material ejection before the end of even short pulses has been demonstrated by Srinivasan et al [87], who found evidence of ablation during 30 ns pulses in cornea. The original description of the steady-state ablation model, which includes a full analytical treatment of the role of heat diffusion, was published by Partovi et al [87]. The following is a version of the steady-state model which has been greatly simplified by the assumption that heat diffusion is not important for ablation with short pulses, as demonstrated in section 2.3.2.

Since steady-state ablation is concerned with the time evolution of the tissue crater, it is described in terms of power density {U(z,t)} and its integral over z, irradiance {I(t)}. A simple energy balance equation may be written for the "ablation cylinder," the volume of tissue directly beneath the incident laser beam and extending down to infinity (see Fig. 2.4). Energy is deposited in this region by incident laser light, and energy leaves this region in the form of vaporized tissue. The energy balance is expressed in terms of the total amount of heat H contained in this region:

$$\frac{d}{dt}H = \frac{\pi d^2}{4} \cdot \int_0^\infty U(z)dz - \frac{\pi d^2}{4} \cdot v \cdot h_a = \frac{\pi d^2}{4} \cdot [I - v \cdot h_a] \ . \tag{2.30}$$

Here h_a may be thought of as the energy per unit volume that the ablated tissue carries away, and v is the ablation velocity, or the rate at which that energy is carried away. The quantity d is the diameter of the incident beam.

The steady-state ablation model assumes that ablation has occurred for long enough that H no longer changes. Under this condition, Eq. (2.30) reduces to the simple relation

$$v = \frac{dl}{dt} = \frac{I}{h_a}, \tag{2.31}$$

where the ablation velocity has been written as the rate of change of the crater depth. Note that in contrast to the blowoff model, the ablation velocity does not depend on the light distribution function, only on its integral. This may be thought of in the following way: the ablation velocity adjusts itself so that the tissue arriving at the ablation front has had h_a energy density deposited in it; in other words, the tissue itself integrates over the light distribution on its way from infinity up to the ablation front.

An expression for crater depth is obtained by integrating Eq. (2.31) over the pulse duration t,

$$l = \int_0^t \frac{I}{h_a} dt = \frac{I}{h_a} \cdot [t - t_0] = \frac{[\phi - \phi_0]}{h_a}. \tag{2.32}$$

Here, the constant of integration represents crater depth which has accumulated before the establishment of the steady state. A solution to Eq. (2.30) for ablation velocity before steady state is reached has not yet been obtained. Under the assumption that steady state

ablation begins as soon as ablation threshold has been reached at the tissue surface, t_0 may been identified as the time to reach ablation threshold. When multiplied by the irradiance, this quantity corresponds to the fluence threshold, and the pulse duration corresponds to the pulse fluence.

Calculation of the fluence threshold may proceed in the same way as it was done for the blowoff model. The threshold condition is that the tissue at the surface must have h_a energy density deposited in it before steady-state ablation begins:

$$h_a = \frac{W(z=0)}{t_0} = u(z=0). \tag{2.33}$$

This is the same calculation which was performed in the previous section, and the results for fluence threshold are the same as those listed in the third column of Table 2.3.

Ablation efficiency in the steady-state model is in general higher than for the blowoff model, because no more than h_a energy density is ever deposited in any tissue volume. The only energy lost is that which is deposited in the sub-threshold region at the bottom of the crater, which is a small proportion of the total heat deposited for deep craters. Plugging Eq. (2.32) into Eq. (2.29) yields for the ablation efficiency

$$\eta_{abl} = \frac{\phi - \phi_0}{\phi}. \tag{2.34}$$

Plots of crater depth and ablation efficiency versus ϕ/ϕ_0 are independent of the sample energy density distribution chosen, and are the same as the predictions of the blowoff model for the inverse distribution. They are thus plotted with the + symbol in Figs. 2.6 and 2.7, respectively.

A simple three-dimensional extension of Equation 2.32 (Eq. 2.41, below) is used to evaluate most of the experimental data in this thesis. Equation 2.32 is the prediction of the steady-state model, and is also the limiting behavior for fluences close to the fluence threshold for the Beer's law blowoff model. Although several numerical models have been published which include the transition from fluence threshold to steady-state ablation behavior, these models provide less physical insight than the approximate solution described here. As evidenced by the scatter of typical ablation dosimetry data presented in chapter 4, a more complicated model is not needed to interpret this data.

2.4.5. Extensions to the Steady-State Model

Two extensions are described here which have been made to the steady-state model. First, attenuation of the incident light by ablated tissue debris which is trapped within the crater for the duration of the laser pulse is considered. Second, light which is lost out the sides of the ablation cylinder due to scattering is quantitatively accounted for.

2.4.5.1. Attenuation by Crater Debris

Fast laser strobe photography of ablation (chapter 5) has shown that bone ablation with irradiation parameters typical of the experimental work in this thesis results in debris ejection velocities on the order of several hundred m/s, which corresponds to several hundred μm/μs. Ablation craters are typically 500-1000 μm wide and deep, and pulse durations are typically 10-1000 ns. Thus, ablation debris which is created early in such laser pulses is for the most part inertially confined within the ablation crater for the rest of the pulse.

The fluence threshold for steady-state ablation, given an exponential light distribution function with 1/e penetration depth D in the tissue, is

$$\phi_0 = h_a \bullet D. \tag{2.35}$$

As a crater begins to form and debris is produced, the incoming laser beam is attenuated by the combined effects of scattering and absorption by the debris before it reaches the bottom of the crater. This attenuation is assumed to be exponential, with a characteristic attenuation depth δ (see Fig. 2.8):

$$I(z=l) = I(z=0)\, e^{-l/\delta}. \tag{2.36}$$

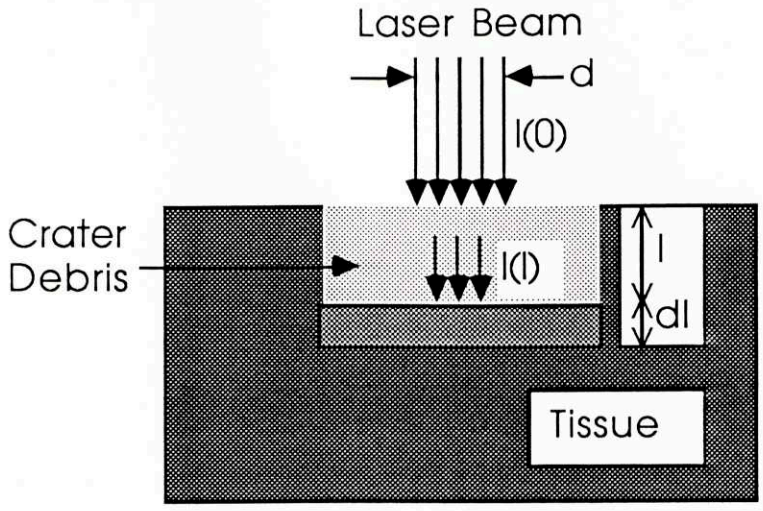

FIGURE 2.8. Schematic of model for light attenuation by crater debris.

An expression for the crater depth is obtained by rearranging Eq. (2.31) and integrating over the depth of the crater and over time from t_0 to t:

$$\int_{t_0}^{t} \frac{dt'}{h_a} = \int_{l'=0}^{l} \frac{dl'}{I(l')}. \tag{2.37}$$

Inserting Eq. (2.36) and using Eq. (2.35), yields

$$l = \delta \bullet \ln\left[\frac{D}{\delta}\left(\frac{\phi}{\phi_0} - 1\right) + 1\right]. \tag{2.38}$$

Overall energy efficiency is obtained by plugging Eq. (2.38) in to Eq. (2.29):

$$\eta_{abl} = \frac{\ln\left[\frac{D}{\delta}\left(\frac{\phi}{\phi_0} - 1\right) + 1\right]}{\frac{D}{\delta}\frac{\phi}{\phi_0}}. \tag{2.39}$$

This expression includes energy which is lost due to attenuation in the crater debris, as well as energy lost in the sub-threshold region at the bottom of the crater.

The debris attenuation extension to the steady-state model has been used for analysis of HF laser bone ablation, where very deep craters can be made at up to ~20 times fluence threshold before plasma formation occurs [Izatt et al 90a]. It is not used to analyze the data

in this thesis, however, because most of the data presented here extends only a few times threshold, and it was impossible to distinguish between debris attenuation and other effects which limit crater depth (see section 4.4.2).

2.4.5.2. Effects of 3-D Light Distribution

The extension of the steady-state model to account for the three-dimensional nature of light distribution in tissue may be done in a simple, phenomenological fashion [Partovi et al 87]. For wavelengths and/or irradiation conditions under which the penetration depth in tissue is comparable to the spot diameter, a considerable fraction of the light incident on the tissue surface may be scattered out of the ablation cylinder of Fig. 2.4, and hence lost to ablation. While the specific shape of the lost light distribution may determine the extent of collateral heating damage, it is unimportant to any of the ablation models discussed above. A simple accounting for this loss may be made by calculating for each potential light distribution a scalar quantity f, called the geometrical efficiency factor. The quantity f represents the fraction of light <u>not</u> lost out of the ablation cylinder. It is incorporated into the steady-state ablation model by multiplying the incident irradiance and fluence. In particular, for the case of the exponential energy density distribution function, the expressions for ϕ_0, l, and η become:

$$\phi_0 = \frac{h_a \bullet D}{f}; \tag{2.40}$$

$$l = \frac{f \bullet (\phi - \phi_0)}{h_a} = Y(\phi - \phi_0); \tag{2.41}$$

$$\eta_{abl} = f \bullet \frac{\phi - \phi_0}{\phi}. \tag{2.42}$$

A new quantity Y, the ablation yield (units mm^3/J), equal to the inverse of the heat of ablation times f, is introduced in Eq. (2.41). Thus the quantities ϕ_0 and Y represent the threshold and slope of a linear fit to depth versus fluence data, respectively.

The value of f depends upon the specific shape of the three-dimensional light distribution. Its value is calculated by Partovi et al [87] for a sample power density distribution which falls off exponentially in both z an r beyond the boundaries of the cylindrically shaped beam of diameter d:

$$U(r,z) = \begin{cases} \frac{f \bullet I}{D} e^{-z/D}; & r \le d/2 \\ \frac{f \bullet I}{D} e^{-z/D} \frac{(d/2)e^{d/2D}}{r \bullet e^{r/D}}; & r > d/2 \end{cases} \qquad (2.43)$$

Integrating Eq. (2.43) over all r and z and setting it equal to the total power in the beam leads to an expression for f:

$$f = \frac{d}{d+4 \bullet D} . \qquad (2.44)$$

The factor of 4 in the denominator of Eq. (2.44) is a result of the fact that the sample light distribution function has the same rate of fall-off in the r and z directions. For light distribution functions which are peaked in the forward direction, this factor is reduced.

The concept of the geometrical efficiency factor is used in the discussion of ablation as a function of laser spot diameter in section 4.4.4.

2.4.6. Gasdynamic Ablation Model

The predictions of the steady-state ablation model are used to evaluate most of the experimental ablation data in this thesis. It was judged to be the best analytical model available, and is accurate enough to allow for fitting of the data for the most important ablation parameters. However, two special features of calcified tissue ablation with pulsed lasers remain poorly understood quantitatively. These are the effects of tissue vaporization and ejection at high irradiance, and the consequences for ablation modeling of the two-component nature of calcified tissue. Brief mention of work in progress on modeling these two phenomena are the subject of this and the following sections.

Preliminary calculations for the effects of high irradiance on tissue, which take the dynamics of the evaporation process into account in the framework of thermodynamics and the kinetic theory of gases, have been performed by Partovi [90]. These calculations are derived in part from a description of metal ablation by Knight [79,82]. In this idealized model, tissue is considered as a single component absorbing liquid, tissue vapors are assumed transparent, and ablation occurs in one dimension in the steady state. As the liquid evaporates, the surface receeds, and it takes the vapor molecules ejected from the surface a few mean free paths to establish translational equilibrium. The thin layer of non-equilibrium vapor flow is called the Knudsen layer. The vapor flow rate at the outside edge of the

Knudsen layer is sonic, but if the irradiance is high enough, the vapor velocity accelerates to a final supersonic value in a second layer just outside of the Knudsen layer. In a third layer, vapor flows outward at a constant supersonic velocity. This layer of vapor in constant velocity flow pushes ahead of it a fourth layer containing air, moving at the same constant velocity. The interface between the fourth layer air at a constant supersonic velocity and undisturbed air further away is a shock front.

Equations for conservation of mass, momentum, and energy across the various layer boundaries, along with expressions for the transport of these quantities through the layers themselves, may be written. These equations may be solved simultaneously to obtain expressions for the tissue surface recession velocity, surface temperature, and the velocity, pressure, and temperature of the escaping vapors. A preliminary solution, assuming the thermal characteristics of water for tissue, and using simple equations of state for the aerodynamic layers, has been obtained. For laser irradiances on the order of MW/cm^2, this solution predicts a tissue surface temperature on the order of 500 °C, a pressure behind the shock front of ~10 atmospheres, and a gas velocity behind the shock front of ~700 m/s.

Further work on the gasdynamic ablation model is under way. This work includes the incorporation of more realistic descriptions of the thermodynamic processes occuring in atmospheric layers. Secondly, since most tissue ejection occurs after the end of the laser pulse for short pulses (see section 5.2), a transient solution is under development. In this case, the shock wave becomes a blast wave, which is just the dissipative form of a shock after the source has been turned off. Nonetheless, the predictions of even the steady-state version compare very favorably with the velocities observed for blast waves caused by pulsed laser ablation of bone, captured using fast laser strobe velocity of ablation (section 5.2).

2.4.7. Two Component Picture for Calcified Tissue Ablation

The composite nature of calcified tissue (section 2.1) also bears on the ablation mechanism. It is assumed that all of the laser energy absorbed in the tissue is quickly transformed into heat, independent of the particular absorbing chromophores at a given wavelength (see section 2.3). In principal, once this occurs, calcified tissue can be ablated by vaporizing all of the material at once. This requires developing sufficient temperature in the tissue to vaporize the calcium salts (>1600 °C), as well as the connective tissue (~300 °C). However, the dual-component structure of such materials suggests a second possibility in which the hard tissue component need not be completely vaporized during

ablation [Izatt et al 90b, Izatt et al 91a]. In this scenario of two-component ablation, the connective tissue component is vaporized sufficiently rapidly that the resulting vapor flow entrains and removes the apatite crystallites from the crater. Since the calcium salts are not vaporized, ablation occurs at a relatively low temperature, resulting in reduced collateral heating damage. Figure 2.9 is a highly idealized schematic of this concept.

The gasdynamic ablation model described above indicates that soft component vapor ejection velocities reach Mach speeds. Preliminary calculations indicate these are just the velocities required to accelerate μm-sized calcium salt particles out of a typical crater [Albagli 91]. Experimental evidence that this condition is satisfied is provided by fast laser strobe photographs of calcified tissue ablation in progress (Figs 5.2(b-c)), which bear a strong resemblance to Fig. 2.9. The fastest ejecta visible in these photographs were travelling at least 600 m/s. Larger debris particles, travelling at slower velocities, are visible near the tissue surface. In addition, the quantity and size distribution of debris captured in flight from ablation experiments (section 4.5.1.3) are consistent with the two-component ablation mechanism.

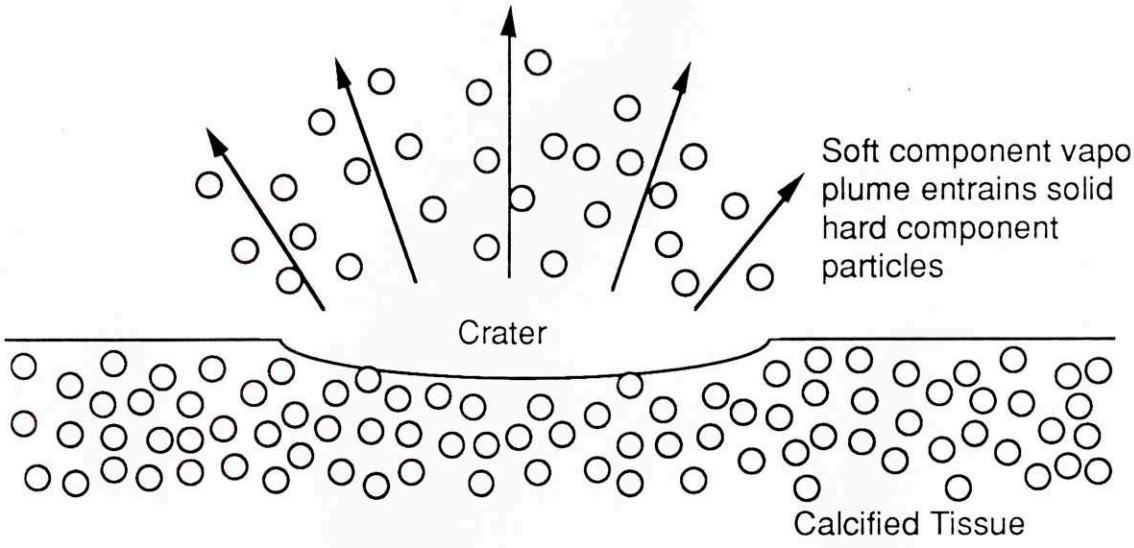

FIGURE 2.9. Idealized schematic of two-component concept picture of calcified tissue ablation.

Since the ablation mechanism depends primarily upon the microscopic structural and thermal properties of the tissue components, it is expected that calcified tissues with similar ratios of soft and hard components (i.e. bone and densely calcified plaque) exhibit similar ablation characteristics.

Being a relatively new suggestion, details of the the two-component mechanism are still being worked out. At the time of this writing, it is probably more appropriately called a picture of ablation than a model. In this thesis, it will be taken as a hypothesis that the type of hard tissue cutting observed for irradiances ~MW/cm^2 in fact occurs by this process (section 4.3). The relationship of experimental observations throughout the thesis to the two-component process is discussed when the observations are presented.

2.5. Conclusions

Compact bone and calcified atherosclerotic plaque are composite structures in which a hard, high melting point component consisting of calcium salts exists in intimate contact with a soft, low vaporization temperature connective tissue component. Bone is used as the primary model for calcified tissue in this thesis. For the purpose of modeling ablation, a simple exponential distribution of light in tissue is assumed, with the penetration depth determined experimentally using Kubelka-Munk theory. Heat diffusion in tissue over distances typical of light penetration depths occurs over a time long compared to typical laser pulse lengths, so it is not a consideration in ablation modeling (except for laser repetition rate effects). The steady-state model of ablation, which predicts an ablation threshold and a steady-state ablation velocity, will be used to analyze near-threshold experimental data. This model was chosen because it is a simple analytical model which provides physical insight into ablation results, and it also corresponds to the near-threshold limit of the Beer's law blowoff model. Detailed consideration of the gasdynamics of ablation at high irradiance indicates that high temperatures and pressures are present during ablation. The composite nature of calcified tissue suggests a two-component ablation process in which the soft component is explosively vaporized, entraining and removing the hard calcium salt component.

Chapter 3
Optical Properties of Bovine Bone

In this chapter, estimates of the optical properties of bone are obtained for the wavelength regions used for ablation in subsequent chapters. These include wavelengths in the near-ultraviolet, visible, and mid-infrared regions of the spectrum. Since the topic of this thesis is ablation, rather than tissue optics or spectroscopy, the results in this chapter are meant as order-of-magnitude estimates primarily for comparison with ablation results.

3.1. Near-Ultraviolet and Visible Wavelength Region

The optical properties of most biological tissues in the visible wavelengths are a complicated function of the intrinsic scattering and absorption coefficients of the tissue, each of which are a strong function of wavelength and tissue type (see section 2.2). In order to obtain reliable estimates for near-ultraviolet and visible light penetration depths in bone, optical property measurements were conducted on native bone samples.

3.1.1. Experimental Methods

Bone samples were machined to their desired thickness while fully calcified. This was done in order to avoid artifacts due to decalcification, mounting, and microtome sectioning, Bovine shank bone samples were obtained no later than two days post-mortem. Areas of the bone surface with flat regions of cortical tissue ~1 mm thick were selected for spectroscopic analysis. The cortical surface layer was separated from the rest of the bone, and cut into plates approximately 1 cm square. For thin section preparation, one surface of a bone plate was machined flat and smooth on a milling machine with a clean, sharp bit. The flat surface was then placed in contact with a 3/8" thick fused silica flat, and tacked in place at its corners with fast-drying epoxy. When the epoxy dried, the silica flat with the bone attached was mounted in the milling machine, levelled, and the position of the silica flat top surface was registered on the machine. Then, the remaining bone was machined to the approximate desired thickness relative to the position of the top of the silica flat.

After machining, the thickness of each bone specimen was measured at each corner with a calibrated microscope. Samples were found to be flat to within ±50 μm, which

corresponded to 25% of the thickness of the thinnest sample used. The average of the four thickness readings was recorded. For the experiments described below, sections of thickness 200 ± 50 μm and 525 ± 50 μm were used.

The machining operation resulted in bone samples which were dried out to the touch. In an experiment to test the optical properties of a "wet" section, a specimen was cut from its backing plate with a razor blade, and placed in a cuvette full of saline.

Total transmission and reflection measurements of bone sections were made in a double-beam spectrophotometer equipped with an integrating sphere. The optical arrangements for the transmission and reflection measurements are illustrated in Fig. 3.1. The integrating sphere was 60 mm in diameter, coated on the inside with a reflectance standard $BaSO_4$ coating. The input face of a photomultiplier tube was located at the bottom of the integrating sphere, equidistant from all ports. The spectrophotometer emitted two collimated beams of approximately 3 x 5.5 mm, directed into sample and reference ports on the integrating sphere. The spectrophotometer operated by comparing the signals at the photomultiplier from the sample and reference beams many times per second. The sample to reference beam ratio was compared with the result of a calibration obtained previously in background subtraction mode. The spectrophotometer was scanned from 190 to 700 nm, with entrance slits set for 5 nm resolution.

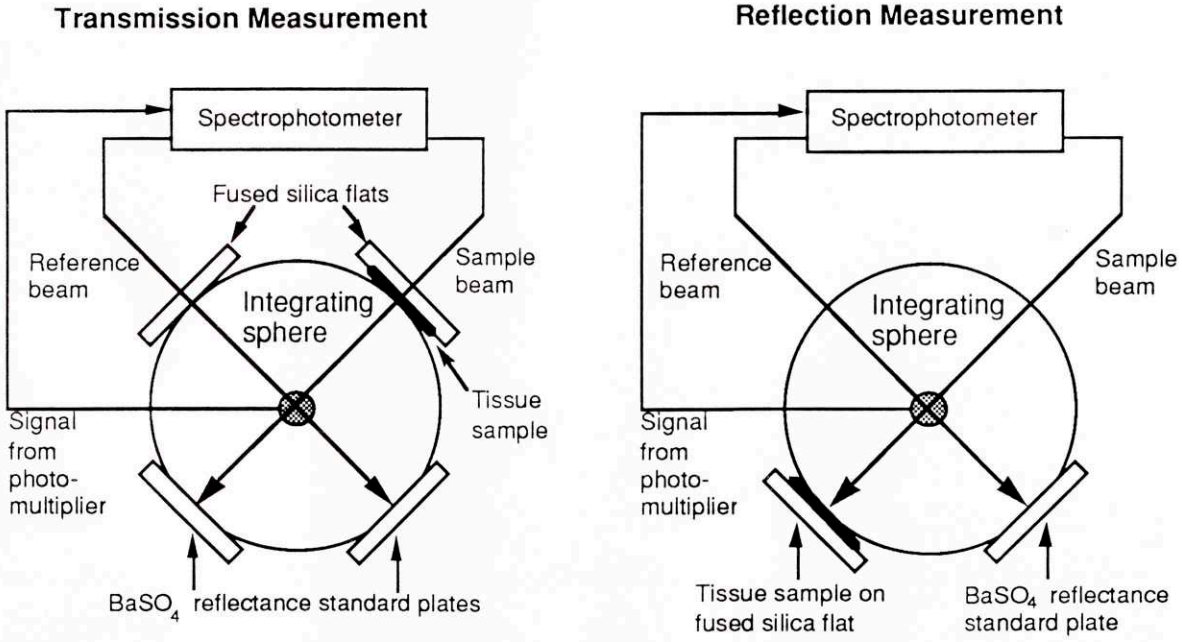

FIGURE 3.1. Schematic of optical arrangement for spectroscopic measurements.

For total transmission measurements, background subtraction was performed with the nothing blocking the integrating sphere entrance ports, and $BaSO_4$-coated reflecting plates positioned over the output ports. Tissue samples, still mounted on fused silica flats, were then positioned over the sample entrance port. At the same time, another fused silica flat was positioned over the reference entrance port. The reference flat compensated for Fresnel surface reflections and attenuation in the flat over the sample port. For testing the wet bone sample, the cuvette containing the specimen was placed in front of the sample port, and another cuvette filled with saline was placed in front of the reference port.

For total reflection measurements, background subtraction was performed with nothing blocking the entrance ports, and reflecting plates positioned over both output ports. Tissue samples on fused silica substrates were placed over the sample beam output port. Specular reflection from the fused silica flat was judged not to be important, since even the thinnest sample appeared opaque, indicating that very little unscattered light penetrated the entire thickness. For wet sample measurements, specular reflection from the front surface of the cuvette was not corrected for.

Total transmission and reflection results were converted into penetration depths, absorption, and reduced scattering coefficients, using the two-flux Kubelka-Munk theory and its connections to transport theory described in section 2.2.1.1.2.

3.1.2. Results

Transmission and reflection measurements of bone samples at the two thicknesses studied were reproducible to within a few percent between different scans taken at the same location on the sample. They were also independent of sample alignment, and the region of the specimen which was probed by the sample beam.

The inverse of the linear attenuation coefficient predicted by Kubelka-Munk theory, the penetration depth, is plotted in Fig. 3.2 (see Eq. 2.10). Values of D for three samples are plotted: 200 μm and 525 μm thick dry samples, and the 200 μm sample after immersion in saline. The values of D obtained from all three samples are similar to within ~50% below 300 nm, and ~30% above 300 nm. They are in best agreement in the 300-450 nm region.

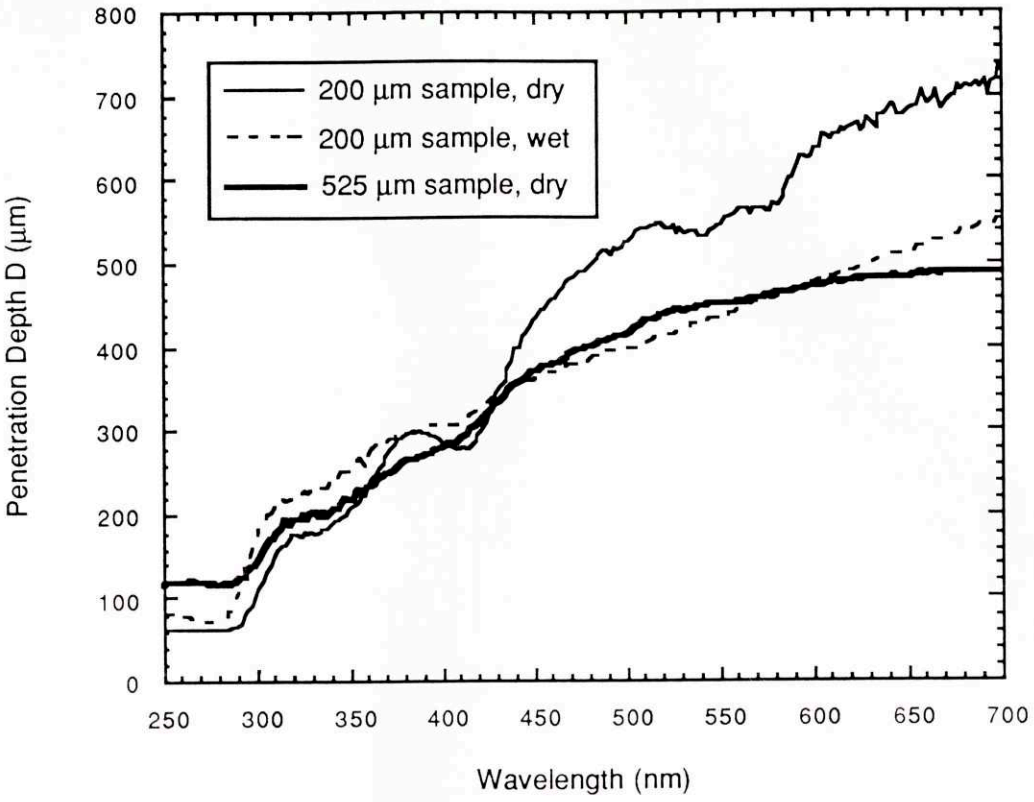

FIGURE 3.2. Penetration depths from Kubelka-Munk theory for all samples.

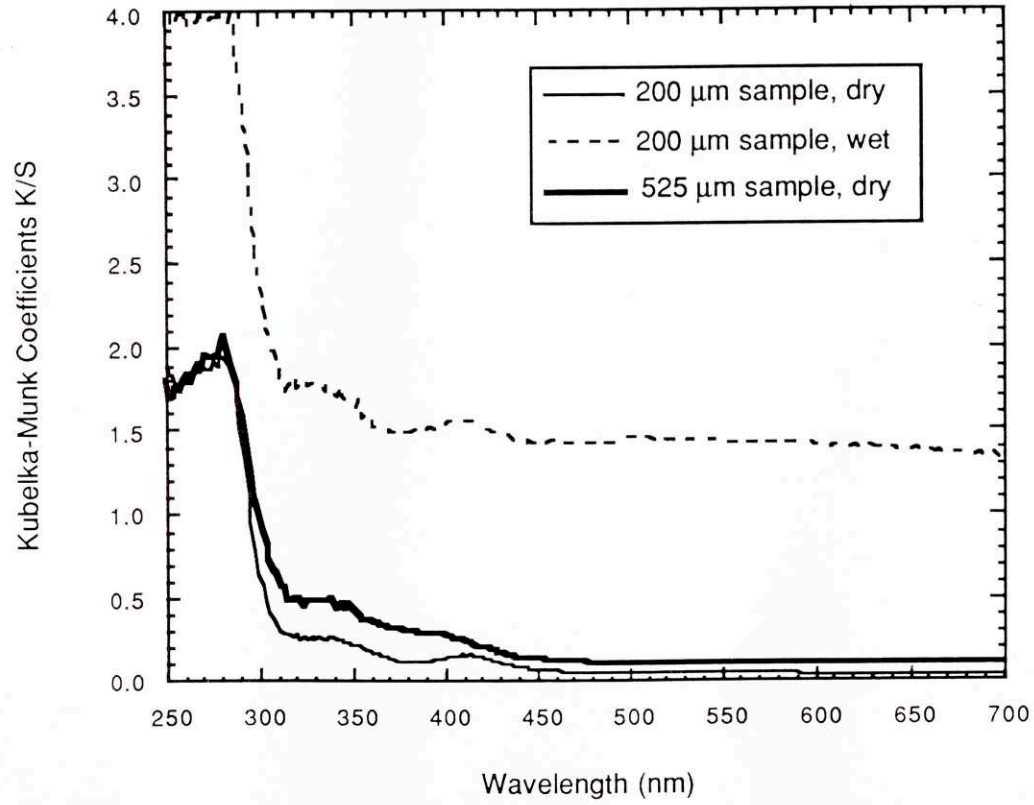

FIGURE 3.3. Ratio of Kubelka-Munk coefficients k/s for all samples.

It is interesting to extract the optical transport properties of bone from the Kubelka-Munk k and s coefficients. Procedures for connecting the k and s coefficients with μ_a and $\mu_s(1-g)$ ($=\mu_s'$) are outlined in section 2.2.1.1.2. As described there, the connection between k, s, μ_a and μ_s' depends upon the ratio k/s, and is simplest in the limits k>>s or k<<s. The ratio k/s is plotted for all samples studied in Fig. 3.3, and satisfies neither limit at all wavelengths. A graphical solution for the variables η and χ connecting k and s to μ_a and μ_s' in the region k~s is given by van Gemert et al [87]. A linear approximation to this solution, valid for k/s <2, was given in section 2.2.1.1.2 and is used here to obtain μ_a and μ_s'.

Values of μ_a and μ_s' for the dry and wet 200 μm sections are plotted in Figs. 3.4. and 3.5, respectively. The absorption coefficient is strongly wavelength-dependent, exhibiting visible bumps at ~340 and ~410 nm, as well as a sharp drop at ~300 nm. The scattering coefficient is a relatively monotonic function of wavelength by comparison. The decrease in scattering coefficient upon wetting the sample is consistent with dissolving of scattering particles. The corresponding increase in absorption coefficient is not expected, however, and may be an artifact due to the extra uncompensated quartz-air surfaces in the total reflection wet sample setup.

3.2. Mid-Infrared Wavelength Region

In subsequent chapters, ablation was studied at several wavelengths in the 3 μm region. As opposed to the situation in the near-ultraviolet and visible wavelengths, in this wavelength region light is much more strongly absorbed than scattered in all tissues, so that the problem of light distribution in tissue reduces to Beer's law (section 2.2.1.1.1). In this case, rough estimates of bone optical properties may be obtained from analysis of the tissue components.

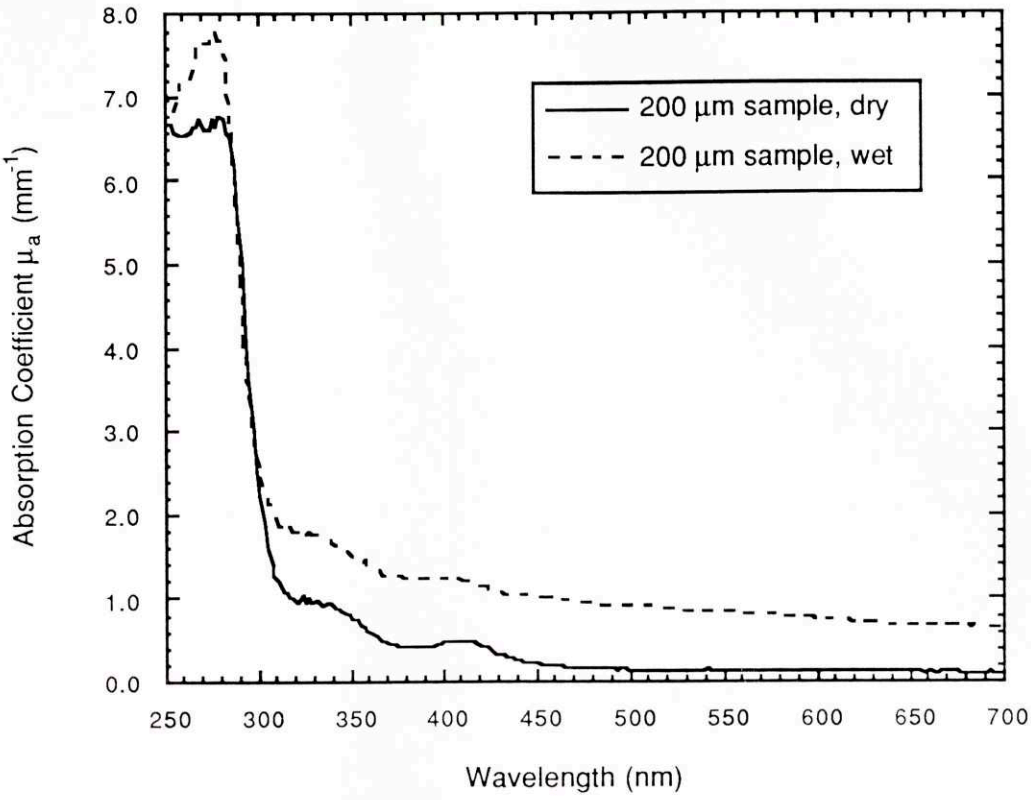

FIGURE 3.4. Absorption coefficients for dry and wet 200 µm bone sample.

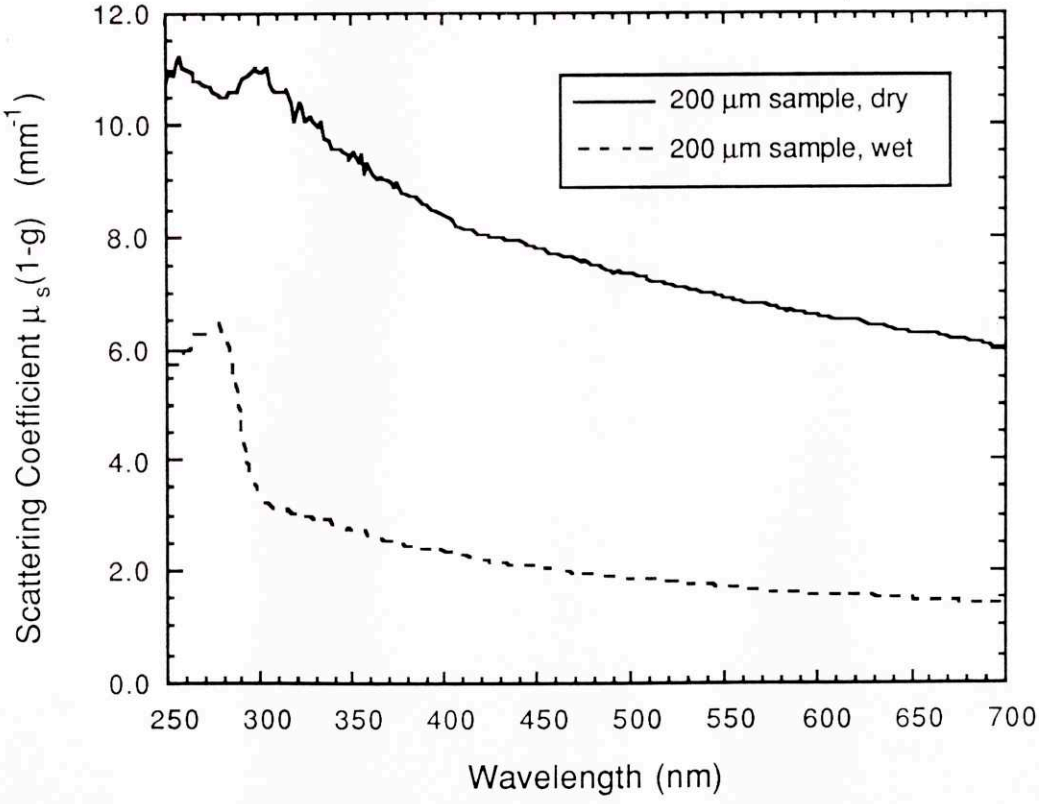

FIGURE 3.5. Scattering coefficients for dry and wet 200 µm bone sample.

The strong absorption of water near 3 μm has motivated considerable attention to ablation in that region [Wolbarsht 84, Valderrama et al 89, Valderrama et al 90, Nuss et al 88, Walsh 88, Izatt et al 90a]. Figure 3.6 contains a plot of pure water absorption coefficients from 2 to 12 μm, exhibiting the strong 3 μm peak [Robertson et al 71]. It is important to note, however, that both of the other primary components of calcified tissue also exhibit strong absorption in the 3 μm region. Table 3.1 contains a comparison of absorption depths in pure water obtained from the data in Fig. 3.6, with absorption depths in collagen and relative absorptions in hydroxyapatite (absolute absorption depths in hydroxyapatite are not available). The absorption depths are listed at the three HF laser wavelengths for which ablation was studied in subsequent chapters. It can be seen from the table that both water and collagen vary in absorption by more than a factor of 10 between the 2.7 and 2.9 μm, whereas absorption in hydroxyapatite is a less strong function of wavelength in this region.

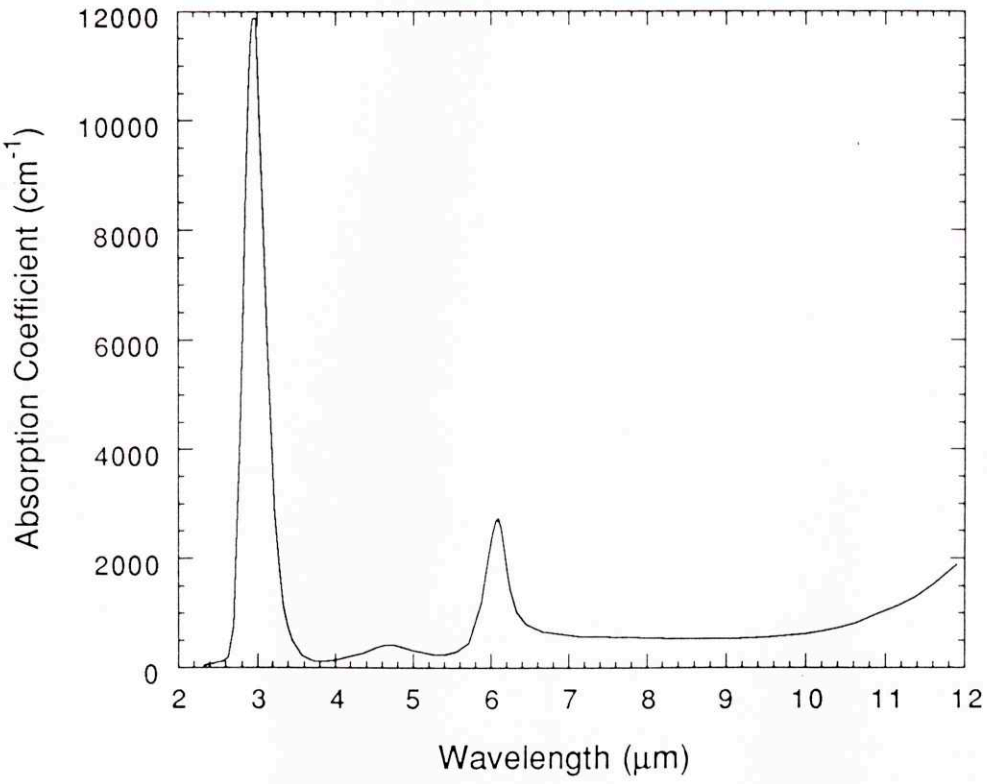

FIGURE 3.6. Lambert absorption coefficients of pure water in the infrared, after Robertson et al [71].

Wavelength (μm)	Absorption Depth (μm)			Reference
	2.707	2.832	2.911	
Pure Water	11 (12.2)	1.4 (1.5)	0.9	Robertson et al [71]
Collagen	54 (11.5)	14 (3.0)	4.7	Yannas [72]
Hydroxyapatite	– (3.4)	– (1.3)	–	Pouchert [67]

TABLE 3.1. Absorption depths of the HF laser lines in the primary constituents of bone. Numbers in parentheses are relative to the values for 2.911 μm.

3.3. Identification of Tissue Chromophores

Several of the prominent features of the bone section abroption spectrum in Fig. 3.4 help to identify the absorbing tissue chromophores. The prominent peaks in absorption at 420, 540 and 580 nm, the latter two of which are more visible as dips in the penetration depth spectrum (Fig. 3.2), are probably due to oxyhemoglobin [Stryer 81]. These peaks disappeared when the 200 μm sample was immersed in saline, consistent with dissolving and dilution of dried blood in the sample. The absorption peak at ~330 nm can be attributed to the collagen cross-linking agent pyridinoline [Fujimoto 77]. Finally, the onset of strong absorption near 300 nm is probably due to a combination of several chromophores. The collagen in bone contains the aromatic amino acids phenylalanine and tyrosine, the latter of which absorbs strongly in the 250-290 nm region Rava et al 85]. The base pairs uracil, thymine, cytosine, guanine, and adenine in DNA and RNA also exhibit absorptions in the 250-300 nm region [Fodor et al 85].

The absorbing chromophores in the 3 μm region have already been identified.

3.4. Conclusions

Penetration depths in compact bovine bone, obtained with Kubelka-Munk theory from total reflection and transmission measurements of thin samples, range from ~100 um at 250 nm to ~600 um at 700 nm. Between ~300 - 700 nm, scattering dominates absorption by up to a factor of ~10. Water, collagen, and hydroxyapatite all combine to cause very strong absorption near the 3 um wavelength region in the mid-infrared.

Chapter 4
Parameter Survey of Calcified Tissue Ablation

In this chapter, the results of a survey of calcified tissue ablation characteristics over a wide variety of irradiation parameters and delivery conditions are presented. The calcified tissues studied were bovine bone and human aortic calcified plaque; normal and softly plaqued human aorta wall were also studied for comparison. The ablation characteristics examined include the quality of the laser cut, the size and distribution of ablation debris, and tissue removal thresholds and yields as a function of laser fluence and ablation conditions.

Knowledge of ablation characteristics as a function of the parameters surveyed here is important for predicting the appropriate laser sources for specific clinical applications. This is true from the points of view of both medicine and engineering. The precision and reproducibility of the laser cut, for example, determine the potential sharpness of surgical margins. The long-term host reponse to laser treatment may depend upon the extent of peripheral damage caused in the tissue, which can be evaluated histologically. The size and composition of the ablation debris determine the extent to which laser cutting can be performed in enclosed regions of the body, at least without elaborate measures taken for debris management, such as irrigation and filtering. Medical engineering considerations, on the other hand, require information about tissue removal dosimetry. The irradiances and fluences necessary for ablation must not destroy the delivery system, and the tissue removal rate must be sufficient to be clinically reasonable for the problem at hand. Many of these engineering considerations are taken up in more detail in chapter 6.

4.1. Fundamental Parameters Governing Ablation

It is important to recognize which of the many parameters describing laser-tissue interaction are fundamental to the ablation process, and should therefore be the experimental variables. Parameters which are controlled through the choice of the ablation laser will be considered first. The thermal model of ablation (see chapter 2) predicts that the steady-state velocity of ablation in tissue is proportional to the irradiance at the tissue surface, independent of the nature of the light distribution under the surface. Later in this

chapter, it is shown that there is an irradiance threshold for calcified tissue ablation. Thus, the first fundamental parameter of ablation is irradiance.

The second fundamental parameter is fluence, or the energy deposited in the tissue per unit area. It is shown in this chapter that for the irradiance and wavelength ranges of interest for clinical applications, fluence is usually the quantity which determines the amount of tissue removed in each pulse. Two exceptions to this rule are also noted; tissue removal is not linear with fluence for different laser spot diameters, and for different numbers of shots fired into each ablation crater.

The third fundamental aspect of ablation determined by the ablation laser is the distribution of the light in the tissue. This determines the depth over which ablation occurs, the threshold fluence which must be deposited before ablation can begin, and the precision with which ablation can be performed. In this thesis, light distribution in tissue is described in simplified terms by a penetration depth D, and a "geometrical efficiency factor" f, which is a function of the spot diameter (d) and the penetration depth (see chapter 2). The penetration of light in the tissue comes about through the interplay of scattering and absorption in the tissue, and is strongly wavelength dependent. This is how wavelength dependence comes into consideration.

The temporal evolution of the laser pulse is important if it contains structure, for example if several pulses are sequenced in time. The pulse structure dependence of both ablation and optical fiber conduction of laser light are considered in chapters 5 and 6, respectively.

The other important component of the laser-tissue interaction is the tissue. The optical penetration depth D is really a tissue parameter, although it is a function of the laser wavelength. Some other tissue properties which are not related to the laser are determined by the tissue type: bone and various stages of plaque in artery wall may each exhibit different thermal and mechanical properties. Several tissue types are surveyed in this chapter.

Finally, the laser-tissue interaction may occur under special conditions imposed externally. Ablation may be done in air, under saline, or percutaneously through a catheter, in which case it happens in a blood field in contact with the catheter or the catheter shield. Several of these ablation conditions are investigated in this chapter.

4.2. Experimental Methods

This section provides details of the experimental methods used for all experiments in the parameter survey.

4.2.1. Tissue Selection & Preparation

Human and bovine artery samples were obtained within a few hours post-mortem, disssected, snap-frozen in isopentane, and stored at -80°C until study. Upon removal from the freezer, the samples were thawed with room-temperature neutral bufferred saline. Bovine shank bone samples were obtained no later than 2 days post-mortem. Areas of the bone surface exhibiting a clean, smooth cortical surface without tissue attachment were prepared by scraping the surface with a razor blade to remove surface refuse and the periosteum. Prepared bone samples were either used immediately, or kept frozen at -80°C until use.

4.2.2. Laser Source Characteristics

The laser sources which were used in the ablation parameter study are listed in Table 4.1. For the wavelength and fluence dependence studies, lasers were chosen which could deliver to the tissue surface (in conjunction with the beam quality of the laser and available beam delivery optics) irradiances on the order of ~10^4 to ~10^6 W/mm^2. Irradiances in this range were found sufficient to ablate calcified tissue at all wavelengths studied, while avoiding plasma formation on the tissue surface ([Izatt et al 90b, 91a], also see below).

Laser Type	Manufacturer	λ (range) (nm)	t_p (nsec)	Max. E_p (λ range) (mJ)	Rep. Rate (Hz)
Flashlamp-Pumped Dye	Candela	(295-590)	750/1500	10 - 500	0.3
Long-Pulse Excimer	Questek	308	100	100	5
Third Harmonic Nd:YAG	Continuum	355	7.5/200	120	10
Frequency-Doubled Alexandrite	Light Age	375	100	80	10
Second Harmonic Nd:YAG	Laserscope	532			
Holmium:YSGG	Schwartz	2090	250,000	400	1
Hydrogen Fluoride	Lumonics	(2700-2900)	350 - 1000	10	0.5

TABLE 4.1. Laser sources used in the ablation parameter study. Parameters listed are wavelength range, pulse durations available, maximum energy per pulse, and repetition rate.

4.2.3. Beam Delivery Optics

For experiments conducted using the flashlamp-pumped dye, Nd:YAG, and HF lasers, the beam exiting the laser was focussed into a spatial filtering pinhole, and then refocussed onto the tissue surface to insure a well-defined beam profile, as diagrammed in Fig. 4.1. The spatial filtering setup was not available for the other lasers, in which case the laser beam was focussed directly onto the tissue surface. The size and profile of the beam spot on the tissue was measured by examining burn patterns on exposed polaroid film placed at the plane of the tissue sample. With the flashlamp-pumped dye, long-pulse excimer, Nd:YAG, and HF lasers, polaroid burn pattern profiles were calibrated using either a reticon diode array, or by translating a pinhole through the focussed beam.

Ablation craters were drilled in a regular array on the tissue samples by positioning them with an x-y translator during ablation experiments. This technique aided in the identification of near-threshold craters by their juxtaposition with higher fluence craters. Ablation was conducted either in air, or in several cases under saline and a 1 mm thick

quartz microscope slide, to imitate the optical shield of the LAS II catheter (see section 1.5).

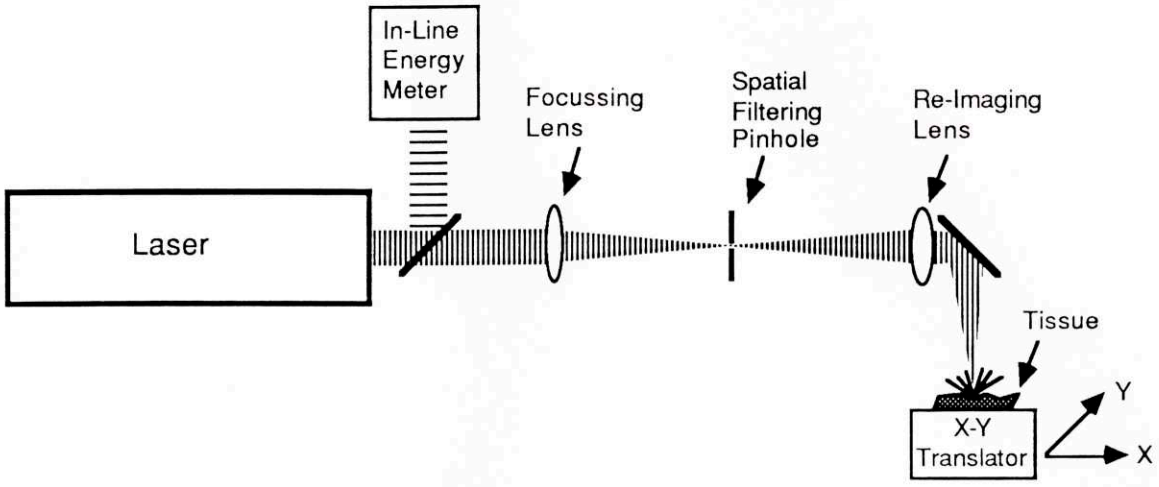

FIGURE 4.1. Ablation beam delivery optics.

Laser pulse energies were monitored either in-line, or else several times during each experiment with either a pyroelectric or thermal detector. The delivered laser fluence as a function of radius from the crater center was obtained from the total pulse energy, E_p, and the measured radial beam profile, R(r), by the formula

$$\phi(r) = \frac{E_p}{\int_0^\infty 2\pi r' \cdot R(r') \cdot dr'} \cdot R(r). \qquad (4.1)$$

For all lasers used in this study, the measured spot profile at the tissue surface was approximately gaussian. Note that for a gaussian profile spot, the fluence delivered at the crater center (where depths were measured) reduces to

$$\phi(r=0) = \frac{E_p}{\pi a^2}, \qquad (4.2)$$

where a is the 1/e radius of the gaussian spot profile.

4.2.4. Ablation Characteristics Evaluation

Representative tissue craters from each set of ablation parameters were photographed through a high-power microscope to record qualitative impressions of the laser cut. Ablation qualities which were observable with this method included the amount of char present, the overall jaggedness of the cut, and the presence of large debris flakes or particles.

Bone samples selected for histological analysis were fixed in 5% neutral buffered formalin, decalcified in HCl solution for 48 hours, and embedded in paraffin. Five micron thick serial sections were cut from the embedded sample and processed routinely with hematoxylin and eosin stain for light micrographic examination.

Crater depths were measured at their centers by monitoring the vertical travel of a high-power microscope between focussing on the top and bottom of laser craters. Crater diameters were measured with a calibrated eyepiece reticule on the same microscope.

Ablation debris was studied by ablating through a 500 μm diameter pinhole in a sheet of aluminum foil placed on the tissue surface. The debris which collected on the underside of the foil near the edge of the pinhole was examined with a scanning electron microscope. The elemental composition of individual debris particles was determined by diffraction analysis with the electron beam of the scanning electron microscope.

4.3. Irradiance Dependence

In the discussion of ablation in chapter 2, physical arguments are used to suggest that irradiance (power per unit area, units W/mm^2) is the parameter which determines the ablation mechanism in calcified tissue. Since irradiances on the order of MW/mm^2 have been found empirically to be attractive for hard tissue ablation, most of the data collected in the present parameter survey has related to fluence, wavelength, and delivery condition dependencies within this irradiance regime. However, sufficient information has been obtained about irradiance dependence to qualitatively confirm the existence of different ablation regimes. Photographs of tissue craters made at several laser irradiances are reproduced in Fig. 4.2. Given the laser sources avaiable for the parameter study, it was not possible to vary irradiance independent of other laser parameters. For the purposes of this qualitative comparison, all ablation experiments were carried out in air, at a fluence equal to a few times threshold, and at wavelengths strongly absorbed in tissue.

CW laser light with irradiance below $\sim 10^3$ W/mm^2 is commonly used to cut soft tissue. In this case the irradiance (not the pulse duration) determines the extent of tissue damage at the periphery of the ablation site, since irradiance determines the ablation velocity and therefore the extent to which the heated material is removed from the crater before thermal diffusion to adjacent tissue occurs [Partovi et al 87]. When such low irradiance is incident on calcified tissue, however, no ablation results. Figure 4.2(a) is a picture of a bovine bone sample which was irradiated with pulses of peak irradiance $\sim 10^2$ W/mm^2 at

λ = 532 nm from a continuously pumped, repetitively Q-switched frequency-doubled Nd:YAG laser. Note the heterogenous structure of the charring in the irradiation spot, corresponding to density variations in the macroscopic bone structure. This severe charring at low irradiance is consistent with the two-component ablation model discussed in chapter 2, in a regime in which the soft component tissue is not vaporized sufficiently rapidly to entrain and remove the apatite component structure. The hard component thus remains behind, transferring the heat it has absorbed to adjacent tissue.

Increasing the irradiance by an order of magnitude leads to the onset of calcified tissue ablation, although still accompanied by severe char formation. The bone ablation crater in Fig. 4.2(b) was made with pulses of peak irradiance ~10^3 W/mm^2 from a Ho:YSGG laser operating at λ = 2.09 μm. While tissue was ablated in this case at the center of the laser spot, the edges and bottom of the crater were still blackened.

Char-free calcified tissue removal was observed for irradiances between ~10^4-10^6 W/mm^2. Figure 4.2(c) depicts craters made with pulses of peak irradiance ~10^5 W/mm^2 from a long-pulse excimer laser operating on XeCl gas at λ = 308 nm.

At irradiances greater than ~10^6 W/mm^2, plasma formation accompanies tissue ablation [Kittrell et al 86, Gitomer et al 90]. Temperatures of several thousand degrees Celsius can be attained in such plasmas, sufficient to vaporize both hard and soft components of calcified tissue. Figure 4.2(d) depicts a crater made with pulses of ~10^7 W/mm^2 peak irradiance from a frequency-tripled Nd:YAG laser operating at λ = 355 nm, in an experiment in which a bright blue-white plasma spark was clearly visible above the tissue surface. While the appearance of the plasma-mechanism laser craters appears similar to those made with two-component mechanism ablation, a qualitative difference between the mechanisms shows up in plots of crater depth versus fluence. As can be seen in Fig. 4.10(b), as pulse fluence is increased sufficiently that the plasma formation irradiance threshold is exceeded, the ablation crater depths cease to increase. This effect is due to the absorption of incident laser light by the plasma itself, and leads to a decreased ablation efficency above plasma threshold.

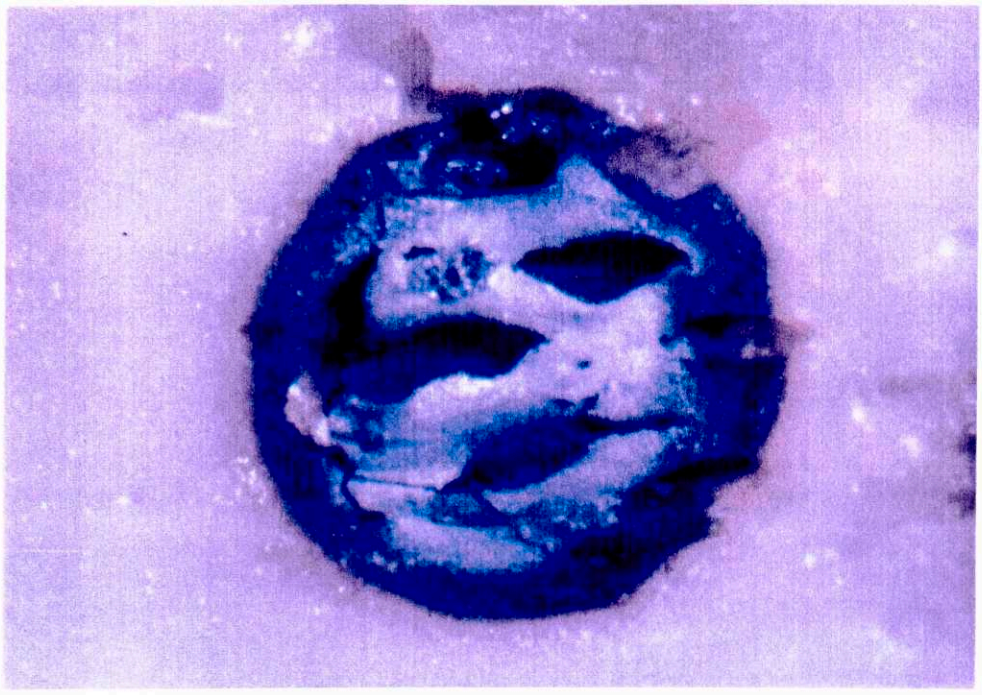

(a)

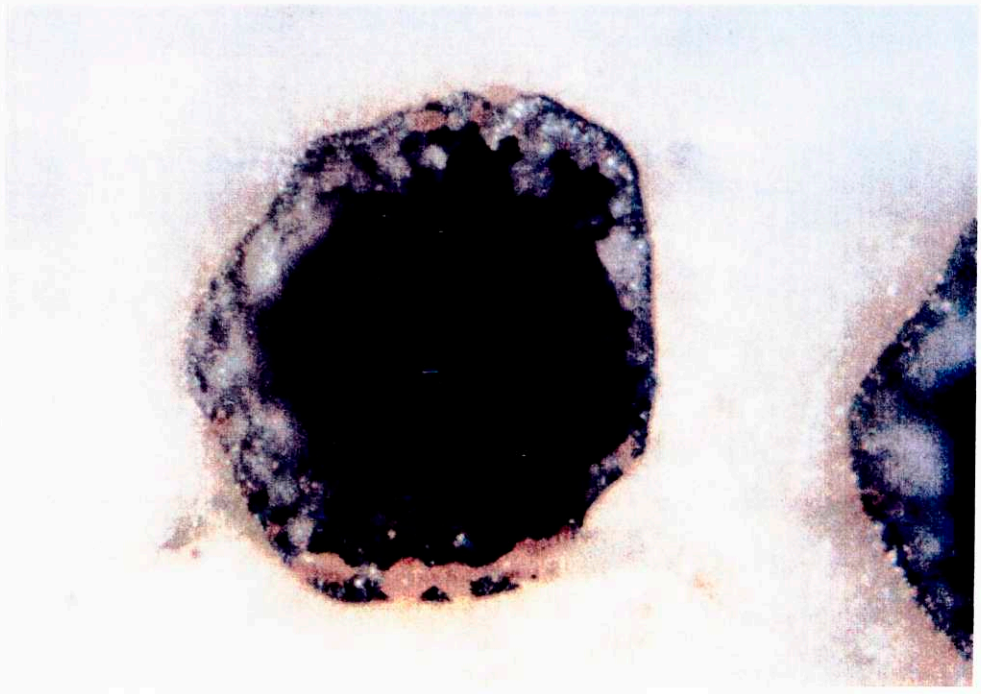

(b)

FIGURE 4.2. Results on bovine shank bone of varying laser irradiance. (a) $I \sim 10^2$ W/mm^2, $\lambda = 532$ nm, spot diameter 1 mm; (b) $I \sim 10^3$ W/mm^2, $\lambda = 2.09$ μm, spot diameter 500 μm.

(c)

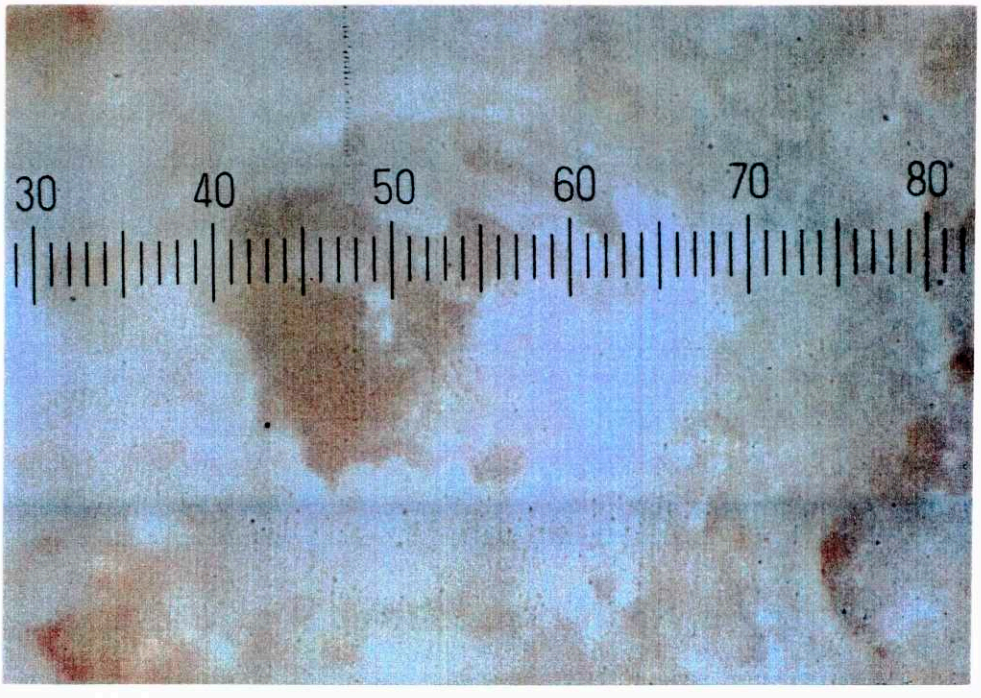

(d)

FIGURE 4.2. Results on bovine shank bone of varying laser irradiance. (c) $I \sim 10^5$ W/mm^2, $\lambda = 308$ nm, spot diameter 500 μm; (d) $I \sim 10^7$ W/mm^2, $\lambda = 355$ nm, spot diameter 500 μm.

4.4. Fluence Dependence

In all of the models of ablation discussed in chapter 2, fluence (energy per unit area, units mJ/mm^2) is the quantity which determines the volume of tissue removed per laser shot. This section details the results of several experiments conducted to investigate the fluence dependence of ablation.

4.4.1. Irradiance-Time Reciprocity

Fluence is the product of pulse irradiance and pulse duration. A test of the reciprocity between irradiance and pulse duration in ablation was carried out using the variable pulse durations available from the hydrogen fluoride laser. With the laser operating on the λ=2.832 μm HF line, laser craters were made in bovine shank bone with two different fluences, each constructed from five different irradiance-time combinations. At each irradiance-pulse duration combination selected, five craters were drilled. The average of the five crater depths at each fluence combination are plotted in Fig. 4.3; the error bars denote crater depth measurement error. In Fig. 4.3, the circle and square data points represent craters formed with different fluences. To within the error bars, the crater depths are constant for constant fluence, independent of the irradiance-pulse duration combination used to construct that fluence. Thus, within the pulse durations available in this experiment, fluence is comfirmed as the basic quantity of dosimetry for tissue removal at λ = 2.8 μm.

Further evidence that crater depth scales with fluence, for irradiances typical of pulsed calcified tissue ablation, is provided by the similarity of data from ablation at λ = 355 nm with 7.5 ns duration pulses (section 4.5), and with 400 nsec stretched pulses (section 9.3).

4.4.2. Observed Fluence Regimes

At all wavelengths studied in the irradiance range for two-component ablation, the fluence dependence of the depth of tissue removed could be divided into three regimes: 1) a fluence threshold, below which ablation does not occur; 2) a region of roughly linear growth of depth with fluence; and 3) a region over which crater depth falls off from the linear (see Fig. 10(a-j)). As derived in chapter 2, the existence of a fluence threshold is due to the fact that the incident laser light is absorbed over some depth in the tissue, and the tissue at the surface must reach a critical energy density before ablation can begin [Partovi et al 87].

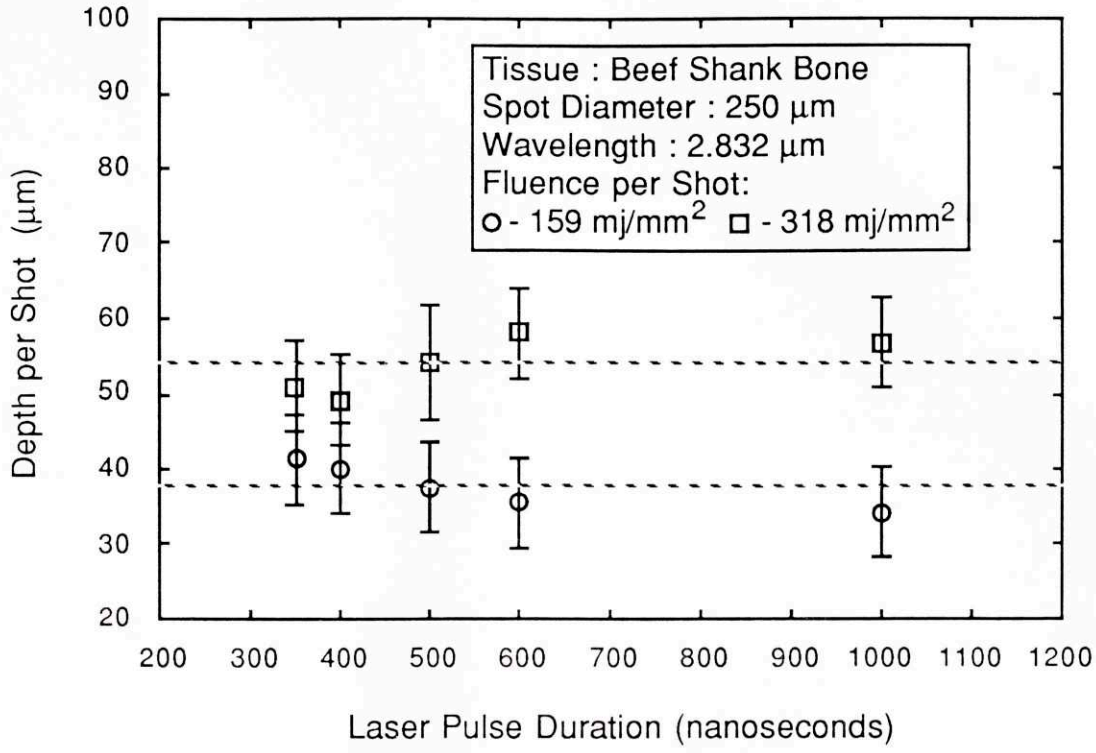

FIGURE 4.3. Fluence reciprocity experiment. Crater depths are constant for constant fluence, independent of the irradiance-pulse duration combination used to construct that fluence.

The observed fall-off of crater depth with fluence at high fluence may be explained by several factors. As has already been mentioned, the onset of a laser induced plasma produces this effect, although the fall-off is also observed in the absence of a plasma. Another contributing explanation is that absorption of incident laser light by debris created early in the pulse leads to a fall-off for high fluences [Izatt et al 90a, Izatt 88, chapter 2]. It should be noted that since high fluence craters were deeper than threshold-region craters, the fall-off could be related to the effects of ablating at the bottom of a deep crater. For example, the solid angle available for tissue ejection narrows as a crater gets deeper, so that a larger fraction of the debris hits the walls and may fall back into the crater. The debris contains molten calcium compounds, and may even re-plate the crater walls and bottom with a more refractory material than native bone. In addition, if the laser light is diverging at the tissue surface, as would happen if it were focussed there with a short depth of focus, or if it were emerging from an optical fiber, then the expansion of the light decreases the local fluence and leads to a fall off of crater depth as well.

The linear portion of the depth versus fluence behavior is probably the most interesting for many practical applications, since fiber delivery systems usually limit the fluence it is possible to deliver to the tissue surface, and this region is usually free of plasma effects for typical pulse durations. For this reason, all of the quantitative analysis of depth versus fluence data in this chapter has been performed using the linear thermal ablation model described in chapter 2. This model predicts linear growth of crater depth with fluence, described by the parameters fluence threshold (ϕ_0, units mJ/mm^2) and ablation yield (Y, units mm^3/J) [Partovi et al 87]. The ablation yield is the slope of the depth versus fluence curve in the linear region. In this work, these parameters are extracted from the data by fitting to the equation

$$l = Y(\phi - \phi_0), \tag{4.3}$$

where l is the measured crater depth and ϕ the incident fluence. In order to include only the linear portion of the curve in data fits, only the data between ϕ_0 and $2 \cdot \phi_0$ are fitted.

The steady-state ablation model seems to fit our data well, and has been sufficient to obtain reasonable values for ϕ_0 and Y in the near-threshold regime. However, we have observed two situations in which crater depths are not linear with total fluence, which are the subjects of the next two sections.

4.4.3. Dependence on the Number of Shots

Crater depths in bone were observed to be nonlinear with respect to the number of shots fired into each crater. This effect was most pronounced for the ultraviolet wavelengths (see section 4.5.2). Figure 4.4 shows a plot of total crater depth versus the number of shots fired in a bone crater for the λ = 355 nm wavelength. In this plot, each data point represents a single tissue crater, and the error bars around each point represent the instrumental error associated with measuring crater depths. As can be seen in the figure, the later shots fired into the crater removed less tissue than the early shots.

The fall-off in crater depth with the number of shots is probably caused by the same mechanisms which cause the fall-off in crater depth versus fluence for high fluences, as explained in section 4.4.2 above. Of particular relevance are narrowing of the solid angle available for debris ejection as the crater deepens, and re-plating of calcified deposits on the crater walls and bottom between shots.

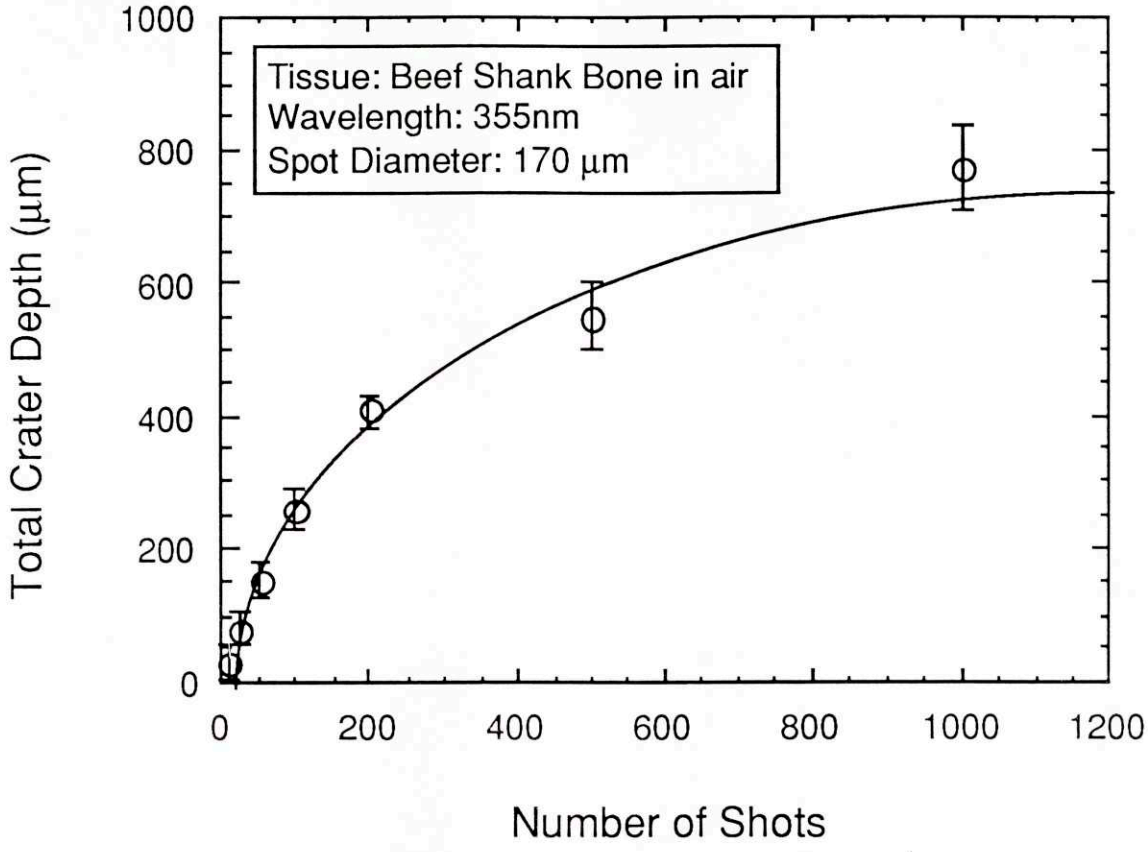

Figure 4.4. Crater depth versus number of shots for the 355 nm wavelength. Ablation fluence was 90 mJ/mm^2.

For practical reasons, in many cases is is not possible to do all experiments in a given study with the same number of shots per crater. In order to be able to compare results among different experiments, the data from an experiment such as the one depicted in the figure above can be used to correct for the expected crater depth at a different number of shots than were actually used. Since the number of shots used does not affect the fluence threshold, this correction takes the form of a "correction factor" which multiplies the ablation yield.

4.4.4. Spot Diameter Dependence

Ablation of bone in air depends upon the spot diameter of the illuminating laser beam, even if the fluence remains the same. Figure 4.5 contains a plot of crater depths in bovine bone as a function of spot diameter, in an experiment in which the pulse energy was adjusted to give the same fluence of 45 mJ/mm^2 for all spot diameters. Each data point in the figure represents an average over five separate bone craters; the error bars reflect the

standard deviation of the crater depths about the mean. Crater depths increased with the spot diameter up to about 600 μm, at which point they evened out.

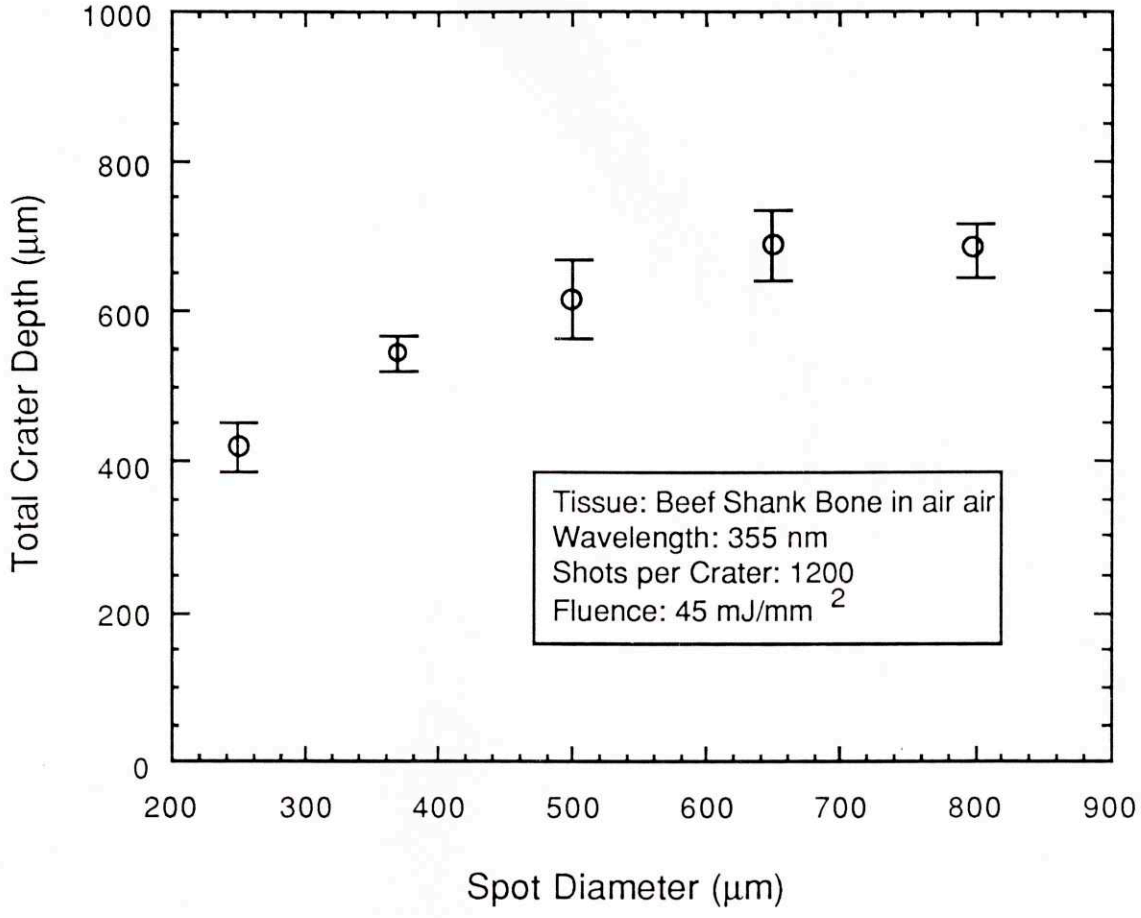

FIGURE 4.5. Spot diameter dependence of bone ablation for fixed fluence.

The data in Fig. 4.5 does not provide direct information about the separate dependencies of fluence threshold and ablation yield on spot diameter, since crater depth at a given spot size depends on both of these quantities (see Eq. (4.3)). Obtaining this information requires a complete depth versus fluence curve for each spot diameter.

Separate crater depth versus fluence studies have been done at the $\lambda = 355$ nm wavelength for two spot diameters of 170 and 1400 μm; the linear portions of the data for both spot sizes are shown on the same plot in Fig. 4.6. Each data point in the figure represents a single bone crater. The results of linear fits to the data for fluence threshold and ablation yield are shown as the solid lines in the figure and are summarized in Table 4.2. The experiment at the 170 μm spot diameter was conducted with 100 shots per crater, and the fitted yield for 100 shots per crater is listed in the fourth column of the table. In

order to compare this data with the data taken at the 1400 μm spot diameter, the former was corrected for the expected yield at 600 shots per crater using the results of the experiment described in the previous section. The corrected ablation yield appears in the fifth column of the table, and the circle data points in the plot have also been corrected. The data in Table 4.2 reveal a large difference, almost a factor of three, in both fluence threshold and ablation yield for the different spot diameters.

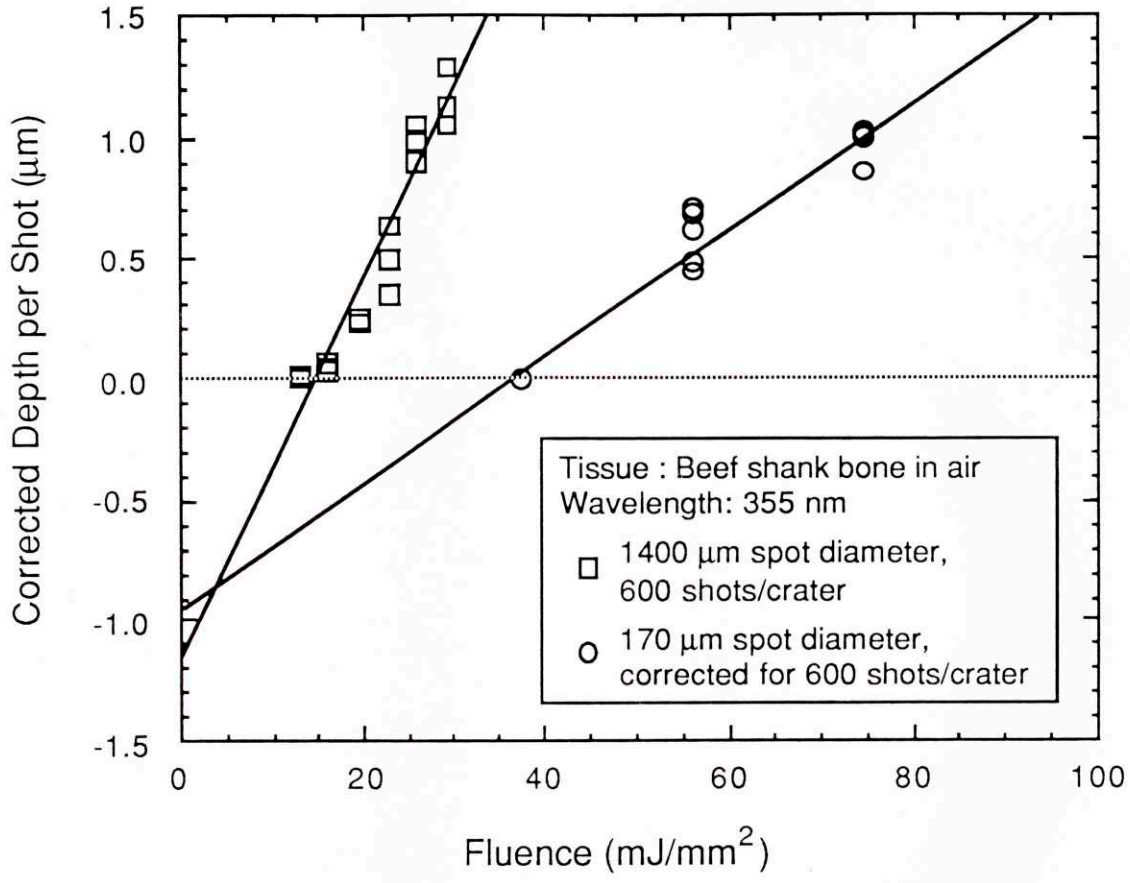

FIGURE 4.6. Depth versus fluence data for two different spot diameters at the λ = 355 nm wavelength. The lines are linear fits to the experimental data, shown extended to the y-axis intercept.

There are several reasons to explain a variation in fluence threshold (ϕ_0) and ablation yield (Y) with spot diameter (d). One explanation which has been offered for variation of ϕ_0 with d is that there may exist a sparse distribution of ablation "initiation sites" scattered over the tissue surface, and the probability of the inclusion of such a site within the illuminated spot increases with the square of d [Tobin 85]. These initiation sites could consist of areas with increased light attenuation, or with altered tissue thermal properties.

Spot Diameter (mm)	Number of Shots per Crater	Fluence Threshold, ϕ_0 (mJ/mm^2)	Original Fitted Ablation Yield, Y (mm^3/J)	Ablation Yield Y Corrected for 600 shots/crater (mm^3/J)
1.4	600	14.8	0.078	.078
0.17	100	36.2	0.066	.026

TABLE 4.2. Dosimetry data for λ = 355 nm incident on beef shank bone in air.

An explanation which is more consistent with the data, accounting for variation of both ϕ_0 and Y with d, has to do with the three-dimensional distribution of light in tissue. When laser light is incident on tissue, some fraction of the light deposited by the laser is scattered out of the volume directly under the laser spot. Light which is radially scatterred beyond some boundary in the tissue no longer contributes to ablation. For a given constant scattering length, the fraction of light lost in this way is larger for small spots. In the steady-state model of ablation described in chapter 2, the observable quantities ϕ_0 and Y are related to the "fundamental" tissue properties h_a (the heat of ablation, units J/mm^3) and D (the penetration depth of light in tissue, units mm) through the geometrical efficiency factor f:

$$\phi_0 = \frac{h_a \bullet D}{f}; \tag{4.4}$$

$$Y = \frac{f}{h_a}. \tag{4.5}$$

The function f is the fraction of light <u>not</u> lost out of the cylinder of tissue directly underneath the laser beam. It is wavelength-dependent, determined by the interplay of scattering and absorption in the tissue. Since the study of light distribution in tissue is an active area of research in biomedical optics, the exact form of f is not known. It is physically reasonable, however, that it should vary with the ratio of spot diameter (d) to penetration depth (D) with the limiting behavior:

$$f \to 0 \text{ as } d/D \to 0; \tag{4.6}$$

$$f \to 1 \text{ as } d/D \to \infty. \tag{4.7}$$

According to this model, both ϕ_0 and Y are functions of the spot diameter, for spot diameters of the same order as the penetration depth of the light in tissue. For spot diameters much larger than this, f ~ 1, and ablation reduces to the one-dimensional case.

Although the form of f is not known, a check of the the compliance of the experimental data with this theory is obtained by examining the product of ϕ_0 and Y, from which the loss function cancels out:

$$\phi_0 \cdot Y = \frac{h_a \cdot D}{f} \cdot \frac{f}{h_a} = D. \qquad (4.8)$$

On a depth versus fluence plot, the product of the fluence threshold and the ablation yield is just the negative of the y-axis intercept of the fitted curve. The fitted curves for both spot diameters in Fig. 4.6 have very nearly the same y-axis intercept. In other words, although the values for ϕ_0 and Y varied for different spot sizes, they varied cooperatively in such a way as to predict the same value of D. Thus, D appears to be invariant with spot diameter, consistent with it being a more fundamental parameter than the observables ϕ_0 and Y.

An apparent inconsistency remains, however. The data in Fig. 4.5 which shows crater depth changing with spot diameter up to ~600 μm imply that f does not approach its limiting value until that point. Yet, the values of D from Fig. 4.6 are on the order of μm. One explanation for this is that f approaches its limit (see Eq. (4.7)) very slowly with d/D. This does not seem physically reasonable, however, given the example f = d/(d+4•D) derived in section 2.4.5.2 from a physically reasonable trial light distribution function.

Another explanation for this discrepancy is that D is not a constant during the ablation process, but is altered from its value in "cold" tissue during ablation. This would also be consistent with the spectroscopy results in chapter 3, which give an attenuation depth in bone at λ = 355 nm of ~200 μm in cold tissue. The possibility of a transient change in tissue optical properties is discussed in more detail in section 4.5.2.4 and in chapter 5.

4.5. Wavelength Dependence

The wavelength of ablating laser light controls the scale of the ablation process by determining the attenuation of the light in tissue, which in turn determines the volume over which energy is deposited. In order to investigate the effects of wavelength on calcified tissue ablation, several ablation characteristics were studied over a wide variety of laser wavelengths.

4.5.1. Quality of the Laser Cut

4.5.1.1. Crater Appearance

The visual appearance of craters with similar diameters, and ablated with similar doses of light (measured in terms of the number of times above fluence threshold) varied substantially with laser wavelength. Photographs of craters made with several of the wavelengths studied are provided in Fig. 4.7. Laser craters drilled with wavelengths between 295 and 375 nm [Fig 4.7(a)] and near 2.8 μm [Fig. 4.7(d)] were sharply cut and followed closely the profile of the illuminating beam, with no debris particles greater than a few μm in diameter observable on the tissue surface near the craters. Craters made with wavelengths between 450 nm [Fig. 4.7(b)] and 590 nm [Fig. 4.7(c)] had shapes which were irregular, clearly dependent on the local morphology of the bone. In addition, flakes of bone as large as 500 μm in diameter were often found attached to the edges of the craters or scattered nearby. For the 530 nm and 590 nm wavelengths, many craters were substantially larger than the diameter of the illuminating beam. Craters made at the 2.1 μm wavelength were moderately sharply cut, but exhibited severe char formation [see Fig. 4.2(c)]. The relatively low Ho:YSGG laser irradiance (~10^3 W/mm^2), the lowest used in this study, probably contributed to the blackening.

4.5.1.2. Histology

Histological examination of laser craters in bone made at 308 nm and 2.8 μm indicated only a very narrow zone of thermal damage in tissue adjacent to the laser cuts (Fig. 4.8). The histology also indicated that the crater walls were smoothly cut to within a few tens of microns of surface roughness. Note, however, that histologic examination of craters made in calcified tissue is of limited usefulness for distinguishing the quality of the laser cut if the tissue is decalcified prior to sectioning, since any crater surface irregularities caused by the presence of calcified material will be removed during sample preparation.

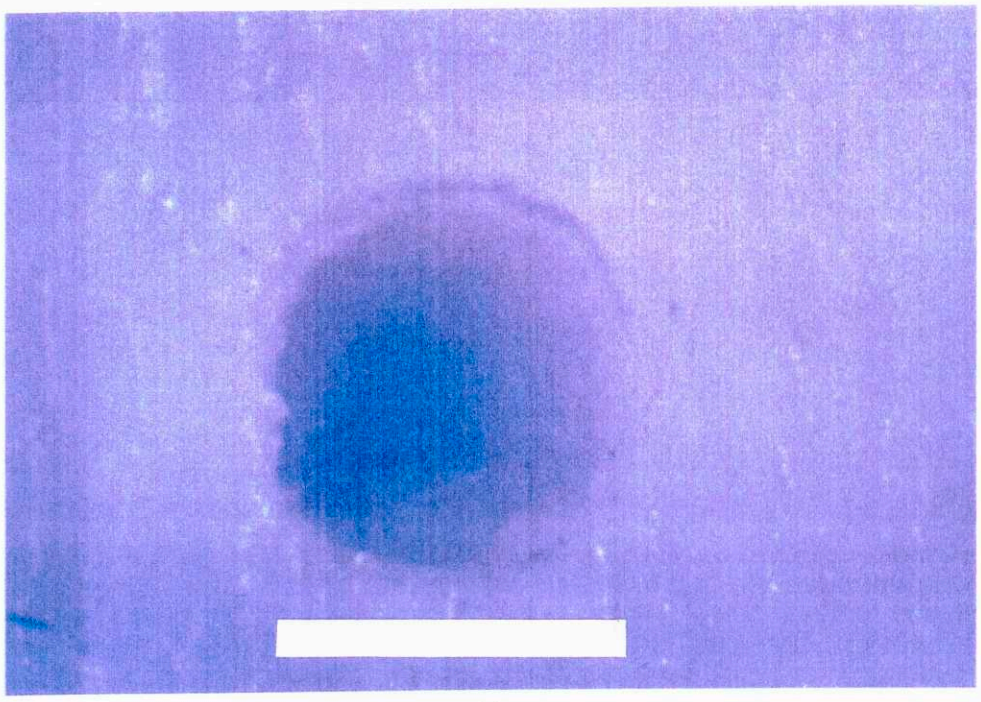

(a)

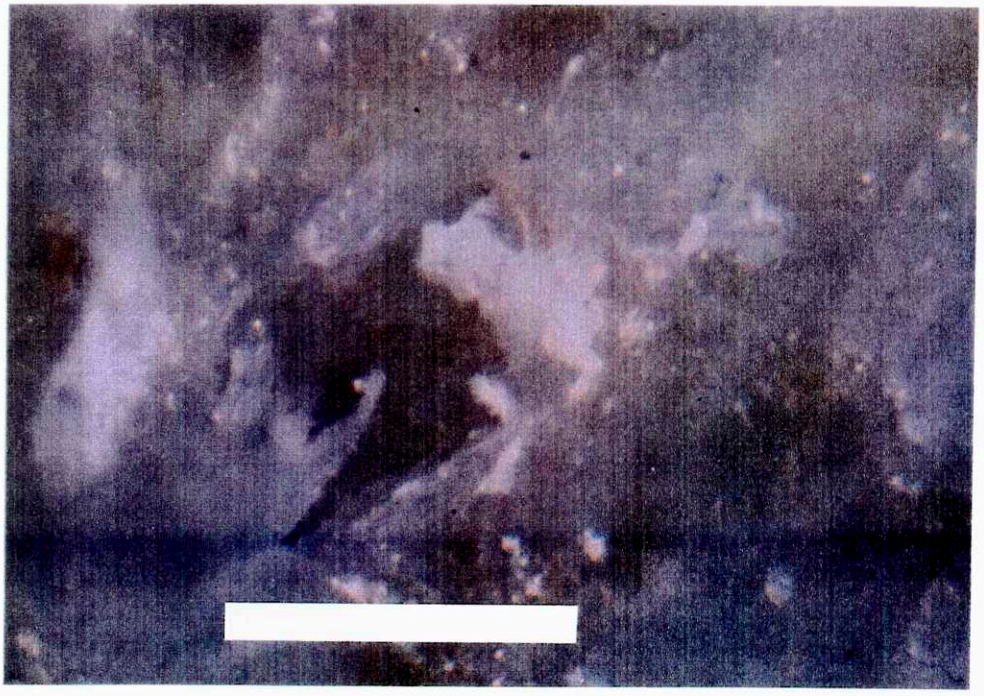

(b)

FIGURE 4.7. Photographs of laser craters made in bovine shank bone by pulses at (a) λ = 355 nm; (b) λ = 450 nm. In all photos, the laser spot size was 500 μm, and the laser fluence was a few times threshold. Scale: length of bar = 500 μm.

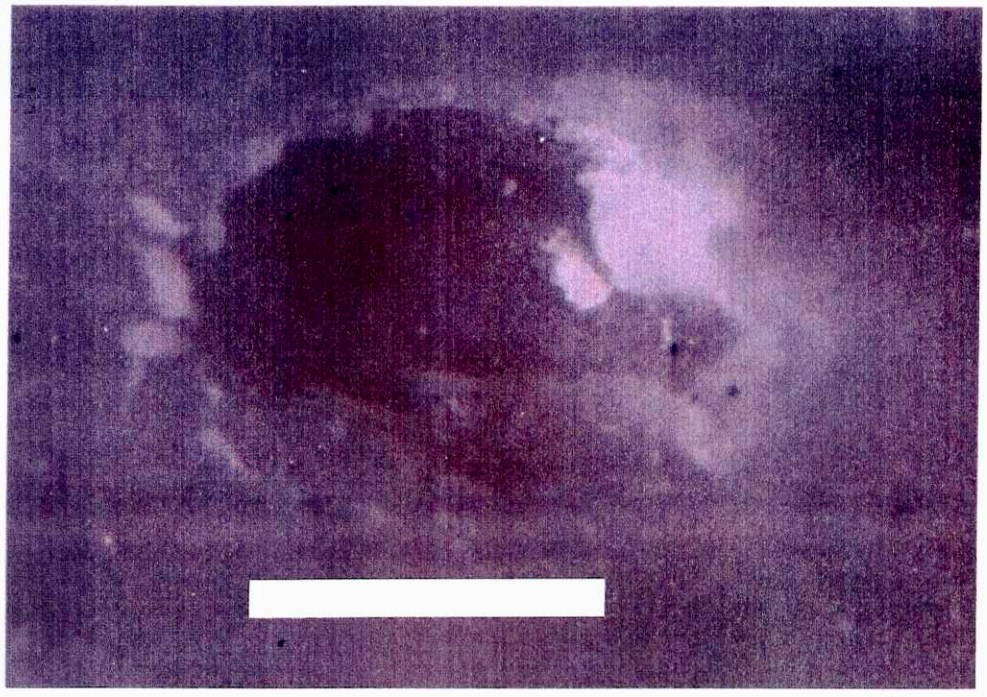

(c)

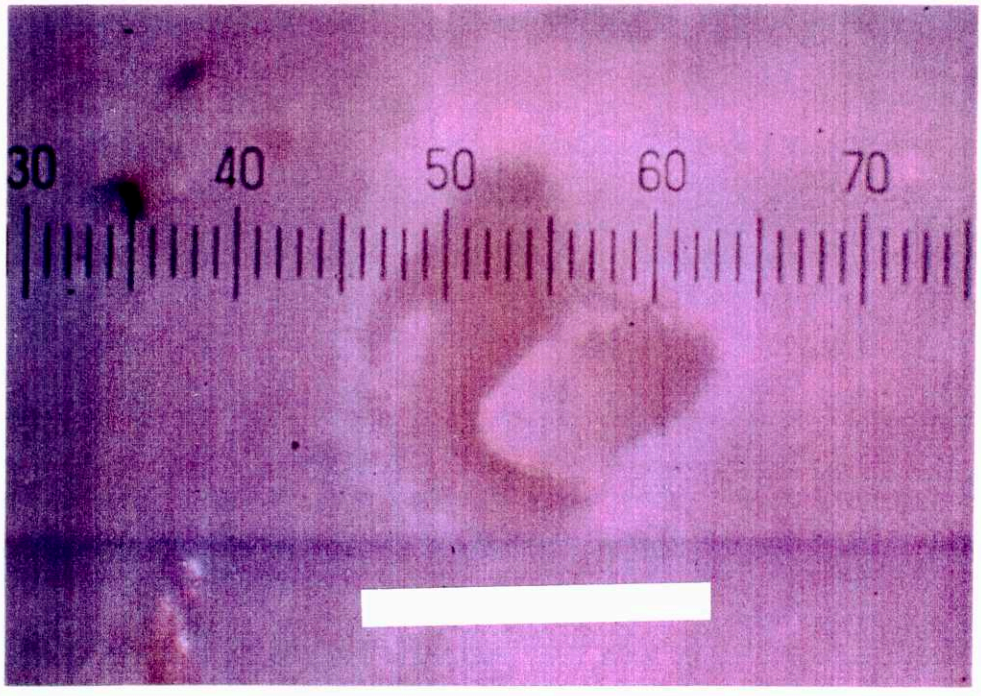

(d)

FIGURE 4.7. Photographs of laser craters made in bovine shank bone by pulses at (c) $\lambda = 590$ nm; (d) $\lambda = 2.8$ μm (ring-shaped beam profile). In all photos, the laser spot size was 500 μm, and the laser fluence was a few times threshold. Scale: length of bar = 500 μm.

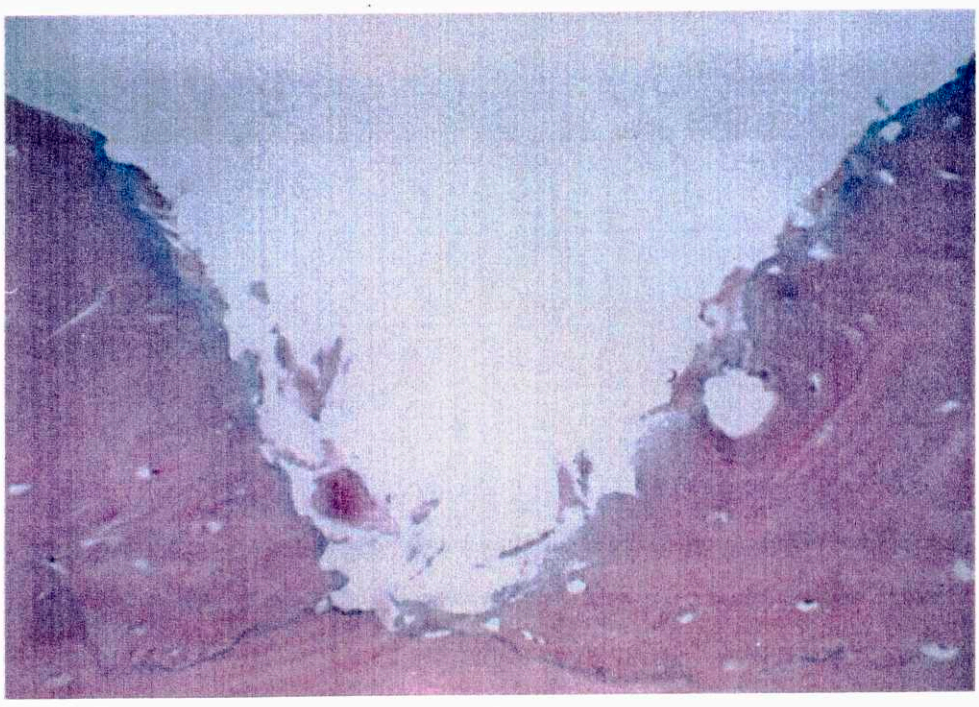

(a)

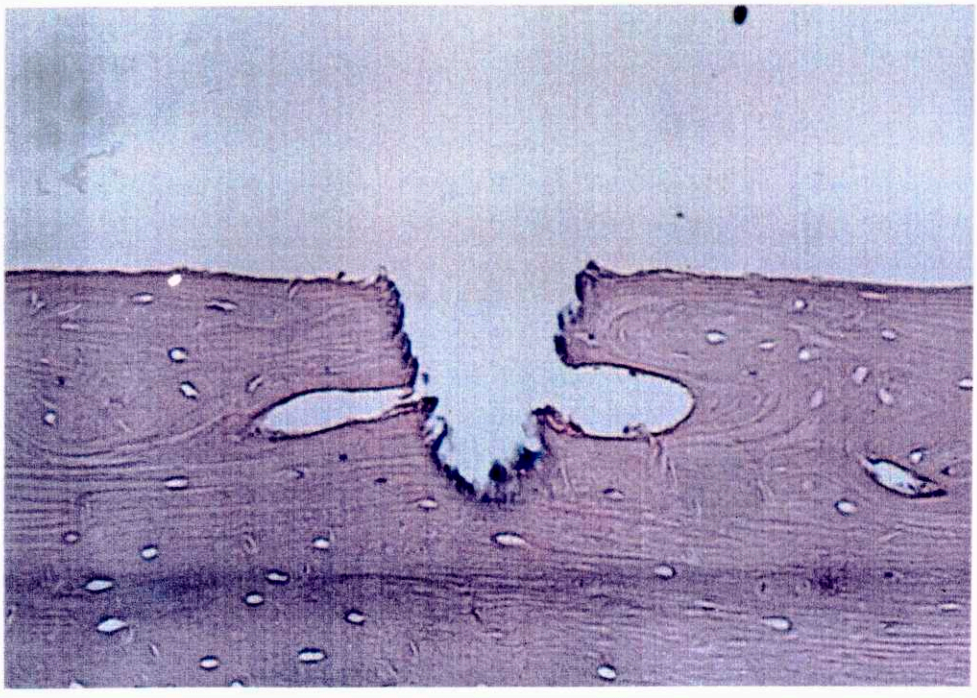

(b)

FIGURE 4.8. Histologic appearance (H & E stain) of craters drilled in bovine shank bone with (a) 308nm, fluence 50 mJ/mm^2, 100 shots fired, crater diameter 500 μm; and (b) 2.8 μm, fluence 200 mJ/mm^2, 5 shots fired, crater diameter 150 μm, crater involving vascular canal. Original magnification 25x.

4.5.1.3. Ablation Debris

Ablation debris captured in flight was studied at the 308 nm, 355 nm, and 2.8 μm wavelengths with scanning electron microscopy. Debris particle sizes at all of these wavelengths ranged from a few hundred nm to a few tens of μm in diameter. Scanning electron micrographs of debris collected from ablation are reproduced in Fig. 4.9. Most of the debris visible in the photomicrographs in Figs. 4.9(a) and 4.9(b) appears as rough-edged particles on the order of 10 μm or less in diameter, although a few particles have the appearance of condensed droplets. A greater fraction of the debris appears as condensed droplets in Fig. 4.9(c), which depicts ablation products from an experiment in which a laser-induced plasma was apparent on the tissue surface during ablation. In this case, the high temperatures occuring within the plasma were sufficient to melt a substantial portion of the apatite portion of the bone in this experiment, after which it recondensed into droplets on the substrate. Note also the presence of many needle-shaped particles covering all of the surfaces of the ejecta; the shape of these particles is reminiscent of individual calcium hydroxyapatite crystals. Figure 4.9(c) indicates another result of exceeding the irradiance range for two-component ablation, the production of molten apatite which can replate onto crater walls or condense into particles.

The elemental ratio of calcium to phosphorous in the debris particles at all three wavelengths was measured by electron diffraction analysis to be approximately 5:3, which corresponds exactly to the stoichiometric ratio of these elements in calcium hydroxyapatite, the primary calcium salt in bone. The elemental composition, size distribution and appearance (mostly rough-edged particles) of the debris particles in Figs. 4.9(a) and 4.9(b) correspond to the properties of calcium hydroxyapatite microcrystallites in bone. The relatively undisturbed appearance of these particles in the ablation debris is consistent with the two-component ablation mechanism postulated above, in which the calcium salt component of the tissue is accelerated out of the crater without being vaporized during ablation.

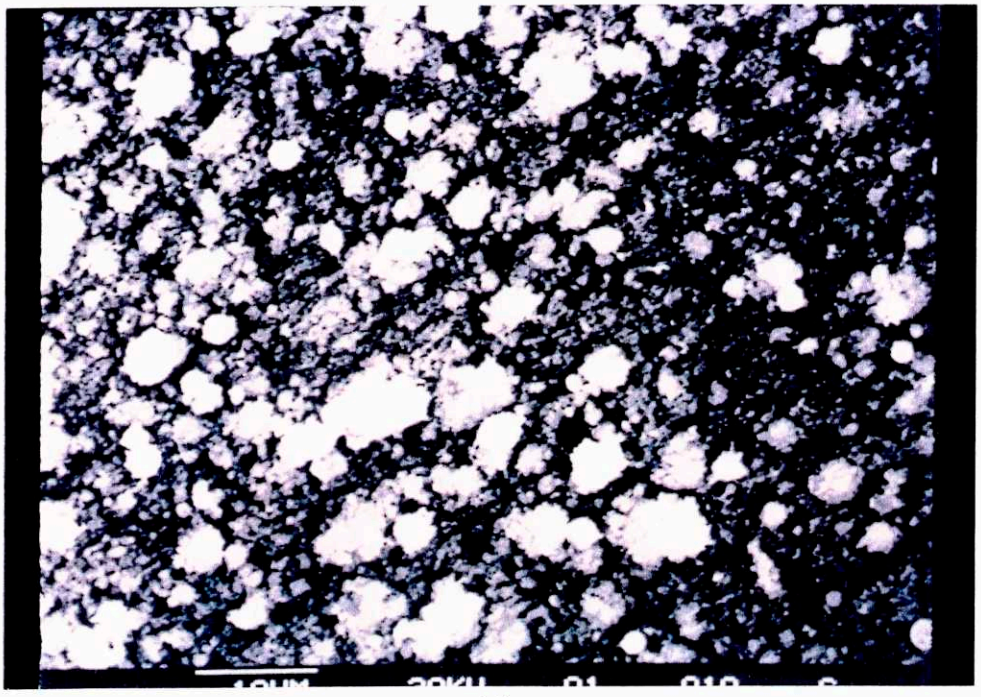

(a)

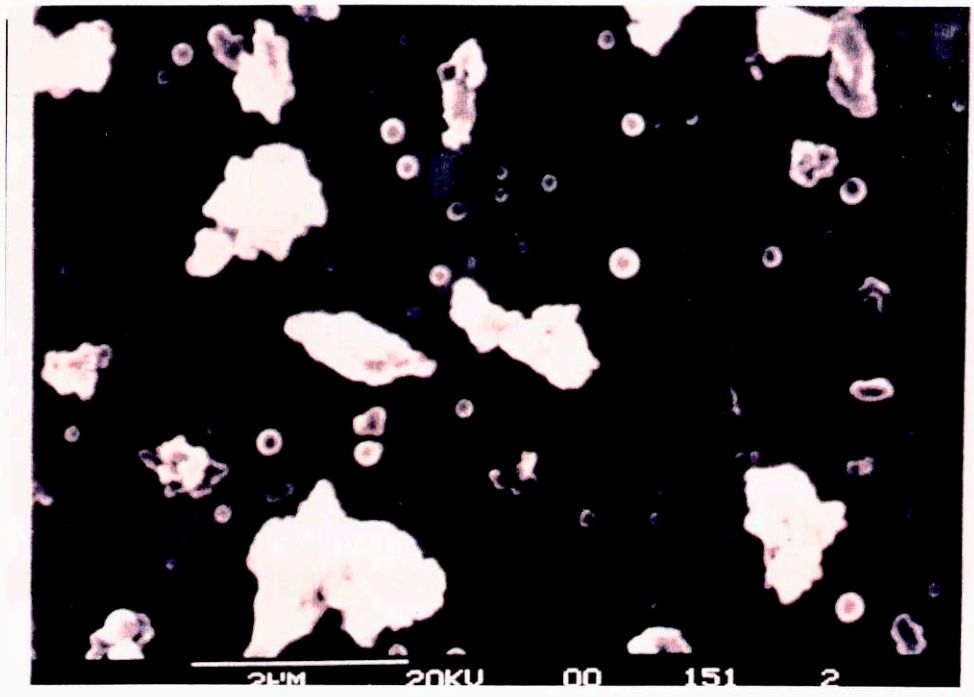

(b)

FIGURE 4.9. Scanning electron micrograph of ablation debris captured on an aluminum substrate. (a) λ = 355 nm, fluence ~100 mJ/mm^2, 100 shots fired, length of bar = 10 μm. (b) λ = 2.8 μm, fluence ~200 mJ/mm^2, 100 shots fired, length of bar = 2 μm.

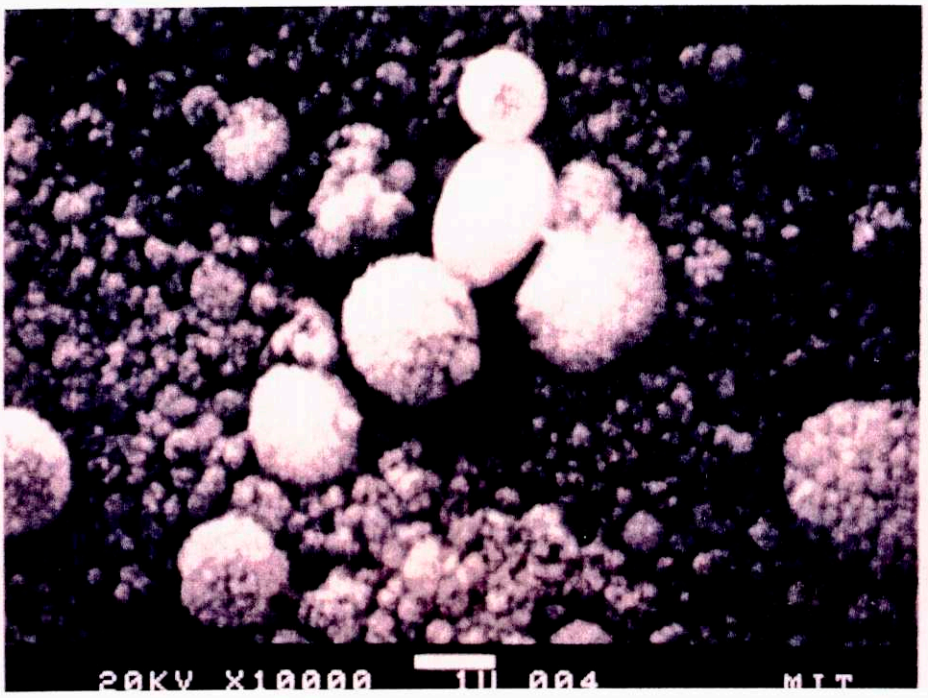

(c)

FIGURE 4.9. Scanning electron micrograph of ablation debris captured on an aluminum substrate. (c) λ = 308 nm, fluence unknown, 100 shots fired, plasma formation observed, length of bar = 1 μm.

4.5.1.4. Discussion

The sharpest laser cuts were made by wavelengths below about 400 nm and near 3 μm. The sharpness of the cuts, the small debris particle size and the minimal thermal damage to peripheral tissue at these wavelengths are desirable features for microsurgical applications. At these wavelengths absorption of laser light in the tissue is very strong, so energy is deposited close to the surface. The vaporization-entrainment process described in chapter 2 is therefore confined to a shallow layer at the surface of the tissue. As the wavelength is increased from the ultraviolet into the visible, light is less strongly absorbed, so that scattering plays a larger role in the light distribution. Light scattering effects can lead to an irradiance peak below the tissue surface, resulting in a subsurface temperature maximum [Haldorssen et al 78, Langerholc 79]. In this case vaporization can begin below the surface, breaking the tissue above into larger particles; this results in rougher cutting. At 503 and 590 nm, where tissue absorption is weakest among all wavelengths studied, the appearance of the laser craters suggests that spallation, in which large tissue chunks are ejected from the surface by thermal expansion, may also play a role [Dingus et al 91]. Note that this process may be more efficient than ablation, because the tissue is not thoroughly disintegrated. This is not a desirable process, however, if sharp cuts and small debris particles are required.

4.5.2. Quantitative Ablation Dosimetry

4.5.2.1. Crater Depth Versus Fluence

At each wavelength available for study, bone removal dosimetry was quantified by ablating craters with varying laser fluences, and subsequently measuring the crater depths. In order to generate craters deep enough for reliable location under the microscope and for accurate depth measurement, dosimetry experiments were conducted with more shots per crater at wavelengths with low ablation thresholds. In order to be able to compare dosimetry results, a separate depth versus number of shots experiment (see section 4.4.3) was conducted at each wavelength. The results for all wavelengths were corrected for the expected crater depth after 10 shots; the correction factor was one for all but the shortest wavelengths.

Plots of crater depth versus laser fluence for all wavelengths studied are reproduced in Figs. 4.10(a-j). The actual number of shots which were fired into each crater in the experiment and the calculated correction factor for 10 shots/crater are noted on the plots.

Unfortunately, due to limitations experienced with several of the laser sources used for the study, not all experiments were conducted with the same spot diameter. The spot diameters used in each experiment are also noted on the plots.

For each wavelength, the fluence threshold and ablation yield were extracted by fitting the ablation data to Eq. (4.3). The linear fit was done to those crater depths lying between just less than the lowest fluence at which a crater was observed, and twice that value, as described in section 4.4.2. The data points included in the linear fit appear as squares in the plots of Figs. 4.10(a-j); the calculated fits appear as solid lines.

Figures 4.10(b) and 4.10(g) deserve special comment, as they contain data taken at irradiance values near the limits of the two-component ablation regime. The data in Fig. 4.10(b) was taken with a frequency-tripled Nd:YAG laser with a 7.5 ns duration pulse, placing the irradiance during the pulse on the order of 10^7 W/mm^2. This was sufficient to cause plasma breakdown on the tissue surface for fluences above ~ 80 mJ/mm^2, and the data exhibits an obvious turn at that point due to shielding of the incident light by the plasma. The data in Fig. 4.10(g) was taken with a free-running Ho:YSGG laser, with an irradiance of only ~10^3 W/mm^2. A photograph of a crater drilled in air with this laser is shown in Fig. 4.2(b); craters exhibited severe char formation, indicating that complete two-component ablation was not taking place.

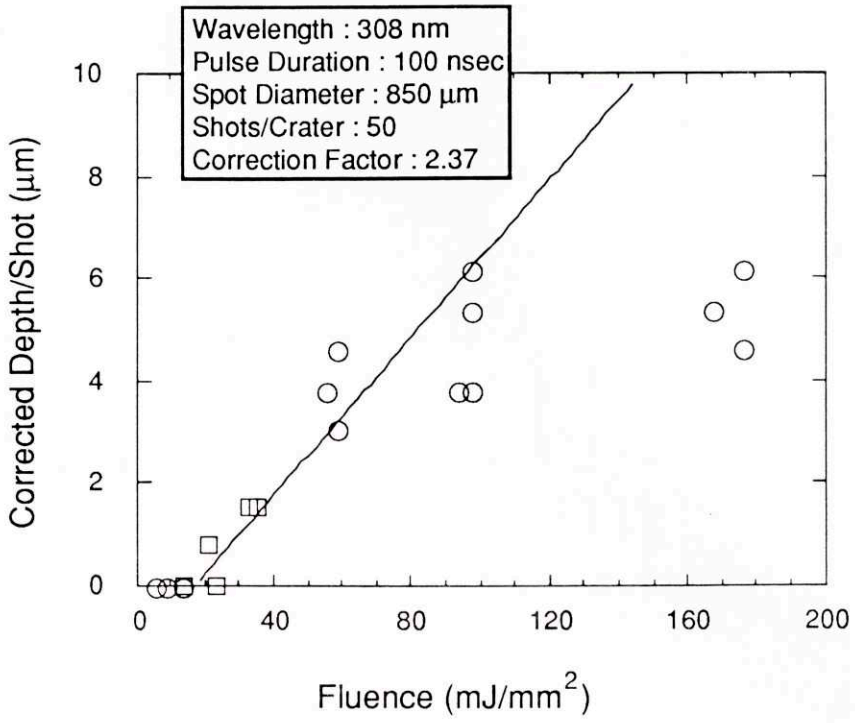

FIGURE 4.10(A). Dosimetry data for the λ = 308 nm wavelength.

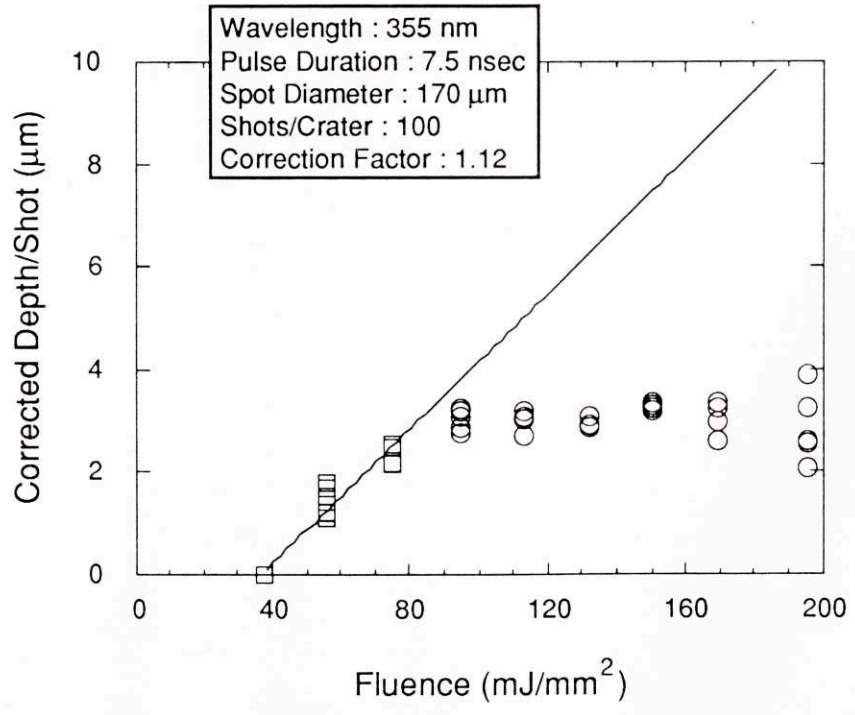

FIGURE 4.10(B). Dosimetry data for the λ = 355 nm wavelength. Plasma generation above the tissue surface was observed starting at ~ 80 mJ/mm^2.

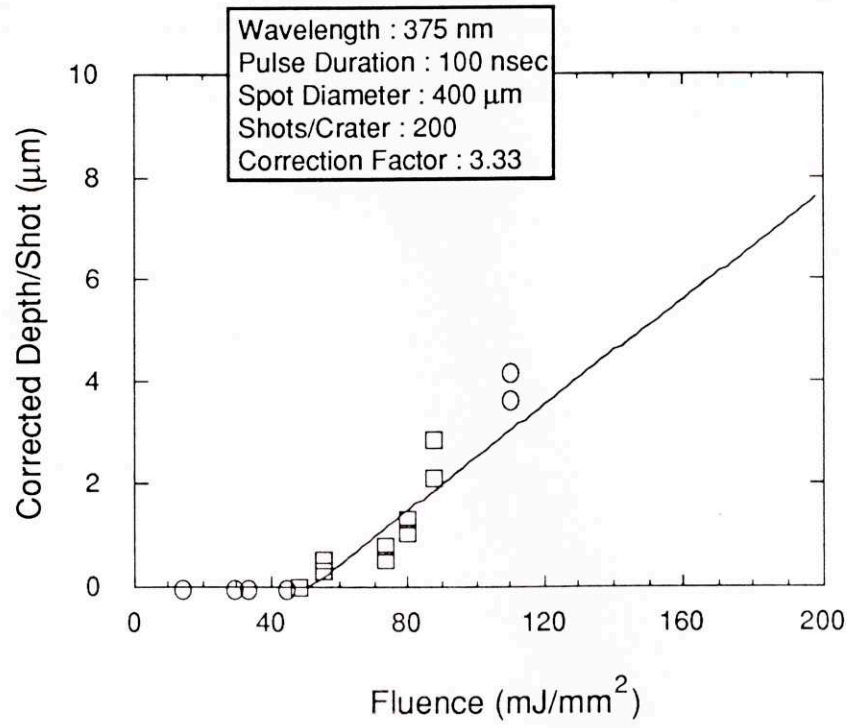

FIGURE 4.10(C). Dosimetry data for the λ = 375 nm wavelength.

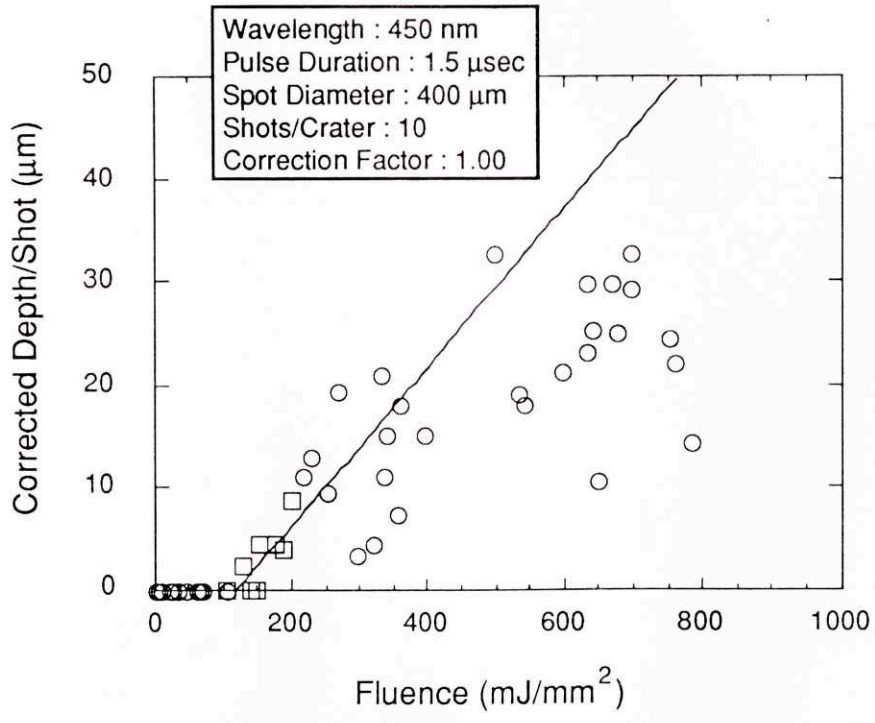

FIGURE 4.10(D). Dosimetry data for the λ = 450 nm wavelength.

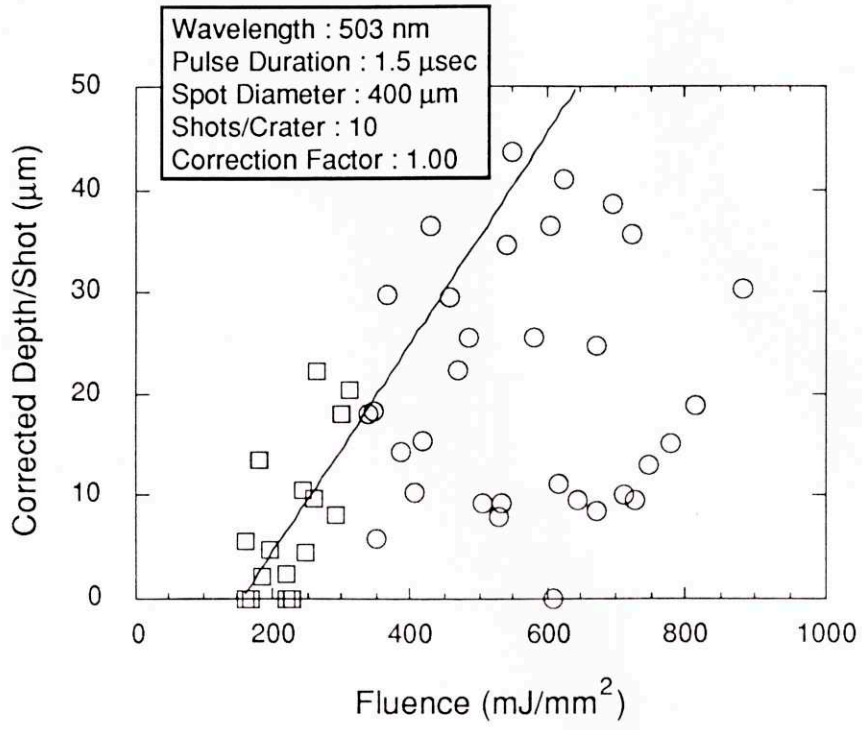

FIGURE 4.10(E). Dosimetry data for the $\lambda = 503$ nm wavelength.

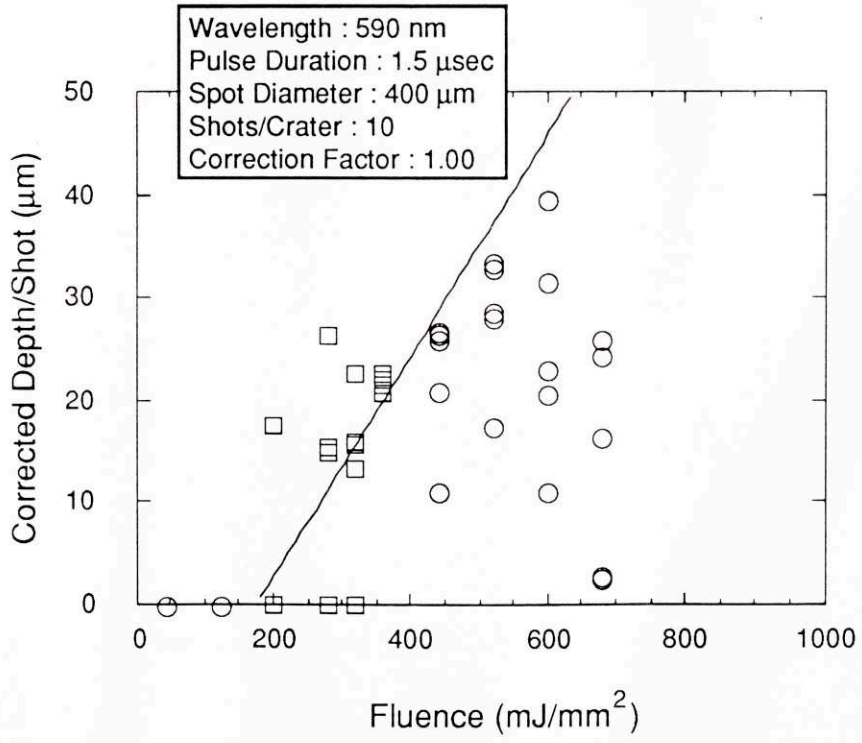

FIGURE 4.10(F). Dosimetry data for the $\lambda = 590$ nm wavelength.

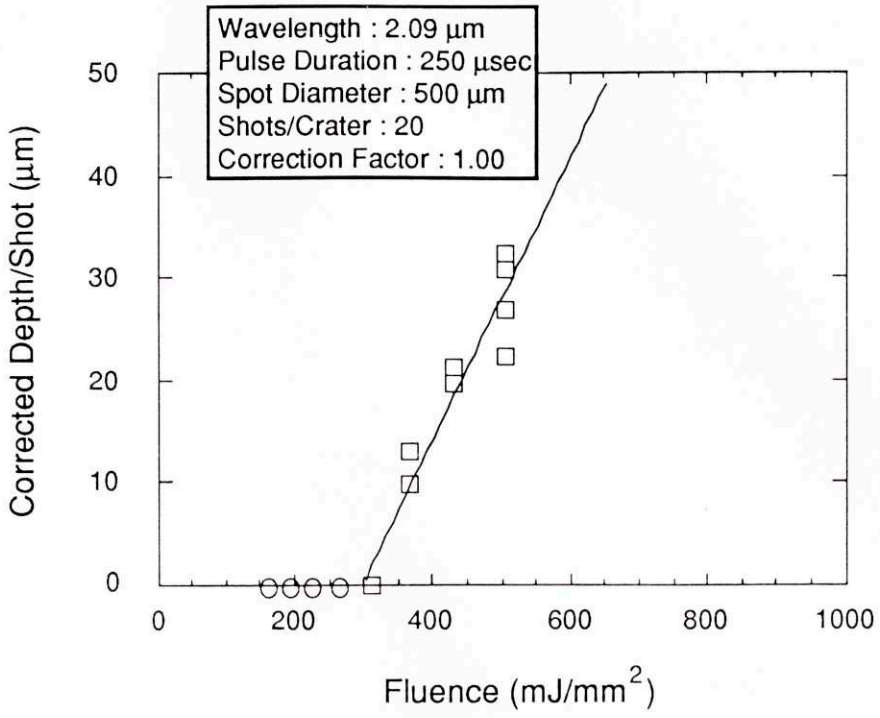

FIGURE 4.10(G). Dosimetry data for the $\lambda = 2.09$ µm wavelength. Craters at this wavelength exhibited severe char formation due to the relatively low laser irradiance (see text).

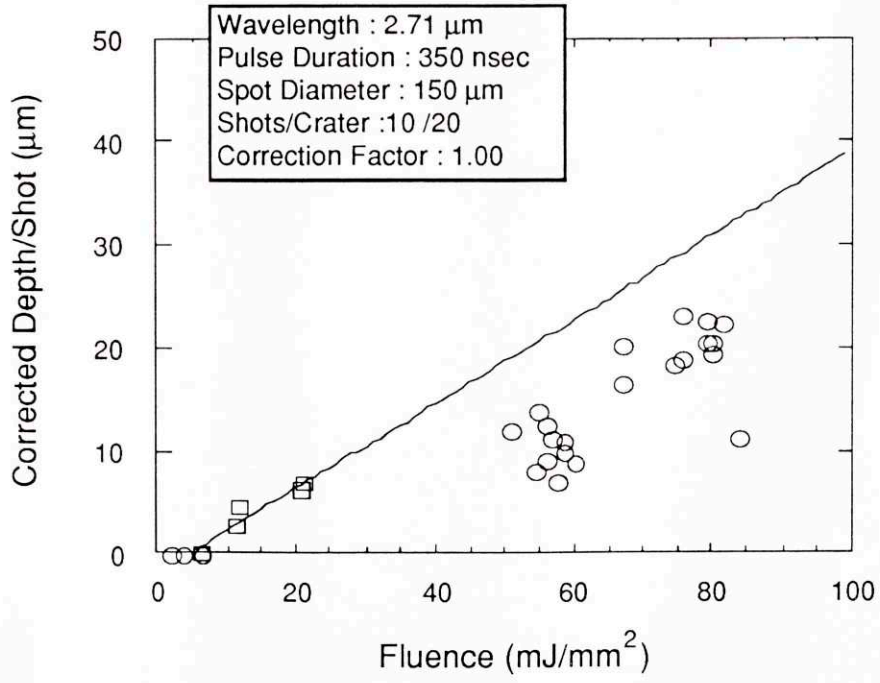

FIGURE 4.10(H). Dosimetry data for the $\lambda = 2.71$ µm wavelength.

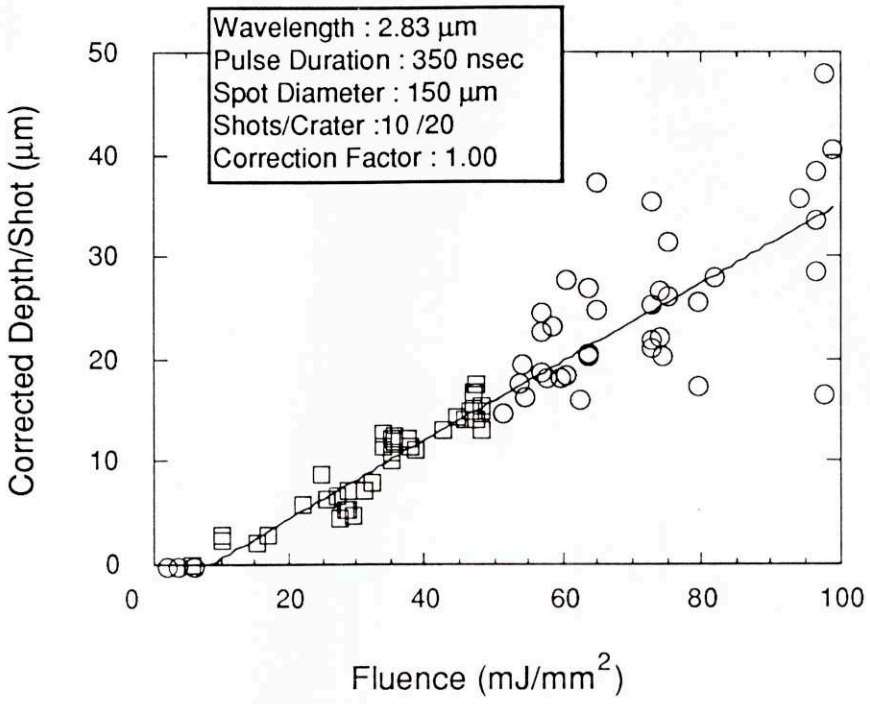

FIGURE 4.10(I). Dosimetry data for the $\lambda = 2.83$ µm wavelength.

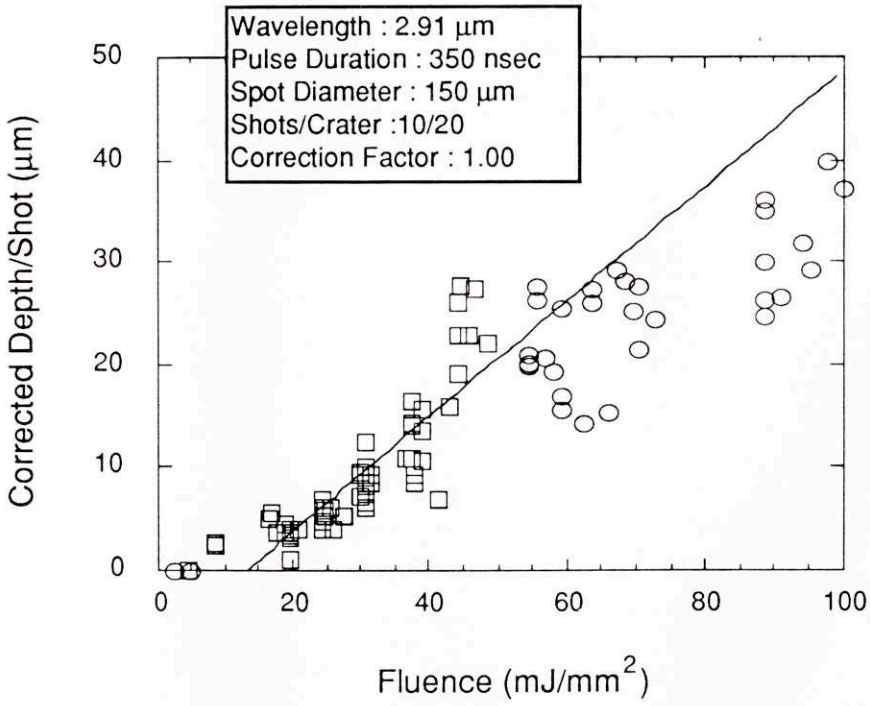

FIGURE 4.10(J). Dosimetry data for the $\lambda = 2.91$ µm wavelength.

The data of Figs. 4.10(a-j) display a large amount of scatter. Variations can be attributed to tissue inhomogeneities, which affect both the light distribution in the tissue and the local mechanical environment in which ablation occurs. The particularly large variability in the visible region of the spectrum indicates reduced predictability when ablation begins below the surface.

4.5.2.2. Fluence Thresholds

A graph of all the fluence thresholds as a function of wavelength appears in Fig. 4.11. Fluence thresholds are also tabulated in Table 4.3. The error bars on the fluence thresholds in the plot represent the standard error of the straight-line data fit, and are a reflection of the amount of scatter in the data. The fluence thresholds generally increased with wavelength through the ultraviolet and visible wavelengths, reached a maximum at 2.1 μm, and were very low for all HF laser wavelengths.

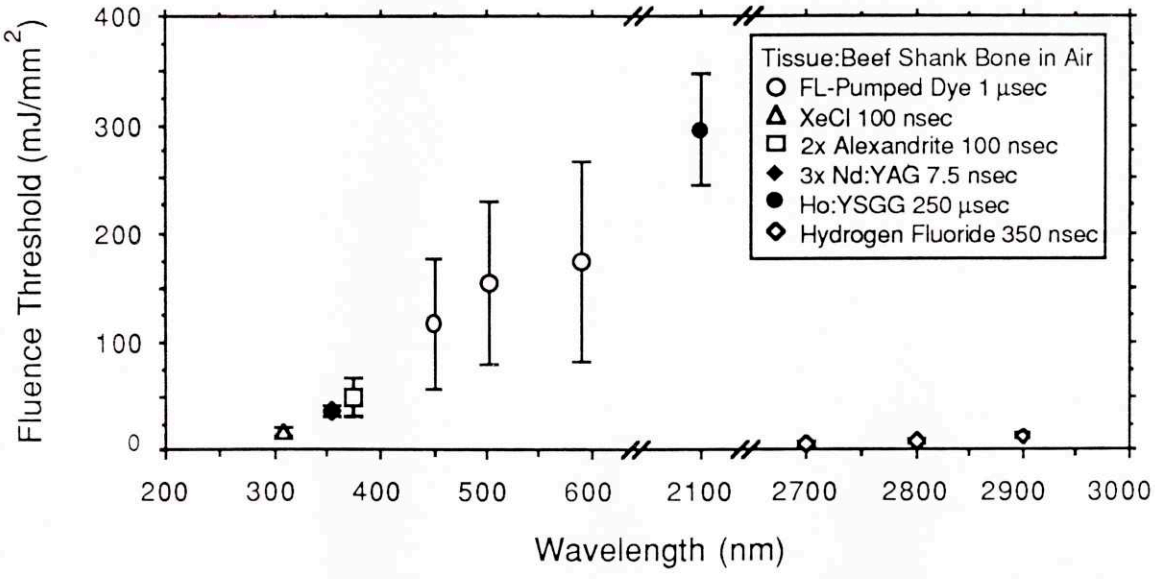

FIGURE 4.11. Fluence thresholds as a function of wavelength for all wavelengths studied; note the breaks in the ordinate axis. The error bars represent the standard error of the straight-line data fit, a reflection of the amount of scatter in the data.

The steady increase in fluence threshold with wavelength from the near-ultraviolet to the visible and near-IR, and the decrease again in the mid-IR, correlate with the changes in attenuation depth over those wavelengths, and is consistent with the explanation of fluence threshold as the deposition of a minimum amount of heat before ablation can begin.

4.5.2.3. Ablation Yields

Ablation yields as a function of wavelength are plotted in Fig. 4.12, and tablulated in Table 4.3. These ablation yields are all corrected for 10 shots per crater. In the plot, the error bars represent the experimental error in measuring laser fluences and crater depths. These errors were greatest for the wavelengths with the lowest thresholds, for which it was necessary to measure the shallowest craters. Ablation yields were highest for the HF laser wavelengths, generally decreased with wavelength through the ultraviolet, and increased again slightly in the visible wavelength region.

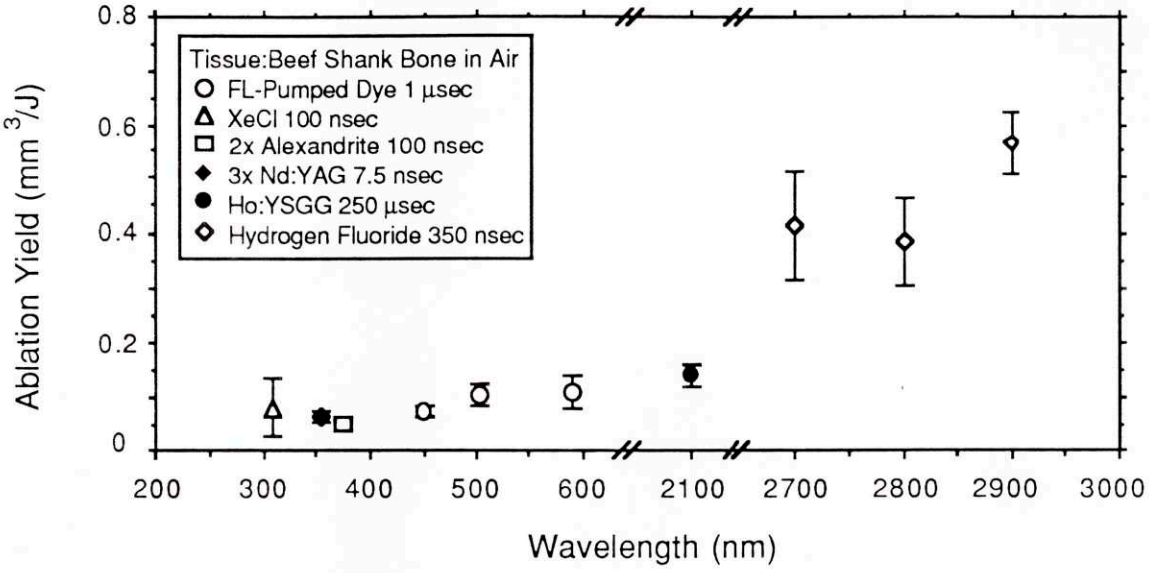

FIGURE 4.12. Ablation yields as a function of wavelength for all wavelengths studied; note the breaks in the ordinate axis. The error bars represent the experimental error in measuring laser fluences and crater depths.

Changes in ablation yields with wavelength may be due to changes in the amount of light which is scattered radially out of the ablation region. As absorption decreases, or scattering increases, more light is lost in this way. The decrease in ablation yield from the 3 µm region, to the near-uv, to the short-wavelength visible may be due to this effect. This trend is reversed around 450 nm, where the better efficiency of the spallation process outstrips the decreasing efficiency due to light scatter.

4.5.2.4. Penetration Depths

The quantitative ablation dosimetry data presented above provides insight into changes which may occur in the optical properties of tissue during ablation. At the high laser irradiances used in this study, ablation proceeds at a rate much faster than thermal diffusion, so the primary heat deposition mechanism is by light absorption. The light distribution profile in the tissue at any time is determined by the interplay of scattering and absorption, but can be approximately characterized by a penetration depth D. Threshold fluence can be considered a measure of the amount of energy per unit area which must be deposited to bring an irradiated volume of tissue up to the ablation temperature. Ablation yield is the volumetric energy efficiency with which that process takes place. As shown in Eq. (4.8), the product of those two quantities is a measure of the depth to which the tissue is heated at any time, and therefore of the penetration depth. A benefit of performing this calculation on the wavelength study data is that the geometrical efficiency factor f due to the three-dimensionality of the light distribution cancels out, so that the penetration depth values obtained are automatically corrected for spot diameter variation.

Values of penetration depth obtained using Eq. (4.8) for the wavelength study data are plotted as the circle data points in Fig. 4.13, and tabulated in Table 4.3. The error bars on the data points in the figure are compounded from the errors on the values of ϕ_0 and Y. The values obtained for penetration depths are only a few microns in the mid-IR and ultraviolet, and tens of microns in the visible.

It is interesting to compare the penetration depth values calculated from the ablation experiments to the the penetration depth spectrum obtained for a thin bone sample in a spectrometer, as described in chapter 3. This penetration depth spectrum, ranging from 300 to 600 nm, is plotted as the solid line in Fig. 4.13. Note, however, that the vertical axes scales are different for the two variables; the calculated penetration depth axis (on the left) is expanded by a factor of 50 relative to the measured penetration depth axis (on the right). This value of 50 was not fitted from the data, but rather chosen as a value which gave good overlap between the two graphs. The shapes of the two curves are similar in the 300 - 600 nm region, indicating that the calculated penetration depth values are roughly proportional to the measured penetration depth values, with a proportionality constant on the order of 50.

One possible explanation for this sizeable discrepancy is that there is a dramatic transient decrease in light penetration depth in tissue during ablation. Several recent reports have discussed irreversible changes in tissue optical properties as a result of heating and coagulation [Thomsen et al 90, Agah et al 90, Levine et al 89]. Transient changes in the optical properties of polymers undergoing ablation have also been reported [Sauerbrey et al 89]. Further studies consistent with a transient change in calcified tissue optical properties during ablation are discussed in chapter 5.

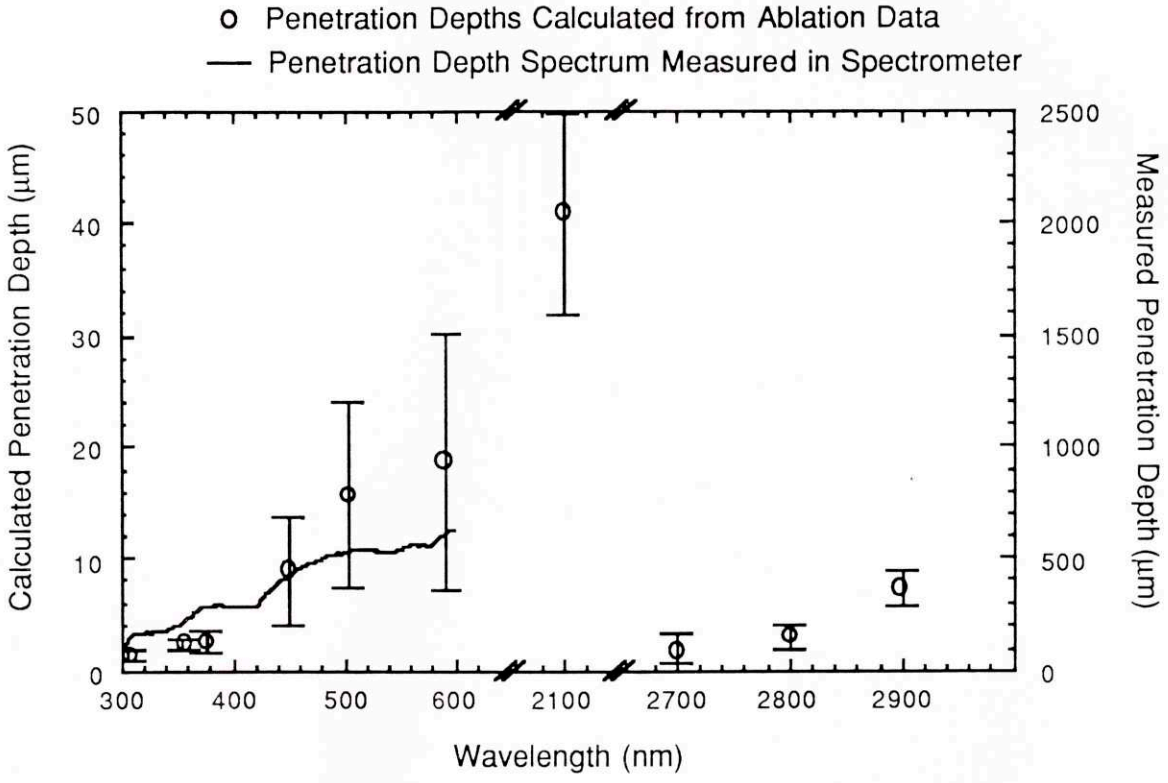

FIGURE 4.13. Bone penetration depths calculated from ablation experiments (circles), and a penetration depth spectrum measured with a thin sample in a spectrometer (line). Note the breaks in the ordinate axis, and the different scales on the coordinate axes.

Wavelength (nm)	Spot Diameter d (μm)	Fluence Threshold ϕ_0 (mJ/mm^2)	Ablation Yield Y (mm^3/J)	Penetration Depth D (μm)
308	850	18 ± 5	0.080 ± 0.060	1.4± 0.4
355	170	36 ± 4	0.066 ± 0.010	2.4 ± 0.4
375	400	50 ± 17	0.051 ± 0.010	2.6 ± 1.0
450	400	117 ± 60	0.077 ± 0.010	9.0 ± 4.8
503	400	154 ± 75	0.102 ± 0.019	15.7 ± 8.26
590	400	173 ± 93	0.108 ± 0.031	18.7 ± 11.4
2100	500	295 ± 53	0.138 ± 0.021	40.8 ± 9.6
2707	150	4.5 ± 3.1	0.41 ± 0.10	1.86 ± 1.35
2832	150	8.1 ± 2.2	0.38 ± 0.08	3.13 ± 1.10
2911	150	12.9 ± 2.5	0.57 ± 0.06	7.33 ± 1.61

TABLE 4.3. Results of ablation wavelength study, for bovine shank bone ablated in air. Fluence thresholds and ablation yields are uncorrected for spot diameter variations. Ablation yield values are corrected for 10 shots per crater.

4.6. Ablation of Different Calcified Tissues

Ablation dosimetry in bone was compared with dosimetry in calcified human aorta, fibrous plaque in aorta, and or normal aorta wall at the 308, 375, and 2.1 μm wavelengths. The results of these experiments at the 308 nm wavelength are shown in Fig. 4.14; fitted ablation thresholds and yields are in Table 4.4. Note that the ablation yield values in the table are uncorrected for the number of shots per crater. For all wavelengths studied, fluence thresholds for both fibrous and calcified plaque in air were similar to thresholds for bone ablation in air, but the ablation yields increased by a factor of 1-5 for calcified plaque, and 2-10 for fibrous plaque. These results of similar thresholds, but decreasing yields with increasing hardness of the tissue are essentially consistent with the results of a recent study conducted by Taylor et al [Taylor et al 90], who studied XeCl laser ablation of calcified plaque as a function of the degree of calcification.

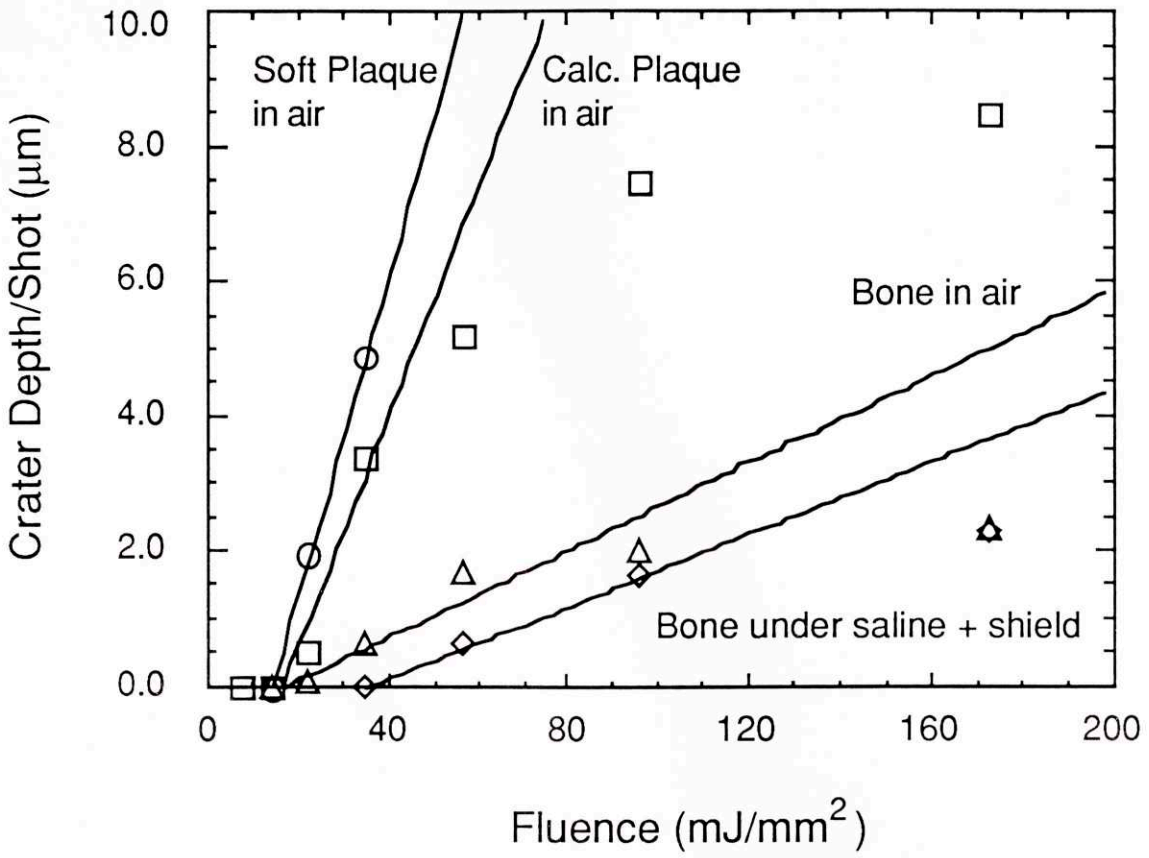

FIGURE 4.14. Comparative results of ablation at 308 nm of soft plaque, calcified plaque, fresh bone in air, and fresh bone under a 1mm layer of saline and a 1mm thick quartz slide.

Tissue Sample	Medium	Fluence Threshold (mJ/mm^2)	Ablation Yield (mm^3/J)
Fibrous Plaque	air	14	.231
Calcified Plaque	air	16	.170
Beef Bone (fresh)	air	16	.032
Beef Bone	saline + shield	34	.026

TABLE 4.4. Fitted ablation thresholds and yields for ablation at 308 nm in air, and under a 1mm layer of saline and a 1mm thick quartz slide.

4.7. Ablation Under Saline and a Shield

At the 308, 375, and 2.1 μm wavelengths, ablation of bone was also studied under a 1mm layer of saline covered by a 1mm thick quartz slide to simulate an optical shield [Cothren et al 86b]. The results of these experiments at λ = 308 nmalso appear in Fig. 4.14 and Table 4.4. For all wavelengths studied, the fluence threshold for bone ablation under saline and a slide was approximately twice the threshold observed in air with the same laser, while the ablation yield remained essentially constant.

4.8. Conclusions

With the appropriate choice of irradiance, fluence, and wavelength, a variety of ablative effects can be achieved in calcified tissue. Irradiances on the order of MW/mm^2 produce char-free cutting without plasma generation. Tissue removal is linear with fluence up to a few times threshold, although crater depths vary nonlinearly with both spot diameter and the number of shots fired into each crater. Ablation of calcified tissue with visible wavelengths longer than about 400 nm creates jagged-edge craters and large debris flakes and particles. Visible and near-ultraviolet wavelengths below 400 nm, as well as wavelengths near 3 μm, are capable of cutting with resolution and debris particle sizes on the order of tens of μm, allowing for the possibility of tissue micromachining. Ablation dosimetry studies indicate that those laser wavelengths which exhibit the sharpest cutting also have the lowest fluence thresholds and the highest ablation yields. Calculated values of penetration depth in tissue during ablation are dramatically smaller than attenuation depth values measured spectroscopically in tissue not undergoing ablation. Ablation thresholds in soft tissue and calcified plaque are approximately the same of lower as for bone, but ablation yields are higher. Fluence thresholds for ablation under saline and a shield are approximately twice air thresholds.

Chapter 5
Time-Resolved Ablation Studies

The high irradiances required for calcified tissue ablation [see chapter 4] have several effects which combine to make it an extremely violent, complex process. The gasdynamic ablation model described in section 2.4.6 indicates that irradiances on the order of MW/mm^2 lead to ablation front velocities on the order of meters per second and tissue surface temperatures on the order of several hundred °C. Blast waves are also predicted to result from pulsed ablation, with velocities up to several times the speed of sound being driven by pressures of tens of atmospheres.

These considerations have stimulated interest in time-resolved ablation studies, including fast photographic and spectroscopic studies [Prince et al 86, Puliafito et al 87, Dyer et al 88, Srinivasan et al 89, Izatt et al 90b, Izatt et al 91a, Walsh et al 91]. Studies of this type are useful for evaluating models of the ablation process, since they provide direct information concerning 1) the time evolution of the ablation process in the tissue; 2) shock wave formation and propagation above the tissue surface; and 3) ablation debris formation, composition, and ejection. In this chapter, results from laser strobe photography of ablation are presented which provide information relevant to all of these aspects of ablation.

The studies presented in this chapter are also relevant to the wavelength dependence of the ablation. The two-component model of calcified tissue ablation [chapter 2] assumes that all laser energy absorbed in the tissue is quickly transformed into heat, independent of the particular absorbing chromophores at any given wavelength. This is in direct contrast to models of ablation which distinguish ablation mechanisms based upon modes of light absorption; for example, several authors have suggested that photochemical processes make ultraviolet laser ablation inherently different from infrared ablation [Srinivasan 86, Grundfest et al 85]. The laser strobe photographic and debris composition studies presented here of both near-ultraviolet and mid-infrared ablation allow for direct comparison of ablation dynamics and results.

Finally, the dynamics of the ablation process in calcified tissue are investigated by ablating with two pulses separated by a variable time delay. The results of these studies

have practical consequences for the design of laser delivery systems, and also provide insight into ablation mechanisms.

5.1. Methods for Monitoring Tissue Properties During Ablation

Transient changes in tissue properties during ablation are implied by some of the results presented in this chapter and the previous one. Several reports in the literature have recently discussed irreversible changes which occur in tissue optical properties as a result of heating and coagulation [Thomsen et al 90, Agah et al 90, Levine et al 89. Theoretical and experimental studies have been conducted of transient changes in optical properties of organic polymeric materials during ablation, including the effects of two-photon absorption [Sauerbrey et al 89, Kuper et al 87, Gorodetsky et al 85, Srinivasan et al 86, Srinivasan et al 87b, Cole et al 86, McGimpsey et al 87]. Published reports of transient changes in optical properties in tissue during ablation have not yet appeared.

In general, at least two methods are available for determining how tissue properties change during ablation. The first is to study macroscopic ablation characteristics and dosimetry, and then infer what processes must have occurred while ablation was occurring to produce the observed results. This is the method which was used in chapter 4, in which transient changes in tissue optical properties were postulated, based upon ablation dosimetry measurements. The main problem with this approach, however, is that it is heavily model-dependent. In the case of the previous chapter, for example, the inference of a drastic increase in light attenuation during ablation was based on the thermal model of ablation. This model has not been independently verified for calcified tissue ablation.

The second method for monitoring tissue properties during ablation is to probe the tissue in real time. In the next section, experiments are described in which the region above the tissue surface has been probed in real time with fast laser strobe photography. Although these experiments contribute information about ablation mechanisms, they do not directly probe tissue properties. Experiments which do probe tissue properties directly, for example by monitoring thin section optical properties in real time, are possible (see chapter 7), although they are difficult to do and interpret.

A compromise approach, and the one which is taken in the later sections of this chapter, is to probe tissue properties by examining the macroscopic ablation results of specially designed experiments. In the case of the experiments described below, ablation with two pulses is studied as a function of the time delay between them. The resulting

analysis is still model-dependent, but at a more fundamental level than previously. It is possible to probe the role of thermal diffusion in ablation, for example, by using pulse separations characteristic of thermal diffusion over distances typical of optical penetration depths in tissue. By putting the time resolution into the experiment, rather than the observation, it is possible to probe the important physical processes individually, without the equipment necessary to monitor them in real time.

5.2. Fast Laser Strobe Photography of Ablation

Several investigators have photographed ablation plumes above tissues and other materials. Prince et al [86] photographed plasma-mediated ablation of calcified plaque with μsec duration visible light pulses. Puliafito et al [87b] discussed the appearance of ablation debris following excimer laser ablation of cornea. We have published strobe photographs of bone ablation with mid-infrared and near-ultraviolet wavelengths [Izatt et al 90b, Izatt et al 91a]. Walsh and Deutsch [91] studied Er:YAG laser plume dynamics. Considerable experience also exists in the strobe photography of polymer ablation. Srinivasan et al [89] photographed excimer laser ablation of polyimide; Dyer and Sidhu [88] also included fast spectroscopic studies. While many of these studies have concentrated on the results of ablation of a particular substrate with a particular laser with a specific application in mind, the attempt has been made here to perform these studies in such a way as to allow for comparison of ablation results across a variety of ablation parameters.

The formation of a shock wave during calcified tissue ablation is a consequence of the explosive nature of the ablation process, and has been cause for concern about accessory damage to peripheral tissues and laser energy delivery devices [Doukas et al 90, Flotte et al 90]. Particularly good images of ablation-induced shock waves are included here, including their observation at the shortest time yet reported (25 nsec). Also, studies of shock wave effects on a simulated laser catheter face are reported.

5.2.1. Experimental Setup

A schematic of the experimental setup used for fast laser strobe photography of ablation appears in Fig. 5.1. In all experiments two separate lasers were used; one to ablate the tissue, and another to provide the illumination strobe pulse. The ablation laser beam passed through an aperture placed directly in front of the laser, and was formed into a reduced image of the aperture on the tissue surface by a 25 cm focal length lens. This arrangement produced a uniform, reproducible spot on the tissue with a diameter

controllable through adjustment of the aperture. The strobe laser beam, which also passed through a limiting aperture, was made to pass directly above the tissue surface orthogonal to the ablation laser beam. The region above the ablation site which was illuminated by the strobe laser beam was imaged by a stereomicroscope fitted with a camera for observation and photographic recording.

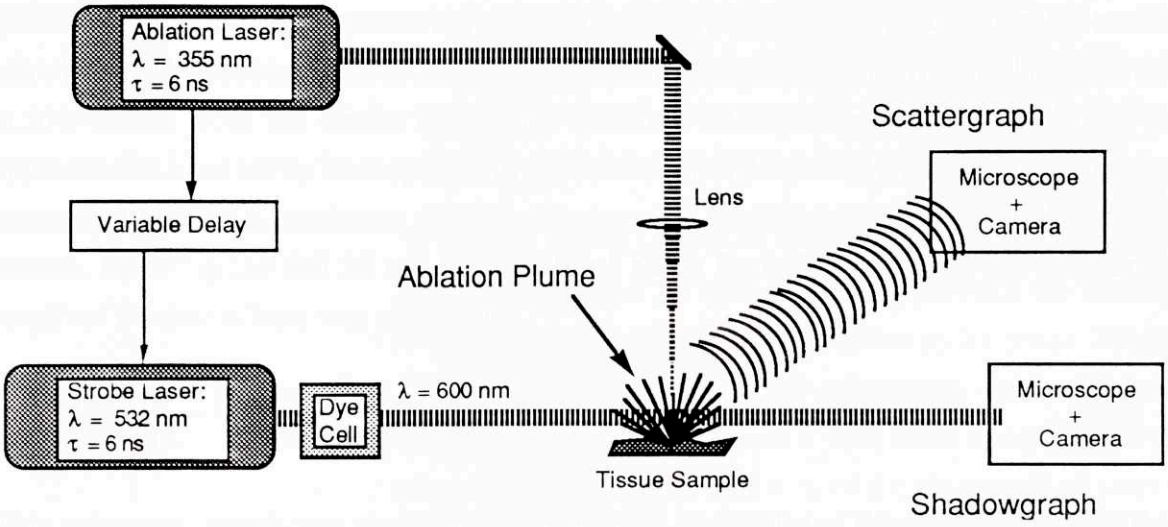

FIGURE 5.1. Experimental setup used for fast laser strobe photography of ablation.

The wavelengths and pulse durations of the ablation and strobe lasers which were used for the experiments are listed in Table 5.1. The delay between the ablation and strobe lasers was controlled electronically, and was continuously variable from zero separation to 100 ms separation. For the λ = 355 nm ablation photography setup, the pulse separation jitter was 1 ns, allowing for precise, reproducible control over the pulse separation timing. For the λ = 2.8 μm ablation photography setup, the pulse separation jitter was approximately 200 ns; in this case, the actual pulse separation for each pair of shots was monitored on an oscilloscope with an accuracy of $\pm$10 ns.

Ablation Wave-length Region	Ablation Laser		Strobe Laser	
	Wavelength (nm)	Pulse Duration (ns)	Wavelength (nm)	Pulse Duration (ns)
Near-Ultraviolet	355	7	596	7
Mid-Infrared	2800	350	590	500

TABLE 5.1. Ablation and strobe laser parameters for fast laser strobe photography of ablation.

As can be seen in Fig. 5.1., two separate imaging geometries were available. In the first geometry, hereafter designated as the scattergraph, the stereomicroscope was positioned to collect light scattered by ablation debris at a large angle (~90°) from the strobe laser beam. This arrangement avoided interference in image formation from light diffracted at low orders from the strobe beam, and therefore allowed the imaging resolution to approach the limit set by laser speckle in the strobe beam [Svelto 82]. Speckle in the strobe beam was kept to a minimum through the use of a broadband dye laser as the strobe source. By using the full 20 nm bandwidth of Kiton Red 620 laser dye, the coherence length of the strobe laser was reduced to

$$\Delta x = \frac{\lambda^2}{\Delta\lambda} \sim \frac{(600\ \text{nm})^2}{20\ \text{nm}} \sim 20\ \mu\text{m}. \qquad (5.2)$$

This coherence length was similar to the resolution capability of the microscope, and the photographs which resulted do not exhibit speckle patterns. It should be noted, however, that structures with dimensions less than ~20 μm are not resolvable in the photographs.

The second imaging geometry used was the shadowgraph. In this arrangement, the stereomicroscope was positioned directly in the strobe beam in the shadow of the ablation debris. This setup produced a complicated pattern of diffraction rings in the region of the ablation debris, providing poor imaging resolution there. However, blast waves propagating ahead of the ablation debris were clearly visible. A blast wave is a classification of shock wave for which no energy is supplied behind the shock front after initiation [Ready 71]. It can be shown that the shadowgraph is sensitive to variations in the second derivative of the index of refraction of the material in the object plane [Dubovik 81]. This is because if the refractive index or its gradient remains constant throughout the illuminated area, all rays will be either deflected, focussed or defocussed equally; it is only if gradient itself changes that the deflection of rays will vary. The strong bimodal pressure wave in a shock front induces a strong variation in the index of refraction of the air, which shows up in a shadowgraph as an adjacent pair of bright and dark bands.

Bovine shank bone samples were obtained no later than 2 days post-mortem. Areas of the bone surface exhibiting a clean, smooth cortical surface were prepared by scraping

the surface with a razor blade to remove the periosteum. Prepared bone samples were either used immediately, or kept in a refrigerator until use. Bone samples were ablated in air.

5.2.2. Strobe Photography of Ablation -- Results

An overview of ablation strobe photography results as a function of strobe delay appears in Fig. 5.2(a-c). Figure 5.2(a) contains shadowgraphs of ablation at $\lambda = 355$ nm, and scattergraphs of ablation at $\lambda = 355$ nm and at $\lambda = 2.8$ μm are in Fig. 5.2(b-c), respectively. The strobe delays are noted below the photographs. All photographs in Fig. 5.2 were taken at the same magnification, which is noted in the figure caption.

The $\lambda = 355$ nm shadowgraphs in Figure 5.2(a) include the earliest strobe delay photographs obtained in the study, starting at just 25 nsec separation between the start of the 7.5 nsec duration ablation pulse and the start of the 6 nsec duration strobe pulse. While just barely discernable in Fig. 5.2(a), examination of a greater enlargement of the 25 nsec strobe delay photograph unmistakably reveals the presence of a blast wave above the tissue surface at this early time. It is interesting to note the irregularity of the blast wave at strobe delays up to ~500 nsec. It is apparent from those photographs that ablation may have begun at several distinct sites on the tissue, and it is not until ~1 μsec that the blast waves from these separate events coalesce to appear as a single spherical wave. At a strobe delay of 5 μsec, the blast wave had already escaped part of the photographic field of view, and at longer strobe delays it was no longer visible at all.

The first resolvable debris particles in the $\lambda = 355$ nm scattergraphs in Fig. 5.2(b) were also visible very early, by 100 nsec. At 5 μsec strobe delay, the fastest visible ejecta had almost travelled the 3 mm to the top of the photographic frame, and the entire debris distribution was visible. On these photographs, individual debris particles appear as small points, but clumps of particles as large as 100 μm in extent also appear. By 50 μsec strobe delay, most of the particles had escaped the field of view, and only a few large clumps and a mist of very small debris remained.

The $\lambda = 2.8$ μm scattergraphs in Fig. 5.2(c) are positioned in the same locations on the page as the $\lambda = 355$ nm scattergraphs for the same strobe delay on the previous page. A few technical differences, as well as the different ablation wavelength, separate the photographs for these two. First, the $\lambda = 2.8$ μm scattergraphs were taken with a 500 ns strobe pulse duration, long enough so that debris particles appeared as streaks rather than as localized particles frozen in time. Second, the ablation fluence in the $\lambda = 2.8$ μm

experiments was approximately five times the fluence in the $\lambda = 355$ nm experiments, with the result that a greater quantity of debris was ejected. Finally, due to the excessive jitter of the pulse separation timing in the $\lambda = 2.8$ μm ablation strobe photography setup, strobe delay times of less than 5 μsec were not available.

The scattergraph reproduced in Figure 5.3 illustrates the effect on the ejected debris when the laser was fired into a deep hole in the tissue. This photograph was taken of the five hundredth shot into the tissue of the $\lambda = 355$ nm wavelength laser at a fluence of 40 mJ/mm^2. The previous 499 shots had prepared a cylindrical crater in the tissue approximately 500 μm deep, or about twice as deep as the beam width at the surface. The debris particles emerged from the tissue crater much more collimated than debris ablated from the surface.

The dependence of blast wave formation and strength on the fluence of the ablation laser was probed with a series of strobe photographs reproduced in Fig. 5.4. In this series of photographs, the strobe delay was fixed at 1 μsec, and the fluence was increased from 1 to 7 times threshold at $\lambda = 355$ nm. The blue-white flash appearing in the photographs beginning at three times fluence threshold was a plasma generated by the ablation laser pulse. The plasma was visible in the strobe photographs since it was self luminescent, and the camera shutter was open for a long time on the scale of the strobe delay. Thus the photographs provide no information concerning the time evolution of the laser-generated plasma.

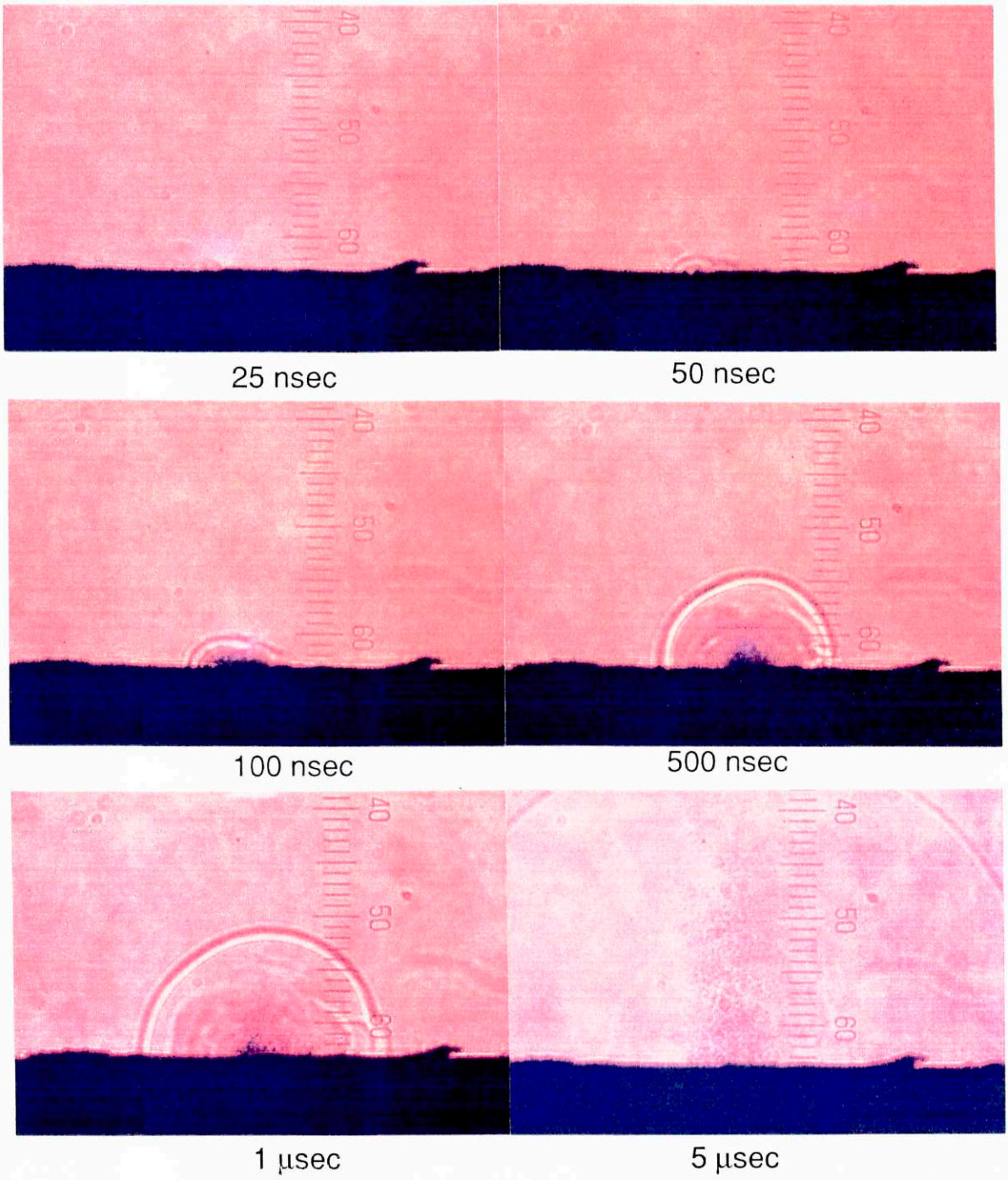

FIGURE 5.2. Overview of ablation strobe photography results as a function of strobe delay. (a) Shadowgraphs of ablation caused by a λ = 355 nm, 7.5 ns duration pulse at 40 mJ/mm2, illuminated by a λ = 600 nm, 7.5 ns duration strobe pulse. Scale: 1 division = 100 μm.

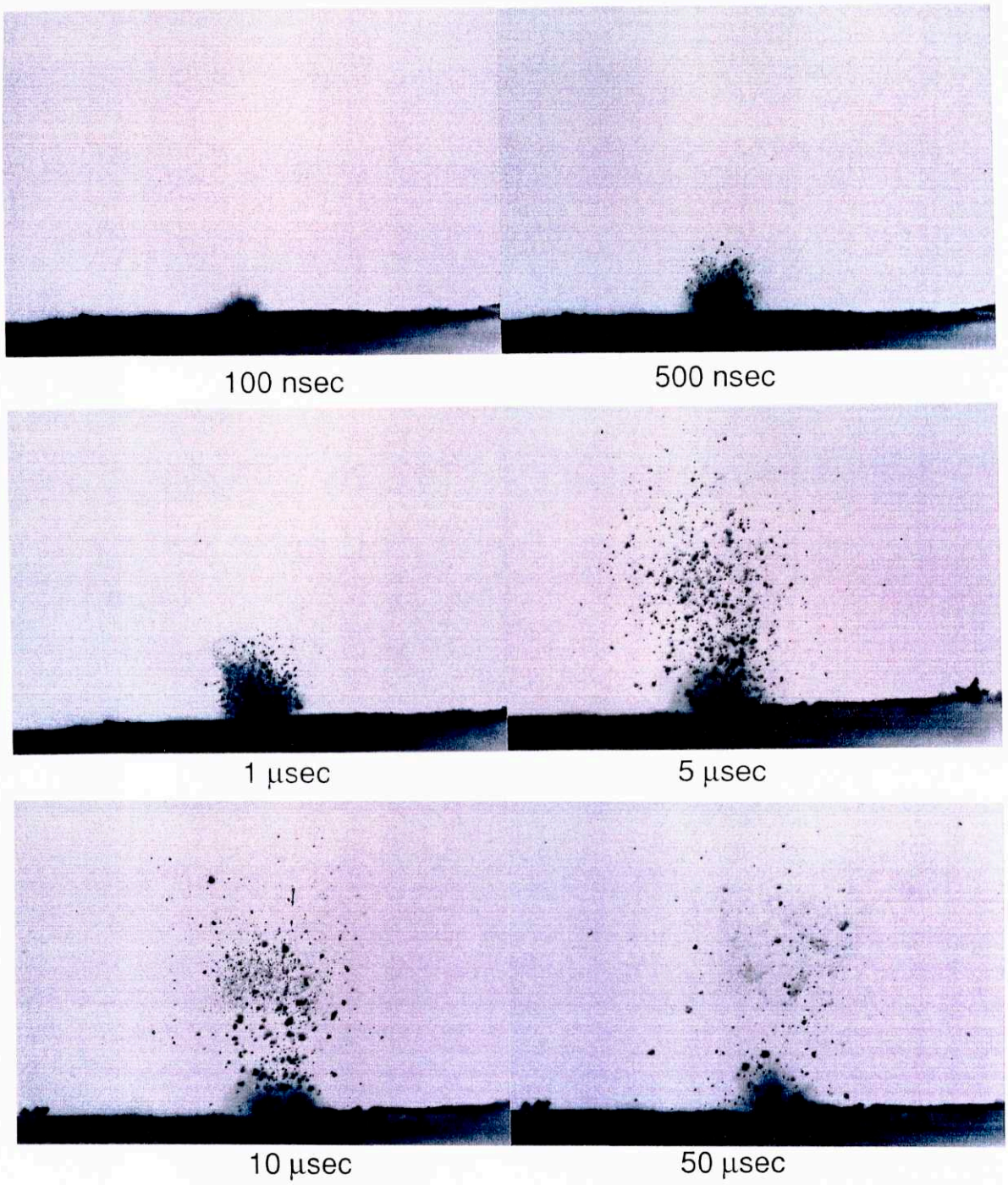

FIGURE 5.2. Overview of ablation strobe photography results as a function of strobe delay. (b) Scattergraphs of ablation caused by a λ = 355 nm, 7.5 ns duration pulse at 40 mJ/mm2, illuminated by a λ = 600 nm, 7.5 ns duratior strobe pulse. Scale: 1 division = 100 μm.

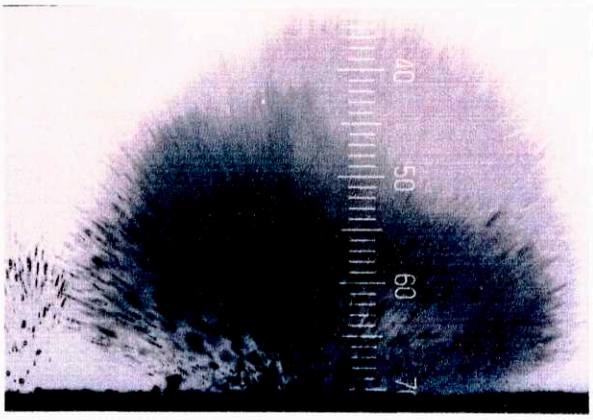

5 μsec

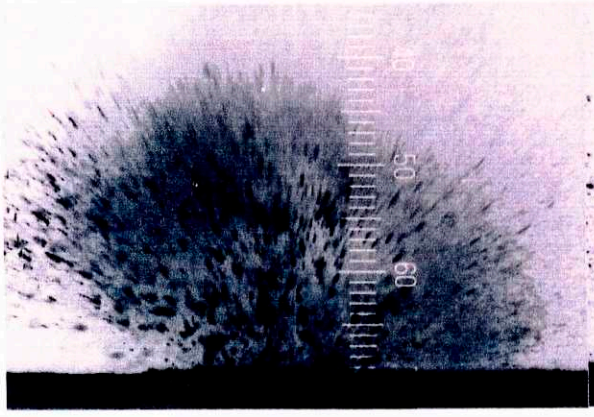

10 μsec

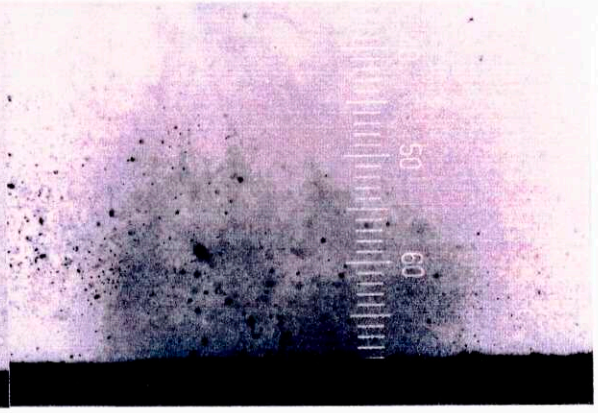

50 μsec

FIGURE 5.2. Overview of ablation strobe photography results as a function of strobe delay. (c) Scattergraphs of ablation caused by a $\lambda = 2.8$ μm, 500 ns duration pulse at 200 mJ/mm2, illuminated by a $\lambda = 600$ nm, 500 ns duration strobe pulse. Scale: 1 division = 100 μm.

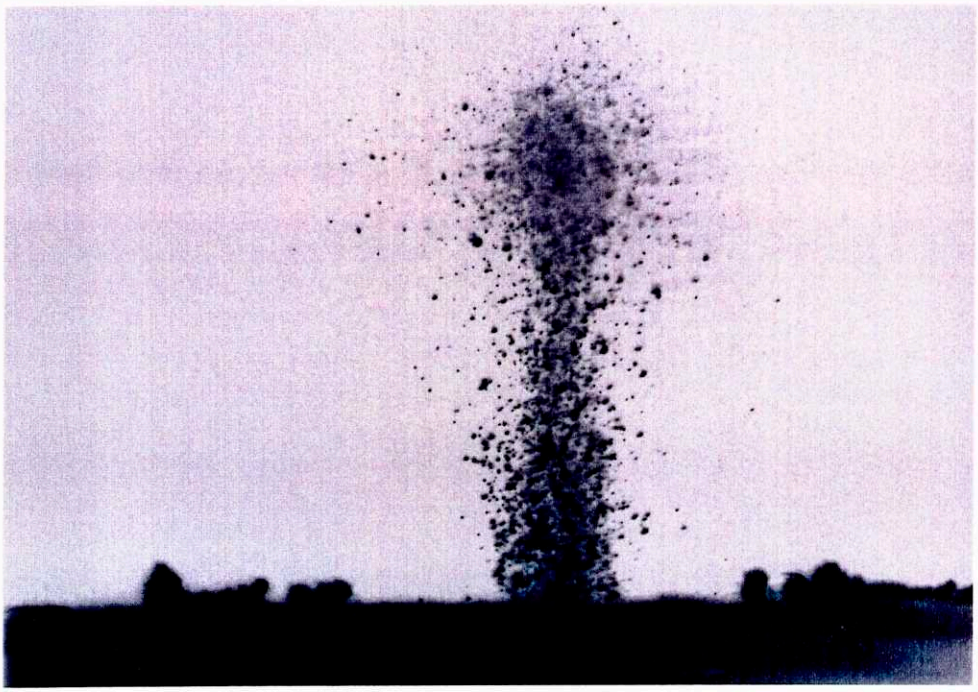

FIGURE 5.3. Scattergraph of ablation caused by the 500th shot of a $\lambda = 355$ nm, 7.5 ns duration pulse at 40 mJ/mm^2, illuminated after 10 μsec strobe delay by a $\lambda = 600$ nm, 7.5 ns duration strobe pulse.

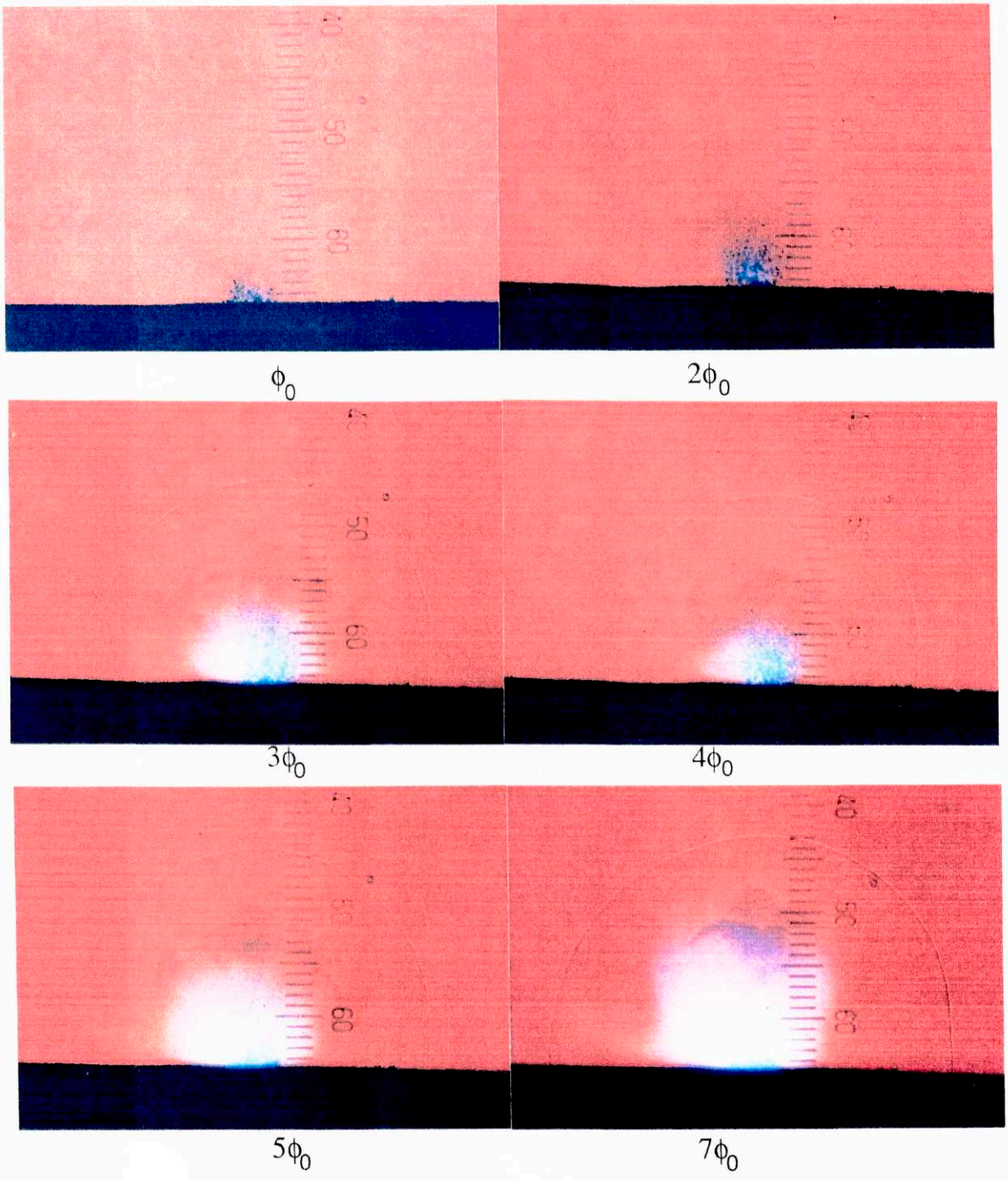

FIGURE 5.4. The dependence of blast wave formation and strength on the fluence of the ablation laser. The photographs are shadowgraphs of ablation caused by a λ = 355 nm, 7.5 ns duration pulse at 40 mJ/mm2 illuminated after 1 μsec by a λ = 600 nm, 7.5 ns duration strobe pulse.

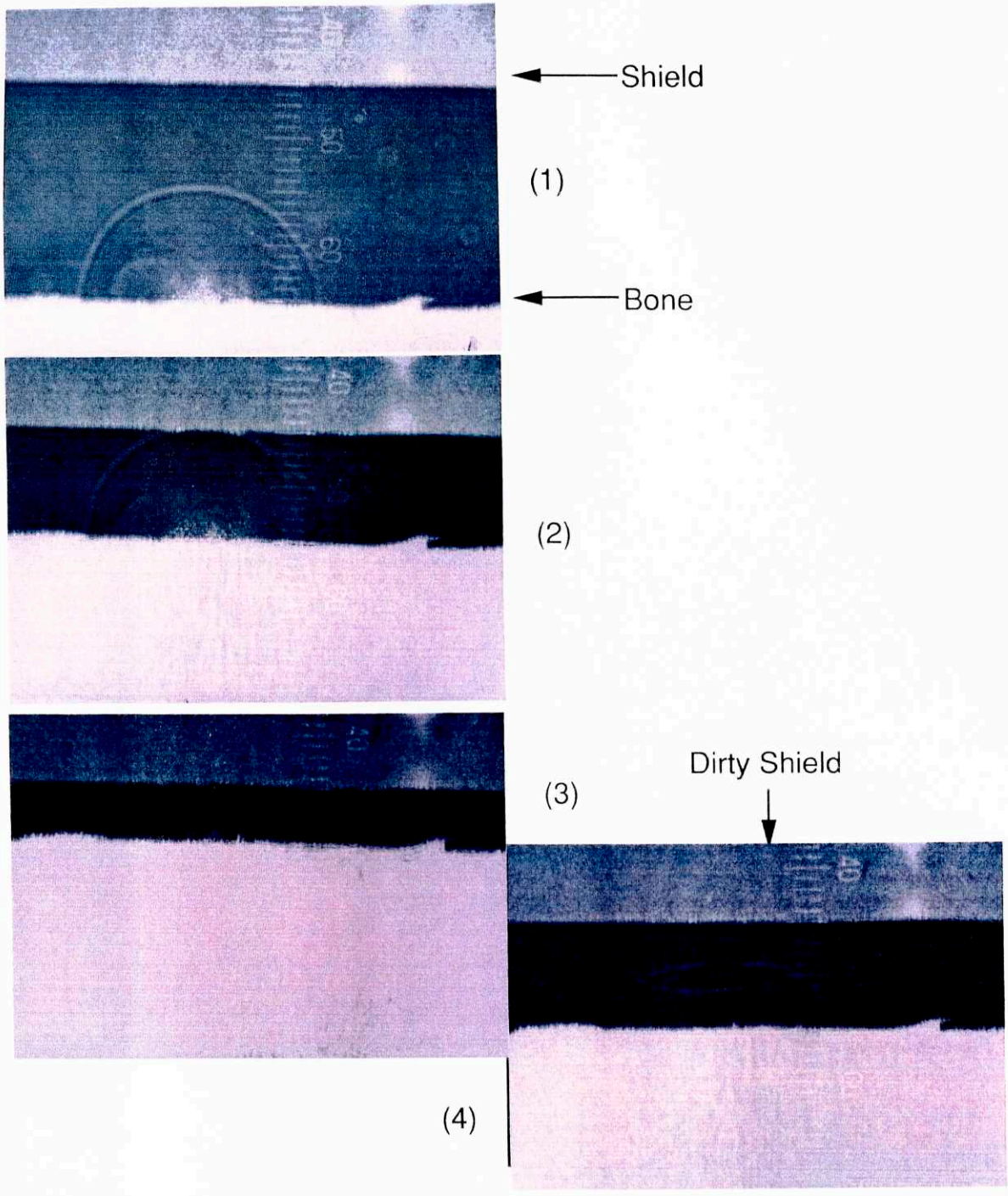

FIGURE 5.5. The effect of a simulated catheter shield on blast wave formation. The photographs are shadowgraphs of ablation caused by a λ = 355 nm, 7.5 ns duration pulse at 40 mJ/mm2, illuminated after 1 µsec by a λ = 600 nm, 7.5 ns duration strobe pulse.

The final series of strobe photographs illustrates the effect of a simulated catheter shield on blast wave propagation. In these photographs, reproduced in Fig. 5.5, a glass microscope slide was positioned above the tissue target, and the tissue was irradiated through the slide. Shadowgraphs were taken with 1 μsec strobe delay.

In the first three photographs, the shield was advanced toward the tissue until it intercepted the blast wave. The blast wave was not discernably reflected from the microscope slide. The ablation laser was fired many times with the slide just 500 μm from the tissue surface, coating the shield with ablation debris. For the fourth photograph, the dirty slide was moved 1 mm away from the tissue surface. A second blast wave, resulting from ablation of debris from the dirty shield, was clearly evident.

5.2.3. Strobe Photography of Ablation -- Discussion

It is interesting to compare the scattergraphs of ablation at $\lambda = 355$ nm and $\lambda = 2.8$ μm in Fig. 5.2(b-c). Recall that the strobe pulse for ablation at $\lambda = 2.8$ μm was longer than for ablation at $\lambda = 355$ nm, resulting in the debris particles appearing as streaks, and that more tissue was removed by the infrared laser pulses because they were many times fluence threshold. Except for these differences, the scattergraphs of ablation at these widely separated wavelengths appear remarkably similar. The smallest particles visible in the photographs in both cases were travelling ~600 m/s, with larger clumps of debris up to ~100 μm in extent travelling more slowly away from the tissue surface. Scanning electron micrographs of debris from ablation at $\lambda = 355$ nm and at $\lambda = 2.8$ μm were discussed in chapter 4, appearing in Fig. 4.9(a-b). The size distribution of particles from ablation at the two wavelengths was found to be very similar, while the composition of the particles was measured to be identical. The debris in the photomicrographs in chapter 4 was obtained under ablation conditions very similar to the conditions present in the scattergraphs in Fig. 5.2, so it is reasonable to assume that the photomicrographs accurately reflect the microscopic appearance of the debris in flight in the scattergraph photos. Thus, even at times as short as a few hundred ns after the ablation pulse, there is very little difference observable above the tissue surface between ablation caused by near-ultraviolet and mid-infrared light.

Additional information is available from the scattergraphs concerning the angular distribution of debris ejection during ablation. The solid angle over which debris was ejected in the photographs in Fig. 5.2 was ~1.8π steradians for $\lambda = 2.8$ μm ablation, and

~0.6π steradians for λ = 355 nm ablation. This difference is probably due to the amount of debris created in the two cases. When ablation occurred at the bottom of a ~500 μm deep crater, however, in Fig. 5.3, the ejected debris was nearly collimated, coming out over ~0.1π steradians. The debris in this case was probably initially ejected over a larger solid angle, but a fraction of the particles encountered the crater walls and either 1) were deflected back toward and out of the crater opening, 2) fell back to the crater bottom, or 3) plated onto to the crater walls. These observations are consistent with the results from sections 4.4.2 and 4.4.3 that ablation is less efficient at high fluence and for large numbers of shots per crater, since each of these circumstances involve ablating at the bottom of deep craters.

The position of the blast wave produced by 40 mJ/mm^2, 7.5 ns duration pulses at λ = 355 nm as a function of strobe delay is plotted in Fig. 5.6. The blast wave positions plotted in the figure are an average of two measurements from each photograph: the radius of the blast wave perpendicular to the tissue surface, and one-half of the blast wave diameter at the tissue surface. Except for the very first measurement on the plot at 50 ns, all of the data points fall close to a straight line on the log-log plot; the least-squares linear fit to this data has a slope of 0.61, and is overlayed on the data. Although the velocity of the blast front was a function of time and fluence in all cases blast wave velocities were on the order of 1000 m/s, consistent with the predictions of the gasdynamic model of ablation (section 2.4.6).

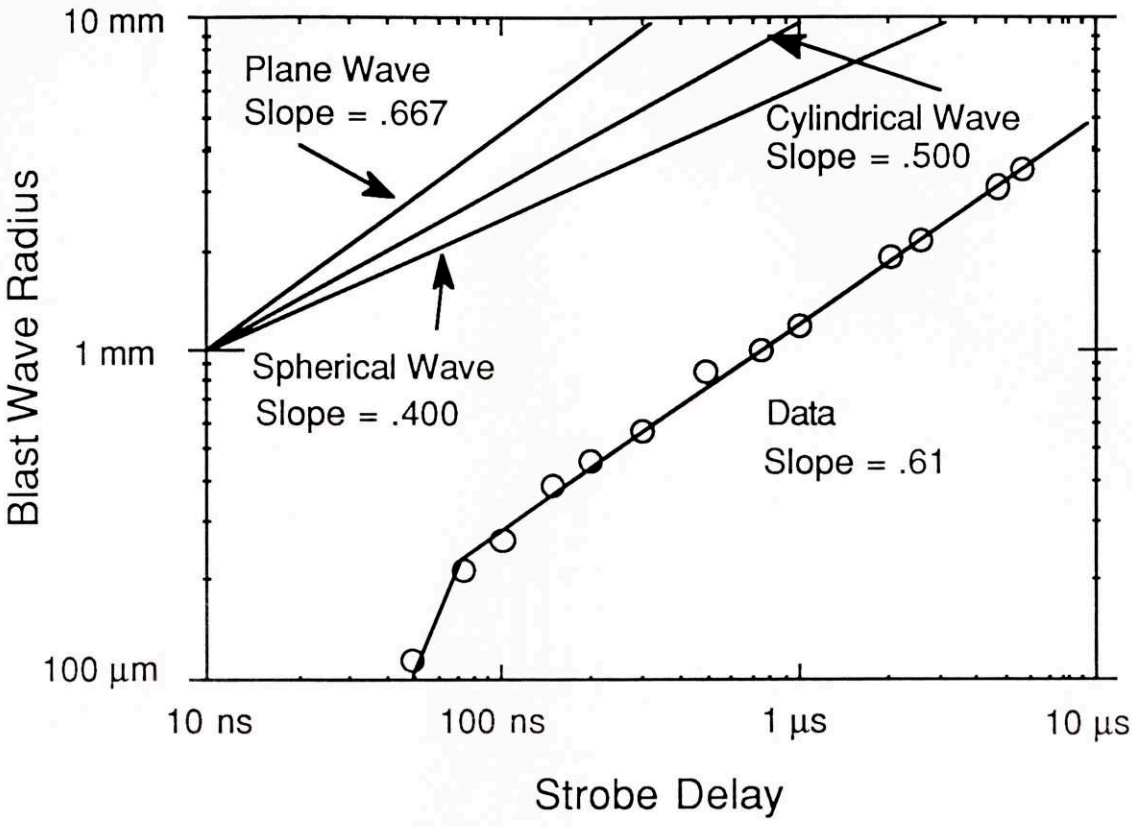

FIGURE 5.6. Blast wave position versus time strobe delay. Ablation was caused by $\lambda = 355$ nm, 7.5 ns duration pulse at 40 mJ/mm^2, illuminated by a $\lambda = 600$ nm, 7.5 ns duration strobe pulses.

The slope of the blast wave versus strobe delay data may be compared with the expected scaling of blast wave radius with time predicted from dimensional analysis, derived in Sedov [59]. This analysis predicts that the blast wave radius should scale with time to the 2/3 power in one dimension, to the 1/2 power in two dimensions, and to the 2/5 power in three dimensions. These cases correspond to plane, cylindrical, and spherically expanding blast waves, respectively. The slope of the blast wave data from the shadowgraphs, however, is approximately 0.6, even though the appearance of the blast waves are clearly spherical. Other authors have also reported the observation of apparently spherical blast waves with faster than expected growth. Srinivasan et al [89] reported a time exponent of 0.76 for 248 nm light ablating PMMA, and Walsh et al [91] found superlinear growth (time exponent 1.1-1.6) for 2.9 µm light ablating human skin. One explanation for these findings is that some exothermic process, perhaps combustion in the ablation plume, contributes energy to the expanding gases.

The first few photographs in the series in Fig. 5.4 illustrate that the velocity of the blast wave initially increased with pulse fluence. Figure 5.7 contains a plot of the blast wave radius as a function of fluence. Each data point in the figure represents information from one shadowgraph; the error bars are an estimate of the pulse-to-pulse variability. As seen in the figure, the blast wave radii are a decreasing function of fluence, probably due to increasing absorption by the plasma which effectively shields the tissue surface.

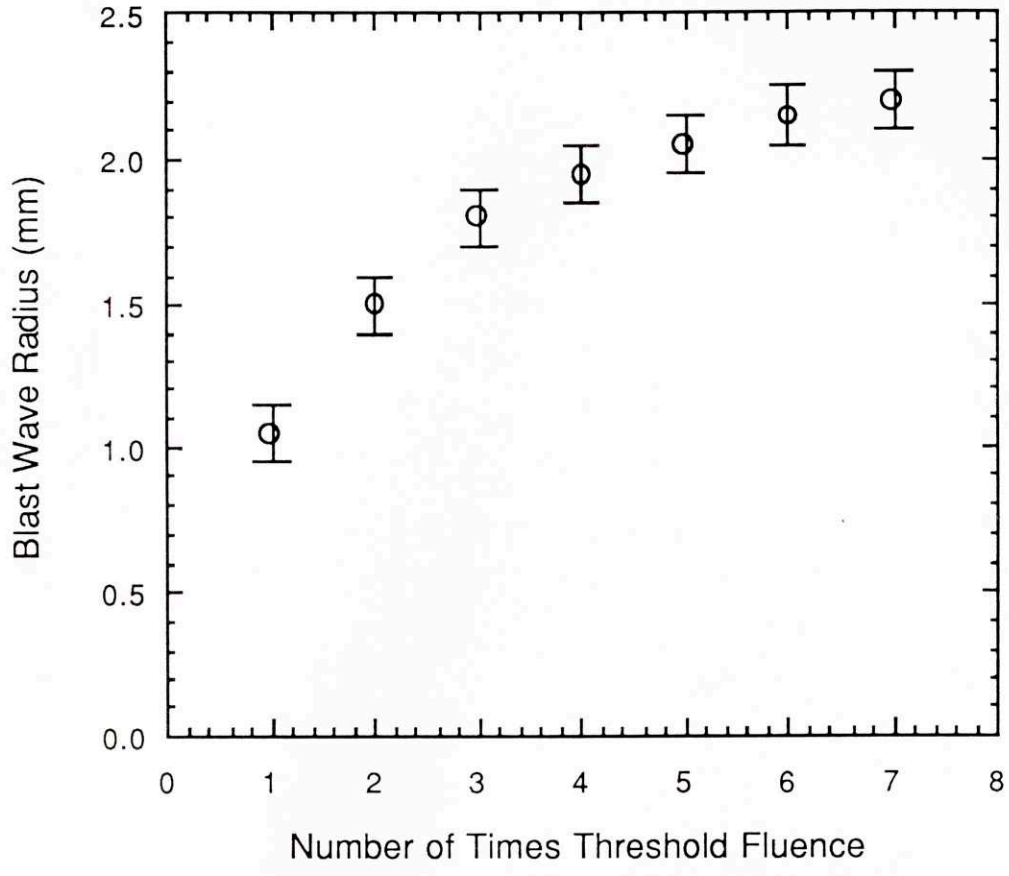

FIGURE 5.7. Dependence of blast wave radius on fluence, for λ = 355 nm, 7.5 ns duration pulses, illuminated by λ = 600 nm, 7.5 ns duration strobe pulses.

Finally, the blast waves produced during ablation of bone at λ = 355 nm appear to have no effect on a simulated laser catheter shield. This includes observation of neither shield damage, nor reflection of the shock front back into the tissue. Tissue debris which collects on the shield over time is ablated, however, accompanied by a very similar blast wave to that produced by ablation of native tissue.

5.3. Ablation with Sequenced Pulses

Experiments designed to investigate the dynamics of tissue ablation in a time-resolved manner contribute both to the development of accurate models of the ablation process, and also to practical solutions of clinical problems involving tissue removal. While fast strobe photography of ablation yields important information about the results of ablation above the tissue surface, the information it yields about processes occurred within the tissue can only be inferred.

This study probes the ablation process directly by examining the characteristics of calcified tissue ablation with two pulses separated by a variable time delay. Investigation of the time dependence of ablation with sequenced pulses yields clues about the physical processes which contribute to ablation. For example, the role of thermal storage of laser energy during ablation is probed by performing ablation with pulses separated by delays characteristic of thermal diffusion times. In addition, information may be inferred concerning the role of transient changes in tissue optical and thermal properties which may occur during ablation, and the time constants for those changes.

The information gained in the present study was critical to the design of the prototype system for laser angiosurgery, described in Part II of this thesis. Information about ablation dynamics may be alternatively cast as information about the "memory time" of tissue during ablation, which can then be compared to, and optimized with respect to the recovery time for avoiding optical damage in fibers.

5.3.1. Experimental Methods

Two identical Q-switched Nd:YAG lasers emitting 7.5 nsec duration, $\lambda = 1.064$ nm pulses at 10 Hz were used to perform ablation experiments. For single wavelength experiments, the third harmonic of each laser ($\lambda = 355$ nm) was used. For dual wavelength experiments, one laser was operated at the Nd:YAG second harmonic ($\lambda = 532$ nm), with the other operating at the third harmonic. The pulse separation between the two laser firings was controlled by a variable electronic delay circuit between the laser Q-switch triggers. The pulse separation jitter was <10 nsec. Pulse separations were measured on an oscilloscope with a fast diode.

Each Nd:YAG laser emitted a cylindrically symmetric beam with a diameter of 6 mm. The beam irradiance profiles were measured to be uniform to within 10% over their inner 3

mm of radius, and less uniform outside of that radius. The beams exiting the two lasers were overlapped in position and direction with a 50% reflective beamsplitter, as shown in Fig. 5.8. The inhomogenous outer portions of the beam profiles were blocked with a 3 mm diameter aperture. Light passing through the aperture was directed through a 25 cm focal length lens to create a 1.4 mm diameter, demagnified image of the aperture on the tissue surface. This scheme of re-imaging the known, uniform light distribution within the aperture onto the tissue surface assured a top-hat profile ablation spot. Complete overlap of the beams from the two lasers was checked both at the aperture and at the tissue surface by examining burn patterns made on exposed polaroid film.

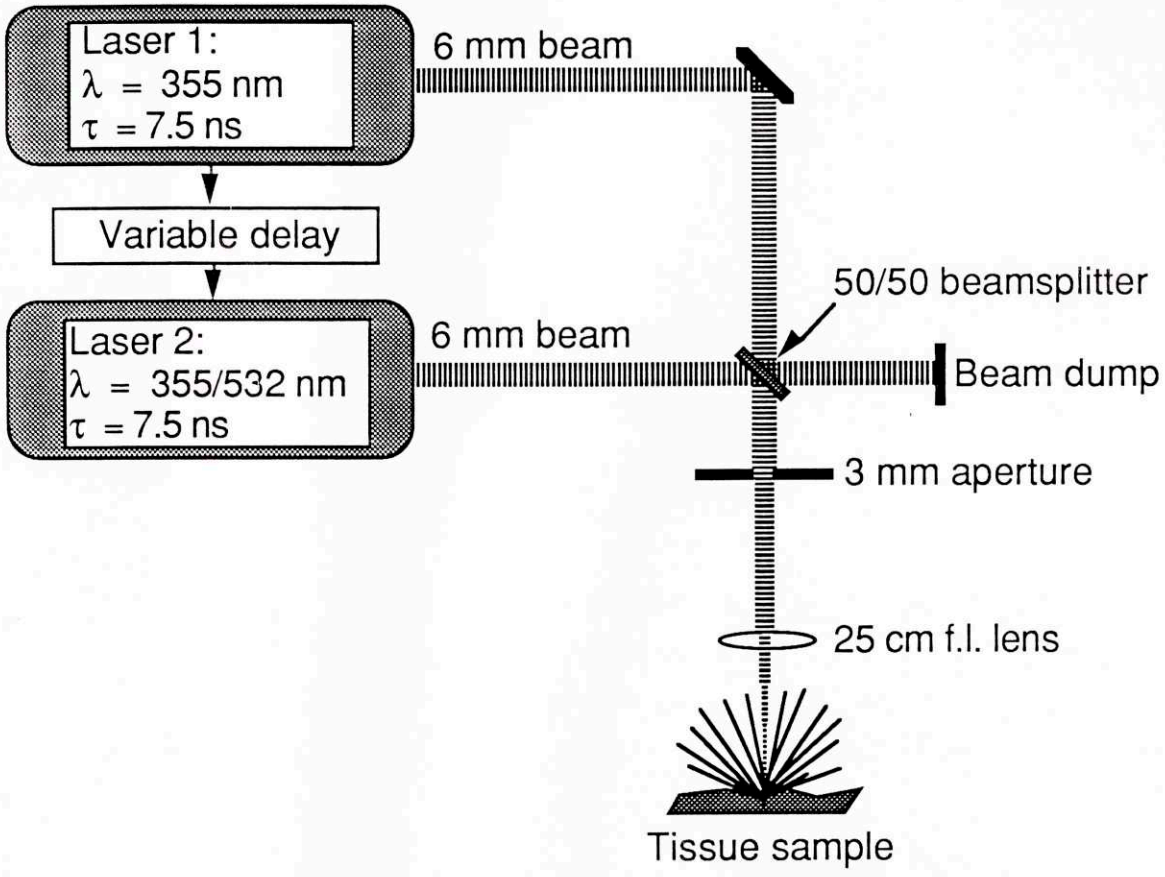

FIGURE 5.8. Schematic of sequenced pulse ablation experiment.

Pulse energies were measured several times during each experiment with a thermopile detector placed immediately after the beam limiting aperture. Crater depths were measured at their centers by monitoring the vertical travel of a high-power microscope between focussing on the top and bottom of laser craters.

The tissue studied in the experiments was bovine shank bone. Bone samples were obtained no later than 2 days post-mortem. Areas of the bone surface exhibiting a clean, smooth cortical surface were prepared by scraping the surface with a razor blade to remove the periosteum. Prepared bone samples were either used immediately, or kept in a refrigerator until use. Ablation was done in air.

5.3.2. Determination of Threshold Fluence

A careful choice of working fluence was essential for obtaining statistically significant, reproducible results. Optimal discrimination in crater depth was obtained with each pulse just below fluence threshold, so that two completely overlapped pulses delivered almost twice threshold, while pulses separated by long times did not remove any tissue (there was a slight amount of tissue charring, probably due to heat buildup at the 10 Hz laser repetition rate -- see section 2.3.2).

In order to accurately determine threshold fluence for the relevant tissue and laser parameters, a crater depth versus fluence study using single pulses with the sequenced pulse ablation setup was carried out. The results of this study, obtained using 600 shots per crater (60 seconds at 10 Hz) on beef bone at the 1.4 mm spot diameter, have already been discussed in chapter 4. They are plotted in Fig. 4.6, and the fitted values for fluence threshold and ablation yield are listed in Table 4.2.

Based on the data in Table 4.2, a working fluence of 13 mJ/mm^2 was chosen as a value which would give no crater at infinite pulse separation, and craters on the order of 1 μm per shot at zero pulse separation (complete temporal overlap). Except where specifically noted, all sequenced pulse experiments in this chapter were done with a 1.4 mm spot diameter.

5.3.3. Single Wavelength Sequenced Pulse Ablation -- Results

Ablation with sequenced pulses was carried out with each laser delivering a fluence of 13 mJ/mm^2 to the tissue surface, for pulse separations (τ_{sep}) varying logarithmically between 1 nsec and 100 msec. Three qualitative changes occurred in the appearance of the laser craters over this range. For τ_{sep} between 1 nsec and 10 μsec, laser craters had smooth bottoms and only mild discoloration (charring) on the sides. At a τ_{sep} of 20 μsec, the bottoms of the craters began to take on the appearance of valleys separated by char-covered peaks. As τ_{sep} was increased from 20 μsec to 10 msec, more and more char-covered peaks

appeared, although deep valleys were still evident. Finally, at a τ_{sep} of 100 msec, there were no valleys and no evidence of tissue removal. The bone surface was completely covered with char.

Quantitative measurements of crater depth as a function of pulse separation are shown in Fig. 5.9. Five craters were drilled at each value of τ and averaged to give the data values. The error bars on the data between τ_{sep} = 1 ns and τ_{sep} = 1 μsec represent the standard deviation among the crater depths measured for those pulse separations. Measurement of crater depths for τ_{sep} values between 2 μsec and 10 ms was complicated by the crater geometry. Average crater depths were estimated by measuring the depth of the valleys in the craters, and estimating the percentage of the crater bottom area which was at that depth. The error bars for those τ values were based on both the standard deviation of the depth measurements, and the error associated with valley area estimation.

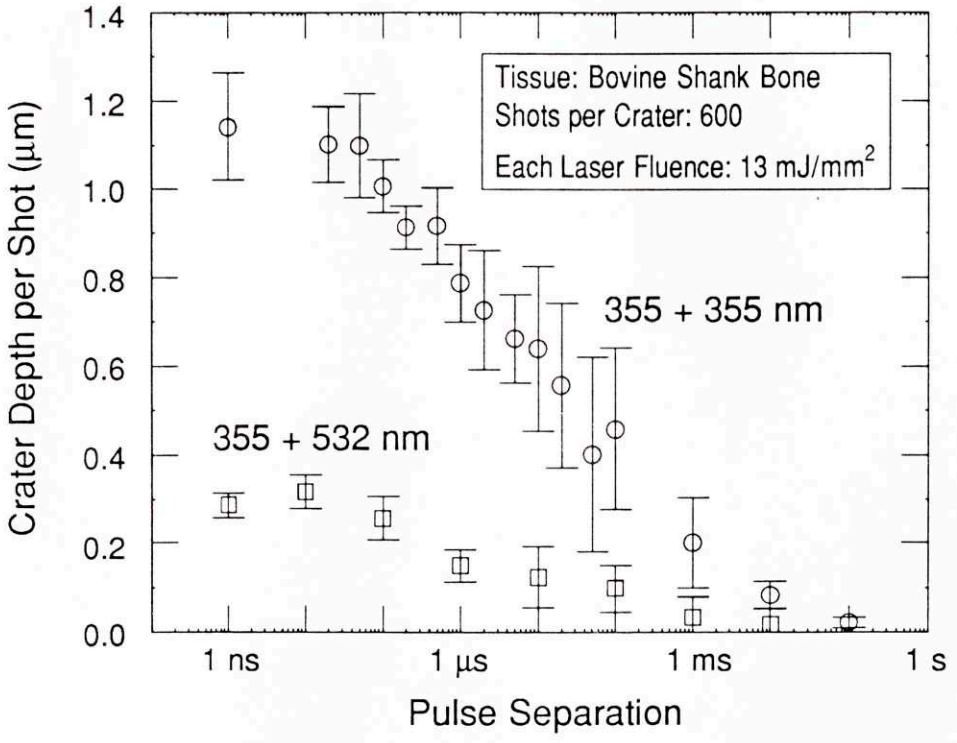

FIGURE 5.9. Crater depths for the single and dual wavelength sequenced pulse experiments.

5.3.3.1. Discussion of Single Wavelength Results

Several aspects of the pulse separation dependence of sequenced pulse ablation deserve comment. First, the effect of individual sub-threshold pulses is not permanent; with sufficient delay, all memory of each pulse is lost. The data points at the longest pulse separation in Fig. 5.10, τ_{sep} = 100 msec, were taken with 600 shots at 10 Hz. Although there was some charring, no tissue removal was observed.

Second, the tissue did not differentiate between pulse separations of up to a few hundred ns, indicating that pulse contiguity is not essential—the tissue "remembers" the presence of the first pulse over this period. Beyond this time, crater depth decreased monotonically to zero over 6 decades of pulse separation. Thermal diffusion of the heat deposited in the tissue by the first pulse probably contributes to the decrease in crater depth in the μs to ms regime, since these times are characteristic of thermal diffusion over distances typical of optical penetration depths in tissue. However, the fall-off is too gradual to be explained by simple thermal diffusion (i.e. with constant optical and thermal parameters), since most of the heat deposited by the first pulse would diffuse out of the volume to be illuminated by the second pulse within a few thermal time constants.

Thermal diffusion might not be the only source of energy loss. Processes such as radiative cooling and coupling into acoustic modes of the tissue might also contribute to dissipate the energy delivered by the first pulse. Transient changes in the optical and/or thermal properties of the tissue could also contribute to the extended fall-off time. The first pulse could produce a transient change in the attenuation coefficient, for example, by populating a long–lived electronic triplet state. The attenuation coefficient could also be a function of local tissue temperature. Transient changes in thermal diffusivity could also extend this interaction time.

The memory time during which the tissue is insensitive to pulse separation may be used to advantage in the design of optical fiber light delivery systems. The memory time of the tissue may be directly compared to the memory time of fused silica, the best waveguide material in the near ultraviolet region. In experiments described in chapter 7, the recovery time for avoiding optical breakdown between irradiation with sequenced pulses in fused silica substrate samples was observed to be less than ~10-15 nsec, consistent with electronic relaxation processes in the dielectric [Albagli et al 91]. This difference in characteristic times between the two materials opens a window of between ten and a few

hundred ns over which ablation light may be delivered without inducing optical fiber damage and yet without diminishing ablation. This has been used to advantage in the design of the prototype laser angiosurgery system described in Part II of this thesis.

5.3.4. Dual Wavelength Sequenced Pulse Ablation -- Results

A striking and potentially useful effect was observed when the second pulse in the sequenced pulse experiment was replaced with a pulse of another wavelength, the $\lambda = 532$ nm second harmonic of the Nd:YAG laser. In the study of bone ablation dosimetry in chapter 4, craters drilled with single pulses of $\lambda = 355$ nm light exhibited sharp cuts at their margins and the solid debris from the ablation process was found to be composed mostly of hydroxyapatite granules on the order of a few μm in diameter. Craters drilled in the $\lambda = 450$–600 nm wavelength region, on the other hand, were very roughly cut, often extending beyond the boundaries of the illuminating beam, and large flakes and particles of debris were found attached to the edges of the craters and otherwise strewn about. The cutting quality exhibited by a laser wavelength was not found to depend upon the spot diameter, except of course that a given degree of cutting roughness appeared worse compared to a small crater.

Figure 5.10(a) illustrates the quality of the laser cut obtained by a sequence of 30 mJ/mm^2 at $\lambda = 355$ nm followed by 30 mJ/mm^2 at $\lambda = 532$ nm with 200 nsec pulse separation. The light was delivered by a 200 μm core optical fiber, which was in contact with the tissue. Each pulse alone was below fluence threshold for that wavelength and spot diameter, so the ablation crater was made by a cooperation between both wavelengths. For reference, the gross appearance of a typical bone cut on a larger crater in the 450–600 nm wavelength region is reproduced in Fig. 5.10(b) (also see Fig. 4.7(b-c)). Strikingly, the crater made with the combination of wavelengths exhibited a cutting quality far superior to craters made with any of the visible wavelengths; in fact, the cutting quality was equal to craters cut with the $\lambda = 355$ nm wavelength alone.

The dependence of dual wavelength sequenced pulse ablation crater depths on pulse separation are also plotted in Fig. 5.9. The square data points in the figure were obtained in the same manner as for the single wavelength study; each dual wavelength data point is an average over three tissue craters. The dependence of crater depth on pulse separation for those data points was very similar to the results for single wavelength sequenced pulse ablation. Note also that the dual wavelength crater depths were about one fourth of the single wavelength crater depths at all positive pulse separation times.

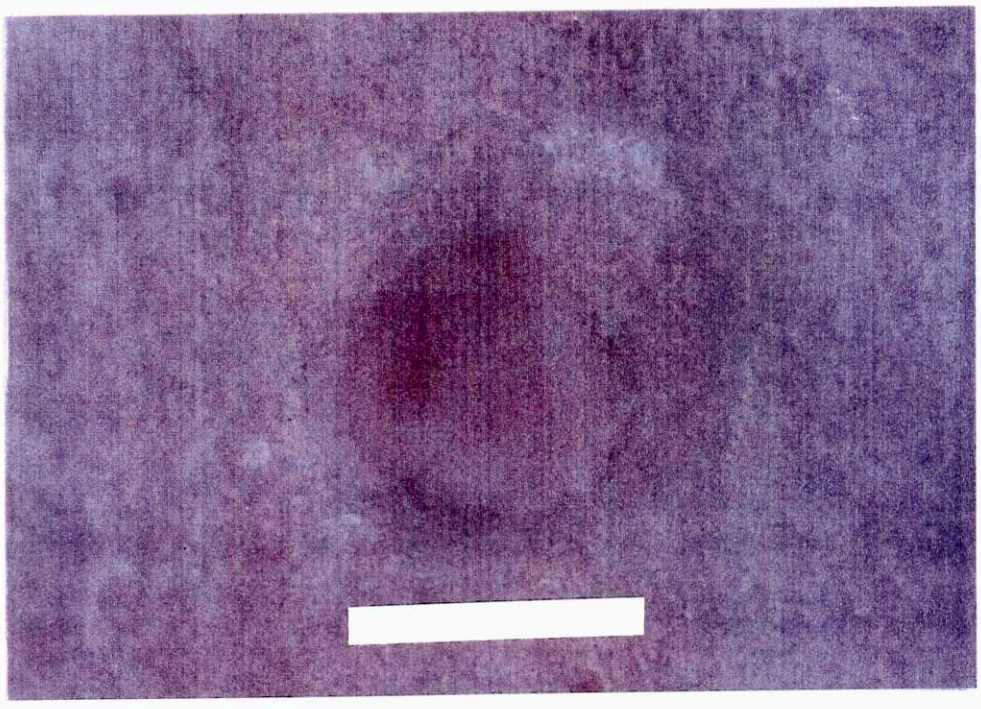

(a)

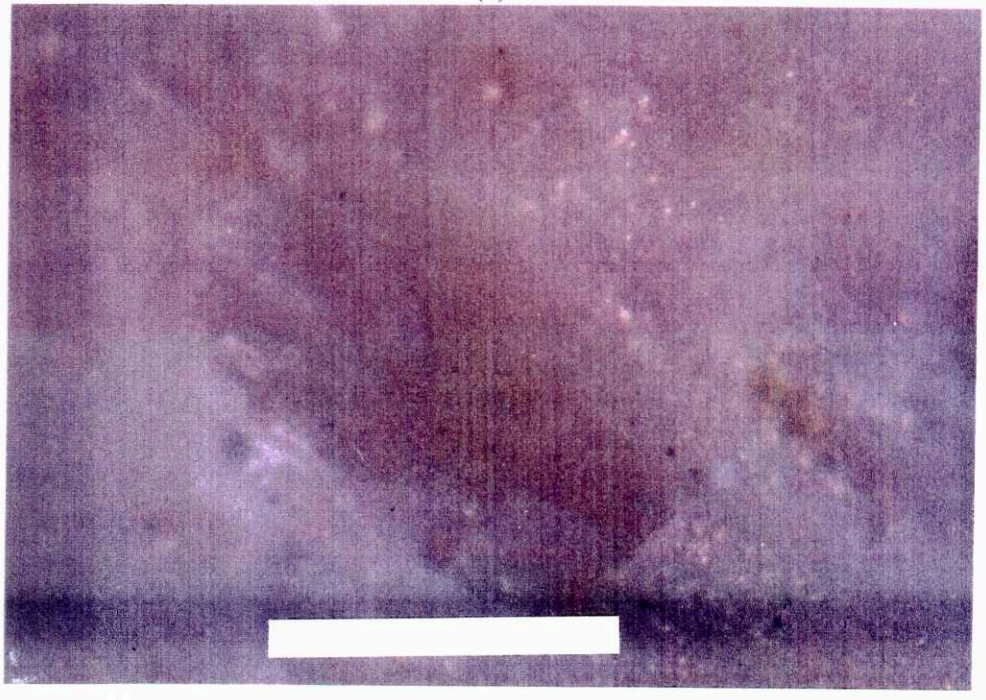

(b)

FIGURE 5.10. (a) Crater in bovine bone from dual wavelength ablation at $\lambda = 355 + 532$ nm, 200 nsec pulse separation, spot diameter = 200 μm, $\phi = 2 \times 30$ mJ/mm^2 exhibits excellent cutting characteristics. Length of bar = 200 μm. (b) Bone crater from single pulses at $\lambda = 503$ nm, spot diameter = 500 μm. Crater is larger than laser spot and exhibits rough cutting. Length of bar = 500 μm.

Figure 5.11 illustrates the behavior of dual wavelength ablation as the fluences at both wavelengths were independently varied. The pulse separation was fixed at 100 nsec, with the $\lambda = 355$ nm pulse always coming first. Each data point represents the measured depth of one bone crater. Note that for sufficiently high $\lambda = 532$ nm fluences, though still below threshold for $\lambda = 532$ nm alone, even $\lambda = 355$ nm pulses well below threshold were sufficient to begin the ablation process. All bone craters in this matrix exhibited a quality of cut at least equal to the crater reproduced in Fig. 5.10(a).

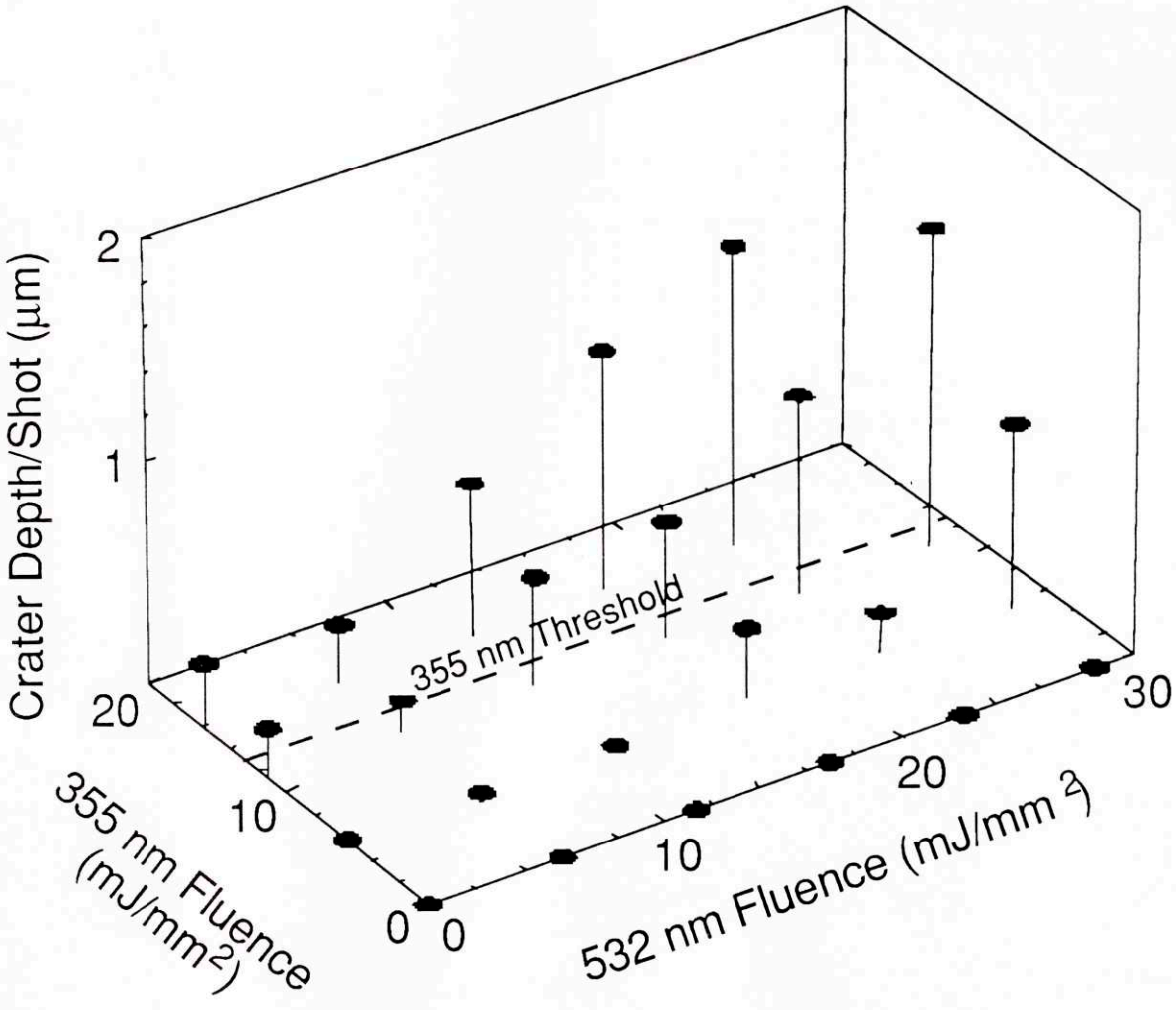

FIGURE 5.11. Dual wavelength ablation crater depths as a function of both wavelength fluences. All pulse separations were 100 nsec, 355 nm pulse first.

5.3.4.1. Discussion of Dual Wavelength Results

The similarity in the time dependence of the dual wavelength studies to the single wavelength studies, illustrated in Fig. 5.11, suggests that the same physical processes are involved. Craters made with two wavelengths were shallower than craters made with one, consistent with a smaller attenuation coefficient at $\lambda = 532$ nm than at $\lambda = 355$ nm.

The ability to ablate with a combination of $\lambda = 532$ and $\lambda = 355$ nm light while maintaining excellent tissue cutting quality suggests an application in which a small quantity of ultraviolet "priming" light is followed by a larger quantity of visible "cutting" light. This possibility is especially attractive if the visible light is substantially cheaper to produce and/or deliver to the tissue surface than the ultraviolet light, which is certainly the case with present laser sources and optical fibers.

5.4. Conclusions

Fast laser strobe photography reveals that bone ablation with near-ultraviolet and mid-infrared light have very similar results above the tissue surface. Using a shadowgraph viewing configuration, blast waves resulting from ablation are clearly visible. Blast waves generated by $\lambda = 355$ nm ablation of bone grow with time to the 0.6 power. Blast wave velocity increases with ablation fluence until plasma shielding of the incident light occurs. The blast waves have no discernable effect on a simulated laser catheter.

Sequenced pulse ablation studies indicate that bone is insensitive to pulse separation over the first few hundred ns. Crater depths fall off monotonically beyond this time, indicating either that competing physical mechanisms combine to contain and dissipate the energy deposited by the first pulse, or that transient changes in the optical and/or thermal tissue properties occur which modulate the energy deposition and/or dissipation processes.

Dual wavelength sequenced pulse ablation studies exhibit approximately the same temporal behavior as the single wavelength studies, and illustrate that two sub-threshold pulses of different colors may combine to ablate tissue with the cutting characteristics determined by the more strongly absorbed wavelength. This effect may prove useful in medical applications such as the delivery of ablation light through optical fibers to locations within the body.

PART II

A PROTOTYPE SYSTEM FOR LASER ANGIOSURGERY

Chapter 6
Design Considerations for the LAS II System

In Part II, a prototype clinical system is described which has brought the research on calcified tissue ablation described in previous chapters into practical application. The clinical application chosen in this case is laser treatment of coronary artery disease. Methods for laser treatment of atherosclerosis have been outlined in section 1.5. That section included a brief description of the salient features of a new system for laser angiosurgery, the MIT LAS II system. As mentioned there, development of the LAS II system at MIT included three major technical innovations: design of the LAS II catheter, design and implementation of a clinically effective ablation and light delivery scheme, and invention of a tissue fluorescence-based catheter guidance system. The primary contributions of the author to the LAS II system, and the subject of Part II of this thesis, fall into the second category.

This first chapter of Part II treats the design of the LAS II "ablation subsystem" in more detail, including the details of the choice of the ablation laser, and the implications of the design of the LAS II catheter for ablation subsystem engineering. The remaining chapters in Part II deal with limits imposed on system design by high-irradiance laser light conduction in optical fibers, the engineering of the working prototype system, and tissue dosimetry studies using the completed LAS II system.

6.1. Choice of the Ablation Laser

Successful laser recanalisation of coronary arteries containing complicated atherosclerotic plaque requires a light source capable of ablating densely calcified tissue with a desirable clinical end point, without destroying the optical fibers in its own delivery system. For this reason, some understanding of the mechanisms of both laser ablation of calcified tissue and laser-induced breakdown of optical fibers is a prerequisite to selecting a suitable ablation laser. The preceding chapters in Part I of this thesis have described progress which has been made in understanding the physical mechanisms of the calcified tissue ablation process, and their manifestations in terms of tissue cutting quality and dosimetry. Some recent work which has been done on understanding laser-induced breakdown in optical materials is described in chapter 7. However, the general approach to

deciding upon a laser source for the LAS II system was to concentrate primarily on the laser cutting characteristics and dosimetry and how they interacted with catheter design. Considerations of laser availability and optical design were secondary, under the assumption that a sufficiently robust light delivery system could be designed around the optimal laser choice. It is interesting to note that this ordering of priorities is not always so in the design of laser angioplasty systems, where the availability or marketability of novel laser systems often drives the development of new clinical initiatives.

The primary selection criteria for for the laser source were the sharpness of the laser cut in fibrous and calcified tissue, the size of ablation debris particles, crater histology, removal dosimetry considerations (including fluence threshold and ablation yield), and the avoidance of any forseeably deleterious host response, such as the the potential of the wavelength for mutagenicity. Chapter 4 of this thesis describes a parameter survey of calcified tissue ablation (including comparisons with fibrous tissue ablation) which included variation of all of the light delivery parameters controllable through the choice of the ablation laser. Of particular interest for the choice of a clinical laser angiosurgery laser was the comprehensive wavelength ablation study conducted as a part that survey, performed within the irradiance range appropriate for efficient, two-component hard tissue ablation.

The potential of ultraviolet radiation for cytotoxicity (cell killing), mutagenicity (inheritable mutation), and carcinogenicity (tumor generation) has been studied for many years as a major research topic in photobiology. Historically, most cell line and animal model studies have employed conventional ultraviolet light sources. The extrapolation of results obtained in these studies to the effects of pulsed radiation from lasers, although possible in some cases, is difficult [Kochever 89]. This is because even though two-photon processes are probably not important at typical ablation irradiances, mutagenic effects may still depend on irradiance and/or the time separation between treatments. Fractionation of x-ray doses is a common method in radiation dosimetry, for example, to enhance cytotoxic effect [Hall 78]. Thus, considerable primary research remains to be done on the photobiological effect of ultraviolet laser radiation.

Ultraviolet light is conventionally divided into the wavelength regions UV-A (320-400 nm), UV-B (290-320 nm), UV-C (200-290 nm), and vacuum UV (<200 nm). Wavelengths in the VUV, UV-C, and UV-B regions are absorbed in DNA, in decreasing order [Ito et al 86]. Photobiological effects have been observed in all four wavelength regions, however. The action spectra for UV-induced cytotoxicity and mutagenicity have

been measured with cw radiation sources in many cell lines and bacteria, and is closely related to the DNA absorption spectrum, with the exception that VUV wavelengths are often less active than wavelengths in the UV-C region [Peak et al 84, Jones et al 87]. This may be due to the fact that VUV wavelengths are so strongly absorbed in cell membranes and cytoplasm that they are strongly attenuated by the time they reach the nucleus, or else that by exciting higher electronic states in DNA they produce different, less active photoproducts [Kochever 89]. Cytotoxicity and mutagenicity are typically several orders of magnitude less in the UV-B region than in the UV-C region, and the same trend continues into the UV-A region. Since UV-A radiation is not strongly absorbed in DNA itself, its photobiological effect appears to be the result of chemically active photoproducts produced by light absorption in other tissue chromophores.

Vacuum UV radiation is usually not considered a candidate for laser surgical applications because it is absorbed in the atmosphere, and optical fibers are not available in that wavelength range. One exception to this rule is ArF excimer radiation at $\lambda = 193$ nm which is used in corneal surgery, where fibers are not required and the attenuation in air is outweighed by the wavelength's excellent tissue cutting qualities [Krauss et al 86, Trokel et al 83]. UV-C radiation is commonly used as a germicidal agent, and no clinical applications of lasers in this wavelength region are known to the author. Even in the less active UV–B range, cytotoxicity, mutagenicity, and carcinogenicity have been observed in cell line and animal models in doses even less than the threshold for pulsed ablation of calcified tissue at, for example, $\lambda = 308$ nm (where $\phi_0 \sim 20$ mJ/mm^2) [Rasmussen et al 89, Collela et al 86, Tiphlova et al 88, Freeman 78, Hsu et al 75, Strickland et al 79]. Although most of the tissue irradiated during ablation with a 308 nm laser is removed, sub-threshold doses of light are unavoidably deposited at the bottom and sides of every ablation crater. Thus, when light in the UV-B region is used, potentially dangerous fluence levels are deposited in healthy tissue.

Wavelengths below 320 nm, although excellent tissue cutters, were excluded from consideration for the LAS II system because of the risk of mutagenic and carcinogenic effects. Visible wavelengths above about 400 nm were eliminated because they exhibited unsatisfactory cutting and debris, accompanied by substantial cracking and fissuring [see chapter 4]. Although the 2.1 μm region wavelength exhibited satisfactory cutting qualities, the combination of high threshold and low yield at that wavelength raised concerns about collateral damage effects due to the substantial heat deposition in the sub-threshold tissue

region. Wavelengths between 320–400 nm, and in the 3 μm region, exhibited excellent ablation quality by all selection criteria.

Secondary considerations related to beam quality and the survival of the light delivery system further limited the choices for the ablation laser. No fibers were available which could deliver sufficient light in the 3 μm region to ablate tissue, unfortunately disallowing that otherwise highly desirable wavelength range from consideration. Fiber breakdown considerations constrained the range of possible irradiances usable in the remaining 325-400 nm wavelength region, as will be discussed in detail in a later section. Finally, high laser beam quality was necessary to implement the advanced features of LAS II, such as passing through the pulse stretching network described below, and the ability to separately address each fiber or any group of fibers in the catheter tip.

With all of these considerations in mind, the $\lambda = 355$ nm third harmonic wavelength of the Nd:YAG laser was chosen as a proven, reliable and commercially available laser system which had sufficient beam quality to allow for external optical pulse stretching to satisfy fiber transmission requirements. The tripled Nd:YAG laser is especially attractive in the hospital environment in comparison to excimer lasers, which have low beam quality, contain toxic gases which need to be replaced periodically, and are notoriously unreliable. From Table 4.3, the threshold fluence and ablation yield for ablation of bovine bone in air are $\phi_0 = 36 \pm 4$ mJ/mm^2, and $Y = 0.066$ mm^3/J, respectively. According to the results in section 4.7, the fluence threshold is expected to approximately double under saline and a shield, to ~70 mJ/mm^2. In order to give a healthy working fluence range, the nominal design fluence at the catheter tip was set at twice this value, or $\phi_{design} = 140$ mJ/mm^2.

6.2. Catheter Design Constraints on System Engineering

As described in section 1.5, the LAS II catheter incorporates several advanced features which allow for delivery of laser light to diseased arterial tissue in such a manner as to minimize deleterious host response to the procedure. These characteristics include the use of multiple individually addressable optical fibers, the use of an "optical shield" at the catheter tip, and the incorporation of a guidewire. These catheter characteristics combine with the carefully chosen ablation wavelength and fluorescence–based spectroscopic feedback to provide maximum selectivity of diseased tissue and minimal trauma to normal tissue. The requirements which these catheter characteristics place on the design of the optical delivery system are the subject of this section.

A schematic of a prototype catheter consisting of 12 x 200 μm core diameter fused silica optical fibers constructed for intraoperative use appears in Fig. 1.1. The catheter is 1.6 mm in diameter, with a 500 μm guidewire lumen. Thus, the catheter shield area is

$$A_{shield} = \frac{\pi}{4}\left[(1.5\ mm)^2 - (0.6\ mm)^2\right] = 1.48\ mm^2. \qquad (6.1)$$

The energy per fiber required to be delivered to achieve the design fluence at the catheter tip is then

$$E_{fiber} = \frac{\phi_{design} \cdot A_{shield}}{\#\ of\ fibers} = \frac{140\ mJ/mm^2 \cdot 1.48\ mm^2}{12} = 17.3\ mJ. \qquad (6.2)$$

Thus, the fluence at each 200 μm core diameter fiber tip is required to be:

$$\phi_{fiber} = \frac{E_{fiber}}{\frac{\pi}{4}\ [200\ \mu m]^2} = 550\ mJ/mm^2. \qquad (6.3)$$

Note that these calculations represent the energy and fluence requirements at the output end of the catheter. Due to losses in the catheter fibers, and at the fiber-air and shield-air interfaces, the energy required at the input end of the catheter is even higher. In addition, the LAS II system incorporates a 15 m long transmission line which conducts light from the laser table to the operating room (see chapter 8). Taking all of these losses into account, at one point in the system it is necessary to conduct almost twice the values calculated above through each of several 200 μm core optical fibers (for a detailed accounting of energy transmission through the LAS II system, see section 8.3.2).

In the actual LAS II catheter, the light from each individual 200 μm core diameter fiber diverges to form a spot approximately 540 μm in diameter on the output face, yielding an expansion factor in area from the fiber to the shield of 7.3. Since the sum of twelve spots of that diameter is much larger than the shield area, the spots are overlapped on the catheter face. On average, each location on the shield is illuminated by 1.83 fibers, so there is double spot overlap almost everywhere. This has important ramifications for the minumum number of fibers which can be fired at once to ablate tissue. If only one fiber is illuminated, the energy it must have to achieve fluence threshold in its 540 μm spot on the catheter shield is

$$E_{1\ fiber} = \phi_0 \cdot \frac{\pi \cdot [540\ mm]^2}{4} = 16\ mJ. \qquad (6.4)$$

It takes almost all of the design energy per fiber to reach fluence threshold, and it is the fiber overlap which brings that spot on the shield up to the design fluence. Thus, it is expected that no fewer than two adjacent fibers should be able to ablate tissue (see section 9.2).

The expected catheter advancement rate in the densest calcified tissue, assuming $P_{av} = 1$ watt average power at the catheter tip, may be calculated from the above considerations, the ablation yield for bone, and the ablation efficiency $\eta_{abl} = [\phi_{design} - \phi_0]/\phi_0$ (see section 2.4.4):

$$v_{catheter} = \frac{P_{av}\ (J/s) \cdot Y\ (mm^3/J)}{A_{shield}\ (mm^2)} \cdot \frac{\phi_{design} - \phi_0}{\phi_{design}} = \frac{2.5\ J/s \cdot 0.66\ mm^3/J}{1.48\ mm^2} \cdot 0.5$$

$$= 222\ \frac{\mu m}{s}. \qquad (6.5)$$

The primary constraints which catheter design places on system engineering are twofold. First, the laser energy reaching the catheter input must have sufficient beam quality to be divided up and directed into a subset of 12 separately addressable, 200 μm core diameter fibers. Second, the optical fibers comprising the optical delivery system must be able to conduct not just the ablation working fluence of 140 mJ/mm^2, but up to 8 times that amount to allow for light expansion through the optical shield and losses in the system.

6.3. Conclusions

The components of a new system for laser angiosurgery responsible for tissue ablation and laser light delivery are described in Part II of this thesis. Frequency-tripled light at $\lambda = 355$ nm from a solid-state Nd:YAG laser was chosed for the LAS II system due to its excellent tissue cutting characteristics, avoidance of the potential for mutagenicity, and the laser's intrinsic advantages of beam quality, safety, and reliability. The advanced features of the LAS II catheter impose tough constraints on the beam quality and energy of the laser light which must be delivered to the catheter tip.

Chapter 7

Optical Fiber Delivery of High Intensity Light at $\lambda = 355$ nm

High pulse energy frequency-multiplied Nd:YAG lasers of the type chosen for the LAS II system typically have pulse durations on the order of 10 ns. Short, Q-switched pulses are necessary in these systems in order to gain high frequency conversion efficiency into the third harmonic. As described in the previous chapter, the LAS II catheter design requires the delivery of high fluence through the catheter fibers; delivering this fluence in a 10 ns pulse results in a peak irradiance on the order of GW/cm^2. Since this is above the threshold for optical damage in fused silica optical fibers, an understanding of the relationship between irradiance, fluence, and pulse width in the breakdown mechanism of fused silica is important to the design of an optical system for processing the raw laser pulses into pulse shapes which existing fibers can transmit.

The lead role in consideration of laser damage in fused silica optical fibers for the LAS II system was taken by Douglas Albagli. Insight into the theoretical aspects of the problem was contributed by Michael Feld and Iriving Itzkan, while the experiments described here were conducted with the aid of Gary Hayes and Bryan Banish.

7.1. Mechanisms for Optical Damage in Fused Silica

Two mechanisms dominate optical breakdown in fused silica in the ns pulse duration regime [Albagli et al 91, Feld et al 91]. Self-focussing is the focussing of a beam in a material due to a change in the index of refraction of the material induced by the beam itself [Chiao et al 64, Shen 84]. Self-focussing is independent of beam diameter or pulse fluence, being a purely power-dependent phenomenon. At a threshold power P_1, self-focussing just cancels beam spreading due to self-diffraction, and the beam maintains its size as it propagates. At a higher power P_2, the beam self-focusses to a singularity. Damage in the material typically occurs in the bulk of the material at some power in between these two values. Self-focussing scales as the square of the wavelength, rendering it a more important phenomenon in the ultraviolet than in the visible wavelengths. Values of P_1 and P_2 for fused silica at 355 nm are listed in Table 7.1 [Smith et al 77]. Neglecting system losses, and assuming that the design energy E_{fiber} = 17.3 mJ must be delivered by each fiber to the

end of the catheter, the pulse widths τ_1 and τ_2 corresponding to P_1 and P_2 are also listed. These values of τ_1 and τ_2 assume a top-hat temporal pulse profile, and represent the shortest duration in which a 17.3 mJ pulse can be delivered with a peak power less than the corresponding values of P_1 and P_2. Thus, pulse durations in excess of ~100 ns are necessary to avoid optical breakdown due to self-focussing in the LAS II system.

λ (nm)	P_1 (kW)	P_2 (kW)	τ_1 (nsec)	τ_2 (nsec)
355	125	462	138	37

TABLE 7.1. Critical values for self-focussing in fused silica [Smith et al 77].

The second mechanism for optical breakdown in fused silica is surface breakdown, which is probably a surface-enhanced form of bulk breakdown. Fused silica is normally optically transparent because it is an insulator with an electronic band gap (~8 ev) wider than visible photon energies. This is also true at λ = 355 nm, where $h\nu$ = 3.5 eV, and three photons are necessary to span the band gap. Thus, optical damage can only be induced if the material is first turned into an absorber. This can be accomplished if sufficient electrons are excited into the conduction band, where they become absorbers since there are a large number of allowable unoccupied states there. Due to inclusions and defects in the material, some electrons are always in the conduction band; others may be excited into the conduction band in strong optical fields by multiphoton ionization. Once electrons are in the conduction band, they may be accelerated by the incident optical field until they obtain sufficient momentum to ionize electrons in lower bands. The potential for impact ionization in the optical frequency range was first described by Bloembergen [74]. If the rate of free electron production by this process exceeds the rate of electron loss from the conduction band due to electron-hole recombination, there can be a net buildup of free electrons. Bloembergen [74] obtained an equation for the population of free electrons, N, as a function of time, in the limit where multiphoton ionization is not important:

$$N = N_0 \exp\left[\left(\eta_{IC}(E) - \frac{1}{\tau_{rec}}\right) \cdot t\right]. \qquad (7.1)$$

Here N_0 is the resting electron population, $\eta_{IC}(E)$ is the probability per unit time for an electron to undergo an ionizing collision, E is the electric field of the laser, τ_{rec} is the characteristic time for electron-hole recombination, and t is the pulse duration. $\eta_{IC}(E)$ has been measured in fused silica in several experiments to have the form $\eta_{IC}(E) \sim E^n$, where n

ranges between about 4 and 7 [Smith et al 77, Fradin et al 73]. The rate of electron production is thus a very strong function of the irradiance, which of course goes as E^2. The electron-hole recombination time been measured to be ~8 ns by Hughes [78].

Equation (7.1) may be used to obtain the scaling of breakdown fluence with pulse duration, assuming a top-hat profile pulse of duration t. It is assumed that once the number of free electrons has been increased by some fixed amount, the energy that they absorb is sufficient that when it is transferred to the lattice, stress is induced leading to mechanical breakdown. When the exponent in Eq. (7.1) becomes equal to a constant, K, the breakdown fluence may then be shown to scale according to

$$\phi_{bkdn} \sim \left[K + \frac{t}{\tau_{rec}} \right]^{\frac{2}{n}} \bullet t^{\left(1 - \frac{2}{n}\right)}; \tag{7.2}$$

which has the limits

$$\phi_{bkdn} \sim t^{\left(1 - \frac{2}{n}\right)}; \qquad t << K \bullet \tau_{rec}; \tag{7.3}$$

$$\phi_{bkdn} \sim t; \qquad t >> K \bullet \tau_{rec}. \tag{7.4}$$

A rough estimate for K can be obtained by assuming that 1) there are ~10^{20} available electronic states per band in the material, 2) the lowest empty band actually contains ~ 10^8 electrons/cm^3 due to impurities and inclusions, and 3) when the population of that band reaches about 1% of its capacity, or ~10^{18} electrons/cm^3, breakdown occurs [Feld et al 91]. Under these assumptions, $N/N_0 \sim 10^{18} \sim e^{23}$, leading to K ~ 23. Thus, according to Eq. (7.3-4) and using K = 23 and τ_{rec} = 8 ns, the changeover from a power-law type growth of fluence breakdown with time to a linear relationship should occur at pulse durations on the order of a few hundred ns.

Bulk breakdown is observed in practice only when a beam is focussed into a material. This is because breakdown at the material surface usually occurs at irradiances 2-10 times lower than bulk breakdown, even for clean, polished optical surfaces [Reif 89]. Several mechanisms have been suggested for this effect. Bloembergen [73] suggested that the incident electric field could be enhanced due to microscopic pores and cracks on the surface. More recently, Reif [89] has suggested that the surface defects could also cause resonant enhancement of the multiphoton absorption process, or alternatively that surface-assisted dielectric air breakdown may also play a role.

Some experimental data exists in the literature for surface breakdown thresholds. By convention, these studies have investigated breakdown by studying breakdown fluence as a function of pulse duration. Singleton et al [88] found that the surface damage threshold for fused silica optical fibers scaled as the square root of pulse width in the range 10-300 ns at $\lambda = 308$ nm. This finding is consistent with $\eta_{IC}(E) \sim E^4$. Rainer et al [83] also found a square root dependence at $\lambda = 248$ nm in MgF_2 and CaF_2. More extensive data exists for bulk breakdown in fused silica at 1.06 μm, where fluence was also found to scale approximately as the square root of the pulse duration [Van Stryland 80]. Unfortunately, many of the studies cited relied on several different lasers systems and optical setups to obtain the necessary variation in pulse duration. Also, there was no data available at $\lambda = 355$ nm in fused silica.

The interplay of surface breakdown and self-focussing places limits on the shape of the laser pulse profile, if sufficient light is to be delivered down the catheter to ablate tissue. Unfortunately, the data on surface breakdown available from the literature was insufficient to characterize this process with sufficient accuracy at the wavelength of interest to decide upon a pulse duration. For this reason further breakdown studies were necessary, and they are described in the next two sections.

One additional degree of freedom in the temporal pulse profile which was available for incorporation into the LAS II system was the insertion of a variable time delay between different portions of the same pulse. This idea, more simply viewed as the sequencing of two or more pulses, allowed for the possibility of circumventing time-dependent optical breakdown mechanisms by allowing sufficient relaxation time between pulses for what had built up to a critical level to relax. If electron avalanche ionization were the dominant process, for example, this time could allow free electrons to relax back down into bound states. On the other hand, such a relaxation time would have no effect on self-focussing, since the nonlinear index change is essentially instantaneous. The idea of using sequenced pulses to avoid optical breakdown in fibers is directly analogous to the sequenced pulse ablation experiments described in section 5.3 above, in which it was observed that the tissue could not discriminate between pulses separated by up to several hundred ns. Thus, if the mechanisms responsible for fiber breakdown were found to relax more quickly than tissue, this effect could be taken to advantage. With this motivation, sequenced pulse breakdown studies were also conducted in fused silica.

7.2. Fused Silica Flat Optical Breakdown Studies

In order to characterize surface breakdown, self-focussing, the relaxation time between sequenced pulses, and the interaction between these processes in fused silica at $\lambda = 355$ nm, breakdown studies were carried out in both optical fibers and fused silica flats. Because of the difficulties and uncertainties associated with the polishing and preparation of optical fibers for testing, most quantitative tests of breakdown were performed on fused silica flats; the resulting trends were confirmed with a lesser number of optical fiber breakdown studies. These experiments were carried out using a single laser with a variable pulse duration, a substantial improvement over previous surface breakdown studies. Fused silica flat studies are described in the following subsections, while the optical fiber results are described in section 7.3.

7.2.1. Experimental Methods

The variable optical delay system described in detail in chapter 8 was employed to stretch the pulse duration from a frequency-tripled Nd:YAG laser a variable amount between 7.5 and 150 ns. The pulse delay network was passive, using internal refocussing to assure that the exit beam size and divergence were constant during each pulse. A second laser was aligned coaxial through the optical delay network with the first, and could be triggered to fire at any time relative to the first laser.

The experimental arrangement used is shown in Fig. 7.1. After passing through the optical delay network, laser beams were focussed onto a fused silica substrate with a two lens system designed to give a large depth of focus, to simplify positioning of the substrate. Two different focal spot diameters, 45 and 70 μm, were used in different pulse duration regimes. The spatial profile of the beam focus was measured with a reticon diode array for each focal diameter size. Light which passed through the substrate was viewed on a screen. When optical breakdown of the substrate occurred, the transmitted light pattern abruptly and permanently changed. The substrate used was Suprasil 2, polished to a flatness of 1/2 wave at 633 nm with 20-10 scratch-dig surface quality.

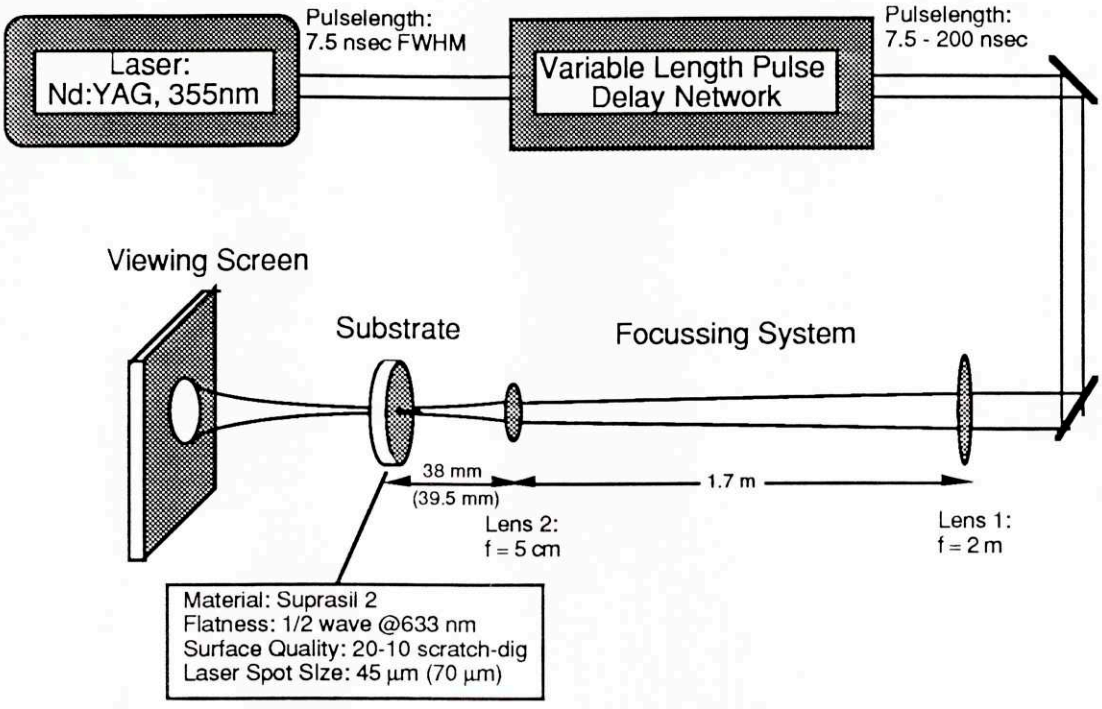

FIGURE 7.1. Experimental setup for the fused silica breakdown experiments.

7.2.2. Results and Discussion

In the first experiment, fluence breakdown threshold was measured as a function of pulse duration for pulse durations varying between 7.5 and 150 ns. At each value of pulse duration, at least five different fluences were tested. For each fluence tested, 100 shots were fired onto each of five different sites on the substrate, and the number of breakdown events was recorded. The number of damaged sites minus the number of undamaged sites at each fluence was plotted as a function of fluence. This data showed statistical variation, so for the purpose of obtaining breakdown threshold numbers and error bars it was fitted to a hyperbolic tangent function,

$$Y_{bkdn} = 5 \cdot \tanh[\, b \cdot (\phi - \phi_0)]. \qquad (7.5)$$

Here Y is the probability of breakdown, ϕ is the fluence, ϕ_0 the fluence at which 50% of sites break down, and b is related to the spread of the data. The experimental data for the 120 ns pulse duration, and the resulting data fit, are illustrated in Fig. 7.2.

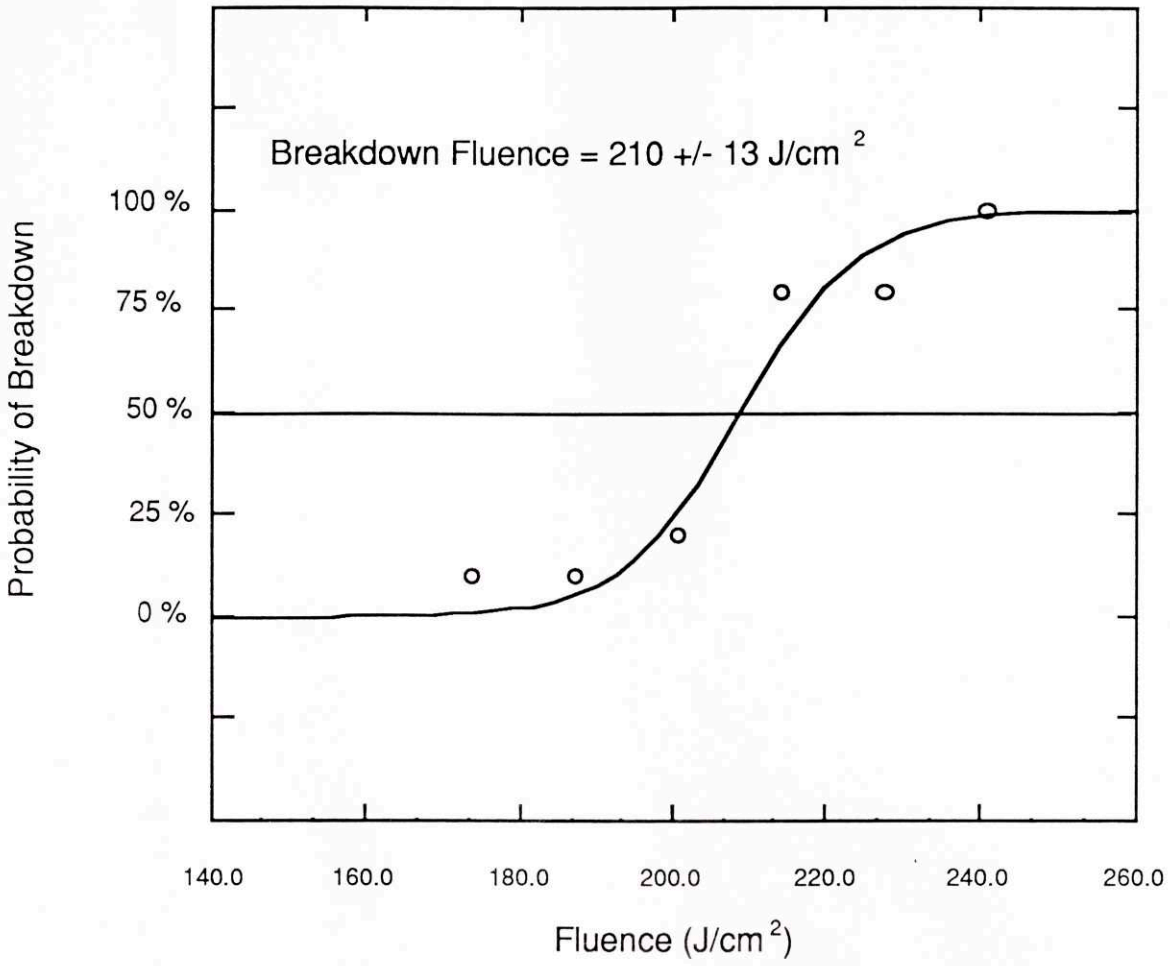

FIGURE 7.2. Fused silica breakdown data for the 120 ns pulse duration.

Figure 7.3 shows the results of breakdown fluence versus pulse duration. A reasonably good fit to the data was obtained by the equation shown on the figure, that breakdown fluence scales as pulse duration to the 0.85 power. No improvement in the quality of the fit was obtained by fitting the data to Eq. (7.2), indicating that the data is insufficient to distinguish between a simple power law and the more complicated equation predicted by electron avalanche ionization. This scaling is stronger with pulse duration than the results of previous studies mentioned above. Possible reasons for the difference are that two of those studies were conducted at wavelengths were only two photons are required to span the fused silica band gap, and the third was conducted in the near infrared, where breakdown mechanisms may be substantially different.

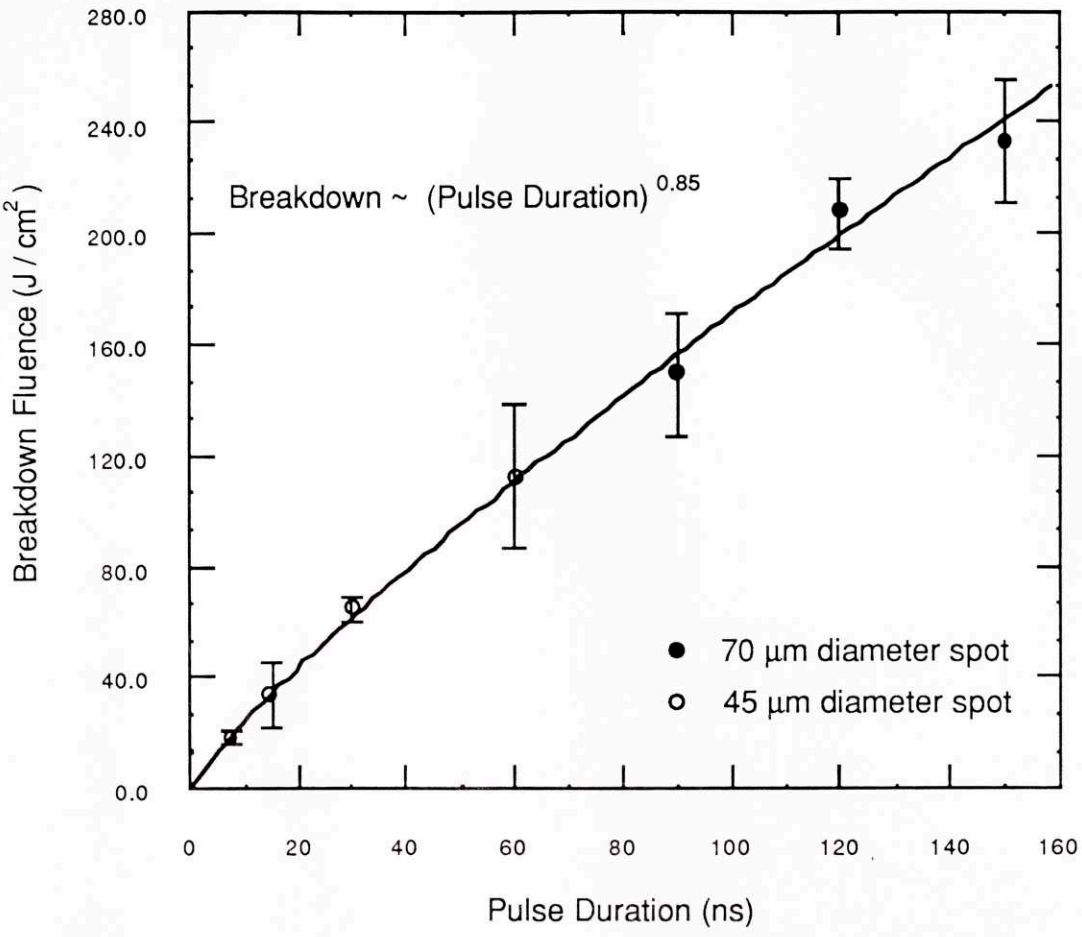

Figure 7.3. Plot of breakdown fluence versus pulse duration in fused silica at $\lambda = 355$ nm.

In a second experiment, the fluence breakdown threshold was determined for two 7.5 ns duration pulses as a function of the time separation between them. The results of this experiment are plotted in Fig. 7.4. What was measured by the experimental methodology in the first experiments was the fluence at which a single pulse would break down the substrate 50% of the time, so two such pulses separated by more than the recovery time should cause breakdown 75% of the time. Thus, the "total recovery" line in Fig. 7.4 is drawn at 3/2 the value of the single pulse breakdown value.

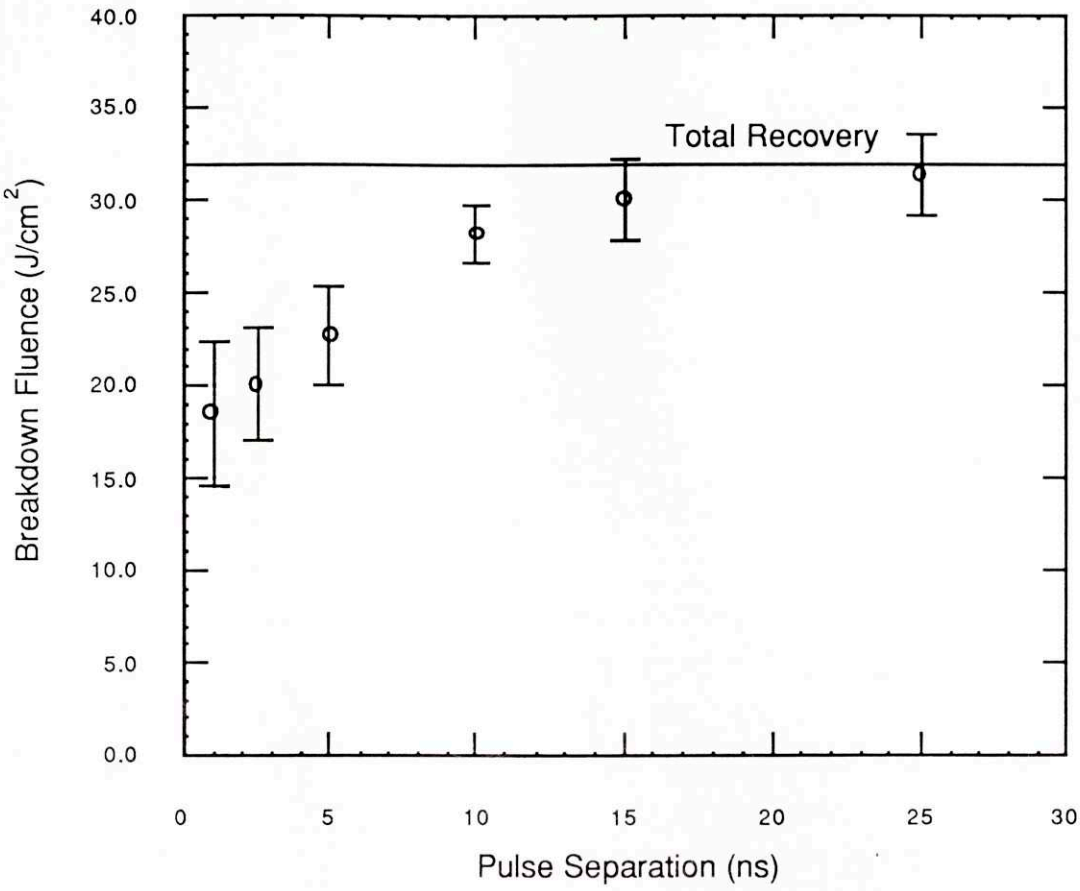

FIGURE 7.4. Breakdown fluence versus pulse separation for two 7.5 nsec duration pulses.

Since the pulses themselves were of 7.5 ns duration (FWHM), for pulse separations less than 7.5 ns the peak irradiance seen by the substrate was changing. For pulse separations between 7.5 and 15 ns, there was still some some overlap between the pulse tails. Thus, the irradiance seen by the substrate was a function of pulse separation up to 15 ns. The fact that the fluence breakdown threshold changed mostly in the first 7.5 ns, and then the rest of the way over the next 7.5 ns, confirms that the breakdown threshold depends much more strongly on irradiance than on recovery time. The only quantitative information gained about the recovery time of the material is that it appears to be less than ~25 ns. This observation is consistent with the electron-hole recombination time of 8 ns mentioned above [Hughes 78]. Even this information is very useful in practical applications, however, because it means that the fluence transmitted through the material can be effectively doubled if the energy is delivered in sequenced pulses separated by more than the recovery time.

7.3. Optical Fiber Breakdown Studies

Several problems accompanied breakdown studies in optical fibers which were not a factor in the fused silica substrate studies. While hundreds of sites with identical polish and preparation were available on each fused silica substrate, each fiber sample required individual preparation. Because of this, many fewer fiber samples could be tested, and the preparation of different samples was not guaranteed to be uniform. For these reasons, the data in this section represents a compilation of experience gained by several workers over approximately one year's time (primarily B. Banish and G. Hayes, assisted by the author and D. Albagli), rather than one carefully controlled study.

7.3.1. Experimental Methods

The optical fibers used in these studies were made of UV grade fused silica of 200 μm core diameter, encased in a 220 μm diameter hard cladding and a 245 μm diameter polyimide buffer. The fibers had a numerical aperture of 0.22. All fibers were polished on their input and output faces with a three-step process terminating with 0.05 μm grit alumina oxide polish. Experiments were also conducted with cleaved fiber faces. Fiber transmission was found to depend critically upon the surface preparation. In general, polished fibers performed best, even though there was substantial variation even among fibers prepared by the same worker.

All fiber results were obtained by imaging the central, homogenous portion of the laser beam onto a 170 μm diameter spot on the 200 μm core diameter fiber face. The fiber buffer coating was stripped away from the input end of the fiber for all experiments.

7.3.2. Results and Discussion

A compilation of results for energy transmission through 3 m lengths of 200 μm core fiber is presented in Table 7.2. Four different pulse profiles are listed in the table; single 7.5 ns duration pulses, a sequence of 6 x 7.5 ns pulses separated by 30 ns, singe 210 ns duration pulses, and two 210 ns duration pulses separated by 200 ns. Two transmission results are presented: the best result ever obtained, and a consistent working value.

Pulse Profile	Energy Throughput (mJ)	
	Best Value Ever	Consistent Working Value
Single 7.5 ns pulse	2.5	1.0 - 1.5
Train of 6 x 7.5 ns pulses separated by 30 ns	8.4	6.0
Single 210 ns pulse	15.7	12
Two 210 ns pulses with 200 ns separation	31	24

TABLE 7.2. Compilation of results for energy transmission through 200 μm core fused silica fibers at $\lambda = 355$ nm.

Several aspects of the data in Table 7.2 deserve comment. First, in many instances there was a qualitative change between the type of breakdown observed for the 7.5 ns duration pulses (single pulses or a train) and the 210 ns pulses (either one or two). In these cases, the location of the breakdown was several mm into the fiber in the case of 7.5 ns pulses, while breakdown was observed at the fiber face for the 210 ns duration pulses. This result probably indicates that self-focussing was occuring for some of the shorter pulses, while surface breakdown took over for longer pulses. This is consistent with predictions of self-focussing thresholds from the literature: the 1.5 mJ throughput result for a single 7.5 ns pulse corresponds to a power of ~200 kW, which is between P_1 and P_2 for self-focussing (see Table 7.1); while the 12 mJ throughput result for a single 210 ns pulse corresponds to a power of ~60 kW, well below P_1.

Secondly, the data in the table tends to confirm the result obtained in fused silica substrates that pulses separated by more than ~25 ns are completely independent. This was confirmed both with a train of 6 short pulses each separated by 30 ns, and by two long pulses separated by 200 ns. In both cases, the consistent working values for a train of pulses are just the sum of the working values for the individual pulses. The fact the "best ever" value for a train of 7.5 ns pulses is less than six times the value for a single pulse is most likely a reflection of the variability of single measurements.

A comparison of the fiber transmission results, converted into fluence units, and the scaling law obtained from fused silica substrates is illustrated in Fig. 7.5. It is seen in the figure that fiber breakdown obeys approximately the same scaling law as was obtained from the substrate experiments, although the fiber fluence breakdown thresholds are about

a factor of seven below the substrate results. Several factors may contribute to this difference. First, consistent working values are substantially less than 50% damage threshold probabilities, since working values are chosen to give many hours of operation without breakdown. Second, fiber numbers were calculated assuming a 200 μm diameter uniform spot on the fiber face, which is results in an underestimate of peak fluence. Finally, it is believed that a much better surface polish is available on the substrate than can be achieved on the fiber tips.

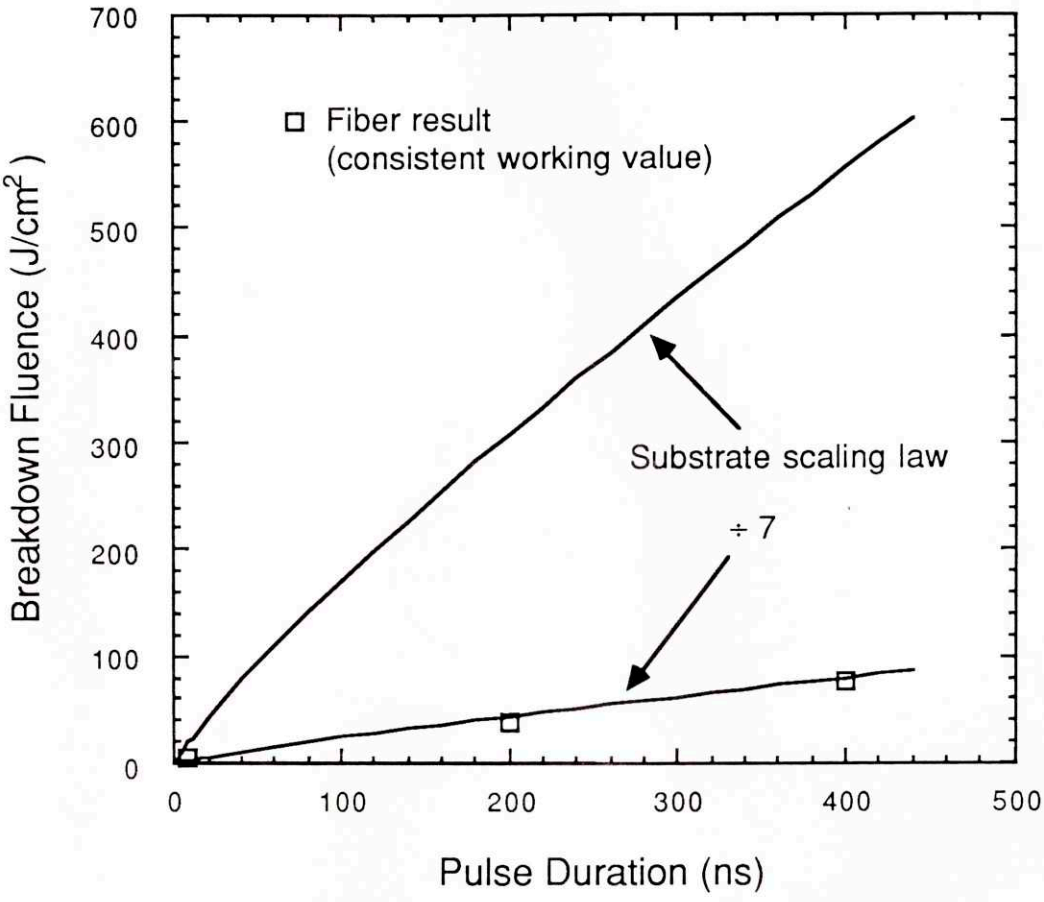

FIGURE 7.5. Comparison of fiber breakdown results with substrate scaling law (top curve), and substrate scaling law divided by 7 (bottom curve).

Fig. 7.6, contains a plot of the consistent working values for 200 μm core fiber transmission, compared with the estimated breakdown thresholds from self-focussing and surface breakdown. The self-focussing breakdown threshold was estimated by extrapolating from the 7.5 ns duration fiber breakdown number, which gives a reasonable critical power for self-focussing of 200 kW. The surface breakdown threshold was estimated by assuming that the fiber results have the same scaling with pulse duration as the

substrates but are a factor of 7 lower. These rough estimates are useful primarily for illustrating the role of the different breakdown mechanisms. As can be seen in the figure, it appears that for 200 μm core fibers there is no pulse duration range where self-focussing breakdown threshold should be lower that surface breakdown threshold. The macroscopic observations of self-focussing breakdown occurred in a region where the two thresholds are very close. For the pulse duration range of interest for ablation through the LAS II catheter, surface breakdown is the dominant mechanism.

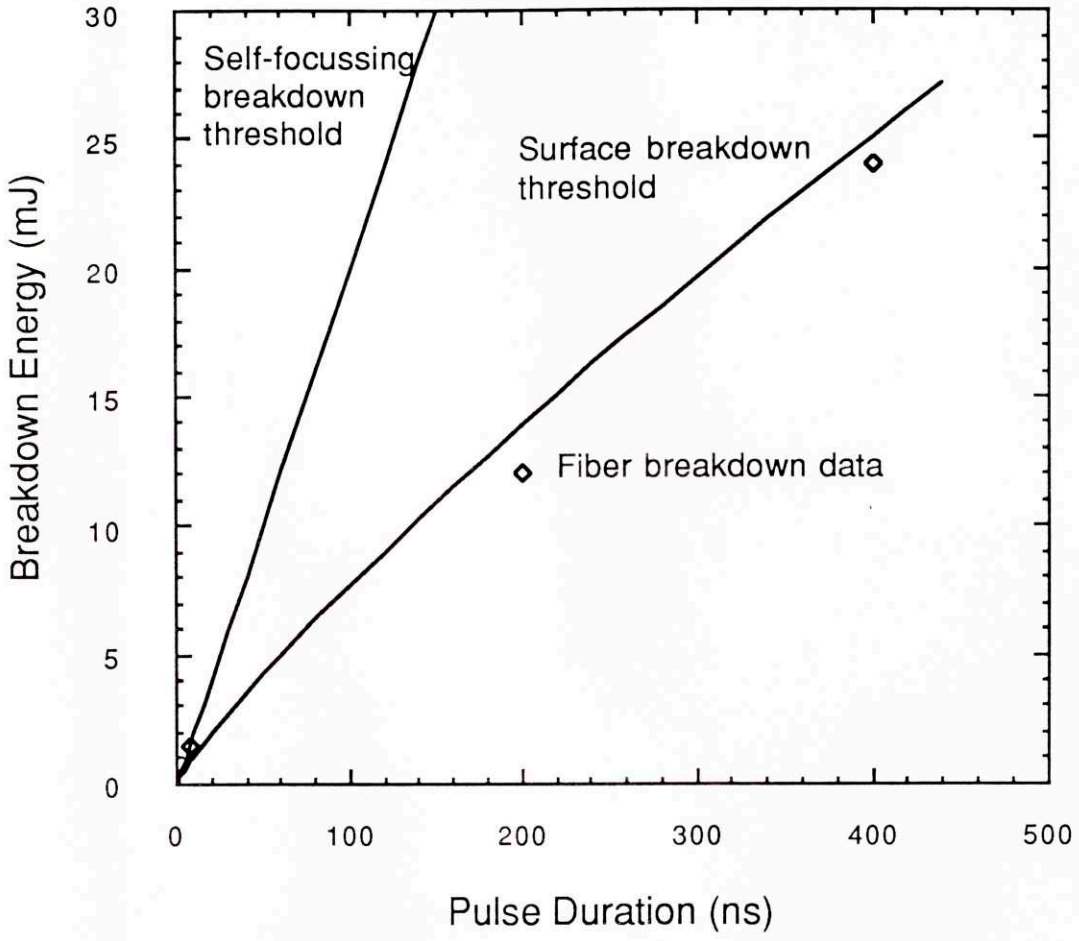

FIGURE 7.6. Consistent working fiber transmissions compared with estimated breakdown thresholds from self-focussing and surface breakdown.

The role of different breakdown mechanisms in fused silica at $\lambda = 355$ nm is further illustrated by the plot of pulse power at breakdown versus spot diameter in Fig. 7.7. The critical powers for self-focussing appear as horizontal lines on the graph. The curves for surface breakdown were obtained from the consistent working values for 200 μm core

fiber transmission, scaled with the 0.85 power scaling law. Curves are drawn in the plot for two values of pulse duration. As seen in the figure, for a 200 μm diameter spot, the short pulse duration is in the range for self-focussing, consistent with the observation reported above of a qualitatively different breakdown there.

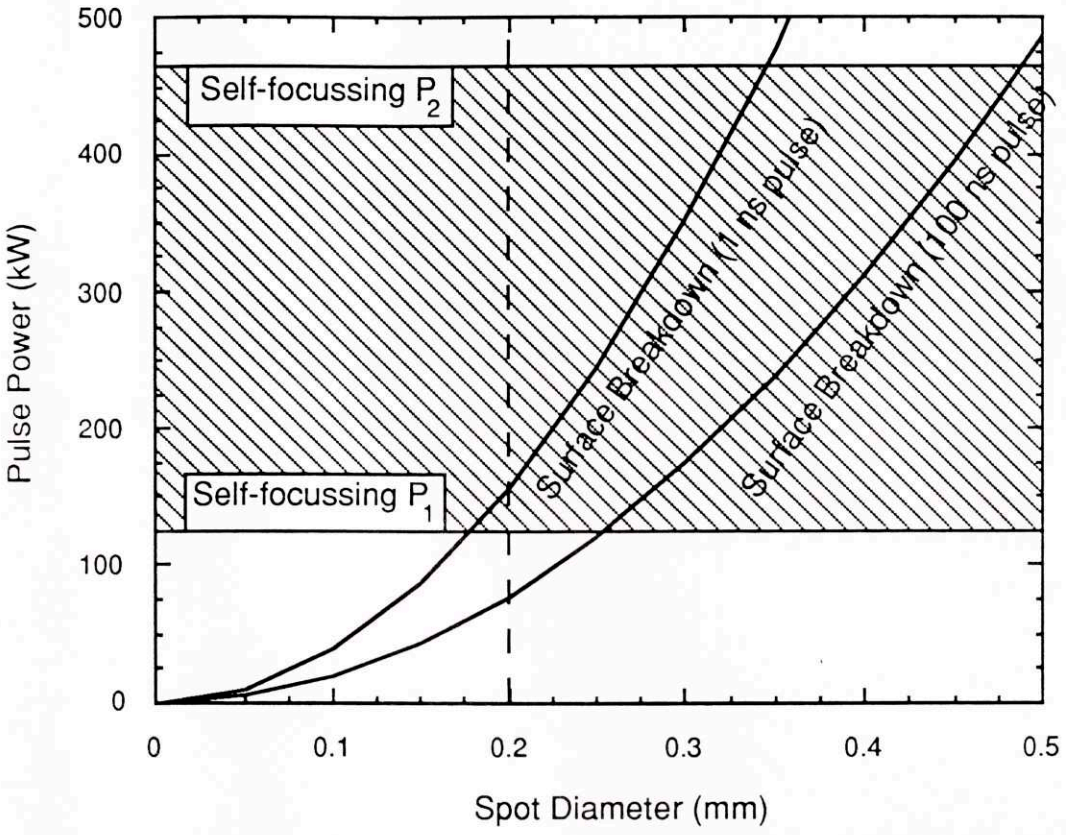

FIGURE 7.7. Illustration of the role of different breakdown mechanisms in fused silica as a function of spot diameter.

7.4. Conclusions

Two primary mechanisms have been identified for laser-induced breakdown in fused silica. These are self-focussing and surface breakdown. For 200 μm core fused silica diameter fibers at λ = 355 nm, surface breakdown appears to be the dominant mechanism, especially for pulse durations of a few hundred ns. Laser-induced surface breakdown was found to scale with pulse duration to the 0.85 power in the nsec regime. Sequenced pulses which are each just below fluence threshold for breakdown do not cause breakdown when they are separated by more than ~25 ns.

Chapter 8
Implementation of the LAS II System

In this chapter, the implementation of the LAS II system is described. First, an overview of the complete system is provided to serve as background, and to illustrate how ablation interacts with spectral diagnosis. Then, the implementation of the ablation subsystem is described in detail, including a description of the pulse stretching network which allows for conduction of high pulse energies through the optical fibers in the system. A detailed accounting of laser pulse energy transmission through the system is given.

8.1. LAS II System Overview

Figure 8.1 provides a block diagram of the LAS II system. The system has four principle components: the (disposable) catheter, the ablation subsystem, the spectroscopy subsystem (which performs fluorescence-based spectral diagnosis of tissue), and the computer. The computer interprets diagnostic information from the spectroscopy subsystem and controls the interaction between the other system components. The LAS II catheter was described qualtitatively in section 1.5 and quantitatively in section 6.2. The catheter is addressed by both the ablation and spectroscopy subsystems. Interfacing of both of the subsystems with the catheter is accomplished in the multiplexer, under computer control. The multiplexer is described in section 8.2.2. In order to describe how the subsystems interact in the catheter, a brief description of the spectral diagnosis technique used to identify pathogenic tissue is necessary.

The use of tissue fluorescence as a diagnostic tool for guidance of laser angiosurgery has been suggested by several authors [Cothren et al 86b, Leon et al 88, Fitzmaurice et al 89]. The analysis of atherosclerotic tissue autofluorescence has been a research topic in the MIT group for some time, and has culminated in the development of a model which describes the observed fluorescence spectra in terms of constituent tissue chromophores and absorbers [Richards-Kortum 89a, Richards-Kortum 88, Richards-Kortum 90]. In the LAS II spectroscopy subsystem, low-energy pulsed light at $\lambda = 476$ nm from a nitrogen-pumped dye laser is sequentially coupled into each of the 12 fibers in the LAS II catheter [Feld et al 91]. This coupling occurs in the multiplexer (see section 8.2). Tissue fluorescence which returns from the same fiber as the excitation light was sent

is dispersed by a monochromator onto an optical multichannel amplifier (OMA). Spectral signatures received in this way then fitted to the fluorescence model, yielding information about the relative concentration of three important arterial chromophores in the tissue in front of the catheter: structural proteins, ceroid and hemoglobin. This information is then converted into a classification of the tissue into normal, non-calcified plaque, or calcified plaque, and a degree of confidence in the classification.

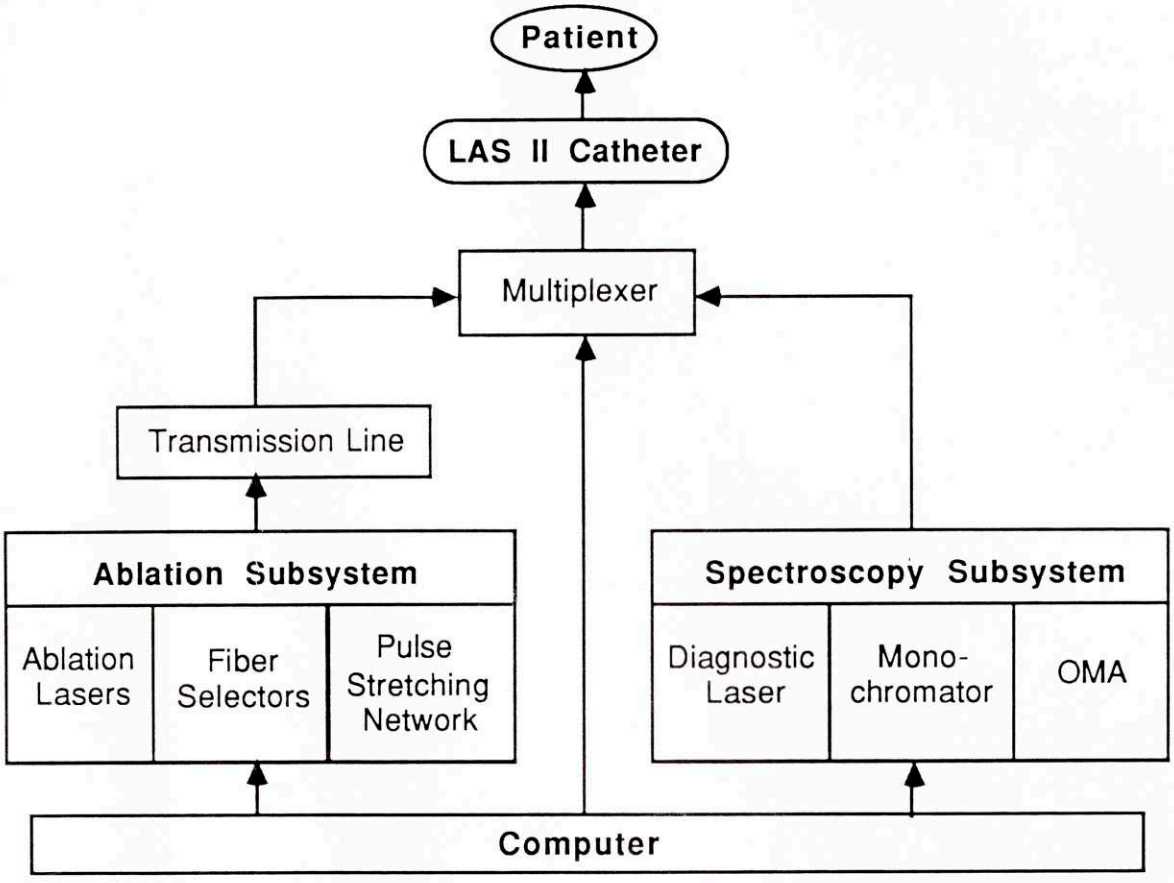

Figure 8.1. LAS II system block diagram.

Once the entire catheter face has been sampled spectroscopically, the resulting image is analyzed by the computer to determine which fibers should be fired upon with the ablation subsystem. The computer considers the contiguity of the classifications delivered by the spectroscopic subsystem and also the degrees of confidence. If three or more contiguous fibers are determined to be atherosclerotic, the computer calculates the "dose" of ablating light to be directed into those fibers from stored tissue ablation data for the type of plaque in front of that fiber group (see chapter 9). The dosimetry is adjusted to remove

approximately 100 μm of tissue before stopping to look again, insuring that ablation never overruns the look-ahead capability of the diagnostic (~500 μm). After ablation is done under the direction of the surgeon, control is returned to the spectroscopic subsystem, and the cycle is begun again.

8.2 Ablation Subsystem Engineering

The prototype LAS II system is built specifically to fit into space available in the operating suite of the Cleveland Clinic Hospital in Cleveland, Ohio. An important constraint on system design is that in this operating suite, the space which is available for the optical table holding the ablation laser is approximately 15 m removed from the operating table. It is impractical for the catheter to be this long, particularly since one end of it would have to extend out of the operating room. For this reason, the ablation subsystem incorporates an optical fiber transmission line which conducts laser light from the optical table into the operating room, where it is interfaced with the input end of the catheter (see section 8.2.2).

Based upon the catheter energy requirement calculations in section 6.2, and estimated losses in the catheter and transmission line, the design goal for consistent working value energy input to the fiber optic delivery system in LAS II was set at 28 mJ. Referring to Fig. 7.7, this requires a pulse duration on the order of 450 ns to avoid fiber breakdown. This energy transmission goal has been achieved using a novel optical delay system in which 7.5 ns duration pulses from two frequency-tripled Nd:YAG lasers are first stretched to 210 ns duration each, then sequenced 200 ns apart.

8.2.1 Waveform Engineering

This section describes the variable length pulse stretching network which not only is a primary feature of the LAS II ablation subsystem, but was also used to obtain the fused silica substrate and fiber optical breakdown results in chapter 7. This pulse stretching network has proved to be a unique and versatile tool for studying pulse length dependent phenomena. It can be set up to deliver top-hat pulse profiles variable in 7.5 ns increments from 7.5 to 30 ns duration, and in 30 nsec increments from 30 to 210 nsec duration. In addition, two separate lasers are aligned through the delay network, and may be sequenced with respect to each other with any time delay.

The pulse stretching network is entirely passive, containing only highly reflecting mirrors and beam splitters. The network in effect splits the input beam up into many

beamlets each containing a fraction of the original energy. It then sends each beamlet through a different path, and relies upon the speed of light in air to delay each beamlet relative to the rest. Finally, all of the beamlets are recombined. Importantly, each beam path is corrected for any divergence which occurs relative to the shortest path through the system. At the output all temporal components of the beam have the exactly the same size and divergence. This is especially important in experiments such as optical breakdown studies, where the spatial profile of the laser spot must not vary as a function of time during the laser pulse.

The pulse stretching network is surprisingly efficient. Each laser normally supplies 160 mJ in 7.5 ns pulses to the input of the delay network. At each of the two outputs, with the maximum stretching configuration set up (210 ns duration), 90 mJ pulses are routinely obtained. This corresponds to ~60% efficiency in a system which stretches pulse durations by a factor of 28. This efficiency is remarkable, given that the each pulse strikes between 27 and 80 optical surfaces. As will be seen in the next section, the average pulse strikes six 45° incidence reflectors, 33 0° incidence reflectors, and 15 anti-reflective coatings. The 60% throughput efficiency of the optical delay network is consistent with losses in these three types of optics of 1.5%, 1%, and 0.3%, respectively. Thus, although the concept of passive optical pulse stretching could probably have been described by Galileo, its realization depends on state-of-the-art mirror coating technology.

8.2.1.1. Pulse Filler

The first stage of the pulse stretching network is the pulse filler. The original suggestion for the pulse filler was from Dr. G.S. Janes. The filler takes up to two inputs and if no beams are blocked, it produces two outputs of 30 ns duration each. Figure 8.2 contains a schematic of the pulse filler. Light from the two different lasers enters the filler symmetrically through both sides of a 50% beam splitter. The laser beams are exactly overlapped on the beamsplitter in both position and direction, so that at all points later on they may be considered spatially coincident and colinear. Half of the light passing through the beamsplitter is directed by a flat mirror back to a second 50% beamsplitter. The other half of the light, however, is diverted an extra 7.5 feet before being directed back to the second beamsplitter. Thus, half the light reaching the second beamsplitter has been delayed by 7.5 ns. To compensate for divergence in the beam which travels the extra distance, the input of the extra 7.5 feet (optic #8) is optically imaged onto the output of the extra distance (optic #10) with three concave mirrors.

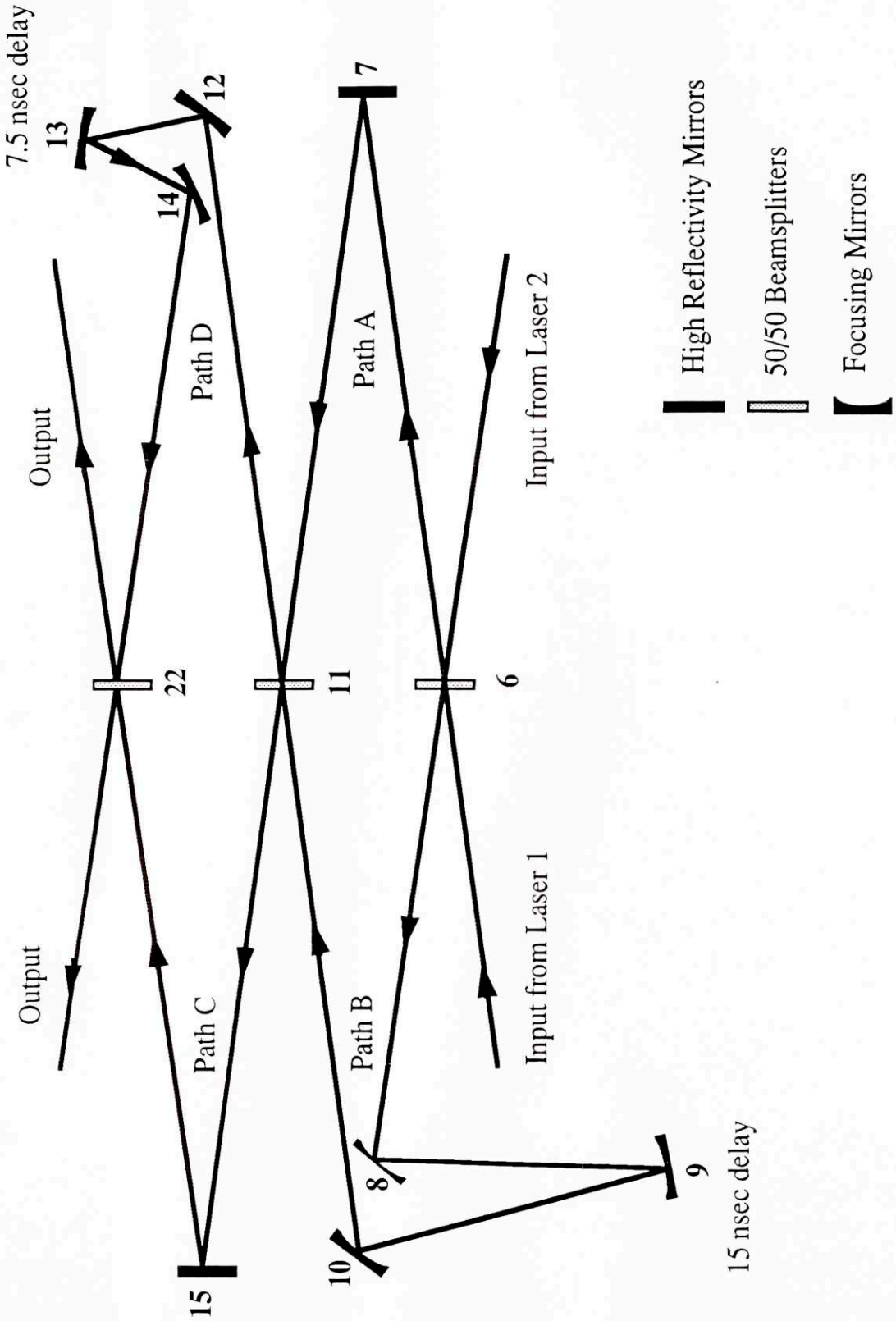

FIGURE 8.2. Schematic of the pulse filler.

The second part of the filler is exactly analogous to the first, except that this time the delay in the longer path is 15 ns. Thus, the two beams exiting the third beamsplitter are each 30 ns duration. Alternatively, since each 7.5 ns duration beamlet travels along a different spatial path, it may be blocked, yielding any desired combination of 7.5 ns duration pulses at the output.

Close examination of Fig. 8.2 reveals that the filler cannot be constructed in on a flat surface while maintaining the necessary symmetric inputs on all of the beamsplitters to avoid abberrations. To actually construct the beamsplitter it was necessary to go into three dimensions, as illustrated schematically for the case of only one input beam in Fig. 8.3.

Figure 8.4 contains an oscilloscope trace of one 7.5 ns duration pulse, the output of the tripled Nd:YAG lasers. Figure 8.5 is a trace of a completely filled, 30 ns duration pulse obtained at the filler output.

8.2.1.2. Pulse Extender

The second stage of the pulse stretching network is the pulse extender, schematically illustrated in Fig. 8.6. The pulse extender is a commercial product sold by Excitech Inc., which was designed to take as input a single pulse, and to output a train of six equal amplitude pulses, each separated by 30 ns, plus an exponentially decreasing tail. The pulse extender contains eleven focussing mirrors (M1 - M11) and six beamsplitters (R1 - R6) of varying reflectivity between 10% (R1) and 100% (R6). The beam splitters are sequentially spaced along an optical path at 30 foot intervals. Their reflectivities are chosen so that the six primary reflected beams are of equal amplitude. The focussing mirrors serve to fold the long optical path so that it fits in a reasonably sized box, and also to correct for beam divergence by re-imaging the light from each beamsplitter onto the next. The entrance optics, consisting of a input lens and one focussing mirror, double the beam spot size on the first beamsplitter to avoid optical damage on it and all subsequent optics.

A particularly tricky problem arose in attempting to propagate both beams coming out of the pulse filler through the extender at the same time. It was soon realized that any number of beams could be propagated through the extender, as long as they were spatially coincident on the beam splitters, and still passed through all limiting apertures. Thus, two beams were successfully passed through by bringing them to cross at a distance in front of the stretcher such that the crossing point would be re-imaged by the input lens onto the first beamsplitter mirror. Then, that image of the crossing point automatically be re-imaged onto

each subsequent beamsplitter. The only restriction on this scheme was that the angle of the beams heading into the first crossing point had to be small enough so that both beams passed through the extender input lens; this was accomplished with the aid of a beam diverting wedge which was inserted into one of the beams.

Figure 8.7 contains an oscilloscope trace of the output of the pulse extender, given a single 7.5 ns duration pulse as input. As can be seen in the figure, the first pulse of the exponential decay (the seventh pulse) is as high as the average of the first six pulses. Figure 8.8 illustrates the output of the extender given a single 30 ns pulse as input; a fairly uniform, 210 ns duration pulse is the result. Finally, the pulse profile resulting from sequencing two 210 ns duration pulses separated by 200 ns is shown in Fig. 8.9. This pulse profile has successfully transmitted 30 mJ down a 200 μm core fused silica fiber without breakdown (see section 7.3.2).

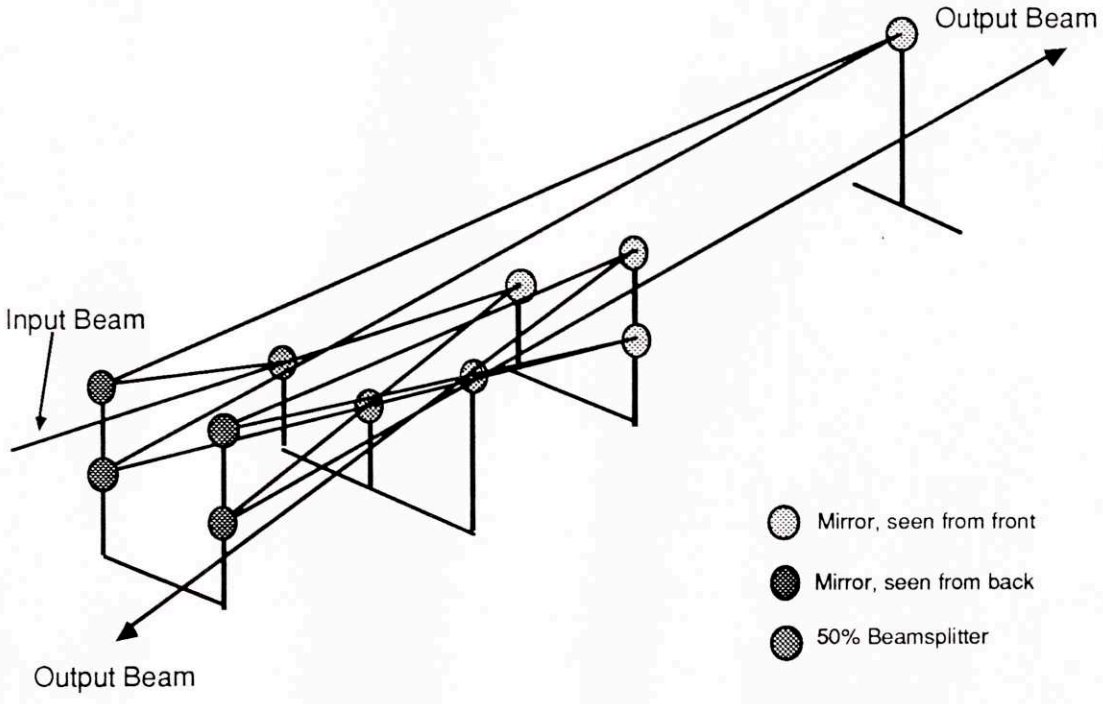

FIGURE 8.3. Three-dimensional filler schematic for one input beam.

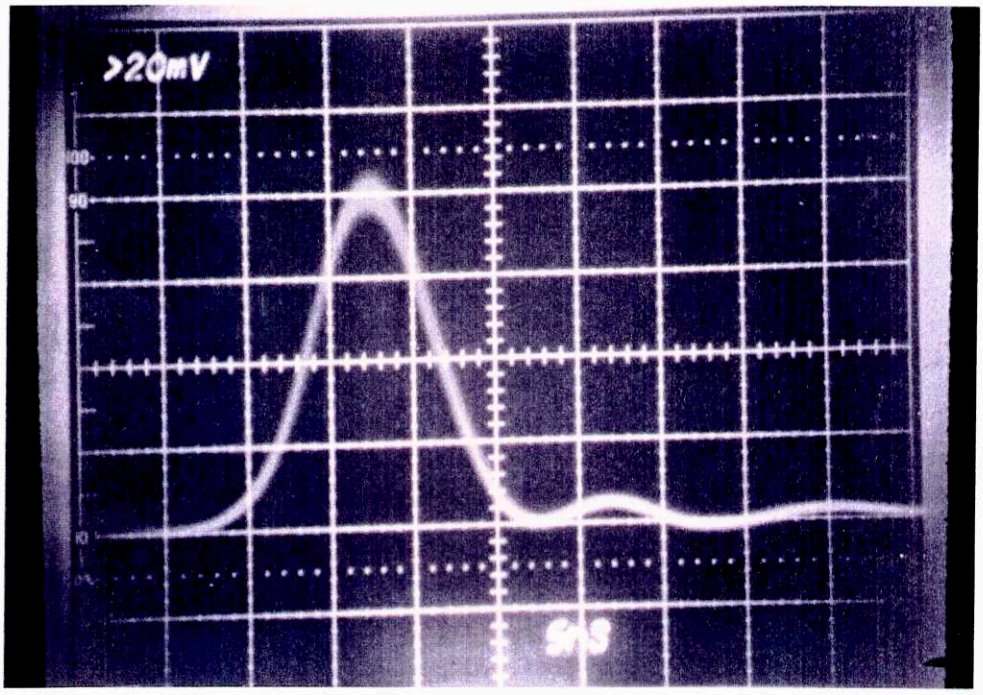

FIGURE 8.4. Oscilloscope trace of a single 7.5 ns duration pulse.

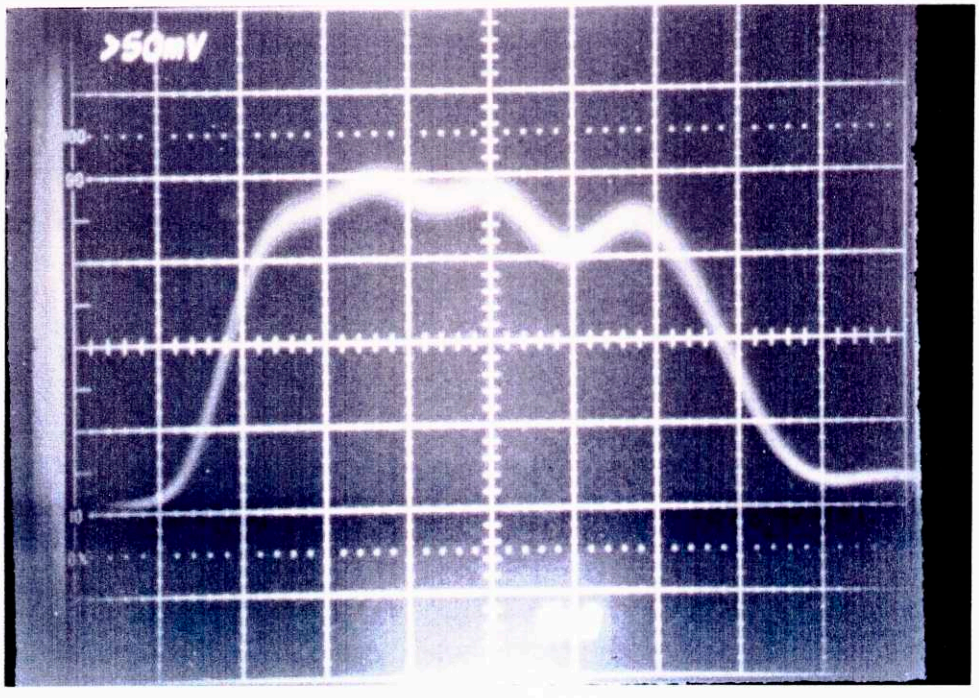

FIGURE 8.5. Oscilloscope trace of a 30 ns duration pulse exiting the filler.

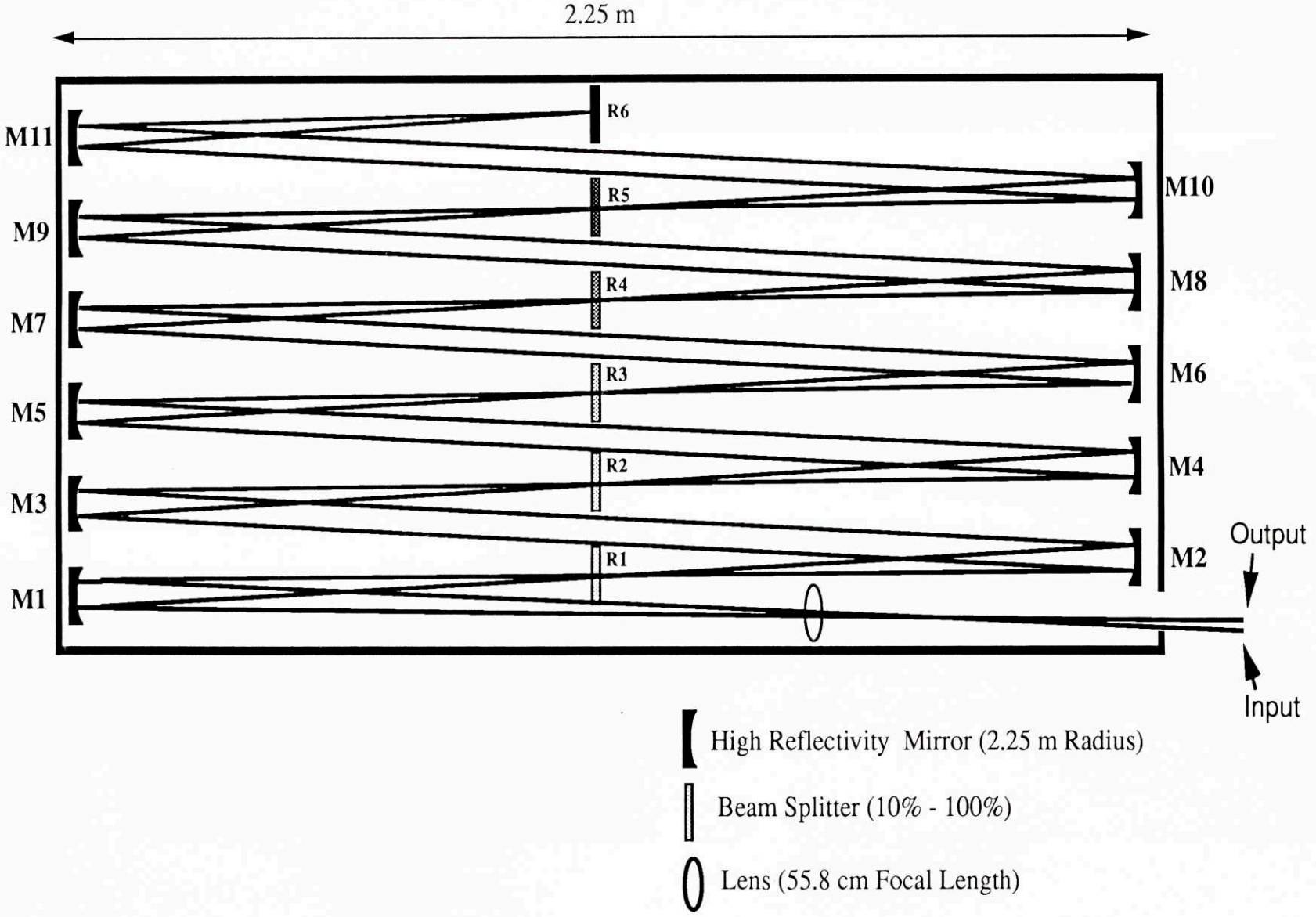

FIGURE 8.6. Schematic of pulse extender.

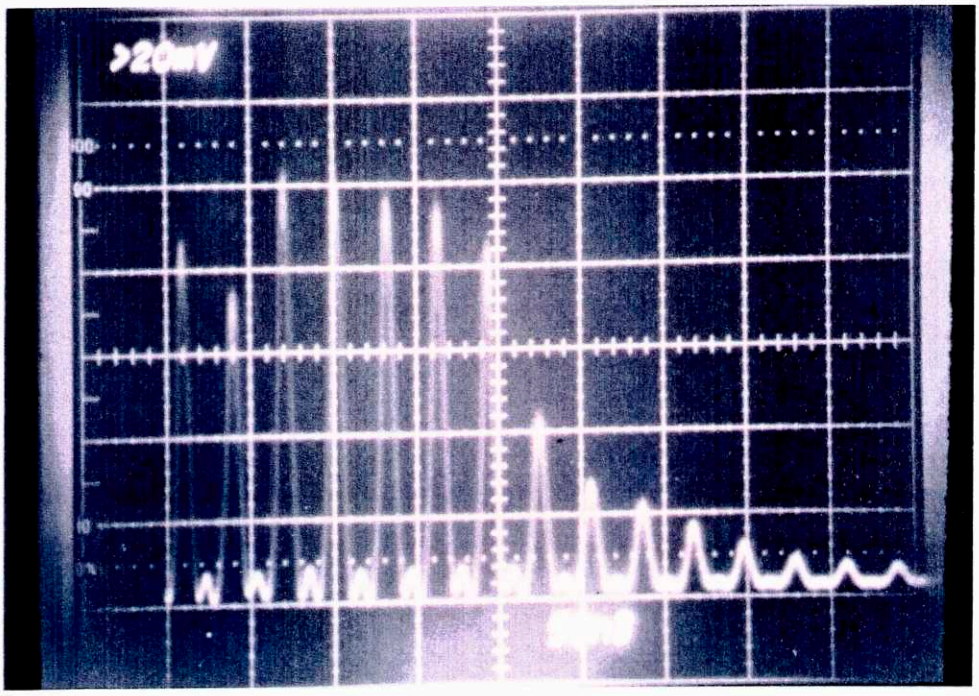

FIGURE 8.7. Oscilloscope trace of pulse extender output for a 7.5 ns duration input pulse.

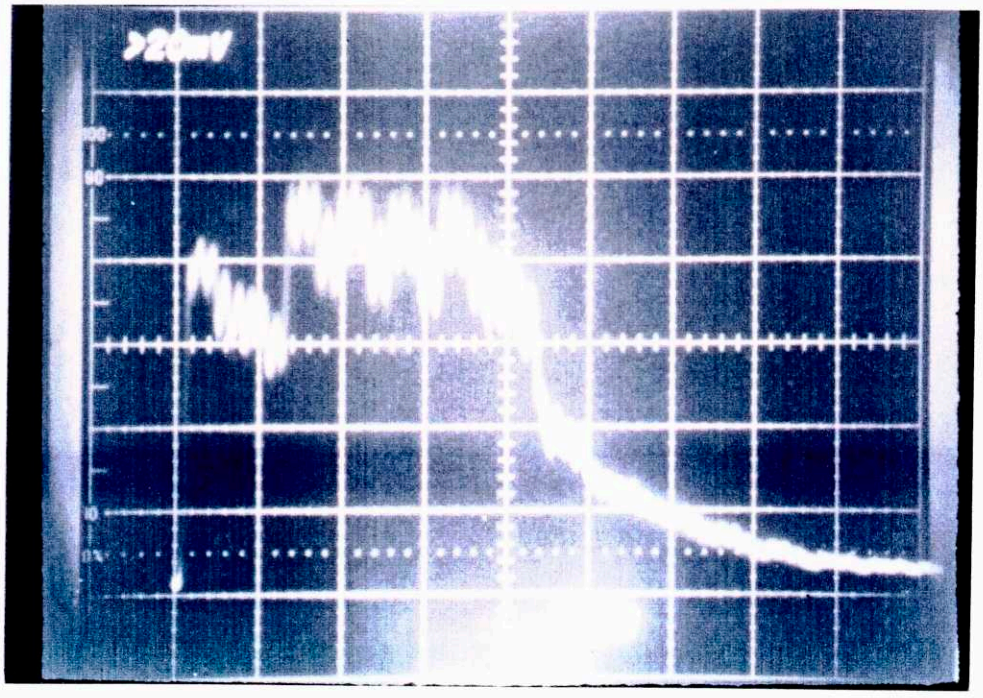

FIGURE 8.8. Oscilloscope trace of pulse extender output for a 30 ns duration input pulse.

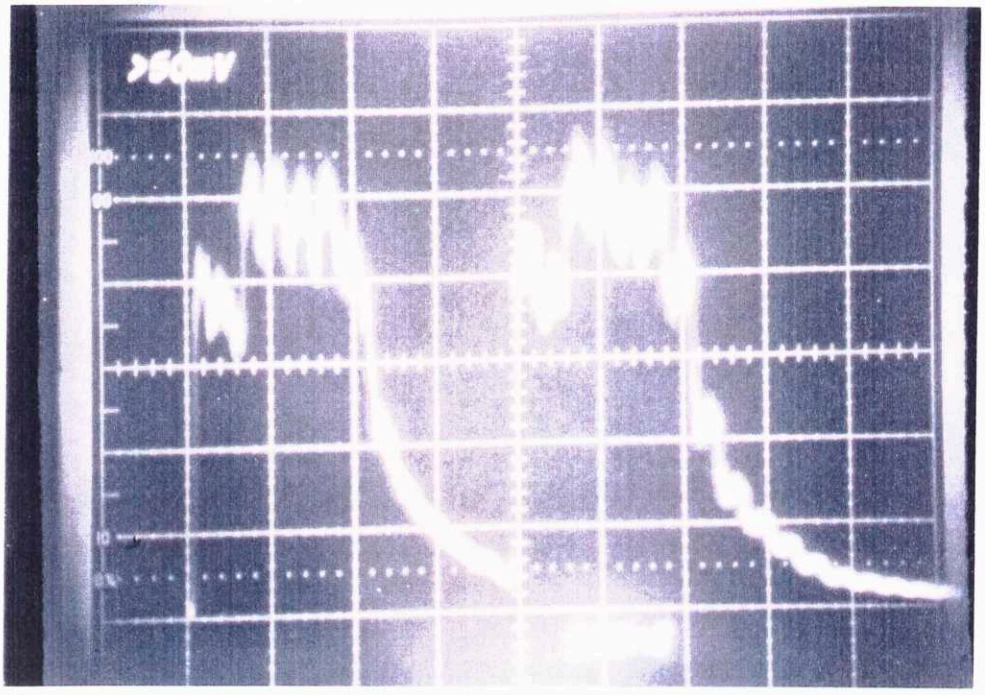

FIGURE 8.9. Oscilloscope trace of pulse extender output for two 30 ns duration input pulses separated by 400 ns.

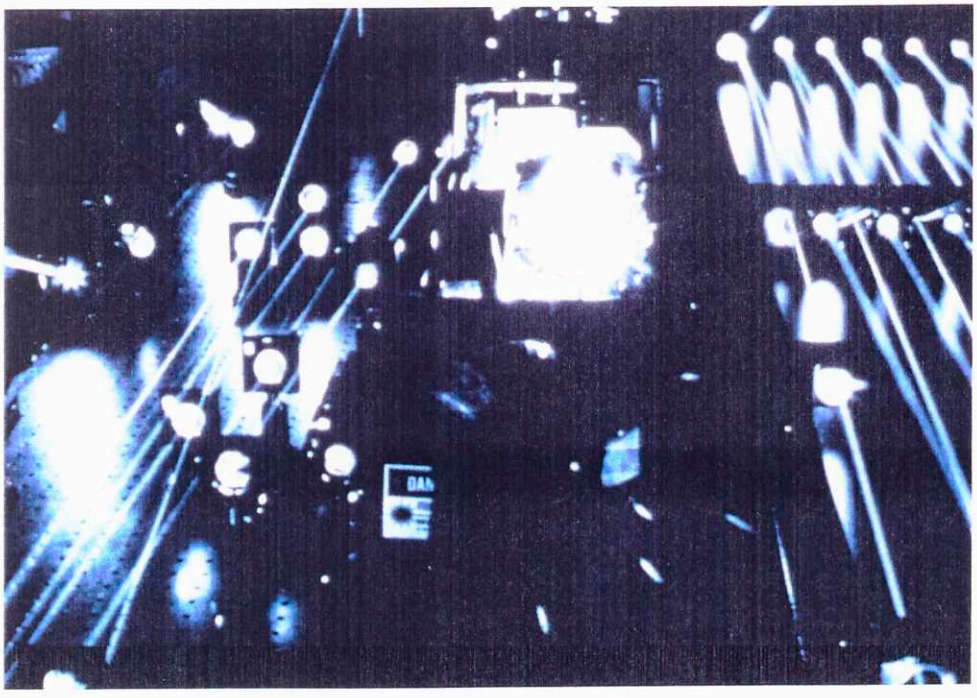

Figure 8.11. Photograph of the lasers/filler/extender table in operation taken in a darkened room with ultraviolet-sensitive film.

8.2.2. Ablation Subsystem Implementation

The ablation subsystem consists of four primary components and the interfaces between them: the lasers, the pulse stretching network, the transmission line, and the catheter (which is considered a component of both subsystems). This section describes how each of these components are implemented to give the system the capabilities described in section 8.1.

The ablation lasers and the pulse stretching network fit onto a single 5' x 8' optical table. The layout of components on the table is shown in Fig. 8.10. Two Continuum model NY-61 tripled Nd:YAG lasers operating at 10 Hz and producing 7.5 ns duration pulses of 160 mJ energy per pulse each are located near the center of the table. Using a Stanford Research Pulse Generator, the Q-switch of one of the lasers is set to fire 400 ns after the other. This delay is set longer than necessary from fiber breakdown considerations to reduce the probability of jitter in the Q-switch trigger causing both lasers to fire simultaneously, which would cause optical breakdown throughout the system.

Taking into account all of the losses throughout the system, the pulse energy generated by the two lasers is sufficient to illuminate four catheter fibers simultaneously. Thus, the transmission line, which runs from the lasers/pulse stretcher optical table into the operating room, contains only four fibers. Control over which of the catheter fibers are illuminated is exerted in two ways. First, the computer chooses which of the twelve catheter fibers the transmission line illuminates; this switching occurs at the transmission line-catheter interface (multiplexer). Second, the computer selects which of the transmission line fibers are illuminated by activating solenoid-controlled shutters on the lasers/pulse stretcher table.

Directly in front of each laser are located two shutters, one controlled by the computer and the other controlled by the surgeon via a foot switch in the operating room. Two additional computer-controlled solenoids containing partially reflecting mirrors are located slightly further along the optical path. These mirrors can be switched into the beam, directing the laser light into a power meter for monitoring. When the power meter solenoids are not activated, the beams from the two lasers pass into the pulse filler. The numbers assigned to the optical elements in the filler in Fig. 8.10 correspond to their numbering in Fig. 8.2. Note that the last beam splitter in the filler is separated from the rest of the filler by optics leading to the pulse extender. This is done for ease of alignment of the system,

and because it was the only way to fit all of the necessary components onto one 5' x 8' table. Upon exiting from the extender, the two beams are finally mixed in the last beam splitter of the filler. At this point the beams have obtained their final temporal profile, illustrated by the oscilloscope trace in Fig. 8.11.

The final section of table splits the two output beams of the filler/extender system into four equal beams, focuses them into the four transmission lines, and selectively controls which fibers are illuminated. The first function is performed with two more 50% beam splitters. Light is coupled into the transmission line fibers by re-imaging and demagnifying the beam exiting the last beam splitter of the filler to a 600 μm diameter spot on the surface of each transmission line fiber. This task is accomplished for each fiber by a two-element imaging system which accomplishes the demagnification with a very small fiber entrance numerical aperture (0.02) in a relatively small space. The third function is accomplished with four more solenoid-driven opaque shutters placed in front of each transmission line fiber holder, which may selectively block any beam under computer control.

A photograph of the lasers/pulse stretcher optical table taken in a darkened room with ultraviolet-sensitive film is reproduced in Fig. 8.11. The photograph was taken from the same perspective as Fig. 8.10, with the lasers in the center, the filler on the left, and the extender on the right. The photograph amply demonstrates the complexity of the many folded optical paths.

The transmission line is comprised of four 15 m long optical fibers which taper in diameter from 800 μm at the input end to 200 μm at the output. Tapered fibers were chosen for the transmission line for several reasons. First, the large input face provides a bigger target and is much more forgiving of small misalignments on the lasers/pulse stretcher table. Second, while sufficient energy was at one point conducted down a single 200 μm core diameter fiber to serve as a transmission line (see table 7.2), this was accomplished only when the most uniform portion of the laser beam was imaged onto the fiber face. Use of a tapered fiber allows the entire beam to be coupled into the transmission line without exceeding breakdown fluence at the center. In addition, the tapered fiber itself serves as a beam homogenizer for the catheter fiber inputs. The only cost is that light must be coupled into the tapered fiber at a sufficiently small solid angle so that the light which emerges still couples into the catheter fibers, even though the numerical aperture of the light grows in the taper. This is accomplished, as described above, by coupling into the transmission line at a numerical aperture of 0.02. The light typically emerges from the transmission line at a numerical aperture of 0.20, smaller than the 0.22 numerical aperture of the catheter fibers.

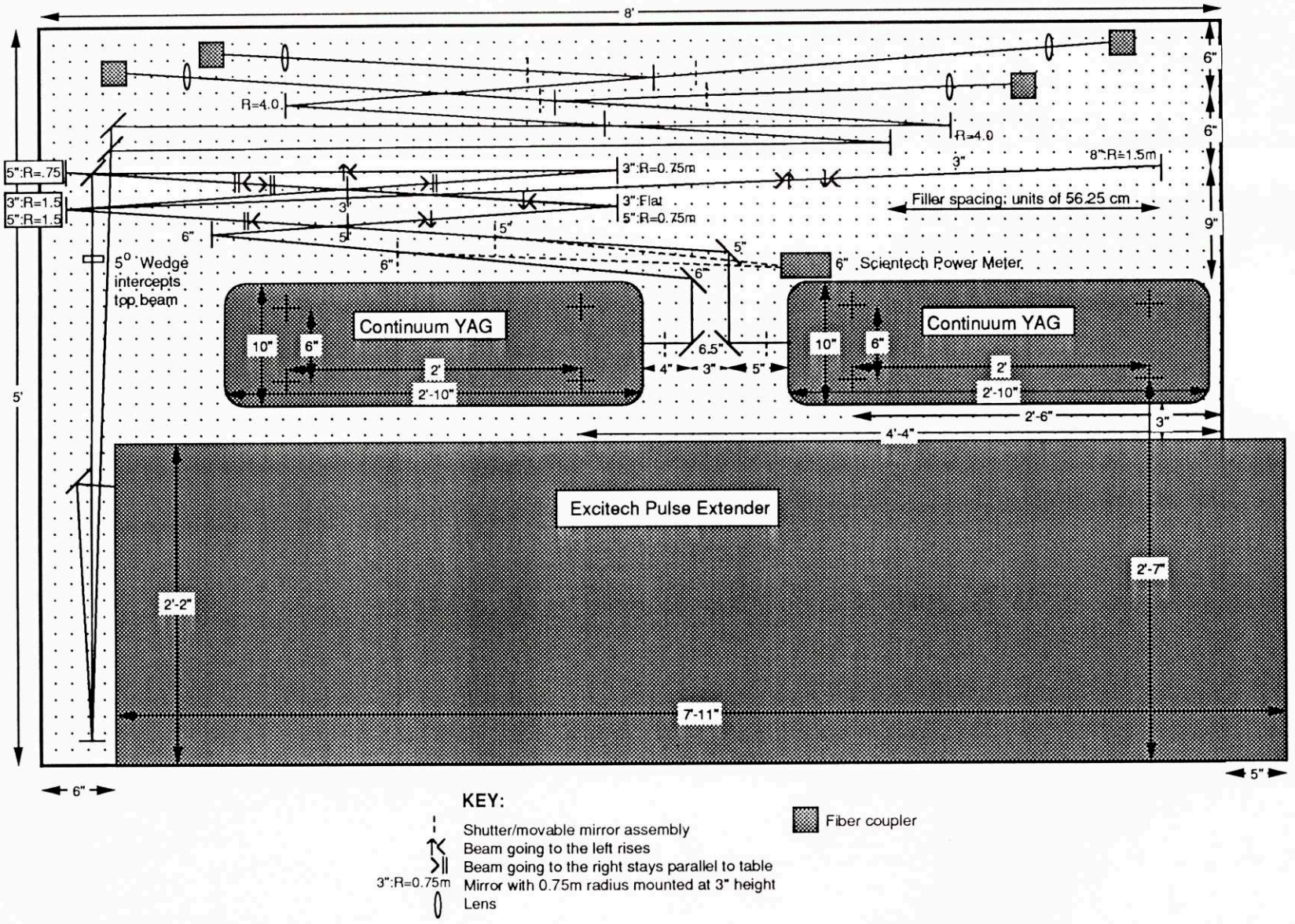

FIGURE 8.10. Layout of the lasers/pulse stretcher optical table.

The transmission line-catheter interface, or multiplexer, is illustrated in Fig. 8.12. At the output end of the transmission line, the four transmission line fibers plus a spectroscopy fiber are fastened in a linear array. This array is attached to a computerized, motorized translator which moves in the direction shown. The catheter fibers are also fixed in a linear array parallel to the transmission line array. Coupling of the light from the transmission line to the catheter is obtained by bringing the opposing fiber arrays to 100 μm axial separation. As will be described below, this direct illumination coupling technique is quite efficient. Selection of which catheter fibers are illuminated by the transmission line is obtained by linear motion of the translator. Thus, the computer can fire any desired fiber or set of fibers by positioning the transmission line in front of the catheter fibers of interest, and then firing the desired transmission line fibers by opening the appropriate shutters on the lasers/pulse stretcher table.

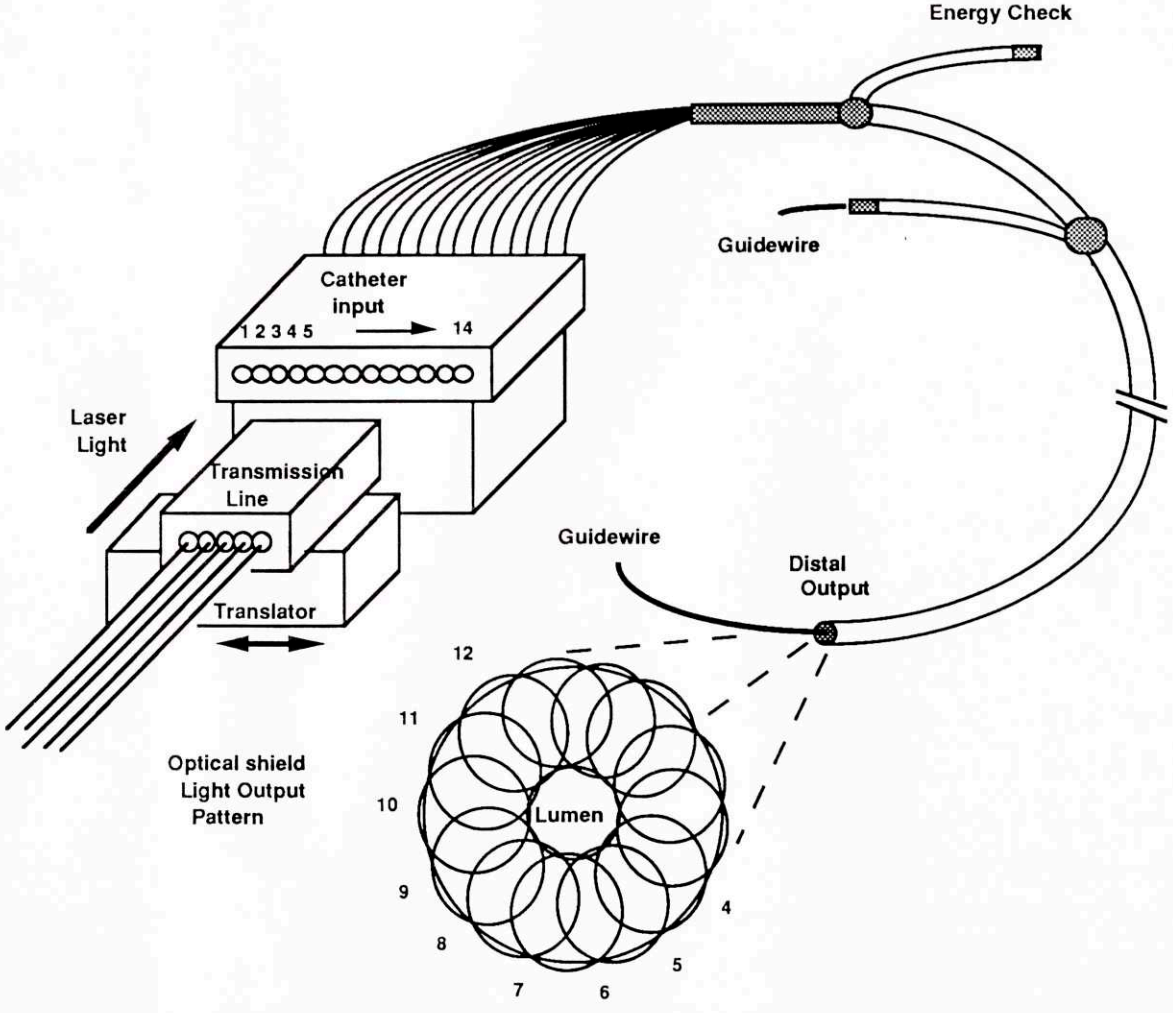

Figure 8.12. Schematic of transmission line-catheter interface [Hayes 91].

The catheter input end has 14 fibers fixed in a linear array. The middle twelve fibers in the array are the ablation fibers, while the two extra fibers on the array ends are used for power and alignment checking. The LAS II catheter is approximately 3 m long and incorporates a guidewire. The output end of the catheter has already been described in section 1.5.

Finally, the computer controls the solenoid-driven shutters and the translator at the transmission line-catheter input interface. The computer illuminates the twelve catheter fibers in three separate groups of four. Three variables control the way energy is delivered through the catheter. The energy delivered per fiber is denoted by E. This is set by varying the Q-switch delay in the lasers, and is not altered during an ablation sequence. The number of shots which are fired through a group (4 or less) of catheter fibers before moving on to the next group is n. Finally, the number of times all three groups are sequentially fired is called the number of rounds, m. Both of these latter quantities are available to the computer for adjustment according to the dosimetry required.

8.2.3. Energy Budget

An accounting of the energy losses throughout the ablation subsystem is provided in Table 8.1. The first three columns list energy per pulse measurements taken at the output of each subsystem section. The fourth column lists the number of outputs each section has, leading to the fifth column which is the total energy present at all corresponding locations. Finally, the last column lists the percentage energy lost in the section just completed.

The first loss of 41% occurs in the pulse stretching network, and it has already been described as remarkably low given the number of optical surfaces encountered by each beam in the network. The second loss, 40%, occurs in the transmission line. About 8% of this loss is due to Fresnel reflections at the silica-air interfaces at both ends of the fibers. The remaining loss is primarily due to absorption in the fiber core material itself. The final loss of 40% occurs in the catheter. This loss has three components. First, there is some loss associated with the direct fiber-to-fiber coupling, since some of the light exiting each transmission line fiber misses the corresponding catheter fiber. This loss is relatively small, however; under ideal conditions it has been measured to be as small as a few percent, while the typical working value seems to be closer to about 10-15%. The second catheter loss is about 12% due to three Fresnel reflections, one each at the input of each fiber, the output of each fiber, and the internal air-shield interface. Since the catheter shield normally operates

in contact with tissue, the outer edge of the shield is usually indexed-matched to the tissue. The remaining catheter loss of about 10% is absorption loss in the fiber.

Measurement location	Best value ever measured (mJ)	Consistent working value (mJ)	Number of locations	Total energy in system (mJ)	Through -put in section %
Laser output	175	160	2 lasers	320	-
Output of filler/extender	53	47	4 output arms	188	59
Output of transmission line	32	28	4 transmission. line fibers	112	60
Catheter output	24	16	4 illuminated catheter fibers	64	60

TABLE 8.1. Trace of energy losses throughout the ablation subsystem.

It is seen from Table 8.1 that the ablation subsystem delivers 64 mJ of energy to the tissue, out of the total 320 mJ output from the lasers. This represents an overall throughput efficiency of 20%. This efficiency could be improved in future systems. First, elimination of the transmission line by moving the optical table into the operating room would remove some, but not all, of the 40% lost there. It would not remove the entire loss because the taper in the transmission line also acts as a beam homogenizer for the input of the catheter fibers. The total loss in the transmission line could only be recouped if the catheter fibers themselves had tapers, or if another, lossless beam homogenizer could be built. The energy lost in the pulse stretching network, and quite a bit of space as well, could be saved if a laser were obtained which emitted long pulses without the need for external pulse stretching.

8.4 Conclusions

A novel two-stage passive pulse stretcher has been designed and built to stretch the 7.5 nsec duration pulses from two Q-switched Nd:YAG lasers to 210 nsec each, while maintaining high beam quality. When these stretched pulses are sequenced ~200 nsec apart, sufficient long-pulse laser energy is available to simultaneously illuminate 4 out of the 12

catheter fibers. A computer-controlled opto-mechanical switching and multiplexing system fires the fibers which the spectral diagnosis system has previously interrogated, and identified as pointing at pathogenic tissue.

Chapter 9
Dosimetry with the LAS II System

In this chapter, the initial in vitro ablation dosimetry studies with the LAS II system are described.

9.1. Experimental Design

One of the first tasks in characterizing ablation dosimetry involves isolating those variables which are critical to system performance. The experimental variables available for dosimetry testing with the LAS II catheter are listed in Table 9.1. These variables are divided into three levels, where the level structure defines the interaction between the variables. The primary variables are the categories of tissue to be studied; for every major tissue type dosimetry information is required as a function of all of the other categories of variables. The secondary variables represent the degrees of freedom of energy delivery through the catheter, each of which controls the fluence delivered to the tissue in a different way (see Table 9.1). This redundancy preserves the freedom to readjust treatment protocols if necessary; for example, if the highest fiber energies are found in clinical trials to cause intolerable tissue dissection, the same tissue volume can be removed at lower fiber energy through adjustment of the other variables. The tertiary variables represent information which is critical to dosimetry testing, but not necessarily for every combination of the other variables.

Since the LAS II system is designed for coronary laser angiosurgery, it was not necessary to test ablation in aorta. Aorta was included, however, because dosimetry testing was much simpler and more reproducible in aorta, and insufficient coronary tissue was available for full testing of all of the necessary variables. In addition, although the structure of normal aorta is elastic rather than muscular like coronary tissue, the structure of soft and hard plaque in both tissues is thought to be identical. Aorta was thus the primary tissue studied, while selected comparative tests were performed in coronary artery.

All three secondary variables could not be examined independently of the other two for each tissue type. The number of catheter rounds, m_{round}, was chosen as the quantity most likely to be linearly proportional to crater depth. Then for each tissue type, a matrix of

craters was made by varying n_{fiber} on one axis, and E_{fiber} on the other. The ranges of n_{fiber} and E_{fiber} values were chosen so that crater depths on the order of 100 μm per round would be drilled. The entire range of values for n_{fiber} and E_{fiber} were tested in aorta, while only selected critical values were tested in coronary artery. This two-dimensional approach was designed both to establish the reciprocity relationship between n_{fiber} and E_{fiber}, and also as a mechanism of gathering a large quantity of depth versus fluence data. The highest pulse energy per fiber available in this study was 16 mJ. In a separate experiment, the linearity of crater depth versus m was tested in normal aorta.

Variable Level	Variable	Symbol	Range of Values
Primary	Tissue Type		• Aorta: normal, fatty/fibrous plaque, calcified plaque • Coronary: normal, fatty/fibrous plaque, calcified plaque • Thrombus
Secondary (determines total fluence)	Energy per Fiber	E_{fiber}	8-16 mJ
	Number of Shots	n_{fiber}	5-60
	Number of Rounds	m_{round}	1-5
Tertiary	Number of Pixels		3-12
	Catheter Force		5-30 gm
	Histology		• Cutting quality, peripheral damage
	Ablation Media		• Saline • Iced cardioplegia (no blood) • Iced cardioplegia (with blood) • Blood
	Ablation Debris		• Particle size range • Particle composition

TABLE 9.1. Variables for in vitro catheter ablation testing.

The tertiary variables were probed in separate experiments. All experiments described in the previous paragraph were done by illuminating all 12 catheter fibers, and advancing the catheter between rounds to a constant force of 10 gm. 10 gm was selected as the nominal applied force after several different people tried holding the catheter onto the scale with what seemed to them light force, and it was sufficient to hold the often slippery or unevenly shaped tissue steady during the experiment. Ablation with just 3 fibers illuminated was probed by ablating one row and one column of the matrix mentioned above for only one round. The dependence of the crater depth on the force with which the catheter

was pressed onto the tissue surface was probed in an experiment on normal aorta. Ablation at a selection of secondary variable values was performed in coronary artery samples, which were subsequently fixed in formalin and sent for histological analysis. All experiments were performed under iced, clear cardioplegia obtained from the Cleveland Clinic Foundation.

9.2. Ablation Crater Characteristics

The LAS II system has ablated all tissue types on which it has been attempted, from normal soft tissue to rock-hard calcified plaque. Ablation occurs only when at least two adjacent fibers were fired at the same time, as anticipated in section 6.2. When two fibers are fired, a slit-shaped overlap ablation pattern is not observed, but rather almost the entire region illuminated by both fibers is ablated. When an entire catheter round is fired, a complete cylinder of tissue is removed in soft tissue, except for a plug of tissue at the crater bottom. The plug of tissue appears to be the tissue in front of the guidewire lumen, which actually enters the lumen during ablation. In some calcified tissue craters, whole cylinders of tissue are removed, but other craters exhibit bridges of tissue between the outer diameter and the central plug. These bridges appear at the locations of the three gaps in between the four adjacent fibers which are fired simultaneously. It has been demonstrated that by dithering the fiber firing sequence, so that different sets of four fibers are fired each round, all but one of these tissue bridges can be eliminated. The one remaining bridge is between the first and last fiber on the transmission line-catheter interface translator, since it is never possible to illuminate those two fibers at the same time.

Full catheter craters at 90° incidence in normal aorta and coronary artery had the most complicated shape of all craters observed. Figure 9.1 illustrates a typical normal tissue crater profile, with all of the relevant crater characterization parameters noted. Figure 9.2 is a photograph of a full catheter crater in normal aorta. The typical normal tissue crater was cylindrically shaped, with a ridge of tissue surrounding the crater opening and a plug of tissue at the center of the crater bottom. Crater widths (W1) were typically 1000-1500 μm, while ridge ring widths (W2) were 1500-2000 μm. Ridges could be up to a few hundred μm in height (H2). Crater depths (H1) varied with the ablation energy, and were in the range 200-1000 μm. The lumen plug was typically ~500 μm in diameter (W3) and up to 500 μm tall (H3), in tissue which had been dried with a paper towel for crater measurement. It was found that after ~10 minutes of soaking in cardioplegia, the lumen plug could swell in size to fill almost the entire crater.

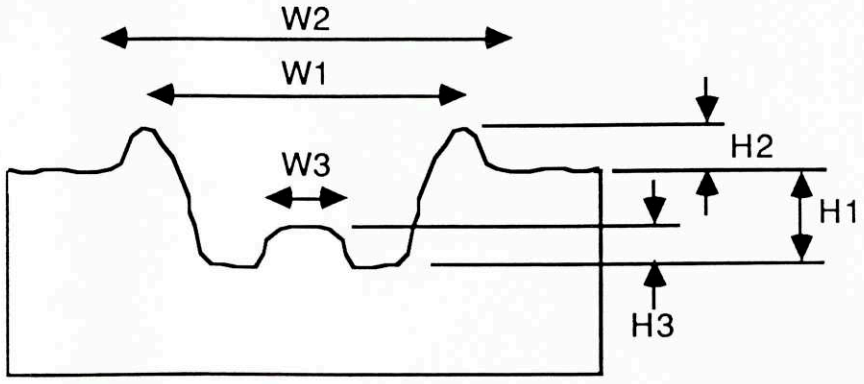

FIGURE 9.1. Normal tissue crater characterization.

Normal tissue craters varied in appearance with their depth. Experiments done with the lowest energy (8.5 mJ), or with low numbers of shots per crater, did not make a single crater, but rather three oblong-shaped slits, in positions directly beneath the three four-fiber groups which were fired. Craters with depths between ~200-600 μm were very cleanly cut, with flat bottoms and a profile similar to the sketch in Fig. 9.1. Craters with depths greater that ~800 μm were more ragged in shape, often partially closing up. This was particularly true in coronary artery samples.

Craters made in fibrous/fatty tissue had no ridges around the crater tops, and were generally more roughly cut and more likely to partially re-close before measurement. Some craters only a few hundred μm deep were not circular. Once again, craters in coronary tissue were generally rougher than their counterparts in aorta. Figure 9.3 is a photograph of full catheter craters made in fibrous/fatty coronary artery.

Excellent craters were made in both aorta and coronary artery calcified tissue samples. Hard tissue craters were always very cleanly cut and cylindrical in shape, typically 1300-1500 μm in diameter with a 500 μm diameter lumen plug. Some fracturing at the tissue surface was occasionally observed, particularly in inhomogenously calcified samples. Large debris granules (~10-100 μm diameter) were observed in some calcified aorta craters. Figure 9.4 is a photograph of a full catheter crater made in aortic calcified plaque.

Ablation in all tissue types was accompanied by an audible crack, following which bubbles of vapor emerged from the catheter tip area and rose to the cardioplegia surface. Ablation also produced a pronounced catheter jerking movement along its axis, predominantly in calcified tissue.

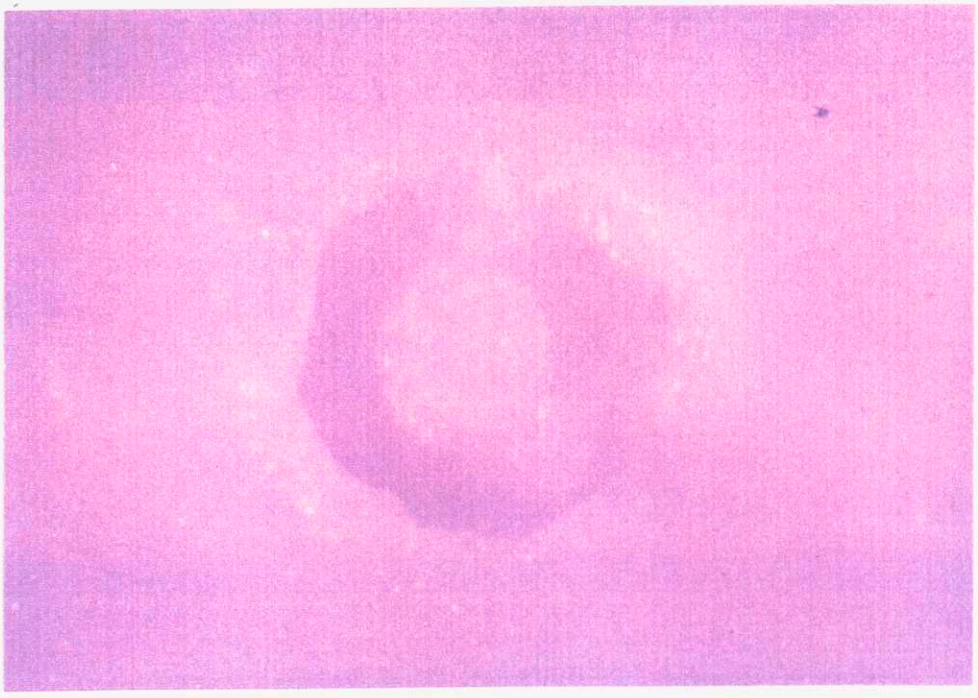

FIGURE 9.2. Full catheter crater in normal aorta. Ablation parameters: E_{fiber} = 13.5 mJ, n_{fiber} = 3, m_{round} = 5.

FIGURE 9.3. Full catheter craters in fibrous/fatty coronary artery. Ablation parameters: E_{fiber}(bottom left crater) = 15 mJ, E_{fiber}(other craters) = 11 mJ, n_{fiber} = 10, m_{round} = 3.

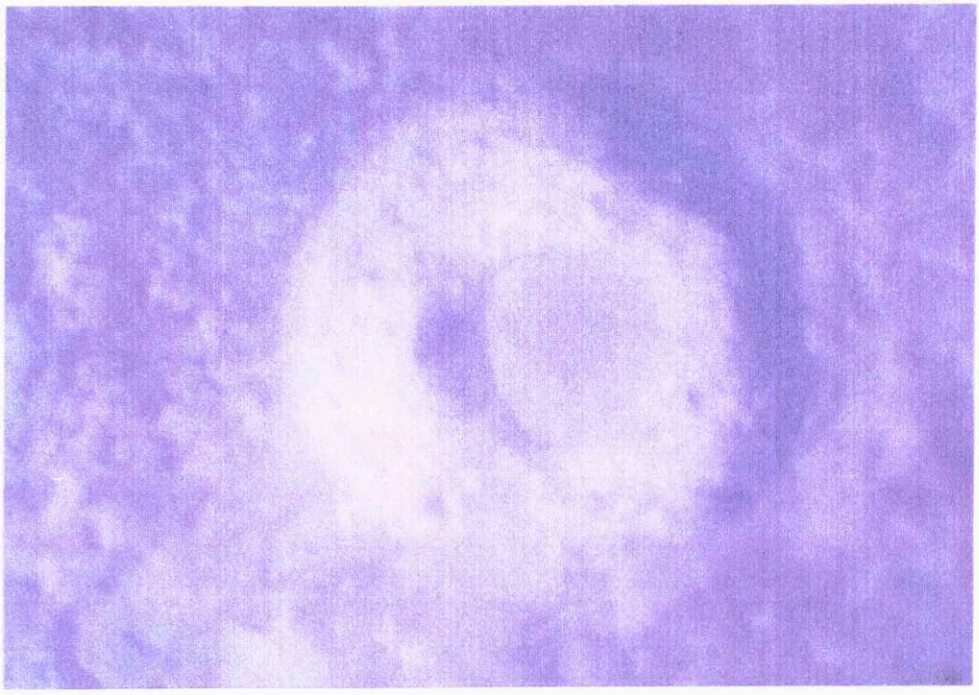

FIGURE 9.4. Full catheter crater in aortic calcified plaque. Ablation parameters: E_{fiber} = 13.5 mJ, n_{fiber} = 60, m_{round} = 5.

9.3. Dosimetry Results

9.3.1. Full Catheter E_{fiber}–n_{fiber} Reciprocity Study

The most extensive catheter dosimetry study examined crater depth as a function of both E_{fiber}, the energy per shot and n_{fiber}, the number of shots per fiber. Plots of depth versus energy per fiber are plotted in Figs. 9.5 and 9.6 for aorta and coronary artery, respectively. In Fig. 9.5, the data from different values of n_{fiber} were averaged at each fluence for each tissue type. The standard deviation with n for each fluence appears as error bars in the aorta data figure. As will be discussed below, this is a reasonable approximation given the scatter of the data.

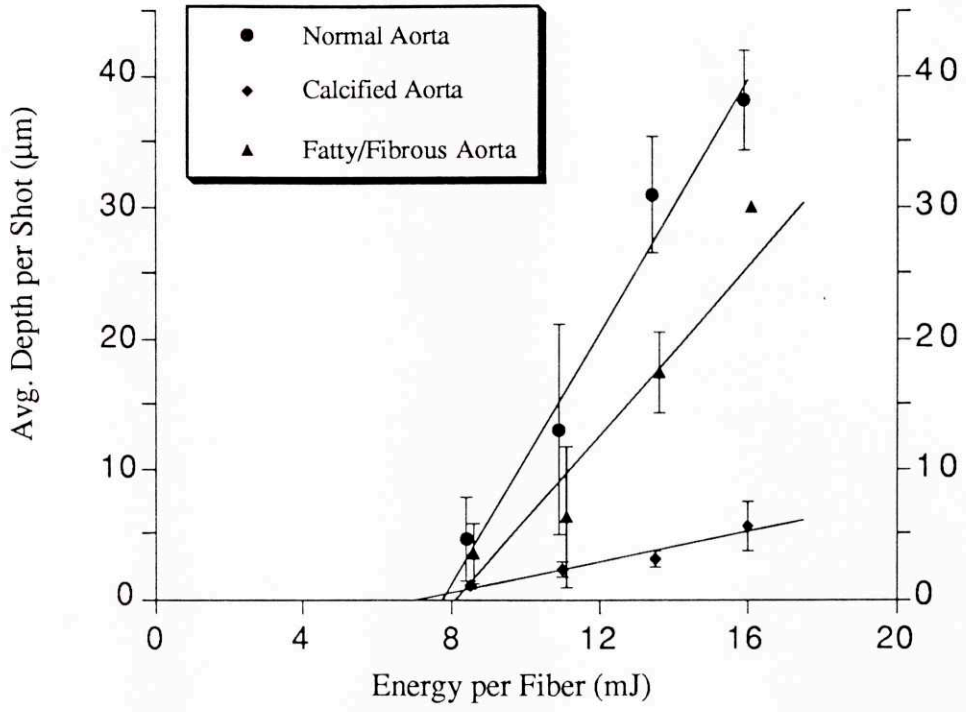

FIGURE 9.5. Dosimetry data for aorta. Three rounds were fired in soft tissue; five rounds in calcified tissue. The number of shots per fiber per round varied from 5 to 60.

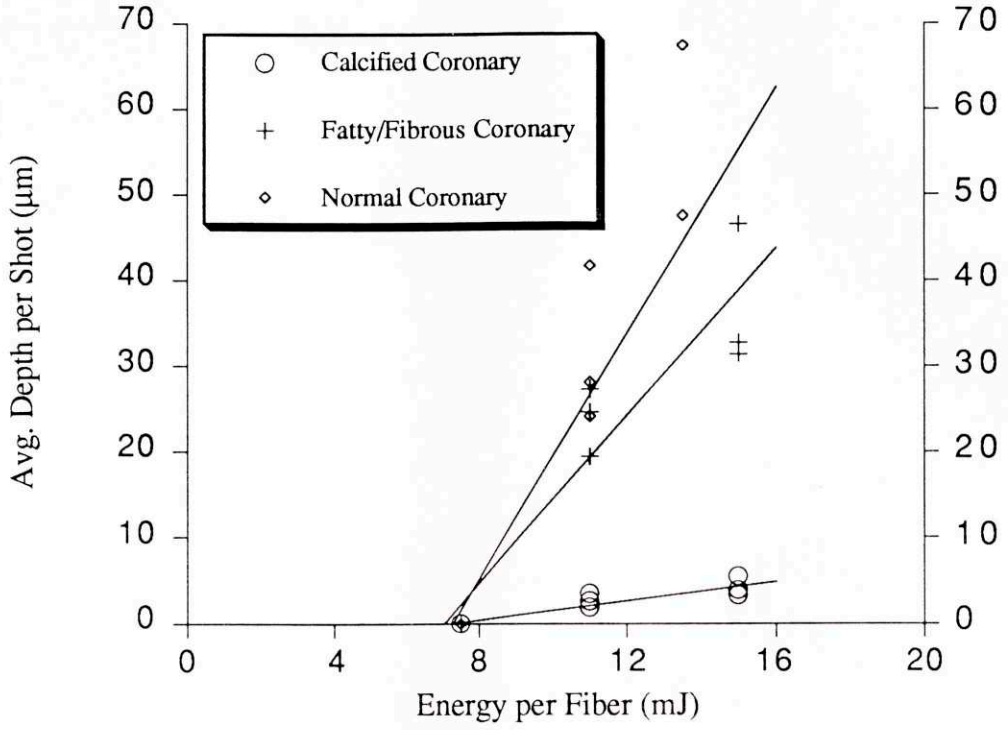

FIGURE 9.6. Dosimetry data for coronary artery. Three rounds were fired in soft tissue; five rounds in calcified tissue. The number of shots per fiber per round varied from 5 to 60.

The fluence at the catheter tip was estimated from the measured quantities of energy exiting the catheter per fiber by assuming the light from each fiber expanded to a 500 μm diameter spot on the catheter surface.

The results of straight-line fits of the depth versus energy data for values of threshold fluence, ϕ_0, and ablation yield, Y, are summarized in Table 9.1. Threshold fluences for all tissue types and sources were consistently near 70 mJ/mm^2, very close to the values measured for bovine bone, reported in chapter 4. Recall from section 4.7 that fluence threshold was not expected to change between different tissues. Ablation yields, on the other hand, showed considerable variation. For both aorta and coronary artery, yields in soft plaque were ~5-10 times yields in calcified plaque, and yields in normal tissue were ~1.5 times yields in soft plaque (consistent with the results of section 4.6). Yields in aorta calcified plaque were similar to yields in coronary artery calcified plaque, while yields in the other tissue types in coronary artery were ~1.5 times yields in aorta. Yields in both calcified aorta and calcified coronary were very similar to the yield reported for bone in chapter 4.

Tissue Type	Tissue Source	Number of Shots per Fiber, n_{fiber}	Fluence Threshold, ϕ_0 (mJ/mm^2)	Ablation Yield, Y (mm^3/J)
Normal	Aorta	5-20	78	0.48
	Coronary	5-20	73	0.72
Fibrous/Fatty	Aorta	5-20	81	0.32
	Coronary	5-20	70	0.49
Calcified	Aorta	15	68	0.08
		30	76	0.07
		45	70	0.05
		60	48	0.03
	Coronary	30	71	0.06
	Bovine Bone*	10	70	0.07

*estimated from data in chapter 4.

TABLE 9.1. Results of E_{fiber}–n_{fiber} reciprocity study.

Table 9.1 also describes the dependence of crater depth on the combination of energy per fiber and shots per fiber used to construct the fluence which was delivered per round. For normal and soft plaque tissues from both sources, there was sufficient scatter in the data to prevent the appearance of any consistent pattern to the number of shots per fiber data. Thus, to the resolution of the experimental data, the average depth per crater did not depend upon the number of shots per fiber fired, for n_{fiber} ranging between 5 and 20. As noted below, however, there is some evidence that crater depth per shot drops off for n_{fiber} values less than 5. In aorta calcified plaque, in the other hand, there was a clear dependence of ablation yield on n_{fiber}.

9.3.2. Full Catheter m_{round} Linearity Study

The reduction of the number of secondary variables requiring full testing in Table 9.1 from three to two depended upon the assumption that crater depth would be linear with the number of catheter rounds fired. This assumption was tested by selecting a practical value for E_{fiber} (16 mJ), and a value for n_{fiber} which would allow the linearity test to be performed without perforating the artery sample. The results of this experiment are plotted in Figure 9.7, illustrating that crater depth was linear with the number of rounds.

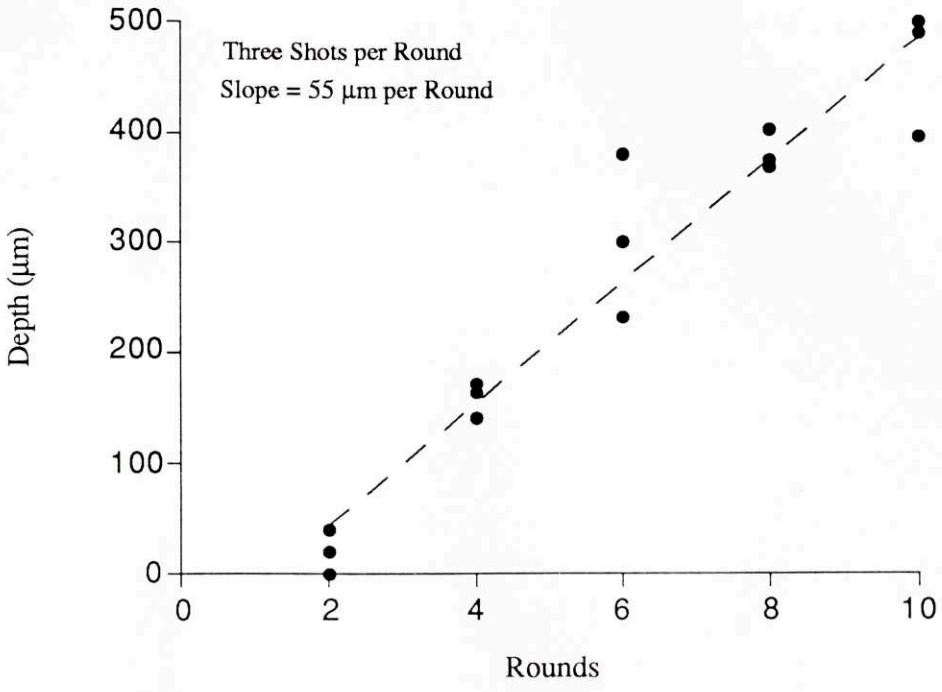

FIGURE 9.7. Results of full catheter m_{round} linearity study. Tissue was normal aorta, energy per fiber was 16 mJ, 3 shots per fiber were fired before catheter advancement.

9.3.3. Three Fiber Study

In order to verify proper dosimetry when less that the full catheter is required to be illuminated, a study was conducted of ablation with three fibers and no catheter advancement. In this experiment, performed on normal and softly plaqued aorta, crater depth versus fiber energy curves were generated. The results of this study are plotted in Figs. 9.8 and 9.9. Also included on the plots are the data for the corresponding values of n from the full catheter study. As can be seen from the plots, ablation yields were less by a factor of ~3 in normal aorta and ~2 in soft plaque aorta than the values for the full catheter. This difference is probably due to the fact that the catheter could advance after each of the full catheter rounds, when of course it could not advance after firing only a 3 fiber group.

This experiment points out the importance of good contact between the catheter tip and the tissue in front of it. The ablating light normally exits the fibers at the output end of the catheter at the full fiber numerical aperture (NA) of 0.22 (see Fig. 1.1). Upon entering the shield at its flat inner surface, the NA is reduced to ~0.15. The shield is placed such that

the light from each fiber forms a spot on its outside surface of 540 μm diameter, so that if the tissue is in contact with the shield, the fluence incident on the tissue is as calculated in section 6.2. If the shield is not in contact with the tissue, however, the light continues expanding after it leaves the catheter, to form a larger spot on the tissue with reduced fluence. If saline, which has an index of refraction close to that of quartz, fills in the gap between the shield and the tissue, then the light exits the shield at 0.15 NA. This means that the light spot increases in diameter by 30 μm for every 100 μm of shield-tissue gap, or that the fluence is reduced to one-half its original value at a gap of 750 μm. Recall that the design working fluence was set at twice fluence threshold, so when the fluence is cut by half, crater depth goes to zero. If for some reason air or vapor gets into the shield-tissue gap, then refraction at the output surface of the shield increases the NA beyond the original 0.22 due to the curvature of the shield, and fluence falls off even more rapidly with distance. It is conceivable that water vapor resulting from previous ablation shots may accumulate in this region (see the next section).

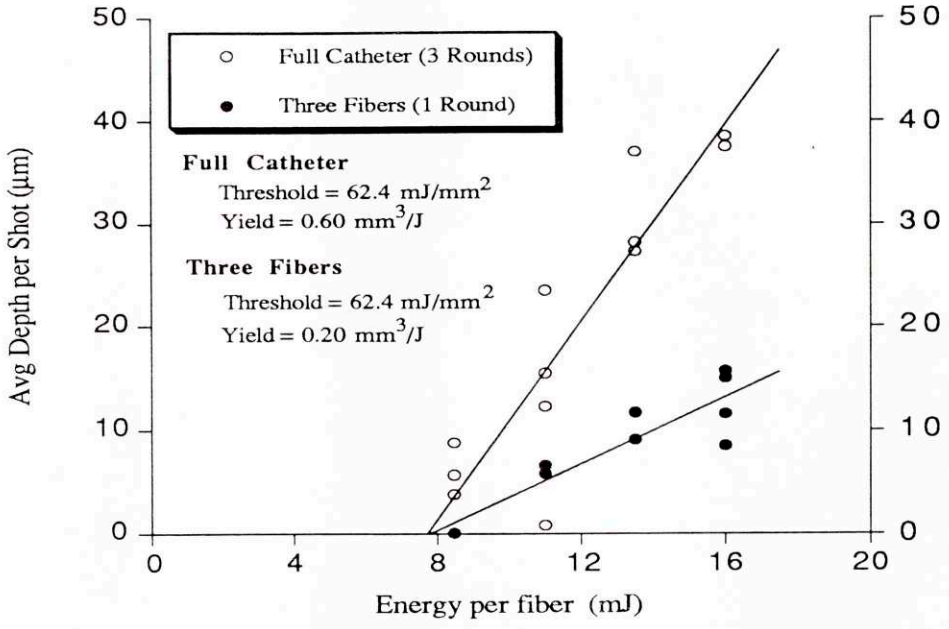

FIGURE 9.8. Crater depth per shot for 3 and 12 fibers in normal aorta.

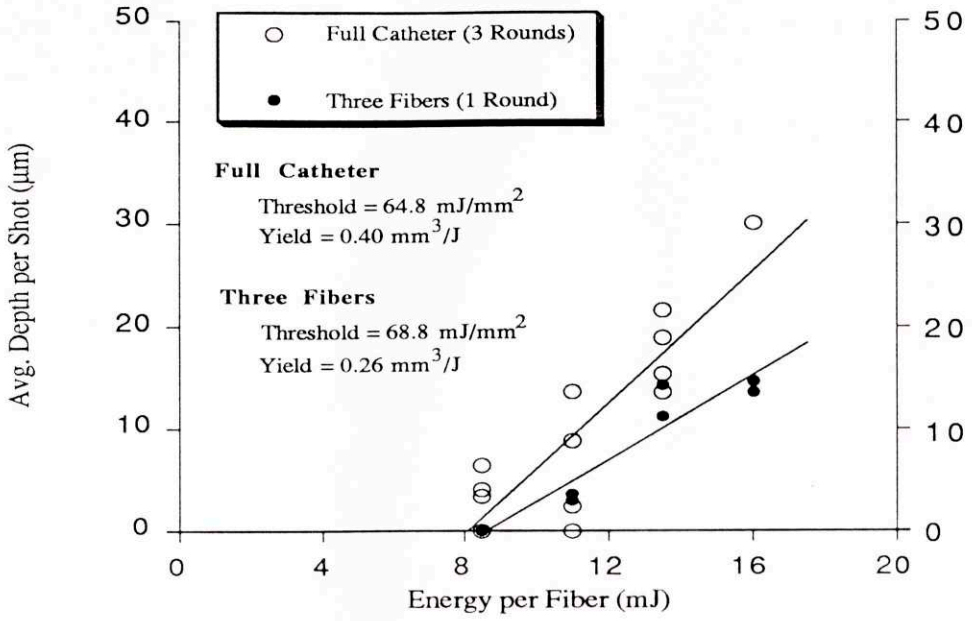

FIGURE 9.9. Crater depth per shot for 3 and 12 fibers in soft plaque in aorta.

9.3.4. Full Catheter Applied Force Study

The results of a study of crater depth versus catheter applied force on a sample of normal aorta are plotted in Fig. 9.10. It is interesting to compare the ablation yield as a function of applied force with ablation yields measured in soft tissue with a focussed beam under saline in chapter 4. Unfortunately, soft tissue dosimetry studies were not done at $\lambda = 355$ nm. However, since bone was studied at $\lambda = 355$ nm, by using the ratio of soft tissue to bone yield at a nearby wavelength, it is possible to extrapolate what soft tissue yields should be at $\lambda = 355$ nm. The closest wavelength for which comparison data is available for yield values between bone and soft tissue is at $\lambda = 308$ nm (see Table 4.4). Performing this extrapolation, the yield for full catheter ablation of normal aorta under saline matches the expected yield for ablation of soft tissue with a focussed beam under saline at an applied force of ~10 gm.

Although the reason for the variation in yield with applied force is not completely understood, one potential explanation is simply the extent of catheter-tissue contact. Since the catheter tip is rounded, it is reasonable that the degree of contact between the catheter

shield and the tissue in front it is sensitive to the force exterted by the catheter on the tissue, since that force will bend the tissue surface to conform to the catheter shield shape. The results of losing contact between the catheter shield and the tissue have already been discussed in the previous section, where it was shown that the problem of a shield-tissue gap is exacerbated if vapor accumulates in that region between shots. If the catheter applied force is large enough, it may force the vapor out of the gap. The consequences of forcing this steam into the tissue are discussed in the next section on histology.

A potentially useful result of this study was that the catheter in light contact with the tissue (1 gm) ablates very little. This result is beneficial, since the LAS system is designed to ablate only that tissue which is directly in contact with the catheter shield, and hence in view of the spectroscopic guidance system. This may provide an automatic safety feature whereby release in pressure on the catheter by the surgeon stops ablation from proceeding.

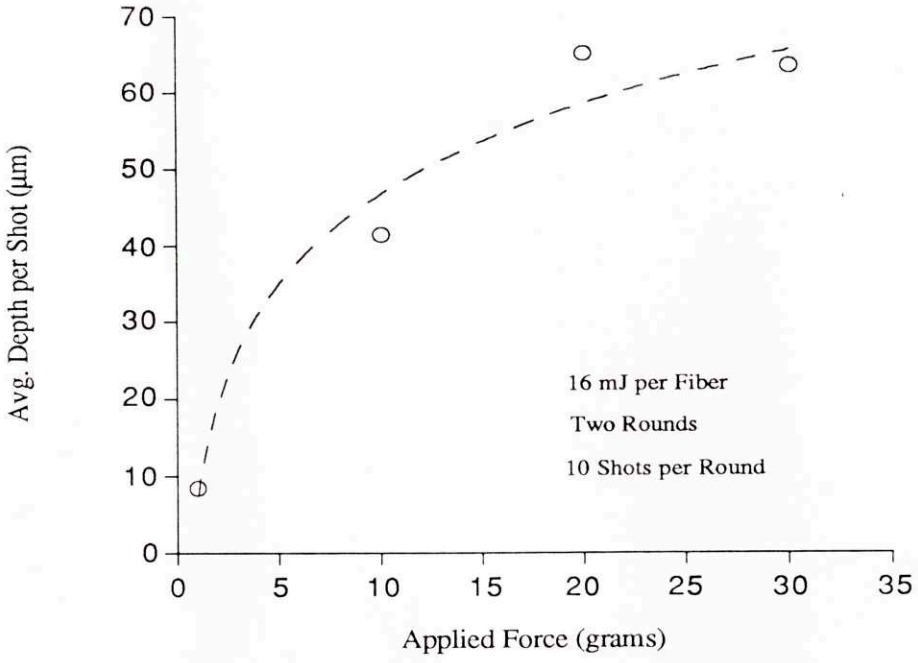

FIGURE 9.10. Full catheter applied force study on normal aorta. The dotted line is merely an estimated trend to guide the eye.

9.4. Histology of LAS II Catheter Craters

Several tissue samples used during the catheter dosimetry study were prepared for histological analysis. Photographs of two 5 μm tissue sections, stained with hematoxylin & eosin, are reproduced in Fig. 9.11(a-b). The crater in in (a) was made by placing the catheter in contact with 20 gm force with a normal aorta wall sample under iced cardioplegia, and firing 3 adjacent fibers a total of 20 shots at 16 mJ per fiber. The crater is ~400 μm wide at the tissue surface, ~500 μm deep, and a pathologist estimated that there was ~100 μm of thermal coagulation at the crater edges. The craters in (b) were made with the catheter in contact with 10 gm applied force with a sample of ulcerative, calcified aorta. In this case, two sets of two adjacent fibers on opposite sides of the catheter were each fired a total of 200 shots at 12 mJ per fiber. The dual craters each measure approximately 500 μm in diameter by 450 μm deep, with ~50 μm of thermal coagulation at the edges.

It is somewhat difficult to correlate the dimensions of the craters as they appear in the histology samples with the dimensions of the catheter, since it is not known whether the sections were taken through the center of the tissue crater, and if the plane they lay in was tangent or perpendicular to the circle of fibers at the catheter tip. The crater widths from both (a) and (b) in the figure are consistent with sections taken radially, since the spot on the catheter face from each fiber has a 540 μm diameter. The crater depth in (a) was approximately 1.5 times the depth predicted by the three-fiber dosimetry study (Fig. 9.8), consistent with the extra depth expected due to the 20 gm applied force (Fig 9.10). The crater depths in (b) were ~80% the depth of full-catheter craters in calcified plaque, which is deeper than expected from the ratio of three-fiber to full-catheter crater depths in soft tissue (~30%). However, examination of other histology slides for two-fiber craters in calcified plaque reveals substantial variation in crater depths in different samples, ranging from 15% to 80% of the expected full-catheter crater depth (which itself is an average of many individual craters). In addition to purely statistical variation, this additional variation in calcified tissue crater depths may be due to the variable extent of calcification in different samples.

Apart from the variability just described, the photographs in Fig. 9.11 are typical of histological findings from a large number of samples which were examined. None of the ablation craters showed any evidence of charring. Craters in calcified tissue were always cleanly cut to ~20 μm of surface roughness, with ~50 μm of thermal coagulation at the edges. This cutting quality is comparable to the bone section histology at λ = 308 nm and

2.8 μm, described in section 4.5.1.2. Soft tissue craters made with applied forces of 10 or 20 gm all looked like Fig. 9.11(a), with a cutting roughness on the order of 150 μm, combined with a zone of thermal coagulation of about the same depth. This type of result was also observed by Gijsbers et al [90], who observed very rough cutting in aorta under saline with a 308 nm multifiber laser catheter. In our experiments, soft tissue craters made with 1 gm applied force had no visible tissue disruption and very little heat damage, but as mentioned in the previous section, had very low yield. Some craters in both kinds of tissue, although predominantly in calcified tissue, exhibited a much larger zone of thermal damage directly beneath the crater, particularly at the higher energies (E_{fiber} = 13 or 16 mJ). This zone extended up to 250 μm deep in some cases, and was manifested as a zone of darker staining, occasionally accompanied by small vacuoles and sites of lateral tissue dissection.

The larger-than-expected zone of thermal coagulation in the craters, particularly at their bottoms, and the extent of disruption in soft tissue at high applied forces, may be related to steam production at the catheter shield-tissue interface. As discussed in sections 9.3.3 and 9.3.4, vapors produced during ablation significantly alter the optics there. A potential explanation for all of these results is as follows. When the catheter is brought into contact with soft tissue at only 1 gm force, only the center of the shield is in contact with the tissue. Expansion of the light exiting the shield (see section 9.33) results in a reduced fluence on the tissue surface, and therefore low ablation yield. Most of the vapors produced during ablation escape out the side of the ablation region into saline. When the catheter is pressed with 10 or 20 gm of force, the tissue is deformed so that the entire shield is brought into contact. The fluence at the tissue surface is therefore the design fluence, and as has been pointed out, the ablation yields which result are approximately the same as for soft tissue ablated with a focussed beam under saline. As the crater deepens, however, the pressure of the catheter on the tissue forces the steam created during ablation into the tissue, causing a deep zone of disruption and and thermal coagulation. The region of thermal coagulation is particularly deep because in disrupting the tissue, the steam has burrowed deep into the tissue. This steam then recondenses, depositing its heat at that depth. In calcified tissue being ablated with high applied force, less steam is produced, due to the lower water content, and the steam that is created is prevented from piercing the tissue by its hardness. In this case, the steam either remains in the gap created at the catheter bottom, or else slowly escapes along the side of the catheter crater. The steam being somewhat trapped in the gap is consistent with the catheter jerking motion when ablating calcified tissue described in section 9.2. In this case, the recondensing steam deposits a large

amount of heat into the tissue, although the depth of heat deposition resulting from diffusion in this case is not as deep as the depth of heat deposition resulting from tissue disruption in the soft tissue case.

If this explanation of tissue disruption and thermal damage is correct, a few options may be considered for obtaining high yields in soft tissue without disruption. The first involves ablating at a low applied catheter force, where tissue disruption does not occur. Since it appears that yields are low with a small applied force because the fluence is reduced due to light expansion out of the catheter, the catheter tip would need to be redesigned to either 1) include optics to modify the light divergence to deliver the design fluence to the tissue, rather than to the shield surface, or 2) change the shield shape so that it remains in full tissue contact at low applied force. Another option for obtaining high yields in soft tissue without disruption involves providing an escape valve for the steam generated during ablation, so that it is not forced into the tissue. This may accomplished in several ways. For example, the catheter guidewire may be withdrawn slightly after positioning the catheter, so that it fills up with saline and provides a volume where the steam can collect and recondense. Although all of the above experiments were performed without a guidewire, the guidewire lumen did become plugged up with tissue. Other potential strategies for providing a steam escape route involve redesign of the catheter. One such redesign might place the fibers in the catheter such that tissue is ablated sequentially around in a circle or a spiral from the inside out, so that the location just ablated always fills up with saline and provides a harmless direction for steam venting. Alternatively, one could imagine catheter designs which hold the tip off of the tissue surface in some fixed way, so that saline fills in the gap.

9.5. Conclusions

Dosimetry with the working LAS II system was consistent with the experiments reported in chapter 4. All tissue types were successfully ablated, generating craters large enough to pass the catheter in soft tissue. Substantially different ablation yields were observed for different types of plaque, consistent with earlier results. Maintenance of good contact betweent the catheter tip and the tissue surface is important to delivering the design fluence to the tissue. Histological examination of tissue craters showed no charring, ~150 um of peripheral thermal damage, and clean cutting in calcified tissue, but significant disruption was observed in soft tissue. Both ablation yield and the amount of disruption in soft tissue varied as a function of applied force on the catheter. A potential explanation for these effects is that steam created by the ablation process is either forced into the tissue or

trapped in between the catheter and the tissue, where it deposits heat in the tissue upon recondensation. Methods for rectifying this situation are suggested.

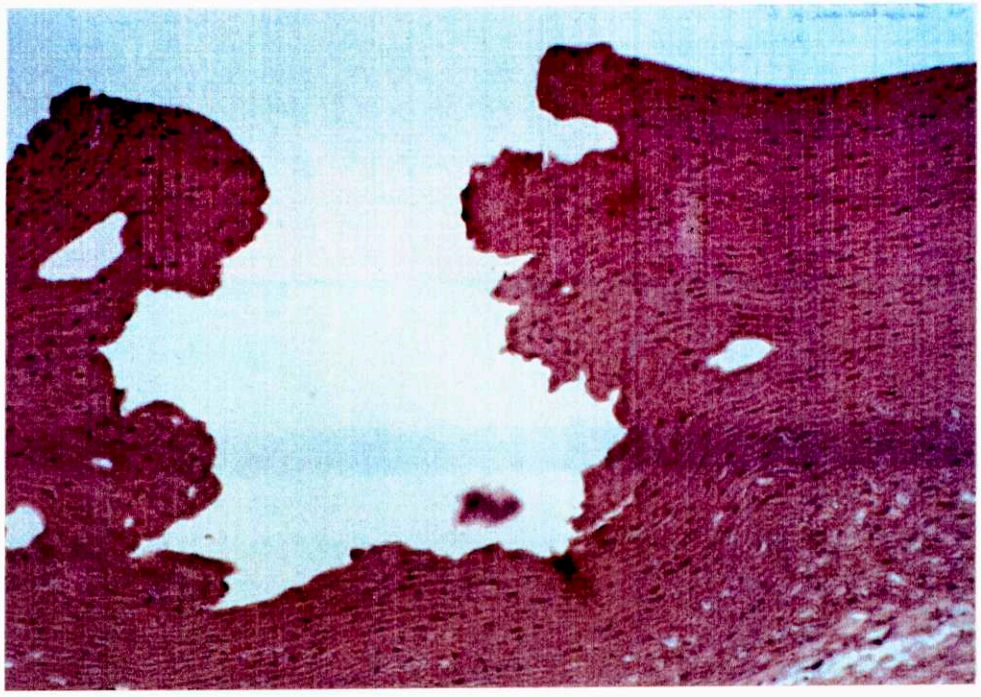

(a)

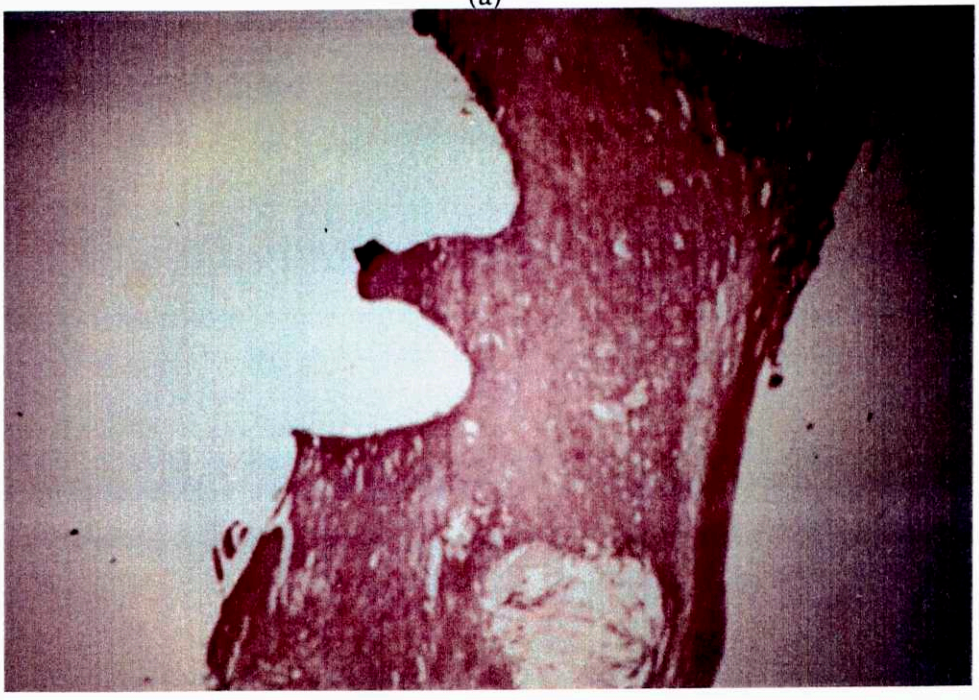

(b)

FIGURE 9.11. Catheter crater histology. (a) 3 fiber crater in normal aorta, 20 g applied force, 16 mJ/fiber, 20 shots. (b) 2 fiber crater in calcified aortic plaque, 10 g applied force, 12 mJ/fiber, 200 shots.

Chapter 10
Conclusions

Since a conclusions section is provided at the end of each chapter, a separate summary of all results is not given here. Rather, a concise list of the major experimental observations is given. Following that, the major implications of these results for theoretical modeling of the ablation process are outlined. Finally, further experiments are suggested to both clarify existing results and conclusions, and to approach the the unanswered questions raised in this work.

10.1. Summary of Experimental Observations

The primary experimental observations of this thesis are as follows.

1. Light penetration depths in compact bovine bone are roughly proportional to wavelength in the near-ultraviolet and visible wavelengths, with values on the order of a few hundred μm. Penetration depths are only a few microns near λ = 3 μm. Throughout the visible region, scattering dominates absorption by a factor of ~5-10.

2. Light from pulsed lasers, with irradiances on the order of MW/cm^2, is capable of producing clean-cut, char-free ablation in calcified tissue, without plasma generation.

3. As a function of pulse fluence, the volume of tissue removed during ablation exhibits a threshold, a region of roughly linear growth up to a few times threshold, and a fall-off from the linear. In the near fluence threshold region, tissue removal is adequately described by two parameters, the fluence threshold and the ablation yield (being the slope of a straight-line fit to depth versus fluence data). Ablation volume varies with the laser spot diameter and the number of shots fired per crater.

4. Through the choice of laser wavelength, a variety of ablation characteristics may be obtained. The best cutting quality for microsurgical applications in calcified tissue is produced by wavelengths which are strongly absorbed in tissue, specifically below λ ~< 400 nm, and near λ = 3 μm. In these wavelength regions, histology reveals that calcified tissue is cut to within ~20 μm of surface roughness, with ~<50 μm of peripheral thermal damage. The ablation debris in this wavelength range is composed of mostly vapor and of rough-edged particles of hydroxyapatite on the order of a few μm in diameter.

5. Ablation thresholds for both fibrous and calcified plaque in aorta wall are similar to thresholds for bone ablation in air, but the ablation yield increases by a factor of 1-5 for calcified plaque, and 2-10 for fibrous plaque. In all tissues studied, fluence thresholds under saline and a quartz slide are approximately twice thresholds in air, while ablation yield remains approximately the same.

6. Fast laser strobe photography (scattergraph configuration) of ablation reveals that material is ejected from the tissue surface beginning as soon as 100 nsec after the ablation pulse. The smallest particles observed are travelling up to 600 m/s, while larger particles are observed travelling more slowly. The velocity and size distributions of debris particules ejected during ablation are very similar for strongly absorbed wavelengths in the near-ultraviolet (λ = 355 nm) and mid-infrared (λ = 2.8 μm) wavelength regions.

7. Fast laser strobe shadowgraphs of ablation reveals spherical blast waves visible as soon as 25 nsec after the ablation pulse, travelling outward from the ablation site at velocities on the order of 1000 m/s. These shocks travel faster than theory predicts for purely dissipative blast waves, implying exothermic processes in the ablation plume.

8. Single-color sequenced pulse ablation results imply that ablation is insensitive to temporal pulse structure for the first few hundred nsec following a laser pulse, that transient changes in tissue optical or thermal properties may be induced during ablation, and that processes induced in the tissue by sub-fluence threshold energy deposition are completely reversible.

9. Dual color sequenced pulse ablation experiments show that two sub-threshold pulses of different wavelengths may combine to ablate tissue, with the cutting characteristics determined by the more strongly absorbed wavelength.

10. The mechanism for laser-induced breakdown in 200 μm core diameter fused silica fibers at λ = 355 nm is surface breakdown. Breakdown fluence in fused silica substrates and optical fibers scales with pulse duration to the 0.85 power in the nsec regime. Sequenced pulses which are just sub-threshold for optical breadkown act separately if separated by more than ~25 nsec. A pulse duration of ~450 nsec is necessary to conduct sufficient light at λ = 355 nm down 200 μm core diameter optical fibers to ablate calcified plaque at the other end, with enough fluence left over to allow the beam exiting the fiber to expand in area by a factor of 5.

11. Dosimetry with the working LAS II catheter is consistent with results obtained previously by ablating vascular tissue under saline and a simulated shield, although yield values depend upon the catheter applied force on the tissue. Histology of tissue craters made with the LAS II system exhibits no charring, ~150 μm of thermal coagulation peripheral to laser craters, and significant disruption in soft tissue ablated at ~>10 gm catheter applied force.

10.2. Summary of Implications for Ablation Modeling

Several of the experimental results of this thesis, in combination with the initial calculations presented herein, have implications for further modeling of the ablation and related processes. These implications fall into the general categories of tissue optics, ablation modeling, and catheter-tissue interaction.

As illustrated in the discussion of ablation modeling in section 2.4, knowledge of the light distribution in tissue is critical for understanding ablation. In this thesis, the simple assumption of a constant, exponential light distribution in tissue is made. This assumption is sufficient to motivate simple ablation models for extracting fluence thresholds and yields from ablation dosimetry data. However, several of the results presented here imply that the light penetration depth in tissue is dramatically reduced during ablation (see sections 4.5.2.4 and 5.3.3.1). In close cooperation with future efforts in ablation modeling, descriptions for the dynamics of light distribution in tissue must be developed.

The second category of experimental implications, for which this thesis provides a rich supply of raw data, is in ablation modeling. As mentioned above, simple models for ablation have been developed for obtaining fluence thresholds and ablation yields from dosimetry data, and for extracting from these quantities such intrinsic tissue properties as heat of ablation and light penetration depth. However, due to the results just referred to concerning the dynamics of the light distribution, these simple models may prove to be over-simplifications for high-irradiance ablation. If it can be shown experimentally that the light distibution in tissue during ablation is indeed dynamic (see the next section), then the ablation models will need to be updated to reflect this.

Another consequence of high-irradiance ablation, which has already been mentioned in section 2.4.6, is the role of gasdynamics and thermodynamics in the air or fluid above the tissue during the ejection process. The fast laser strobe photographs of ablation in section 5.2 clearly show supersonic blast waves caused by ablation in air, followed by

debris ejection at velocities of up to several hundred meters per second. The energy expended in aerodynamic effects, and the consequences of shock wave propagation through the tissue, must be accounted for quantitatively. A related problem is the ablation of composite structures such as calcified tissue. A preliminary two-component picture for how this process may occur, which depends upon the high ejection velocity of vaporized tissue, was described in section 2.4.7.

Finally, several aspects of ablating tissue through a catheter require further experimental and theoretical attention. Of primary importance among these are the consequences of ablating tissue in a volume enclosed by the catheter shield. The pressures generated during ablation, and the mechanisms of their release afterward, must be understood so that alternative methods for their venting may be suggested. Another aspect of catheter ablation which would benefit from further study concerns the optics of the catheter tip, and how future versions may be designed to deliver the design fluence to the tissue while satisfying other requirements such as the catheter applied force.

10.3. Suggestions for Further Studies

This results of this research provide a picture of the calcified tissue ablation process which has been sufficient to aid in the design of a clinical laser angiosurgery system. Several aspects of ablation remain, however, which have been noticed in this work, but are not completely understood. Much of this experimental work parallels theoretical work suggested in the previous section.

The implication of a dramatic decrease in light penetration depth during high-irradiance ablation, discussed above and in sections 4.5.2.4 and 5.3.4.1, may be verified experimentally. One way to do this would be to ablate a thin bone sample of bone in a conventional transient absorption spectroscopy setup, so that the spectrum of transmission of an independent source of white light may be monitored as a function of time after the ablation pulse. A more sophisticated version of this experiment could be done with the sample in an integating sphere, so that both total transmission and reflection may be measured as a function of time after the ablation pulse. With this experiment, any changes in attenuation in the sample would be measured as a function of both time and wavelength.

Several aspects of the ablation process itself may be illuminated by further experiments. Many details of the gasdynamic and two-component ablation processes, for example, are not known. Pressure changes in the ablation plume could be measured

directly by performing fast laser strobe photography in an interferometer. The role of the ratio of soft to hard component in the tissue could be investigated by constructing and ablating artificial tissue, with varying ratios of collagen and water to hydroxyapatite. Heat distributions in the tissue can be measured using magnetic resonance imaging [Bleier et al 90].

Investigation of the characteristics of ablation through the LAS II catheter has just begun, due to the recent completion of the pulse stretching network. One of the surprising results of this work so far is the difference in cutting quality exhibited between ablation with a focussed beam under saline, and ablation with the same fluence through the LAS II catheter (see sections 9.3-4). This effect should be studied in more detail; for example, further applied force studies in different tissues, or strobe photography of the catheter tip during ablation may explain this phenomena. The role of a layer of air, saline, or different fluids between the catheter shield and the tissue may be examined by forcing air or saline through the catheter lumen during ablation.

Finally, clinical applications of this work in other areas of the body besides the coronary arteries may be explored. The LAS II system, which after all delivers ablating doses of laser light through flexible optical fibers, may be ideal with only slight modifications for applications in orthopedics, densitry, or otolaryngology.

References

[Agah et al 90] R. Agah, M. Motamedi, P. Dalmia, E. Ettedgui, L. Song, J.R. Spears, "Potential Role of Collagen in Optical Behavior of Arterial Tissue During Laser Irradiation," in Laser-Tissue Interactions II, S. Jacques, ed., SPIE Proc. **1202**:236-245, 1990.

[Albagli 91] Personal communication.

[Albagli et al 91] D. Albagli, J.A. Izatt, G.B. Hayes, B. Banish, G.S. Janes, I. Itzkan, M.S. Feld, "Time Dependence of Laser-Induced Surface Breakdown in Fused Silica at 355 nm in the Nanosecond Regime," Boulder Damage Symposium XXII, A.H. Guenther and M.J. Solieu, eds., Proc. SPIE **1441**, in press, 1991.

[Altman et al 72] P.L. Altman, D.S. Dittmer, eds., **Biology Data Book**, vol. 1, Federation of American Societies for Experimental Biology, Bethesda, 1972.

[American Heart Association 85] American Heart Association, **Heart Facts**, American Heart Association, Dallas, 1985.

[Ames et al 90] B.N. Ames, L.S. Gold, "Too Many Rodent Carcinogens: Mitogenesis Increases Mutagenesis," Science **249**:970-971, 1990.

[Anderson et al 81] R.R. Anderson, J.A. Parrish, "Microvasculature Can Be Selectively Damaged Using Dye Lasers: A Basic Theory and Experimental Evidence in Human Skin," Las. Surg. Med. **1**:263-276, 1981.

[Apfelberg 87] D.B. Apfelberg, ed., **Evaluation and Installation of Surgical Laser Systems**, Springer-Verlag, New York, 1987.

[APS 87] American Physical Society, "APS Study: Science and Technology of Directed Energy Weapons," Rev. Mod. Phys. **59**:S119-S143, 1987.

[Ashkin et al 86] A. Ashkin, J.M. Dziedzic, J.E. Bjorkholm, S. Chu, "Observation of a Single-Beam Gradient Force Optical Trap for Dielectric Particles," Opt. Lett. **11**:288-290, 1986.

[Ashkin et al 87] A. Ashkin, J.M. Dziedzic, T.M. Yamane, "Optical Trapping and Manipulation of Single Cells Using Infrared Laser Beams," Nature **330**:769-771, 1987.

[ASLMS 91] Las. Surg. Med. Suppl. (abstracts) **3**:1-87, 1991.

[Austin et al 85] G.E. Austin, N.B. Ratliff, J. Hollman, S. Tabei, D.F. Phillips, "Intimal Proliferation of Smooth Muscle Cells as an Explanation of Recurrent Coronary

Artery Stenosis after Percutaneous Transluminal Cornorary Angioplasty," J. Am. Coll. Card. **6**:369, 1985.

[Berns et al 86] M.W. Berns, J.L. McCullough, "Porphyrin Sensitized Phototherapy," Arch. Dermatol. **122**:871-874, 1986.

[Bertolloti et al 81] M. Bertolloti, C. Sibilia, "Depth and Velocity of the Laser-Melted Front From an Analytical Solution of the Heat Conduction Equation," IEEE J. Quant. Elect. **17**:1980-1988, 1981.

[Bierman 83] E. L. Bierman, "Atherosclerosis and Other Forms of Arteriosclerosis," in **Harrison's Principles of Internal Medicine**, R.G. Petersdorf, Ed., McGraw-Hill, New York, 1982, pp. 1465-1475.

[Bleier et al 90] A. R. Bleier, N. Higuchi, L.P. Panych, P.D. Jakab, M.I. Hrovat, F.A. Jolesz, "Magnetic Resonance Imaging of Interstitial Laser Photocoagulation," in Laser-Tissue Interaction, S. Jacques, ed., Proc. SPIE **1202**:188-195, 1990.

[Bloembergen 73] N. Bloembergen, "Role of Cracks, Pores, and Absorbing Inclusions on Laser Induced Damage Threshold at Surfaces of Transparent Dielectrics," Appl. Opt. **12**:661-664, 1973.

[Bloembergen 74] N. Bloembergen, "Laser-Induced Electric Breakdown in Solids," IEEE J. Quant. Elect. **QE-10**:375-386, 1974.

[Bohley et al 90] T.K. Bohley, F. Aparicio, G.S. Derrickson, R.A. Golobic, K.P. Grace, G.A. Murray, I. Trefil, "Excimer Laser System for Coronary Angioplasty," Laser Surgery: Advanced Characterization, Therapeutics, and Systems II, S.N. Joffe, ed., Proc SPIE **1200**, 1990.

[Brain 66] E. Brain, **The Preparation of Decalcified Sections**, C.C. Thomas, Springfield, Ill., 1966.

[Braunwald 84] E. Braunwald, ed., **Heart Disease; A Textbook of Cardiovascular Disease**, W.B. Saunders, 1984.

[Breedlove et al 85] B. Breedlove, D. Schwartz, eds., **Clinical Lasers: Expert Strategies for Practical and Profitable Management**, American Health Consultants, Atlanta, 1984.

[Carslaw et al 47] H.S. Carslaw, J.C. Jaeger, **Conduction of Heat in Solids**, Clarendon Press, Oxford, 1947.

[Chance 88] B. Chance, ed., **Photon Migration in Tissues**, Plenum, New York, 1988.

[Chandrasekhar 60] S. Chandrasekhar, **Radiative Transfer**, Dover, New York, 1960.

[Chato 69] B.T. Chato, ed., **Advanced Heat Transfer**, U. Illinois Press, Chicago, 1969, p. 395.

[Cheong et al 90] W.F. Cheong, S.A. Prahl, A.J. Wech, "A Review of the Optical Properties of Biological Tissues," IEEE J. Quant. Elect. **QE-26**:2166-2185, 1990.

[Chiao et al 64] R.Y. Chiao, E. Garmire, C.H. Townes, "Self-Trapping of Optical Beams," Phys. Rev. Lett. **13**:479, 1964.

[Cohn 85] P.F. Cohn, ed., **Diagnosis and Therapy of Coronary Artery Disease**, Martinus Nijhoff, 1985.

[Cole et al 86] H.S. Cole, Y.S. Liu, H.R. Philipp, "Dependence of Photoetching Rates of Polymers at 193 nm on Optical Absorption Depth," Appl. Phys. Lett. **48**:76, 1986.

[Colella et al 86] C.M. Colella, P. Bogani, G. Agati, F. Fusi, "Genetic Effects of UV-B: Mutagenicity of 308 nm Light in Chinese Hamster V79 Cells," Photochem. Photobiol. **43**:437, 1986.

[Cothren et al 86a] R.M. Cothren, C. Kittrell, G.B. Hayes, R.L. Willet, B. Sacks, E.G. Malk, R.J. Ehmsen, C. Bott-Silverman, J.R. Kramer, M.S. Feld, "Controlled Light Delivery for Laser Angiosurgery," IEEE J. Quant. Elect. **22**:4-7, 1986.

[Cothren et al 86b] R.M. Cothren, G.B. Hayes, J.R. Kramer, B. Sacks, C. Kittrell, M.S. Feld, "A Multifiber Catheter with an Optical Shield for Laser Angiosurgery," Las. Lif. Sci. **1**:1-12, 1986.

[Deckelbaum et al 88] L.I. Deckelbaum, I.J. Sarembock, M.S. Stetz, K.M. O'Brien, F.W. Cutruzzola, A.F. Gmitro, M.D. Ezekowitz, "In-Vivo Fluorescence Spectroscopy of Normal and Atherosclerotic Arteries," in Optical Fibers in Medicine III, A. Katzir, ed., Proc. SPIE **906**:314-319, 1988.

[Deutsch et al 83] T.F. Deutsch, M.W. Geis, "Self-Developing UV Photoresist Using Excimer Laser Exposure," J. Appl. Phys. **54**:7201-7204, 1983.

[Dingus et al 91] R.S. Dingus, R.J. Scammon, "Gruneisen-Stress Induced Ablation of Biological Tissue," in Laser-Tissue Interaction II, S. Jacques, ed., Proc. SPIE **1427**, 1991.

[Dixon 87] J.A. Dixon, **Surgical Applications of Lasers**, Year Book Medical Publishers, Inc., Chicago, 1987.

[Dixon 88] J. Dixon, "Free Electron Laser: Hard Tissue Ablation," plenary session, Eighth Annual Meeting of the A.S.L.M.S., Dallas, 1988.

[Doty et al 76] S.B. Doty, R.A. Robinson, B. Schofield, **Handbook of Physiology**, section 7, vol. VII, American Physiological Society, Washington, 1976, pp. 3-23.

[Doukas et al 90] A.G. Doukas, R. Birngruber, T.F. Deutsch, "Determination of the Shock-Wave Pressures Generated by Laser-Induced Breakdown in Water," in Laser-Tissue Interaction, S. Jacques, ed., Proc. SPIE **1202**:61-70, 1990.

[Dubovik 81] A. Dubovik, **The Photographic Recording of High-Speed Processes**, J. Wiley & Sons, New York, 1981, p. 313.

[Duley 83] W.W. Duley, **Laser Processing and Analysis of Materials**, Plenum Press, New York, 1983.

[Dyer et al 88] P.E. Dyer, J. Sidhu, "Spectroscopic and Fast Photographic Studies of Excimer Laser Polymer Ablation," J. Appl. Phys. **64**:4657-4663, 1988.

[Essed et al 83] C.E. Essed, M. VandenBrand, A.E. Becker, "Transluminal Coronary Angioplasty and Early Restenosis: Fibrocellular Occlusion after Wall Laceration," Br. Heart J. **49**:393, 1983.

[Fanelli et al 90] C. Fanelli, R. Aronoff, "Restenosis following Coronary Angioplasty," Am. Heart J. **119**:357, 1990.

[Feld et al 91] M.S. Feld, J.R. Kramer, D. Albagli, R.M. Cothren, R.R. Dasari, G.B. Hayes, J.A. Izatt, I. Itzkan, G.S. Janes, R.P. Rava, "LAS II: An Integrated System for Spectral Diagnosis, Guidance and Ablation in Laser Angiosurgery," in **Future Directions in Interventional Cardiology II**, J.H.K Vogel, ed., C.V. Mosby & Co., St. Louis, 1991.

[Fitzmaurice et al 89] M. Fitzmaurice, G. Bordagaray, G. Englemann, R. Richards-Kortum, T. Kolubayev, M.S. Feld, N.B. Ratliff, J.R. Kramer, "Argon-Ion Laser Induced Autofluorescence in Normal and Atherosclerotic Aorta and Coronary Artery: Morphologic Studies," Am. Heart. J. **118**:1028, 1989.

[Flotte et al 90] T.S. Flotte, Y. Yashima, "Morphological Studies of Laser-Induced Photoacoustic Damage" in Laser-Tissue Interaction, S. Jacques, ed., Proc. SPIE **1202**:71-79, 1990.

[Fodor et al 85] S.P.A. Fodor, R.P. Rava, T.R. Hays, T.G. Spiro, "Ultraviolet Resonance Raman Spectroscopy of the Nucleotides with 266-, 240-, 218-, and 200-nm Pulsed Laser Excitation," J. Am. Chem. Soc. **107**:1520-1529, 1985.

[Fradin et al 73] D.W. Fradin, N. Bloembergen, J.P. Letellier, "Dependence of Laser-Induced Breakdown Field Strength On Pulse Duration," Appl. Phys. Lett. **22**:635-637, 1973.

[Freeman 78] R.G. Freeman, "Action Spectrum for Ultraviolet Carcinogenesis," National Cancer Institute Monograph **50**:27, 1978.

[Fujimoto 77] D. Fujimoto, "Isolation and Characterization of a Fluorescent Material in Bovine Achilles Tendon Collagen," Biochem. Biophys. Res. Comm. **76**:1124-1129, 1977.

[Fujimoto et al 86] J.G. Fujimoto, S. DeSilvestri, E.P. Ippen, C.A. Puliafito, R. Margolis, A. Osseroff, "Femtosecond Optical Ranging in Biological Systems," Opt. Lett. **11**:150, 1986.

[Garrison et al 84] B.J. Garrison, R. Srinivasan, "Microscopic Model for the Ablative Photodecomposition of Polymers by Far-Ultraviolet Radiation (193 nm)," Appl. Phys. Lett. **44**:849-851, 1984.

[Gerrity et al 88] R.G. Gerrity, F.D. Loop, L.A.R. Golding, L.A. Ehrhart, Z.B. Argenyi, "Arterial Response to Laser Operation for Removal of Atherosclerotic Plaques," J. Thora. Cardiovasc. Surg. **85**:409-421, 1983.

[Gitomer et al 90] S.J. Gitomer, R.D. Jones, "Laser-Produced Plasmas in Medicine," in Laser-Tissue Interaction, S. Jacques, ed., Proc. SPIE **1202**:118-132, 1990.

[Goldenberg et al 90] T. Goldenberg, W.B. Anderson, F. Litvack, W.S. Grundfest, J. Forrester, "Percutaneous Excimer Laser Coronary Angioplasty: Update," Optical Fibers in Medicine V, A. Katzir, ed., Proc. SPIE **1201**, 1990.

[Goldman 81] L. Goldman, ed., **The Biomedical Laser: Technology and Clinical Applications**, Springer-Verlag, New York, 1981.

[Gorodetsky et al 85] G. Gorodetsky, T.G. Kazyaka, R.L. Melcher, R. Srinivasan, "Calorimetric and Acoustic Study of Ultraviolet Laser Ablation of Polymers," Appl. Phys. Lett. **46**:828, 1985.

[Grundfest et al 85] W.S. Grundfest, F. Litvack, J.S. Forrester, T. Goldenberg, H.J.C. Swan, L. Morgenstern, M. Fishbein, I.S. McDermid, D.M. Rider, T.J. Pacala, "Laser Ablation of Human Atherosclerotic Placque Without Adjacent Tissue Injury," J. Am. Coll. Cardiol. **6**:929-933, 1985.

[Gruntzig et al 79] A.R. Gruntzig, A. Senning, W.E. Sergenthaler, "Non-operative Dilatation of Coronary Artery Stenosis: Percutaneous Transluminal Coronary Angioplasty," N. Engl. J. Med. **301**:61, 1979.

[Haase et al 90] K.K. Haase, M Mauser, A. Baumbauch, W. Voelker, K.R. Karsch, "Restensosis After Excimer Laser Coronary Atherectomy," Circulation (abstract) **82(4)**:672, 1990.

[Haldorsson et al 78] T. Haldorsson, J. Langerholc, "Thermodynamic Analysis of Laser Irradiation of Biological Tissue," Appl. Opt. **24**:3948-3958, 1978.

[Hayes 91] Personal communication.

[Henderson et al 89] R.A. Henderson, S. Karani, C.A. Bucknall, A. Dritsas, A.D. Timmis, E. Sowton, "Clinical Outcome of Coronary Angioplasty for Single-Vessel Disease," Lancet **2**:546, 1989.

[Horoszowski et al 87] H. Horoszowski, M. Heim, I. Farine, "The Carbon Dioxide Laser in Orthopaedic Surgery," in **Photomedicine**, vol. 3, E. Ben-Hur, I. Rosenthal, eds., CRC Press, Boca Raton, 1987, pp. 61-65.

[Hsu et al 75] J. Hsu, P.D. Forbes, L.C. Harber, E. Lakow, "Induction of Skin Tumors in Hairless Mice by a Single Exposure to UV Radiation," Photochem. Photobiol. **21**:185, 1975.

[Huang et al 91] D. Huang, J. Wang, C.P. Lin, C.A. Puliafito, J.G. Fujimoto, "Micron-Resolution Ranging of Cornea and Anterior Chamber by Optical Coherence Domain Reflectometry," submitted for publication, 1991.

[Hughes 78] R.C. Hughes, "Charge-Carrier Transport Phenomena in Amorphous SiO_2: Direct Measurement of the Drift Mobility and Lifetime," Phys. Rev. Lett. 30:1333-1336, 1973.

[Ishimaru 78] A. Ishimaru, **Wave Propagation and Scattering in Random Media**, Academic Press, New York, 1978.

[Ito et al 86] A. Ito, T. Ito, "Absorption Spectra of Deoxyribose, Ribosephosphate, ATP and DNA by Direct Transmission Measurements in the Vaccum-UV (150-190 nm) and Far-UV (190-260 nm) Regions Using Synchroton Radiation as a Light Source," Photochem. Photobiol. **44**:379-383, 1986.

[Itzkan 91] Personal communication.

[Izatt 88] J.A. Izatt, "Ablation of Hard Biological Tissue Using Pulsed Hydrogen Fluoride Laser Radiation," S.M. Thesis, M.I.T. Archives, 1988.

[Izatt et al 90a] J.A. Izatt, N.D. Sankey, F. Partovi, M. Fitzmaurice, R.P. Rava, I. Itzkan, M.S. Feld, "Ablation of Calcified Biological Tissue Using Pulsed Hydrogen Fluoride Laser Radiation," IEEE J. Quant. Elect. **QE-26**:2261-2270, 1990.

[Izatt et al 90b] J.A. Izatt, D. Albagli, I. Itzkan, M.S. Feld, "Pulsed Laser Ablation of Calcified Tissue: Physical Mechanisms and Fundamental Parameters," in Laser-Tissue Interaction, S. Jacques, ed., Proc. SPIE **1202**:133-140, 1990.

[Izatt et al 91a] J.A. Izatt, D. Albagli, M. Britton, J.M. Jubas, I. Itzkan, M.S. Feld, "Wavelength Dependence of Pulsed Laser Ablation of Calcified TIssue," Las. Surg. Med., in press, 1991.

[Izatt et al 91b] J.A. Izatt, D. Albagli, I. Itzkan, M.S. Feld, "Study of Bone Ablation Dynamics with Sequenced Pulses," in Laser-Tissue Interactions II, S. Jacques, ed., Proc. SPIE **1427**, 1991.

[Jacques et al 87] S.L. Jacques, S. Prahl, "Modeling Optical and Thermal Distributions in Tissue During Laser Irradiation," Las. Surg. Med. **6**:494-503, 1987.

[Jones et al 87] C. Jones, E. Huberman, M. Cunningham, M. Peak, "Mutagenesis and Cytotoxicity in Human Epithelial Cells by Far-and-Near Ultraviolet Radiations: Action Spectra," Radiat. Res. **110**:244-254, 1987.

[Katzir 86] A. Katzir, "Optical Fibers in Medical Applications," Laser Focus **22(5)**:94-110, 1986.

[Khrokhin 82] O.N. Khrokhin, "Generation of Hihg-Temperature Vapors and Plasmas by Laser Radiation," in **Laser Handbook**, vol. 2, F.T. Arrecchi, E.O. Schultz-Dubois, eds., North Holland, Amsterdam, 1982, p. 1372.

[Kittrell et al 86] C. Kittrell, J. Tobin, J. Rulnick, M.S. Feld, "Plasma Ablation of Tissue," Las. Surg. Med. **6**:267 (abstract), 1986.

[Kjellstrom et al 88] B.T. Kjellstrom, A.L. Bylock, C. Bott-Silverman, G.L. Englemann, R.G. Gerrity, C. Kittrell, R.M. Cothren, G.B. Hayes, M.S. Feld, J.R. Kramer, "Removal of Surgically Induced Fibrous Arterial Plaques by Argon Ion Laser Angiosurgery using a Multifiber Delivery System," J. Thorac. Cardiovasc. Surg. **96**:925, 1988.

[Klier 72] K. Klier, "Absorption and Scattering in Plane Parallel Turbid Media," J. Opt. Soc. Am. **62**:882-885, 1972.

[Knight 79] C.J. Knight, "Theoretical Modeling of Rapid Surface Vaporization with Back Pressure," A.I.A.A. J. **17**:519-523, 1979.

[Knight 82] C.J. Knight, "Transient Vaporization from a Surface into a Vacuum," A.I.A.A. J. **20**:950-954, 1982.

[Kochever 89] I. Kochever, "Cytotoxicity and Mutagenicity of Excimer Laser Radiation," Las. Surg. Med. **9**:440-445, 1989.

[Kramer et al 89] J.R. Kramer, W.L. Proudfit, F.D. Loop, M. Goormastic, K. Zimmerman, C. Simpfendorfer, G. Horner, "Late Follow-up of 781 Patients Undergoing Transluminal Coronary Angioplasty or Coronary Artery Bypass Grafting for an Isolated Obstruction in the Left Anterior Descending Coronary Artery," Am. Heart J. **118**:1144-1153, 1989.

[Kramer et al 90] J.R. Kramer, M.S. Feld, R.M. Cothren, G.B. Hayes, R. Richards-Kortum, B.W. Lytle, C. Kittrell, C. Bott-Silverman, "Laser Angiosurgery: A Biomedical System using Photons to Diagnose and Treat Atherosclerosis," in **Future Directions in Interventional Cardiology**, J.H.K Vogel and S.B. King, eds., C.V. Mosby & Co., St. Louis, 1990.

[Krauss et al 86] J.M. Krauss, C.A. Puliafito, R. Steinert, "Laser Interactions with the Cornea," Surv. Opthalmol. **31**:37-53, 1986.

[Kubelka 48] P. Kubelka, "New Contributions to the Optics of Intensely Light-Scattering Materials. Part I," J. Opt. Soc. Am. **38**:448-457, 1948.

[Kubelka 54] P. Kubelka, "New Contributions to the Optics of Intensely Light-Scattering Materials. Part II:Nonhomogenous Layers," J. Opt. Soc. Am. **44**:330-335, 1954.

[Kuper et al 87] S. Kuper, M. Stuke, "Femtosecond UV Excimer Laser Ablation," Appl. Phys. B **44**:199, 1987.

[Langerholc 79] J. Langerholc, "Moving Phase Transitions in Laser-Irradiated Biological Tissue," Appl. Opt. **18**:2286-2293, 1979.

[Leon et al 88] M.B. Leon, D.Y. Lu, L.G. Prevosti, W.W. Macy, P.D. Smith, M. Granovsky, R.F. Bonner, R.S. Balaban, "Human Arterial Surface Fluorescence: Atherosclerotic Plaque Identification and Effects of Laser Atheroma Ablation," J. Am. Coll. Card. **12**:94-102, 1988.

[Letokhov 91] V. Letokhov, "Quantitative Study of Laser Pulsed Ablation of Biotissue," seminar on Laser Diagnosis of Tissue, M.I.T. Spectroscopy Laboratory, 1991.

[Levine et al 89] L.M.A. Levine, L.G. Fredin, M.J. Berry, "Infrared Absorption Spectra of Cured Epoxy Resin and Human Corneal Tissue at Temperatures up to 450 °C," in Thermal and Optical Interactions with Biological and Related Composite Materials, Proc. SPIE **1064**:131-134, 1989.

[Litvack et al 88] F. Litvack, W.S. Grundfest, T. Goldenberg, J. Laudenslager, J.S. Forrester, "Percutaneous Excimer Laser Angioplasty of Aortocoronary Saphenous Vein Grafts," J. Am. Coll. Cardiol. **14**:803, 1989.

[Marshall et al 86] J. Marshall, S. Trokel, S. Rothery, R.R. Krueger, "Photoablative Reprofiling of the Cornea Using an Excimer Laser: Photorefractive Keratectomy," Las. Opthal. **1**:21, 1986.

[McBride et al 88] W. McBride, R.A. Lange, L.D. Hills, "Restenosis after Successful Coronary Angioplasty," N. Engl. J. Med. **318**:1735, 1988.

[McGimpsey et al 87] W.G. McGimpsey, J.C. Scaiano, "A Two-Photon Study of the 'Reluctant' Norrish Type I Reaction of Benzil," J. Am. Chem. Soc. **109**:2179, 1987.

[Melamed et al 90] M.R. Melamed, T. Lindmo, M.L. Mendelsohn, eds., **Flow Cytometry and Sorting**, Wiley-Liss, New York, 1990.

[Moss et al 86] J.N. Moss, C.D. Scott, eds., **Thermophysical Aspects of Reentry Flows**, A.I.A.A., New York, 1986.

[Nelson et al 88] J.S. Nelson, L. Yow, L.H. Liaw, L. MacLeay, R.B. Zavar, A. Orenstein, W.H. Wright, J.J. Andrews, M.W. Berns, "Ablation of Bone and

Methacrylate by a Prototype Mid-Infrared Erbium:YAG Laser," Las. Surg. Med. **8**:494-500, 1988.

[Nishioka et al 90] N. Nishioka, Y. Domankevitz, "Comparison of Tissue Ablation with Pulsed Holmium and Thulium Lasers," IEEE J. Quant. Elect. **QE-26**:2271-2275, 1990.

[Nuss et al 88] R.C. Nuss, R.L. Fabian, R. Sarkar, C.A. Puliafito, "Infrared Laser Bone Ablation," Las. Surg. Med. **8**:381-391, 1988.

[Partovi et al 87] F. Partovi, J.A. Izatt, R.M. Cothren, C. Kittrell, J.E. Thomas, S. Strikwerda, J.R. Kramer, M.S. Feld, "A Model for Thermal Ablation of Tissue Using Laser Radiation," Las. Surg. Med. **7**:141-154, 1987.

[Peak et al 84] M.J. Peak, J.G. Peak, M.P. Moehring, R.B. Webb, "Ultraviolet Action Spectrum for DNA Dimer Induction Lethality, and Mutagenesis in *E. coli* with Emphasis on the UVB Region," Photochem. Photobiol. 40:613-620, 1984.

[Partovi 90] Unpublished calculations.

[Pouchert 67] C.J. Pouchert, ed., **The Aldrich Library of FT-IR Spectra**, vol. 2, Aldrich Chemical Co., Milwaukee, 1985, p.1267.

[Prahl 88] S.A. Prahl, "Light Transport in Tissue," Ph.D. Dissertation, Univ. Texas at Austin, 1988.

[Prince et al 86] M.R. Prince, T.F. Deutsch, A.H. Shapiro, R.J. Margolis, A.R. Oseroff, J.T. Fallon, J.A. Parrish, R.R. Anderson, "Selective Ablation of Atheromas Using a Flashlamp-Excited Dye Laser at 465 nm," Proc. Natl. Acad. Sci. USA **83**:7064-7068, 1986.

[Puliafito et al 87a] C.A. Puliafito, K. Wong, R.F. Steinert, "Quantitative and Ultrastructural Studies of Excimer Laser Ablation of the Cornea at 193 and 248 nanometers," Las. Surg. Med. **7**:155, 1987.

[Puliafito et al 87b] C.A. Puliafito, D. Stern, R.R. Krueger, E.R. Mandel, "High-Speed Photography of Excimer Laser Ablation of the Cornea," Arch. Opthalmol. **105**:1255-1259, 1987.

[Rainer et al 83] F. Rainer, W.H. Lowdermilk, D. Milam, "Bulk and Surface Damage Thresholds of Crystals and Glasses at 248 nm," Opt. Eng. **22**:431-434, 1983.

[Rasmussen et al 89] R.E. Rasmussen, M. Hammer-Wilson, M.W. Berns, "Mutation and Sister Chromatid Exchange Induced in Chinese Hamster Ovary (CHO) Cells by Pulsed Excimer Laser Radiation at 193 nm and 308 nm and Continuous UV Radiation at 254 nm," Photochem. Photobiol. **49**:413, 1989.

[Rava et al 91] R.P. Rava, J.J. Baraga, M.S. Feld, "Near Infrared Fourier Transform Raman Spectroscopy of Human Artery," Spectrochim. Acta **47A**:509-512, 1991.

[Ready 71] J.F. Ready, **Effects of High-Power Laser Radiation**, Academic Press, New York, 1971.

[Reeder et al 90] G.S. Reeder, J.F. Bresnahan, D.R. Bresnahan, F. Litvack, "ELCA Registry Members: Excimer Laser Coronary Angioplasty (ELCA) in Patients With Restenosis After Prior Balloon Angioplasty (BA)," Circulation (abstract) **82(4)**:672, 1990.

[Reif 89] J. Reif, "High-Power Laser Interaction with the Surface of Wide Bandgap Materials," Opt. Eng. **28**:1122-1132, 1989.

[Richards-Kortum 87] R. Richards-Kortum, "Understanding Laser Induced Fluorescence of Human Artery Wall with Applications to Diagnosis of Atherosclerossis," S.M. Thesis, M.I.T Archives, 1987.

[Richards-Kortum 88] R. Richards-Kortum, R.P. Rava, M. Fitzmaurice, L. Tong, N.B. Ratliff, J.R. Kramer, C. Kittrell, and M.S. Feld, "A Model for Extraction of Diagnostic Information from Laser Induced Fluorescence Spectra of Human Artery Wall," Spectrochim. Acta **45A**:87, 1988.

[Richards-Kortum 89a] R. Richards-Kortum, R.P. Rava, M. Fitzmaurice, L. Tong, N.B. Ratliff, J.R. Kramer, and M.S. Feld, "A One-Layer Model of Laser-Induced Fluorescence for Diagnosis of Disease in Human Tissue: Applications to Atherosclerosis," IEEE Trans. Biomed. Eng. **36**:122-132, 1989.

[Richards-Kortum 89b] R. Richards-Kortum, A. Mehta, G. Hayes, R. Cothren, T. Kolubayev, C. Kittrell, N.B. Ratliff, J.R. Kramer, and M.S. Feld, "Spectral Diagnosis of Atherosclerosis Using an Optical Fiber Laser Catheter," Am. Heart J. **118**:381, 1989.

[Richards-Kortum 90] R. Richards-Kortum, "Fluorescence Spectroscopy as a Technique for Diagnosis of Pathologic Conditions in Human Arterial, Urinary Bladder, and Gastro-Intestinal Tissues," Ph.D. Thesis, M.I.T Archives, 1990.

[Robertson et al 71] C.W. Robertson, D. Williams, "Lambert Absorption Coefficients of Water in the Infrared," J. Opt. Soc. Am. **61**:1316, 1971.

[Sauerbrey et al 89] R. Sauerbrey, G.H. Pettit, "Theory for the Etching of Organic Materials by Ultraviolet Laser Pulses," Appl. Phys. Lett. **55**:421-423, 1989.

[Schober et al 86] R. Schober, F. Ulrich, T. Sander, H. Durselen, S. Hessel, "Laser-Induced Alteration of Collagen Substructure Allows Microsurgical Tissue Welding," Science **232**:1421, 1986.

[Sedov 59] L.I. Sedov, **Similarity and Dimensional Methods in Mechanics**, Academic Press, New York, 1959.

[Seeger et al 90] J.M. Seeger, L.D. Kaelin, G. Barbeau, G.S. Abela, "Laser Recanalization in High Risk Patients," Las. Surg. Med. **10**:105-111, 1990.

[Shen 84] Y.R. Shen, **Principles of Nonlinear Optics**, Wiley, New York, 1984.

[Singer et al 90] J.R. Singer, F.A. Grunbaum, P. Kohn, J.P. Zubelli, "Image Reconstruction of the Interior of Bodies that Diffuse Radiation," Science **248**:990-993, 1990.

[Singleton et al 88] D.L. Singleton, G. Paraskevopoulos, R.S. Taylor, L.A.J. Higginson, "Excimer Laser Angioplasty: Tissue Ablation, Arterial Response, and Fiber Optic Delivery," IEEE J. Quant. Elect. **QE-23**:1772-1782, 1987.

[Smith et al 77] W.L. Smith, J.H. Bechtel, N. Bloembergen, "Picosecond Laser-Induced Breakdown at 5321 and 3547 A: Observation of Frequency-Dependent Behavior," Phys. Rev. B **15**:4039-4055, 1977.

[Srinivasan 86] R. Srinivasan, "Ablation of Polymers and Biological Tissue by Ultraviolet Lasers," Science **234**:559-565, 1986.

[Srinivasan et al 82] R. Srinivasan, W. Leigh, "Ablative Photodecomposition: Action of Far-Ultraviolet (193 nm) Laser Radiation on Poly (ethylene terephthalate) Films," J. Am. Chem. Soc. **104**:6784-6785, 1982.

[Srinivasan et al 86] R. Srinivasan, B. Braren, D.E. Seeger, R.W. Dreyfus, "Photochemical Cleavage of a Polymeric Solid - Details of the Ultraviolet Laser Ablation of Poly(methyl methacrylate) at 193 nm and 248 nm," Macromolecules **19**:916, 1986.

[Srinivasan et al 87] R. Srinivasan, P.E. Dyer, B. Braren, "Far-Ultraviolet Laser Ablation of the Cornea: Photoacoustic Studies," Las. Surg. Med. **6**:514-519, 1987.

[Srinivasan et al 87b] R. Srinivasan, B. Braren, R.W. Dreyfus, J. Appl. Phys. **61**:372, 1987.

[Srinivasan et al 89] R. Srinivasan, B. Braren, K.G. Casey, M. Yeh, "Ultrafast Imaging of Ultraviolet Laser Ablation and Etching of Polymethylmethacrylate," Appl. Phys. Lett. **55**:2790-2791, 1989.

[Steinert et al 85] R.F. Steinert, C.A. Puliafito, **The Nd:YAG Laser in Opthalmology: Principles and Clinical Applications of Photodisruption**, W.B. Saunders, Philadelphia, 1985.

[Stern et al 89a] D. Stern, W.-Z. Lin, C.A. Puliafito, J.G. Fujimoto, "Femtosecond Optical Ranging of Corneal Incision Depth," Invest. Opth. & Vis. Sci. **30**:99-103, 1989.

[Stern et al 89b] D. Stern, R.W. Schoenlein, C.A. Puliafito, E.T. Dobi, R. Birngruber, J.G. Fujimoto, "Corneal Ablation by Nanosecond, Picosecond, and Femtosecond Lasers at 532 and 635 nm," Arch. Opthalmol. **107**:587-592, 1989.

[Strickland et al 79] P.T. Strickland, F.J. Burns, R.E. Albert, "Induction of Skin Tumors in the Rat by Single Exposure to Ultraviolet Radiation," Photochem. Photobiol.**30**:683, 1979.

[Stryer 81] L. Stryer, **Biochemistry**, W.H. Freeman and Co., San Francisco, 1981.

[Svaasand et al 85] L.O. Svaasand, T. Boerslid, M Oeveraasen, "Thermal and Optical Properties of Living Tissue: Application to Laser-Induced Hyperthermia," Las. Surg. Med. **5**:589-602, 1985.

[Svelto 82] O. Svelto, **Principles of Lasers**, Plenum Press, New York, 1982.

[Tan et al 89] O.T. Tan, K. Sherwood, B.A. Gilchres, "Treatment of Children with Prot-Wine Stains Using the Flashlamp-Pumped Tunable Dye Laser," N. Eng. J. Med. **320**:416-421, 1989.

[Taylor et al 90] R.S. Taylor, L.A.J. Higginson, K.E. Leopold, "Dependence of the XeCl Laser Cut Rate of Plaque on the Degree of Calcification, Laser Fluence, and Optical Pulse Duration," Las. Surg. Med. **10**:414-419, 1990.

[Teng et al 87] P. Teng, N.S. Nishioka, R.R. Anderson, T.F. Deutsch, "Optical Studies of Pulsed Laser Fragmentation of Biliary Calculi," Appl. Phys. B **42**:73-78, 1987.

[Thomsen et al 90] S.L. Thomsen, S.L. Jacques, S.T. Flock, "Microscopic Correlates of Macroscopic Optical Property Changes During Thermal Coagulation of Myocardium," in Laser-Tissue Interactions II, S. Jacques, ed., SPIE Proc. **1202**:2-11, 1990.

[Tiphlova et al 88] O.A. Tiphlova, T.I. Karu, N.P. Furzikov, "Lethal and Mutagenic Action of XeCl Laser Radiation on Escheria Coli," Las. Lif. Sci. **2**:155, 1988.

[Tobin 85] J. Tobin, "Laser Induced Plasma Ablation of Biological Tissue," S.B. Thesis, M.I.T. Archives, 1985.

[Tobis et al 89] J. Tobis, M. Smolin, J. Mallery, L. MacLeary, W.D. Johnston, J.E. Connolly, G. Lewis, B. Zuch, W. Henry, M. Berns, "Laser-Assisted Thermal Angioplasty in Human Peripheral Artery Occlusions: Mechanism of Recanalization," J. Am. Coll. Cardiol. **13**:1547, 1989.

[Tomazic et al 88] B.B. Tomazic, W.E. Brown, L.A. Queral, M. Sadovnik, "Physicochemical Characterization of Cardiovascular Calcified Deposits," Atherosclerosis **69**:5-19, 1988.

[Trokel et al 83] S.L. Trokel, R. Srinivasan, B. Braren, "Excimer Laser Surgery of the Cornea," Am. J. Opthalmol. **96**:710-715, 1983.

[Untereker et al 90] W. Untereker, F. Litvack, J. Margolis, D. Rothbaum, D. Bresnahan, K. Kenneth, F. Cummins, "ELCA Investigators: Excimer Laser Coronary Angioplasty of Saphenous Vein Grafts," Circulation (abstract) **82(4)**:680, 1990.

[Valderrama et al 89] G.L. Valderrama, R.F. Menefee, B.D. Krenek, M.J. Berry, "Chemical Laser Interactions with Human Corneal Tissue," in Thermal and Optical Interactions with Biological and Related Composite Materials, SPIE Proc. **1064**, 1989.

[Valderrama et al 90] G.L. Valderrama, R.F. Menefee, B.D. Krenek, M.J. Berry, "Chemical Laser Interactions with Human Cardiovascular Tissue," in Laser-Tissue Interaction, S. Jacques, ed., SPIE Proc. **1202**, 1990.

[Van Stryland 80] E.W. Van Stryland, M.J. Soileau, A.L. Smirl, W.E. Williams, "Pulse-Width and Focal-Volume Dependence of Laser-Induced Breakdown," Phys. Rev. B **23**:2144-2151, 1980.

[van Gemert et al 85] M.J.C. van Gemert, G.A.C.M. Schets, E.G. Stassen, J.J Bonnier, "Modeling of (Coronary) Laser-Angioplasty," Las. Surg. Med. **5**:219-234, 1985.

[van Gemert et al 87] M.J.C. van Gemert, W.M. Star, "Relations Between the Kubelka-Munk and the Transport Equation Models for Anisotropic Scattering," Las. Lif. Sci. **1**:287-298, 1987.

[van Gemert et al 89] M.J.C. van Gemert, S.L. Jacques, H.J.C.M. Sterenborg, W.M. Star, "Skin Optics," IEEE Trans. Biomed. Eng. **36**:1146-1154, 1989.

[Vaughan 70] J.M. Vaughan, **The Physiology of Bone**, Clarendon Press, Oxford, 1970.

[Walsh 88] J.T. Walsh, "Pulsed Laser Ablation of Tissue: Analysis of the Removal Process and Tissue Healing," Ph.D. Dissertation, M.I.T. Archives, 1988.

[Walsh et al 88] J.T. Walsh, T.J. Flotte, R.R. Anderson, T.F. Deutsch, "Pulsed CO_2 Laser Tissue Ablation: Effect of Tissue Type and Pulse Duration on Thermal Damage," Las. Surg. Med. **8**:108-118, 1988.

[Walsh et al 90] J.T. Walsh, J.P. Cummings, "Effect of Pulse Repetition Rate on Erbuim Laser Ablation of Soft and Hard Tissues," in Laser-Tissue Interaction, S. Jacques, ed., Proc. SPIE **1202**:12-21, 1990.

[Walsh et al 91] J.T. Walsh, T.F. Deutsch, "Measurement of Er:YAG Laser Ablation Plume Dynamics," Appl. Phys. B, in press, 1991.

[Weast 78] R. Weast. ed., **CRC Handbook of Chemistry and Physics**, 58th Edition, CRC Press, West Palm Beach, 1978.

[Welch et al 87] A.J. Welch, G. Yoon, M.J.C. van Gemert, "Practical Models for Light Distribution in Laser-Irradiated Tissue," Las. Surg. Med. **6**:488-493, 1987.

[White et al 87] R.A. White, W.S. Grundfest, **Lasers in Cardiovascular Disease**, Year Book Medical Publishers, Chicago, 1987.

[Willenborg 89] G.C. Willenborg, "Dental Laser Applications: Emerging to Maturity," Las. Surg. Med. **9**:309-313, 1989.

[Wilson et al 90] B.C. Wilson, S.L. Jacques, "Optical Reflectance and Transmittance of Tissues: Principles and Applications," IEEE J. Quant. Elect. **QE-26**:2186-2199, 1990.

[Windholtz 83] M. Windholtz, ed., **The Merck Index**, Merck & Co., Rathway, N.J., 1983, p. 233.

[Wolbarsht 84] M. Wolbarsht, "Laser Surgery: CO_2 or HF," IEEE J. Quant. Elect. **QE-20**:1427-1432, 1984.

[Wright et al 90] W.H. Wright, G.J. Sonek, Y. Tadie, M.W. Berns, "Laser Trapping in Cell Biology," IEEE J. Quant. Elect. **QE-26**:2148-2157, 1990.

[Yannas 72] I.V. Yannas, "Collagen and Gelatin in the Solid State," J. Macromol. Sci.-Revs. Macromol. Chem. **C7**:49-104, 1972.

[Yoon et al 87] G. Yoon, A.J. Welch, M. Motamedi, M.C.J. van Gemert, "Development and Application of Three-Dimensional Light Distribution Model for Laser Irradiated Tissue," IEEE J. Quant. Elect. **QE-23**:1721-1733, 1987.

[Yow et al 89] L. Yow, J.S. Nelson, M.W. Berns, "Ablation of Bone and Polymethylmethacrylate by an XeCl (308 nm) Excimer Laser," Las. Surg. Med. **9**:141-147, 1989.

[Zysset et al 89] B. Zysset, J.G. Fujimoto, C.A. Puliafito, R. Birngruber, T.F. Deutsch, "Picosecond Optical Breakdown: Tissue Effects and Reduction of Collateral Damage," Las. Surg. Med. **9**:193-204, 1989.